



---

Publicly Accessible Penn Dissertations

---


1-1-2013

# Approaches to Mitigate Metal Catalyst Deactivation in Solid Oxide Fuel Cell (SofC) Fuel Electrodes

Lawrence Adijanto

*University of Pennsylvania*, [adijanto@seas.upenn.edu](mailto:adijanto@seas.upenn.edu)

Follow this and additional works at: <http://repository.upenn.edu/edissertations>

 Part of the [Chemical Engineering Commons](#), [Nanoscience and Nanotechnology Commons](#), and the [Oil, Gas, and Energy Commons](#)

---

## Recommended Citation

Adijanto, Lawrence, "Approaches to Mitigate Metal Catalyst Deactivation in Solid Oxide Fuel Cell (SofC) Fuel Electrodes" (2013). *Publicly Accessible Penn Dissertations*. 728.  
<http://repository.upenn.edu/edissertations/728>

This paper is posted at ScholarlyCommons. <http://repository.upenn.edu/edissertations/728>  
For more information, please contact [libraryrepository@pobox.upenn.edu](mailto:libraryrepository@pobox.upenn.edu).

---

# Approaches to Mitigate Metal Catalyst Deactivation in Solid Oxide Fuel Cell (SofC) Fuel Electrodes

## **Abstract**

While Ni/YSZ cermets have been used successfully in SOFCs, they also have several limitations, thus motivating the use of highly conductive ceramics to replace the Ni components in SOFC anodes. Ceramic electrodes are promising for use in SOFC anodes because they are expected to be less susceptible to sintering and coking, be redox stable, and be more tolerant of impurities like sulfur. In this thesis, for catalytic studies, the infiltration procedure has been used to form composites which have greatly simplified the search for the best ceramics for anode applications.

In the development of ceramic fuel electrodes for SOFC, high performance can only be achieved when a transition metal catalyst is added. Because of the high operating temperatures, deactivation of the metal catalyst by sintering and/or coking is a severe problem. In this thesis, two approaches aimed at mitigating metal catalyst deactivation which was achieved by: 1) designing a catalyst that is resistant to coking and sintering and 2) developing a new method for catalyst deposition, will be presented.

The first approach involved synthesizing a self-regenerating, "smart" catalyst, in which Co, Cu, or Ni were inserted into the B-site of a perovskite oxide under oxidizing conditions and then brought back to the surface under reducing conditions. This restores lost surface area of sintered metal particles through an oxidation/reduction cycle. Results will be shown for each of the metals, as well as for Cu-Co mixed metal systems, which are found to exhibit good tolerance to carbon deposition and interesting catalytic properties.

The second strategy involves depositing novel Pd@CeO<sub>2</sub> core-shell nanostructure catalysts onto a substrate surface which had been chemically modified to anchor the nanoparticles. The catalyst deposited onto the chemically modified, hydrophobic surface is shown to be uniform and well dispersed, and exhibit excellent thermal stability to temperatures as high as 1373 K. Similar metal catalyst deposition method was also employed to access their suitability for use in SOFC anodes.

## **Degree Type**

Dissertation

## **Degree Name**

Doctor of Philosophy (PhD)

## **Graduate Group**

Chemical and Biomolecular Engineering

## **First Advisor**

Raymond J. Gorte

## **Second Advisor**

John M. Vohs

---

**Keywords**

catalyst, ceramic anode, core-shell nanostructures, intelligent catalyst, solid oxide fuel cells, vanadates

**Subject Categories**

Chemical Engineering | Nanoscience and Nanotechnology | Oil, Gas, and Energy

**APPROACHES TO MITIGATE METAL CATALYST DEACTIVATION IN  
SOLID OXIDE FUEL CELL (SOFC) FUEL ELECTRODES**

Lawrence Adjianto

A DISSERTATION

in

Chemical and Biomolecular Engineering

Presented to the Faculties of the University of Pennsylvania

in Partial Fulfillment of the Requirements for the

Degree of Doctor of Philosophy

2013

Supervisor of Dissertation

Co-Supervisor of Dissertation

---

Raymond J. Gorte, Professor, CBE

---

John M. Vohs, Professor, CBE

Graduate Group Chairperson

---

Raymond J. Gorte, Professor, Chemical and Biomolecular Engineering

Dissertation Committee

Warren D. Seider, Professor, Chemical and Biomolecular Engineering

Paulo E. Arratia, Associate Professor, Mechanical Engineering and Applied Mechanics

*This work is dedicated to my Family*

*With Thanks to Professor Ray Gorte and Professor John Vohs*

## **Acknowledgements**

First and foremost, I would like to express my sincere appreciation to my thesis advisors, Professor Ray Gorte and Professor John Vohs, for their unconditional support, guidance, patience, and encouragement throughout my research work. I would also like to thank all the students that I have worked with during the past four years, particularly, Venu Balaji Padmanabhan. Moreover, I want to give thanks to my committee, Professor Warren Seider and Professor Paulo Arratia for their support and guidance.

My appreciation likewise extends to my colleagues and friends as they are the sources of laughter, joy, and support. My life at Penn would not have been the same without them. I particularly wish to offer my special thanks to:

- Dr. Rainer Küngas, who has been an inspiring, supportive, and patient role model to me, for always entertaining even my trivial questions.
- Dr. Matteo Cargnello for always being there for discussion, tennis and meals at Han Dynasty.
- Lu Yao and Kwadwo Tettey for your time and support during my job search.
- Ami Tiyaboonchai for always providing great support in all my struggles and frustrations in my life and studies.

In addition, I wish to thank the financial support for this project, which was provided by the Office of Naval Research (N00014-11-1-0229), and the U.S. Department of Energy, Office of Basic Energy Sciences (DE-FG02-13ER16380).

Finally, my deepest gratitude goes to my family for their love and support throughout my life. Without whom I could not have made it here.

## ABSTRACT

### APPROACHES TO MITIGATE METAL CATALYST DEACTIVATION IN SOLID OXIDE FUEL CELL (SOFC) FUEL ELECTRODES

Lawrence Adjanto

Raymond J. Gorte

John M. Vohs

While Ni/YSZ cermets have been used successfully in SOFCs, they also have several limitations, thus motivating the use of highly conductive ceramics to replace the Ni components in SOFC anodes. Ceramic electrodes are promising for use in SOFC anodes because they are expected to be less susceptible to sintering and coking, be redox stable, and be more tolerant of impurities like sulfur. In this thesis, for catalytic studies, the infiltration procedure has been used to form composites which have greatly simplified the search for the best ceramics for anode applications.

In the development of ceramic fuel electrodes for SOFC, high performance can only be achieved when a transition metal catalyst is added. Because of the high operating temperatures, deactivation of the metal catalyst by sintering and/or coking is a severe problem. In this thesis, two approaches aimed at mitigating metal catalyst deactivation

which was achieved by: 1) designing a catalyst that is resistant to coking and sintering and 2) developing a new method for catalyst deposition, will be presented.

The first approach involved synthesizing a self-regenerating, “smart” catalyst, in which Co, Cu, or Ni were inserted into the B-site of a perovskite oxide under oxidizing conditions and then brought back to the surface under reducing conditions. This restores lost surface area of sintered metal particles through an oxidation/reduction cycle. Results will be shown for each of the metals, as well as for Cu-Co mixed metal systems, which are found to exhibit good tolerance to carbon deposition and interesting catalytic properties.

The second strategy involves depositing novel Pd@CeO<sub>2</sub> core-shell nanostructure catalysts onto a substrate surface which had been chemically modified to anchor the nanoparticles. The catalyst deposited onto the chemically modified, hydrophobic surface is shown to be uniform and well dispersed, and exhibit excellent thermal stability to temperatures as high as 1373 K. Similar metal catalyst deposition method was also employed to access their suitability for use in SOFC anodes.



## Table of Contents

|  |    |
|--|----|
| <b>Chapter 1. Introduction</b>                         | 1  |
| 1.1 Motivation   | 1  |
| 1.2 Solid Oxide Fuel Cells (SOFCs)                     | 2  |
| 1.2.1 SOFC Operating Principles                        | 2  |
| 1.2.2 Three-Phase Boundary (TPB)                       | 5  |
| 1.3 Materials for SOFC                                 | 5  |
| 1.3.1 Perovskite Materials                             | 6  |
| 1.3.2 Cathode (air electrode)                          | 7  |
| 1.3.3 Electrolyte                                      | 9  |
| 1.3.4 Interconnect                                     | 10 |
| 1.3.5 Anode (fuel electrode)                           | 11 |
| 1.4 Ceramic Electrodes as Alternative Anode Materials  | 12 |
| 1.5 Approaches to Mitigate Metal Catalyst Deactivation | 13 |
| 1.6 References   | 15 |
| <b>Chapter 2. Experimental Techniques</b>              | 26 |
| 2.1 Materials Synthesis                                | 26 |
| 2.1.1 Mixed Oxides                                     | 26 |
| 2.1.2 Pd@CeO <sub>2</sub> Core-Shell Nanostructures    | 26 |
| 2.2 Fuel Cell Preparation                              | 27 |
| 2.2.1 Tape Casting                                     | 28 |
| 2.2.2 Cell Assembly Sintering                          | 30 |

|   |           |
|---|-----------|
| 2.2.3 Cathode Preparation   | 30        |
| 2.2.4 Anode Preparation   | 31        |
| 2.2.5 Preparation for Testing   | 31        |
| 2.2.6 Advantages of the Infiltration Method over Traditional Method         | 31        |
| 2.3 Cell Performance Measurements   | 33        |
| 2.3.1 V-i Polarization Curves   | 33        |
| 2.3.2 Electrochemical Impedance Spectroscopy                                | 34        |
| 2.4 Composite Slabs   | 36        |
| 2.5 Surface Chemical Modification of Metal Oxide Powders or Planar Supports | 36        |
| 2.5.1 Liquid Silanization   | 36        |
| 2.5.2 Gas Silanization  | 37        |
| 2.5.3 Liquid Phosphonation  | 37        |
| 2.6 Materials Characterization Techniques                                   | 38        |
| 2.6.1 Electrical Conductivity Measurements (4 Point DC-Probe)               | 38        |
| 2.6.2 X-Ray Diffraction (XRD)   | 38        |
| 2.6.3 Scanning Electron Microscopy (SEM)                                    | 39        |
| 2.6.4 BET Surface Area Measurements   | 39        |
| 2.6.5 Atomic Force Microscopy (AFM)   | 39        |
| 2.6.6 Coulometric Titration   | 40        |
| 2.7 References  | 43        |
| <b>Chapter 3. SOFC Anodes Based on Infiltration of Tungsten Bronzes</b>     | <b>48</b> |
| 3.1 Introduction  | 49        |

|   |            |
|---|------------|
| 3.2 Experimental  | 51         |
| 3.3 Results   | 54         |
| 3.4 Discussion  | 71         |
| 3.5 Conclusion  | 73         |
| 3.6 References  | 74         |
| <b>Chapter 4. Physical and Electrochemical Properties of Alkaline Earth Doped, Rare Earth Vanadates</b>         | <b>81</b>  |
| 4.1 Introduction  | 82         |
| 4.2 Experimental  | 83         |
| 4.3 Results and Discussion  | 86         |
| 4.4 Conclusion  | 102        |
| 4.5 References  | 103        |
| <b>Chapter 5. Transition Metal-Doped Rare Earth Vanadates: A Regenerable Catalytic Material for SOFC Anodes</b> | <b>108</b> |
| 5.1 Introduction  | 109        |
| 5.2 Experimental  | 111        |
| 5.3 Results and Discussion  | 113        |
| 5.4 Summary and Conclusion  | 129        |
| 5.5 References  | 132        |
| <b>Chapter 6. Polarization-Induced Hysteresis in (CuCo)-Doped Rare Earth Vanadates SOFC Anodes</b>              | <b>139</b> |
| 6.1 Introduction  | 140        |
| 6.2 Experimental  | 141        |
| 6.3 Results and Discussion  | 143        |

|  |     |
|--|-----|
| 6.4 Conclusion   | 156 |
| 6.5 References   | 158 |
| <b>Chapter 7. Exceptional Thermal Stability of Pd@CeO<sub>2</sub> Core-Shell Catalyst Nanostructures Grafted onto an Oxide Surface</b>   | 163 |
| 7.1 Introduction   | 164 |
| 7.2 Experimental   | 164 |
| 7.3 Results and Discussion   | 167 |
| 7.4 Conclusion   | 182 |
| 7.5 References   | 183 |
| <b>Chapter 8. Synthesis and Stability of Monolayer Films of Pd@CeO<sub>2</sub> Core-Shell Catalysts for Solid Oxide Fuel Cell Anodes</b>   | 187 |
| 8.1 Introduction   | 188 |
| 8.2 Experimental   | 189 |
| 8.3 Results and Discussion   | 192 |
| 8.4 Conclusion   | 212 |
| 8.5 References   | 214 |
| <b>Chapter 9. Stability and Performance of Infiltrated La<sub>0.8</sub>Sr<sub>0.2</sub>Co<sub>x</sub>Fe<sub>1-x</sub>O<sub>3</sub> Electrodes with and without Sm<sub>0.2</sub>Ce<sub>0.8</sub>O<sub>1.9</sub> Interlayers</b> | 216 |
| 9.1 Introduction   | 217 |
| 9.2 Experimental   | 220 |
| 9.3 Results and Discussion   | 222 |
| 9.4 Conclusion   | 234 |
| 9.5 References   | 235 |
| <b>Chapter 10. Conclusions</b>   | 241 |

## List of Tables

|                  |  |     |
|------------------|--|-----|
| <b>Table 1.1</b> | Perovskite materials used for different cell components.   | 7   |
| <b>Table 3.1</b> | Summary of the electronic conductivities of the bronze-YSZ composites used in this study reduced in H <sub>2</sub> (3% H <sub>2</sub> O).  | 66  |
| <b>Table 4.1</b> | AE solubility limit in various REAEVO <sub>4</sub> materials.  | 89  |
| <b>Table 4.2</b> | Specific surface areas of Ce <sub>0.7</sub> Sr <sub>0.3</sub> VO <sub>3.85</sub> -YSZ composites fabricated at 973 K, before and after reduction.  | 97  |
| <b>Table 5.1</b> | Transition metal solubility limit in Ce <sub>1-x</sub> TM <sub>x</sub> VO <sub>4-0.5x</sub> .  | 115 |
| <b>Table 5.2</b> | BET surface areas of Ce <sub>0.8</sub> Ni <sub>0.2</sub> VO <sub>3.90</sub> -YSZ composites.   | 119 |
| <b>Table 5.3</b> | The percentage weight changes measured after reducing the samples in humidified H <sub>2</sub> at 973 K for 2 h before exposing them to dry methane at 973 K for 3 h.  | 121 |
| <b>Table 5.4</b> | Maximum power density and anode ASR.   | 124 |
| <b>Table 6.1</b> | Percentage weight changes after exposure to dry CH <sub>4</sub> at 1073 K for 3 h.   | 147 |
| <b>Table 7.1</b> | Ellipsometry thickness and water contact angle measurements.   | 174 |
| <b>Table 8.1</b> | Electrochemical performance of cells with various anode compositions. The anodes were fabricated by impregnation. All the fuel cells are 45 wt. % La <sub>0.8</sub> Sr <sub>0.2</sub> Cr <sub>0.5</sub> Mn <sub>0.05</sub> O <sub>3</sub> -YSZ composite anodes. The anode ASR can be obtained by subtracting from the total resistance the ohmic (0.3 Ω cm <sup>2</sup> ) and cathode (0.2 Ω cm <sup>2</sup> ) contributions. | 199 |

## List of Figures

|                   |  |    |
|-------------------|--|----|
| <b>Figure 1.1</b> | The operating principle of a solid oxide fuel cell.  | 4  |
| <b>Figure 2.1</b> | Cell fabrication by tape-casting and infiltration.   | 28 |
| <b>Figure 2.2</b> | An example V-i polarization curve of an SOFC.  | 34 |
| <b>Figure 2.3</b> | An example electrochemical impedance spectra from an SOFC.   | 35 |
| <b>Figure 2.4</b> | Schematic of Coulometric Titration apparatus.  | 41 |
| <b>Figure 3.1</b> | Colors of $\text{Na}_x\text{WO}_3$ at different x values.  | 50 |
| <b>Figure 3.2</b> | XRD patterns of $\text{Na}_{0.8}\text{WO}_{3-\delta}$ synthesized in humidified (3% $\text{H}_2\text{O}$ ) $\text{H}_2$ at following temperatures: a) 823 K b) 973 K c) 1023 K d) 1073 K, and e) 1123K.  | 54 |
| <b>Figure 3.3</b> | XRD patterns of $\text{Na}_{0.8}\text{WO}_{3-\delta}$ that were a) reduced at 973 K under humidified (3% $\text{H}_2\text{O}$ ) $\text{H}_2$ , b) oxidized at 973 K in air, and c) then re-reduced.  | 57 |
| <b>Figure 3.4</b> | XRD patterns of a) YSZ, b) reduced $\text{Na}_{0.8}\text{WO}_{3-\delta}$ , and c) mixed $\text{Na}_{0.8}\text{WO}_{3-\delta}$ with YSZ reduced at 1023K under humidified (3% $\text{H}_2\text{O}$ ) $\text{H}_2$ .   | 59 |
| <b>Figure 3.5</b> | XRD patterns of a) $\text{K}_{0.5}\text{WO}_{3-\delta}$ , b) $\text{Rb}_{0.2}\text{WO}_{3-\delta}$ , and c) $\text{Cs}_{0.2}\text{WO}_{3-\delta}$ synthesized in humidified (3% $\text{H}_2\text{O}$ ) $\text{H}_2$ at 973 K and 1073K.  | 61 |
| <b>Figure 3.6</b> | XRD patterns of $\text{Na}_{0.8}\text{Nb}_y\text{W}_{1-y}\text{O}_{3-\delta}$ -YSZ composite with different Nb:W ratios ( $y = 0, 0.3, 0.7, 1$ ) synthesized in humidified (3% $\text{H}_2\text{O}$ ) $\text{H}_2$ at following temperatures: a) 973 K, and b) 1123 K.   | 63 |
| <b>Figure 3.7</b> | Electrical conductivities of the 40 wt. % (■) $\text{Na}_{0.8}\text{WO}_{3-\delta}$ -YSZ (♦) $\text{Na}_{0.8}\text{Nb}_{0.3}\text{W}_{0.7}\text{O}_{3-\delta}$ -YSZ, (●) $\text{Na}_{0.8}\text{Nb}_{0.7}\text{W}_{0.3}\text{O}_{3-\delta}$ -YSZ, and (▲) $\text{NaNbO}_{3-\delta}$ -YSZ composites in humidified (3% $\text{H}_2\text{O}$ ) $\text{H}_2$ as a function of temperature. Data were obtained (■, ♦, ●, ▲) on heating and (□, ◇, ○, Δ) on cooling. | 65 |
| <b>Figure 3.8</b> | Microstructure of the (a) YSZ matrix, $\text{Na}_{0.8}\text{WO}_{3-\delta}$ -YSZ composite reduced at following temperatures: (b) 973 K and (c) 1123 K, d) $\text{Na}_{0.8}\text{Nb}_{0.3}\text{W}_{0.7}\text{O}_{3-\delta}$ -YSZ composite, and e) $\text{Na}_{0.8}\text{Nb}_{0.7}\text{W}_{0.3}\text{O}_{3-\delta}$ -YSZ composite reduced at 1123 K in humidified (3% $\text{H}_2\text{O}$ ) $\text{H}_2$ .   | 67 |
| <b>Figure 3.9</b> | (a) V-i polarization curves and (b) electrochemical impedance spectra of cells with infiltrated $\text{Na}_{0.8}\text{WO}_{3-\delta}$ anode (▲) with and   |    |

(●)without Pd catalyst, and (◆) with Pd after exposure to humidified H<sub>2</sub> at 1123 K, operated at 973 K under humidified (3% H<sub>2</sub>O) H<sub>2</sub>. 69

|                   |   |     |
|-------------------|---|-----|
| <b>Figure 4.1</b> | XRD patterns of Ce <sub>1-x</sub> Sr <sub>x</sub> VO <sub>4-0.5x</sub> -YSZ composites with different Ce:Sr ratios (x=0, 0.3, 0.5, 0.7, 1) that were calcined in air at 973 K. The peaks labeled ● and ▲ correspond to Ce <sub>1-x</sub> Sr <sub>x</sub> VO <sub>4-0.5x</sub> and ▲, respectively.  | 87  |
| <b>Figure 4.2</b> | Plots of the position of the (200) diffraction peak as a function of x for both Ce <sub>1-x</sub> Sr <sub>x</sub> VO <sub>4-0.5x</sub> and Ce <sub>1-x</sub> Ca <sub>x</sub> VO <sub>4-0.5x</sub> .   | 88  |
| <b>Figure 4.3</b> | XRD patterns of oxidized and reduced cerium-strontium vanadate: The peaks are labeled as follows: (□) zircon Ce <sub>0.7</sub> Sr <sub>0.3</sub> VO <sub>3.85</sub> , (●) perovskite Ce <sub>0.7</sub> Sr <sub>0.3</sub> VO <sub>3.0</sub> , and (▲) cubic YSZ.   | 91  |
| <b>Figure 4.4</b> | Coulometric titration isotherms for (□) LaVO <sub>4</sub> , (○) PrVO <sub>4</sub> , (◇) CeVO <sub>4</sub> , (▲) Ce <sub>0.7</sub> Sr <sub>0.3</sub> VO <sub>3.85</sub> , and (■) Ce <sub>0.7</sub> Ca <sub>0.3</sub> VO <sub>3.85</sub> , at 973 K.   | 92  |
| <b>Figure 4.5</b> | Electronic conductivities of 30 wt. % (■) LaVO <sub>3</sub> -, (▲) CeVO <sub>3</sub> -, (●) PrVO <sub>3</sub> -, (◆) SmVO <sub>3</sub> -, (+) La <sub>0.7</sub> Sr <sub>0.3</sub> VO <sub>3</sub> -, (×) Ce <sub>0.7</sub> Sr <sub>0.3</sub> VO <sub>3</sub> -, (□) La <sub>0.7</sub> Ca <sub>0.3</sub> VO <sub>3</sub> -, (Δ) Ce <sub>0.7</sub> Ca <sub>0.3</sub> VO <sub>3</sub> -, (○) Pr <sub>0.7</sub> Ca <sub>0.3</sub> VO <sub>3</sub> - YSZ composites in humidified H <sub>2</sub> as a function of temperature. | 94  |
| <b>Figure 4.6</b> | SEM micrographs of (a) the bare YSZ scaffold, and the Ce <sub>0.7</sub> Sr <sub>0.3</sub> VO <sub>3.85</sub> -YSZ composite calcined at 973 K (b) before and (c) after reduction in humidified H <sub>2</sub> at 973 K.   | 97  |
| <b>Figure 4.7</b> | (a) V-i polarization curves and (b) electrochemical impedance spectra of cells with infiltrated 30 wt. % of Ce <sub>0.7</sub> Sr <sub>0.3</sub> VO <sub>3.85</sub> -YSZ anodes with (Δ) and without (▲) Pd catalyst. The cells were operated at 973 K with humidifiedH <sub>2</sub> fuel.   | 100 |
| <b>Figure 5.1</b> | Panel A: Schematic of an intelligent catalyst in which metals move out of and into an oxide host lattice in response to exposure to reducing and oxidizing conditions, respectively. Panel B: Sintering of metal nanoparticles on an oxide which occurs over time for most traditional supported metal catalysts.   | 110 |
| <b>Figure 5.2</b> | XRD patterns of Ce <sub>1-x</sub> Ni <sub>x</sub> VO <sub>4-0.5x</sub> -YSZ composites that were calcined in air at 973 K for x values of 0, 0.2, 0.3, 0.4, 1. The peaks labeled▲, □ and ● correspond to YSZ, Ni <sub>2</sub> V <sub>2</sub> O <sub>7</sub> and Ce <sub>1-x</sub> Ni <sub>x</sub> VO <sub>4-0.5x</sub> , respectively.  | 114 |
| <b>Figure 5.3</b> | Plot of the position of the (112) diffraction peak as a function of x for Ce <sub>1-x</sub> Ni <sub>x</sub> VO <sub>4-0.5x</sub> .  | 115 |

|                   |   |     |
|-------------------|---|-----|
| <b>Figure 5.4</b> | XRD patterns from a $\text{Ce}_{0.8}\text{Ni}_{0.2}\text{VO}_{3.90}$ sample that was (A) oxidized at 973 K in air, (B) reduced at 973 K in humidified $\text{H}_2$ , and (C) re-oxidized in air at 973 K. The peaks are labeled as follows: ( $\blacktriangle$ ) cubic YSZ, ( $\circ$ ) zircon $\text{Ce}_{0.8}\text{Ni}_{0.2}\text{VO}_{3.90}$ , ( $\bullet$ ) perovskite $\text{Ce}_{1-x}\text{Ni}_x\text{VO}_3$ , and ( $\blacksquare$ ) metallic Ni.  | 117 |
| <b>Figure 5.5</b> | SEM images of (a) the bare YSZ matrix, and the $\text{Ce}_{0.8}\text{Ni}_{0.2}\text{VO}_{3.90}$ - YSZ composite (b) oxidized in air at 973 K, and (c) reduced in humidified $\text{H}_2$ at 973 K.  | 118 |
| <b>Figure 5.6</b> | SEM images of of the (a) $\text{CeVO}_3$ -, (b) $\text{Ce}_{0.8}\text{Ni}_{0.2}\text{VO}_3$ -, (c) $\text{Ce}_{0.8}\text{Co}_{0.2}\text{VO}_3$ -, (d) $\text{Ce}_{0.8}\text{Cu}_{0.2}\text{VO}_3$ - YSZ composites that had been exposed to dry methane at 973 K for 3 h.   | 121 |
| <b>Figure 5.7</b> | (a) V-i polarization curves and (b) electrochemical impedance spectra of cells with infiltrated 30 wt. % of ( $\bullet$ ) $\text{Ce}_{0.8}\text{Ni}_{0.2}\text{VO}_3$ -, ( $\blacksquare$ ) $\text{Ce}_{0.8}\text{Co}_{0.2}\text{VO}_3$ -, ( $\blacklozenge$ ) $\text{Ce}_{0.8}\text{Cu}_{0.2}\text{VO}_3$ -, and ( $\blacktriangle$ ) $\text{CeVO}_3$ -YSZ anodes. The cells were operated at 973 K with humidified $\text{H}_2$ fuel.   | 123 |
| <b>Figure 5.8</b> | Electronic conductivities of infiltrated 30 wt. % ( $\Delta$ ) $\text{CeVO}_3$ -, ( $\circ$ ) $\text{Ce}_{0.8}\text{Ni}_{0.2}\text{VO}_3$ -, ( $\square$ ) $\text{Ce}_{0.7}\text{Sr}_{0.1}\text{Ni}_{0.2}\text{VO}_3$ -, ( $\blacksquare$ ) $\text{Ce}_{0.7}\text{Ca}_{0.1}\text{Ni}_{0.2}\text{VO}_3$ -, ( $\blacklozenge$ ) $\text{Ce}_{0.7}\text{Sr}_{0.3}\text{VO}_3$ - YSZ composites in humidified $\text{H}_2$ as a function of temperature.   | 127 |
| <b>Figure 5.9</b> | Maximum power density for a cell with an infiltrated 30 wt. % of $\text{Ce}_{0.7}\text{Sr}_{0.1}\text{Ni}_{0.2}\text{VO}_3$ -YSZ anode as a function of time at 973 K with humidified $\text{H}_2$ (3% $\text{H}_2\text{O}$ ) fuel. The cell was periodically subjected to a redox treatment consisting of oxidation in air for 30 min followed by reduction in humidified $\text{H}_2$ for 15 min, both at 973 K.  | 128 |
| <b>Figure 6.1</b> | XRD patterns of (A) $\text{Ce}_{0.8}\text{Sr}_{0.1}\text{Cu}_{0.05}\text{Co}_{0.05}\text{VO}_{4-\delta}$ , and (B) $\text{Ce}_{0.8}\text{Sr}_{0.1}\text{Cu}_{0.05}\text{Ni}_{0.05}\text{VO}_{4-\delta}$ oxidized at 973 K in air. The peaks are labeled as follows: ( $\blacktriangle$ ) cubic YSZ, ( $\circ$ ) zircon $\text{Ce}_{0.8}\text{Sr}_{0.1}\text{Cu}_{0.05}\text{Co}_{0.05}\text{VO}_{4-\delta}$ and $\text{Ce}_{0.8}\text{Sr}_{0.1}\text{Cu}_{0.05}\text{Ni}_{0.05}\text{VO}_{4-\delta}$ .  | 144 |
| <b>Figure 6.2</b> | XRD patterns of (A) $\text{Ce}_{0.8}\text{Sr}_{0.1}\text{Cu}_{0.05}\text{Co}_{0.05}\text{VO}_3$ , (B) $\text{Ce}_{0.8}\text{Sr}_{0.1}\text{Cu}_{0.05}\text{Ni}_{0.05}\text{VO}_3$ , (C) $\text{Ce}_{0.8}\text{Sr}_{0.1}\text{Ni}_{0.1}\text{VO}_3$ , (D) $\text{Ce}_{0.8}\text{Sr}_{0.1}\text{Co}_{0.1}\text{VO}_3$ , and (E) $\text{Ce}_{0.8}\text{Sr}_{0.1}\text{Cu}_{0.1}\text{VO}_3$ reduced under humidified $\text{H}_2$ at 973 K. The dotted lines indicate the position of the Ni, Co, and Cu metal peaks. The ( $\blacktriangle$ ) peaks correspond to Sr doped- $\text{CeVO}_3$ . | 145 |
| <b>Figure 6.3</b> | SEM images of the (A) $\text{Ce}_{0.8}\text{Sr}_{0.1}\text{Cu}_{0.1}\text{VO}_3$ -, (B) $\text{Ce}_{0.8}\text{Sr}_{0.1}\text{Co}_{0.1}\text{VO}_3$ -, (C) $\text{Ce}_{0.8}\text{Sr}_{0.1}\text{Cu}_{0.05}\text{Ni}_{0.05}\text{VO}_3$ -, (D) $\text{Ce}_{0.8}\text{Sr}_{0.1}\text{Cu}_{0.05}\text{Co}_{0.05}\text{VO}_3$ -YSZ composites that had been exposed to dry methane at 1073 K for 3 h.  | 147 |



- Figure 6.4** V-i polarization curves for cells with infiltrated 30 wt. % of (—, —)  $\text{Ce}_{0.8}\text{Sr}_{0.1}\text{Cu}_{0.05}\text{Co}_{0.05}\text{VO}_3$ , (- -)  $\text{Ce}_{0.8}\text{Sr}_{0.1}\text{Co}_{0.1}\text{VO}_3$ , (- -)  $\text{Ce}_{0.8}\text{Sr}_{0.1}\text{Cu}_{0.1}\text{VO}_3$ , and (— —)  $\text{CeVO}_3$  -YSZ anodes. Inset: Electrochemical impedance spectra of  $\text{Ce}_{0.8}\text{Sr}_{0.1}\text{Cu}_{0.05}\text{Co}_{0.05}\text{VO}_3$  cell measured at (A) 0.4 V and (B) 0.2 V. The cells were operated at 973 K with humidified  $\text{H}_2$  fuel. 150
- 
- Figure 6.5** Schematic of the structure of the Cu-Co particles and the effect of polarization. 154
- 
- Figure 7.1** Overview of the deposition of Pd@CeO<sub>2</sub> nanostructures on (A) clean YSZ(100) and (B) alkyl-siloxane functionalized YSZ(100). On clean YSZ the hydrophobic, alkyl-capped Pd@CeO<sub>2</sub> particles are repelled by the hydrophilic OH-terminated YSZ surface, resulting in the formation of agglomerates during deposition, with further agglomeration occurring upon calcination in air. On the alkyl-siloxane functionalized YSZ surface, the Van der Waals interactions between the capping alkyl groups on the surface and the core-shell particles directs the formation of a monolayer film of the Pd@CeO<sub>2</sub> particles. This Pd@CeO<sub>2</sub> layer is highly stable and remains highly dispersed upon calcination in air. 168
- 
- Figure 7.2** Contact angle measurements. Image of 1  $\mu\text{L}$  water droplet placed on clean YSZ(100) substrate (Panel A) and silanated YSZ(100) substrate (Panel B) with tensiometry. Deposition of the TEOOS layer using the CVD process resulted in an increase in the water contact angle from 70° to 100°. 169
- 
- Figure 7.3** AFM characterization of clean and TEOOS-treated YSZ(100). AFM topography images with representative line scans for clean (A) YSZ(100) and (B) TEOOS-treated YSZ(100) samples. The AFM image of the plasma-cleaned YSZ(100) substrate prior to silane deposition (A) shows it to be featureless with a rms roughness of 0.07 nm which is consistent with a nearly atomically flat surface. A relatively uniform image was also obtained for the silanated/YSZ(100) sample (B), but it contained small wave-like features and had a rms roughness of 2.4 nm. 170
- 
- Figure 7.4** AFM topography images with representative line scans for Pd@CeO<sub>2</sub> and Pd nanoparticles deposited on clean and alkyl-silanated YSZ(100). Panel A corresponds to Pd@CeO<sub>2</sub> deposited on pristine YSZ(100) calcined in air 723 K. Panels B, C, D, corresponds to Pd@CeO<sub>2</sub> deposited on alkyl-siloxane functionalized YSZ(100) after calcination in air at 723 K (B), 973 K (C) and 1373 K (D). Panels E, F, and G corresponds to Pd nanoparticles deposited on pristine YSZ(100) after calcination in air at 723 K (E), 973 K (F)

and 1373 K (G). Comparison of the images for the Pd@CeO<sub>2</sub> and Pd nanoparticles clearly demonstrates the high thermal stability of the Pd@CeO<sub>2</sub> nanoparticles.

172

- 
- Figure 7.5** Ce(3d) XP spectra obtained from Pd@CeO<sub>2</sub> deposited on alkyl-siloxane functionalized YSZ(100) after calcination under different conditions. The sample was calcined in air at 723 K (A) and 973 K (B), and in ultra-high vacuum at 700 K (C). 177
- 
- Figure 7.6** CO-TPD data and schematic representation of changes in shell morphology for oxidized and reduced Pd@CeO<sub>2</sub>/YSZ(100) catalysts. The CO-TPD results obtained after 50 L CO dose at 260 K on Pd@CeO<sub>2</sub> deposited on silanated YSZ(100) calcined at 973 K in air (A) and 700 K in vacuum (B). The y-axis in the figure corresponds to the m/e 28 mass spectrometer signal in arbitrary units. The two spectra have been offset to facilitate comparison. 179
- 
- Figure 7.7** Reaction rate data for CH<sub>4</sub> oxidation. Pd@CeO<sub>2</sub> core-shell catalyst supported on (○) TEOOS-treated γ-Al<sub>2</sub>O<sub>3</sub> and (Δ) TDPA-treated γ-Al<sub>2</sub>O<sub>3</sub> calcined in air at 1123 K for 6 hrs prior to rate measurements. The Pd weight loading in each catalyst was 1 %. 181
- 
- Figure 8.1** SEM images, with the schematic representation of bare YSZ matrix (Panel A), Pd@CeO<sub>2</sub> nanoparticles deposited on: clean YSZ porous electrode (Panel B) and silanated YSZ porous electrode (Panel C). 2 nm un-coated Pd nanoparticles deposited on silanated YSZ porous electrode (Panel D). All samples calcined at 973 K in air. 193
- 
- Figure 8.2** SEM images, with the schematic representation of the agglomeration of Pd@CeO<sub>2</sub> (Panel A) and 2 nm un-coated Pd (Panel B) nanoparticles deposited on silanated YSZ porous electrode after samples calcined at 1373 K in air. 195
- 
- Figure 8.3** Image of hydrophobicity test with YSZ and LSCM, before and after treatment with TEOOS. 0.1 g of each powder was then placed in a test tube filled with 5 ml of H<sub>2</sub>O. 196
- 
- Figure 8.4** (A) V-i polarization curves and (B) electrochemical impedance spectra of cells with infiltrated 45 wt. % LSCM-YSZ (blue ◇) with and (red □) without treatment with TEOOS. Both the cells were then calcined in air at 723 K upon addition of 1 wt. % Pd to the TEOOS-treated LSCM anode by infiltration with aqueous solution of (NH<sub>3</sub>)<sub>4</sub>Pd(NO<sub>3</sub>)<sub>2</sub> to enhance the catalytic activity. In order to produce the Pd phase, both the cells were then calcined in air at 723 K before measurement at 973 K with humidified H<sub>2</sub> fuel (3% H<sub>2</sub>O). 200

|                   |   |     |
|-------------------|---|-----|
| <b>Figure 8.5</b> | (A) V-i polarization curves and (B) electrochemical impedance spectra of cells with infiltrated 45 wt. % LSCM-YSZ after treatment with TEOOS containing (orange □) Pd@CeO <sub>2</sub> and (red ◇) no catalyst. The cells were initially calcined at 723 K in air before measurement at 973 K with humidified H <sub>2</sub> fuel (3% H <sub>2</sub> O).  | 202 |
| <b>Figure 8.6</b> | (A, B) V-i polarization curves and (C) electrochemical impedance spectra of cells annealed under oxidizing conditions at higher temperatures, with infiltrated 45 wt. % LSCM-YSZ after treatment with TEOOS, containing infiltrated (Figure 8.6A) Pd@CeO <sub>2</sub> nanoparticles annealed in air at (□) 723 K and (■) 1123 K, (Figure 8.6B) 2 nm un-coated Pd nanoparticles annealed in air at (Δ) 723 K and (▲) 1123 K. The cells were operated at 973 K with humidified H <sub>2</sub> fuel (3% H <sub>2</sub> O).   | 205 |
| <b>Figure 8.7</b> | (A, B) V-i polarization curves and (C) electrochemical impedance spectra of cells annealed under reducing conditions at higher temperatures, with infiltrated 45 wt. % LSCM-YSZ after treatment with TEOOS, containing infiltrated (Figure 8.7A) Pd@CeO <sub>2</sub> nanoparticles (□) before 1073 K and (■) after 1073 K treatment in humidified H <sub>2</sub> , (Figure 8.7B) 2 nm un-coated Pd nanoparticles (□) before 1073 K and (■) after 1073 K treatment in humidified H <sub>2</sub> . The cells were initially calcined at 723 K in air before measurement at 973 K with humidified H <sub>2</sub> fuel (3% H <sub>2</sub> O). | 208 |
| <b>Figure 8.8</b> | V-i polarization curves of with infiltrated 45 wt. % LSCM-YSZ after treatment with TEOOS, containing infiltrated (□) Pd@CeO <sub>2</sub> and (◇) 2 nm un-coated Pd nanoparticles calcined at 723 K and 1123 K in air, and (○) no catalyst. Measurements were taken at 973 K in dry CH <sub>4</sub> .  | 211 |
| <b>Figure 9.1</b> | XRD patterns of La <sub>0.8</sub> Sr <sub>0.2</sub> Co <sub>x</sub> Fe <sub>1-x</sub> O <sub>3</sub> -YSZ composites that had been calcined to 1123 K with the indicated compositions. The peak positions correspond to: ●-La <sub>2</sub> Zr <sub>2</sub> O <sub>7</sub> , ■-SrZrO <sub>3</sub> , ◇-YSZ, and Δ-La <sub>0.8</sub> Sr <sub>0.2</sub> Co <sub>x</sub> Fe <sub>1-x</sub> O <sub>3</sub> .  | 223 |
| <b>Figure 9.2</b> | XRD patterns of La <sub>0.8</sub> Sr <sub>0.2</sub> Co <sub>x</sub> Fe <sub>1-x</sub> O <sub>3</sub> -YSZ composites that had been calcined to 1373 K with the indicated compositions. The peak positions correspond to: ●-La <sub>2</sub> Zr <sub>2</sub> O <sub>7</sub> , ■-SrZrO <sub>3</sub> , ◇-YSZ, and Δ-La <sub>0.8</sub> Sr <sub>0.2</sub> Co <sub>x</sub> Fe <sub>1-x</sub> O <sub>3</sub> .  | 224 |
| <b>Figure 9.3</b> | a) Performance curves and b) Electrochemical impedance spectra obtained at open circuit for fuel cells with infiltrated LSCF cathodes that had been calcined at 1123 K. The composition of the LSCF used in each cell is indicated in the figure.   | 226 |

**Figure 9.4** a) Performance curves and b) Electrochemical impedance spectra obtained at open circuit for fuel cells with infiltrated LSCF cathodes that had been calcined at 1373 K. The composition of the LSCF used in each cell is indicated in the figure.

228

---

**Figure 9.5** Electrochemical impedance spectra obtained at open circuit for fuel cells with infiltrated LSC, LSC20F, and LSF cathodes with (open symbols) and without (filled symbols) infiltrated SDC interlayers. The cathodes were calcined at 1373 K prior to collecting the data.

231

# **Chapter 1. Introduction**

## **Summary**

A general introduction on fuel cells will be discussed in this chapter. This includes the Solid Oxide Fuel Cell (SOFC) operating principles, the cell components, the advantages and the drawbacks of the current state-of-the-art anode materials. The goals of this thesis will also be presented.

## **1.1 Motivation**

Global demand for energy is rising rapidly due to the increase in industrialization and world population. Additionally, rising concerns in the world today regarding environmental issues have motivated the search for a cleaner, more efficient and sustainable system for power generation. Fuel cells are electrochemical devices that are capable of achieving very high efficiencies in the conversion of chemical to electrical energy. In addition, Fuel cells are of great interest as they are capable of providing a much cleaner and more consistent source of energy.

Thermal power plants are currently the most prevalent source of energy generation. The production of electrical energy in these power plants relies on firstly converting heat into mechanical energy which is then subsequently converted to electrical energy. In comparison, Fuel cells are able to convert chemical energy directly to electrical energy. Therefore, fuel cells are not limited by the Carnot cycle and are generally significantly more efficient than electrical energy production by thermal power plants<sup>1-6</sup>. Furthermore, steam turbines can be incorporated into fuel cells that operate at

higher temperatures to recover some of the waste heat<sup>5,7-10</sup>. The overall efficiency for the combine heat and power (CHP) generation system can be enhanced to above 80 %<sup>4,5,8-10</sup>.

The properties and applications of many types of fuel cell are determined by the chemical nature of the electrolyte material that is used. Most Fuel cells, for example, the Polymer Exchange Membrane Fuel Cells (PEMFCs), rely on the conduction of protons due to the use of the hydrated proton-conducting polymers as the electrolyte. In order for hydrocarbons to be used as a fuel for these types of fuel cells, they must first be reformed to H<sub>2</sub>. On the other hand, Solid Oxide Fuel Cells (SOFCs) offer a key advantage over many other fuel cell types because of their inherent fuel flexibility. This is firstly due to the fact that the membrane is an oxygen ion conductor and secondly because SOFC cells operate at high temperatures (typically above 700°C)<sup>6,11,12</sup>. The high operating temperatures accelerate electrode reaction rates, allowing SOFCs to operate on hydrocarbon fuels after a relatively simple reforming process<sup>2,11,12</sup>. In the next sections, the operating principles and the basic cell components of the SOFC will be discussed.

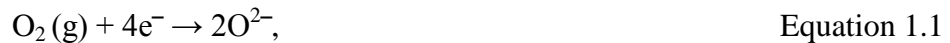
## **1.2 Solid Oxide Fuel Cells**

### **1.2.1 SOFC Operating Principles**

SOFC is a solid-state electrochemical device that directly converts chemical energy to produce electrical energy through a chemical reaction between a fuel and an oxidant. Like other fuel cells, SOFCs consist of three components: two electrodes, a cathode and an anode, and a solid electrolyte, as shown in Figure 1.1. The two electrodes are separated by an electrolyte membrane that allows only ionic transport from one electrode to the other. Ideally, the electrolyte membrane used should exhibit high ionic

conductivity with negligible electronic conductivity. In addition, it must be dense and leak free to separate the direct combustion of the fuel at the fuel electrode from oxygen at the air electrode.

During the operation of a fuel cell, gas phase oxygen molecules first diffuse into the cathode where it is electrochemically reduced by electrons (from the external circuit) into oxygen anions as shown in Equation 1.1.

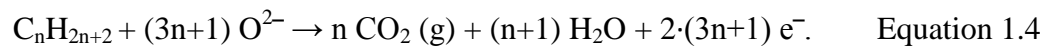


The oxygen anions are then conducted through the ceramic electrolyte by a defect hopping mechanism<sup>5,6</sup> before reaching the anode. Fuel, which can be H<sub>2</sub> or any hydrocarbons (e.g. CO or CH<sub>4</sub>) is fed to the anode where it is oxidized by the oxygen anions supplied from the electrolyte membrane to produce steam and/or carbon dioxide.

At the same time electrons are released to the external circuit:



in the case of hydrocarbon fuels,



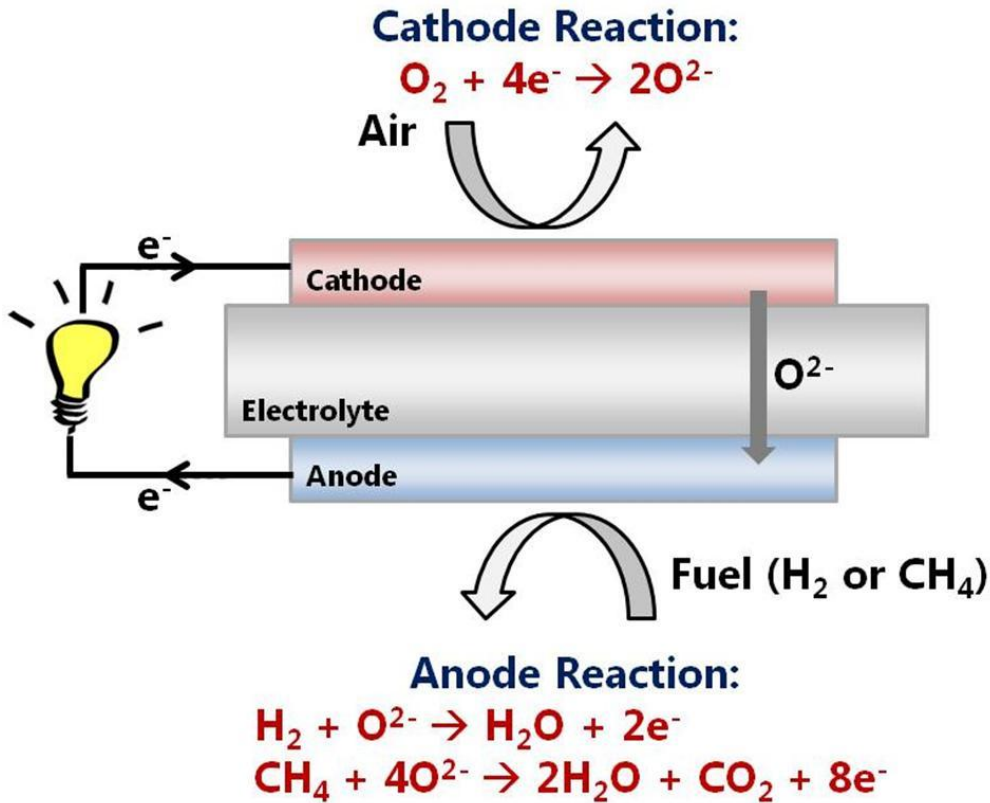


**Figure 1.1** The operating principle of a solid oxide fuel cell.

In an ideal SOFC, the driving force for oxygen ion diffusion is the difference in the oxygen chemical potential between the air and the fuel sides of the electrolyte. This is in turn related to the  $O_2$  fugacities at the cathode and anode. For example, the  $H_2$  oxidation reaction at open circuit would be approximately 1 V when the cell is not loaded, as defined by the Nernst potential given in Equation 1.5:

$$V_{Nernst} = V^o + \frac{RT}{2F} * \ln \left( \frac{P_{H_2,anode} * (P_{O_2,cathode})^{1/2}}{P_{H_2O,anode}} \right) \quad \text{Equation 1.5}$$

where  $V^o$  is the equilibrium potential at standard conditions, and  $F$  is the Faraday constant, the number of Coulombs in a mole of electrons. Multiple SOFC units can be connected in series in order to increase the voltage and power output of the system.



### **1.2.2 Three-Phase Boundary (TPB)**

The microstructure of the composite electrode is one of the key factors to achieve high performance as an ideal microstructure would offer the highest three-phase boundary (TPB) length for electrochemical reactions<sup>13-19</sup>. As shown in Equations 1.2 to 1.4, it is apparent that the gas phase hydrogen/hydrocarbon molecules, oxygen anions from the  $((Y_2O_3)_{0.08}-(ZrO_2)_{0.92})$  abbreviated as YSZ) YSZ electrolyte, and the electrons from the conductive electrode must all be present for the oxidation reaction to occur. For example, the current standard anode material with SOFC based on YSZ as the electrolyte is a Ni-YSZ ceramic-metallic (cermet) composite. The Ni in this composite provides electronic conductivity and catalytic activity, while the YSZ helps maintain porosity in the electrode and provides ionic conductivity to extend the TPB region. This concept also applies for the cathode where the use of composite cathodes will increase the number of oxygen reduction reactions due to the increase in TPB.

### **1.3 Materials for SOFC**

The basic components of a SOFC comprise of the electrolyte, the anode, the cathode and the interconnect. The criteria and current state-of-the-art materials for the cell components of SOFC will be reviewed in the next sections. In addition, as many of the promising oxides used for the cell components of SOFCs have a perovskite-related structure, the structure and properties of perovskite materials will first be discussed.

### 1.3.1 Perovskite Materials

Perovskite oxide materials have a general formula of  $ABO_3$ , where the A-site contains rare-earth or alkaline-earth metals such as lanthanum (La) or strontium (Sr) while the B-site contains transition metals such as iron (Fe), chromium (Cr), and titanium (Ti). The A-sites (corner of the unit cell) are generally occupied by larger cations while the B-sites (cube center) are occupied by the smaller cations.

Both A- and B-site substitutions have been investigated extensively because they can alter the properties of the oxide including the thermal expansion coefficient, the electronic or ionic conductivity, and the chemical stability and compatibility with other cell components of SOFCs<sup>20,21</sup>. For example, for Fe-based compositions such as  $LaFeO_3$ , partial substitution of divalent cations like Sr or Ca for trivalent La creates oxygen vacancies while substitution of Co for Fe results in enhanced electronic conductivity<sup>16,20-22</sup>. While these perovskite materials are a promising cathode material for intermediate temperature SOFCs, unfortunately, the Fe- or Co-based perovskites are not stable at very low oxygen partial pressures which make them unsuitable for use in the fuel electrode operating conditions required for anode materials.

A similar strategy can be applied to design perovskite materials that are stable and compatible for SOFC anodes. For instance, one of the most promising perovskites that are stable under these conditions is the lanthanum-chromite perovskites which is used as the SOFC interconnect (described in more detail in Section 1.2.3.4)<sup>23,24</sup>. In a study by Irvine and Tao, different transition elements such as V, Mn, Fe, Co, Ni, and Cu were introduced into the B-sites of the Sr-doped  $LaCrO_3$ . They found that

$\text{La}_{0.75}\text{Sr}_{0.25}\text{Cr}_{0.5}\text{Mn}_{0.5}\text{O}_3$  is not just stable in both fuel and air conditions, they also show stable electrode performance in methane<sup>25,26</sup>.

A wide variety of perovskite oxides are being investigated for use as cell components in SOFCs (this will be further discussed in more detail in the next sections) and some examples are presented in Table 1.1 below

**Table 1.1:** Perovskite materials used for different cell components.

| Cell Components | Perovskites  | Sections |
|-----------------|--|----------|
| Cathode         | Sr-doped $\text{LaMnO}_3$ (LSM)                              | 1.3.2    |
|                 | Sr-doped $\text{LaFeO}_3$ (LSF)                              |          |
|                 | Sr-doped $\text{LaCoO}_3$ (LSCo)                             |          |
|                 | Sr-doped $\text{LaCo}_{1-y}\text{Fe}_y\text{O}_3$ (LSCF)     |          |
| Electrolyte     | Sr and Mg-doped $\text{LaGaO}_3$ (LSGM)                      | 1.3.3    |
| Interconnect    | Sr-doped $\text{LaCrO}_3$ (LSCr)                             | 1.3.4    |
| Anode           | Sr-doped $\text{LaVO}_3$ (LSV)                               | 1.3.5    |
|                 | La-doped $\text{SrTiO}_3$ (LST)                              |          |
|                 | Sr-doped $\text{LaCrO}_3$ (LSCr)                             |          |
|                 | Sr-doped $\text{LaCr}_{0.5}\text{Mn}_{0.5}\text{O}_3$ (LSCM) |          |

### 1.3.2 Cathode (air electrode)

The air electrode operates in an oxidizing condition in which the oxygen in the gas phase (air or pure oxygen) undergoes an oxygen reduction reaction which consumes two electrons in the process to form oxygen ions, as shown in Equation 1.1. The

perovskite materials, Sr-doped  $\text{LaMnO}_3$  ( $\text{La}_x\text{Sr}_{1-x}\text{MnO}_{3-\delta}$ , LSM, where  $x$  is between 0.5 and 0.85) is the standard air electrode material owing to its high electronic conductivity ( $\sim 300 \text{ S/cm}$  at  $1000^\circ\text{C}$ <sup>5</sup>) and activity towards the oxygen reduction reaction<sup>27,28</sup>. In addition, LSM is both chemically (no solid state reaction) and physically (thermal expansion match with other cell components) compatible with YSZ<sup>29</sup>.

While LSM has good electronic conductivity, the ionic conductivity of LSM is very low ( $\sim 10^{-8} \text{ S/cm}$  at  $800^\circ\text{C}$ <sup>28</sup>), implying that the oxygen reduction reaction can only occur at the TPB line contact between the LSM, the YSZ, and the gas phase. Therefore, the use of composites with YSZ to increase the TPB length is required in order to achieve high performance with LSM. In contrast to LSM, other SOFC cathodes based on the ferrites or cobaltites, for example Sr-doped  $\text{LaCoO}_3$  (LSCo), Sr-doped  $\text{LaFeO}_3$  (LSF), or Sr-doped  $\text{LaCo}_x\text{Fe}_{1-x}\text{O}_3$  (LSCF)<sup>16</sup> are mixed ionic and electronic conductors (MIEC). The use of MIEC electrode materials extends the electrochemically active region by allowing the oxygen adsorption and reduction to take place not only on the TPB sites, but also on the perovskite bulk material<sup>16,19,30,31</sup>.

The chemical stability of composite electrodes produced by the infiltration of LSCF into a porous YSZ scaffold was investigated as a function of the Co:Fe ratio in the LSCF and the LSCF calcination temperature is discussed in Chapter 9. In addition, the effectiveness of infiltrated SDC interlayers in preventing reactions at the LSCF-YSZ interface and their influence on the overall performance of LSCF/YSZ composite electrodes was studied.

### 1.3.3 Electrolyte

SOFCs are based on the conduction of oxygen anions ( $O^{2-}$ ) from the air electrode through the electrolyte and to the fuel electrode before reacting with the fuel to generate an electrical voltage. YSZ is the most common electrolyte in SOFCs because of its adequate level of ionic conductivity, negligible electronic conductivity and its high stability in both oxidizing and reducing environments<sup>6,32</sup>. While pure  $ZrO_2$  is an insulator, direct substitution of a trivalent metal oxide such as  $Y_2O_3$  for  $ZrO_2$  results in a large concentration of oxygen vacancies and also stabilizes the cubic fluorite structure<sup>6</sup>. The composition of 8 mol%  $Y_2O_3$  in  $ZrO_2$  was chosen because it has been shown to provide the highest ionic conductivity as well as stabilizing the high temperature cubic phase in  $ZrO_2$  over a wide range of SOFC operating and manufacturing temperatures<sup>6</sup>.

Another promising material for use as a SOFC electrolyte is the rare-earth doped ceria electrolyte which also has a fluorite structure<sup>6,32,33</sup>. Among these ceria electrolytes, the gadolinium-doped (GDC) and samarium-doped ceria (SDC) exhibit the highest oxygen ion conductivity at a certain doping level ( $Ce_{0.8}Sm_{0.2}O_{1.9}$ ) and have been shown to have good compatibility with electrodes for SOFCs compared to other electrolytes<sup>6,33</sup>. The high ionic conductivity exhibited by the rare-earth doped ceria at intermediate temperatures means that the operating temperature can potentially be reduced from  $1000^\circ C$  to  $500-800^\circ C$ <sup>6,33,34</sup>. While the doped-ceria electrolytes are promising due to their high ionic conductivity, there are many limitations such as difficulty in sintering these compounds to obtain high density and also doped-ceria exhibit electrical conductivity under reducing conditions<sup>6</sup>.

### 1.3.4 Interconnect

As mentioned in section 1.2.1, multiple SOFC single cells can be connected in series to increase the voltage and power output of the system. This can be done by using an interconnect, which provides the conductive path for electrical current to pass between the electrodes to the external circuit. The requirements of the interconnection are the most severe of all cell components. Firstly, the interconnect material must have good electrical conductivity and be stable (microstructure, chemistry, and phase) under both oxidizing and reducing environments at all cell operating temperatures since it is exposed to air or oxygen on one side and fuel on the other side<sup>23,24</sup>. Secondly, as SOFCs operate at high temperatures, the coefficient of thermal expansion (CTE) has to be close to the other cell components to minimize thermal stresses. Other requirements to make a good interconnect material also include good thermal conductivity, resistance to oxidation, sulfidation, carburization and reaction with other cell components. It is also important that the interconnect material has low permeability for oxygen and hydrogen, should be easy to fabricate and have adequate mechanical strength<sup>23,24</sup>.

Only a few materials have been able to meet the rigorous requirements needed for an interconnect. The most commonly used material for SOFC interconnects are alkaline-earth (Ca- or Sr-) doped-LaCrO<sub>3</sub><sup>23,24</sup>. While LaCrO<sub>3</sub> based materials appear to have met most of these stringent requirements, they are difficult to sinter to full density making fabrication expensive.

### 1.3.5 Anode (fuel electrode)

The anode (fuel electrode) of the SOFC is the main focus in this thesis. Ni–YSZ composites (cermets) are the most commonly used anodes in SOFC due to the high electronic conductivity and catalytic activity of Ni, as well as their ease of fabrication. As discussed in section 1.2.2, the electrochemical reaction (hydrogen/hydrocarbon oxidation reaction) can occur only at the TPB line where the electronic conductor (Ni), the oxygen-ion conductor (YSZ), and the gas phase ( $H_2$ ) meet<sup>13,14,19</sup>. While Ni/YSZ cermets have been used successfully in SOFCs, they also have several limitations, including low tolerance to sulfur impurities which are present in most fuels<sup>35</sup>, and promotion of coke formation from hydrocarbons<sup>36-38</sup>. Other limitations include the slow loss of surface area due to the sintering of Ni at operating temperatures, and the problematic thermal stresses and volume instability during cycling caused by the poor redox stability of Ni<sup>39-41</sup>. Because of these limitations, there has been extensive research focused on trying to decrease the operating temperature<sup>34,42</sup> and also to search for alternative anode materials<sup>35-41,43-57</sup>. However, as the operating temperature is decreased, fuel flexibility becomes limited because both the conversion efficiencies and tolerance to impurities will decrease due to reduced electrode reaction rates. Therefore, the first objective in this thesis is to search for a compatible and highly stable alternative anode material which will be described in more detail in the next section.

## 1.4 Ceramic Electrodes as Alternative Anode Materials

Overcoming the limitations of Ni cermets has motivated research into using conductive ceramics to replace the Ni components in SOFC anodes if they were able to provide comparable performance. Ceramic electrodes are expected to be less susceptible to sintering and coking, be redox stable, and be more tolerant of impurities like sulfur<sup>35-41,43-57</sup>.

Before ceramic electrodes can be widely implemented, several important issues need to be resolved. First and foremost, since the conductivities of most ceramics are much lower than that of metals, ceramic electrodes with reasonable electronic conductivities need to be developed. The conductivity problem is further exacerbated by the fact that high-performance electrodes take the form of porous composites and the conductivities of composites are a factor of at least 10 to 100 lower than that of the corresponding bulk conductor<sup>58-60</sup>. The need for high conductivity in the composite electrode is decreased by using very thin electrodes<sup>61</sup>. This strategy has been successfully employed using infiltrated  $\text{La}_{0.8}\text{Sr}_{0.2}\text{Cr}_{0.5}\text{Mn}_{0.5}\text{O}_3$  (LSCM)<sup>49,62</sup>,  $\text{La}_{0.3}\text{Sr}_{0.7}\text{TiO}_3$  (LST)<sup>44,45</sup>, and ceria<sup>63</sup>. However, the use of thin electrodes simply transfers the conduction requirements onto the current collector. As a general rule, the electrode composite should have a minimum conductivity of  $1 \text{ S/cm}$ <sup>3,64</sup>, the approximate conductivity of SOFC cathodes based on composites of YSZ and Sr-doped  $\text{LaMnO}_3$ <sup>65</sup>. Second, most ceramics are conductive only over a specific range of  $P(\text{O}_2)$ , and conductivity for SOFC anodes must be achieved at conditions corresponding to roughly equal molar concentrations of  $\text{H}_2$  and  $\text{H}_2\text{O}$  over a wide range of temperatures. Most conductive oxides in these low  $P(\text{O}_2)$  conditions exist in a partially reduced state, and reduction to their metallic forms must be



avoided. A third major issue is that many conductive ceramics undergo solid-state reactions with YSZ at the sintering temperatures typically required for forming an electrode that is well connected to the YSZ electrolyte.

To minimize the problems of low conductivity and solid-state reactions between components, our group has been preparing composite electrodes using infiltration methods (the method will be discussed in more detail in Chapter 2.2)<sup>16,66-68</sup>. This fabrication procedure involves synthesizing a porous layer of the electrolyte that has been pre-sintered to the dense electrolyte, then infiltrating the catalytic and electronically conductive components into the porous scaffold<sup>69</sup>. The first goal of this thesis is to search for highly conductive ceramics that are stable and tolerant under SOFC operating conditions. The synthesis, characterization and use of the highly conductive tungsten bronzes and alkaline-earth doped rare-earth vanadates for SOFC anodes are investigated and described in Chapter 3 and 4, respectively.

### **1.5 Approaches to Mitigate Metal Catalyst Deactivation**

While promising results have been obtained with ceramic-based anodes, these anodes unfortunately have relatively low catalytic activity for oxidation reactions. This results in high electrode overpotentials unless the anodes are decorated with nanoparticles of a highly catalytic metal (e.g. Ni, Pt, or Pd)<sup>45,48,52-54,62,69-76</sup>. The catalytic metals are generally added using standard wet infiltration techniques.

Due to the high operating temperatures, deactivation of the metal catalyst by sintering and/or coking is a severe problem as loss of metal surface area due to sintering limits catalyst lifetime and efficiency. Therefore, the second goal of this thesis is to

develop approaches to mitigate the metal catalyst deactivation. This can be achieved by: 1) designing a catalyst that is resistant to coking and sintering and 2) developing a new method for catalyst deposition. Two approaches aimed at mitigating the metal catalyst deactivation are presented in chapters 5 to 8.

The first approach involved synthesizing a self-regenerating, “smart” catalyst, in which Co, Cu, or Ni were inserted into the B-site of a perovskite oxide under oxidizing conditions and then brought back to the surface under reducing conditions. This restores lost surface area of sintered metal particles through an oxidation/reduction cycle. The physical and electrochemical properties of cerium vanadates in which a portion of the cerium cations have been substituted with transition metals ( $\text{Ce}_{1-x}\text{TM}_x\text{VO}_{4-0.5x}$ , TM = Ni, Co, Cu) were investigated and is described in Chapter 5. In order to produce catalytic materials that have relatively high hydrocarbon tolerance using the exsolution method, the cerium cations are substituted with mixed transition metal systems ( $\text{Ce}_{0.8}\text{Sr}_{0.1}\text{Cu}_{0.05}\text{TM}_{0.05}\text{VO}_{4-0.5x}$ , TM = Ni or Co) and their suitability for use in SOFC anodes are assessed in Chapter 6.

The second strategy involves depositing novel highly active and thermally stable Pd@CeO<sub>2</sub> core-shell nanostructure catalysts onto a substrate surface which had been chemically modified to anchor the nanoparticles. This work is described in Chapter 7. The catalyst deposited onto the chemically modified, hydrophobic surface is shown to be uniform and well dispersed. Furthermore they exhibit excellent thermal stability to temperatures as high as 1373 K. Similar metal catalyst deposition method was also employed to assess their suitability for use in SOFC anodes and this work is described in Chapter 8.

## 1.6 References

- 1 Goodenough, J. B. & Huang, Y. H. Alternative anode materials for solid oxide fuel cells. *J Power Sources* **173**, 1-10, doi:DOI 10.1016/j.jpowsour.2007.08.011 (2007).
- 2 Fergus, J. W. Oxide anode materials for solid oxide fuel cells. *Solid State Ionics* **177**, 1529-1541, doi:DOI 10.1016/j.ssi.2006.07.012 (2006).
- 3 Cowin, P. I., Petit, C. T. G., Lan, R., Irvine, J. T. S. & Tao, S. W. Recent Progress in the Development of Anode Materials for Solid Oxide Fuel Cells. *Adv Energy Mater* **1**, 314-332, doi:DOI 10.1002/aenm.201100108 (2011).
- 4 Choudhury, A., Chandra, H. & Arora, A. Application of solid oxide fuel cell technology for power generation-A review. *Renew Sust Energ Rev* **20**, 430-442, doi:DOI 10.1016/j.rser.2012.11.031 (2013).
- 5 Minh, N. Q. Ceramic Fuel-Cells. *J Am Ceram Soc* **76**, 563-588, doi:DOI 10.1111/j.1151-2916.1993.tb03645.x (1993).
- 6 Fergus, J. W. Electrolytes for solid oxide fuel cells. *J Power Sources* **162**, 30-40, doi:DOI 10.1016/j.jpowsour.2006.06.062 (2006).
- 7 Granovskii, M., Dincer, I. & Rosen, M. A. Performance comparison of two combined SOFC-gas turbine systems. *J Power Sources* **165**, 307-314, doi:DOI 10.1016/j.jpowsour.2006.11.069 (2007).
- 8 Baniasadi, E. & Alemrajabi, A. A. Fuel cell energy generation and recovery cycle analysis for residential application. *Int J Hydrogen Energ* **35**, 9460-9467, doi:DOI 10.1016/j.ijhydene.2010.03.015 (2010).

- 9 Chan, S. H., Ho, H. K. & Tian, Y. Multi-level modeling of SOFC-gas turbine hybrid system. *Int J Hydrogen Energ* **28**, 889-900, doi:Pii S0360-3199(02)00160-X, Doi 10.1016/S0360-3199(02)00160-X (2003).
- 10 Chan, S. H., Ho, H. K. & Tian, Y. Modelling of simple hybrid solid oxide fuel cell and gas turbine power plant. *J Power Sources* **109**, 111-120, doi:Pii S0378-7753(02)00051-4, Doi 10.1016/S0378-7753(02)00051-4 (2002).
- 11 Gorte, R. J., Vohs, J. M. & McIntosh, S. Recent developments on anodes for direct fuel utilization in SOFC. *Solid State Ionics* **175**, 1-6, doi:DOI 10.1016/j.ssi.2004.09.036 (2004).
- 12 McIntosh, S. & Gorte, R. J. Direct hydrocarbon solid oxide fuel cells. *Chem Rev* **104**, 4845-4865, doi:Doi 10.1021/Cr020725g (2004).
- 13 de Boer, B., Gonzalez, M., Bouwmeester, H. J. M. & Verweij, H. The effect of the presence of fine YSZ particles on the performance of porous nickel electrodes. *Solid State Ionics* **127**, 269-276, doi:Doi 10.1016/S0167-2738(99)00299-4 (2000).
- 14 Bieberle, A. & Gauckler, L. J. Reaction mechanism of Ni pattern anodes for solid oxide fuel cells. *Solid State Ionics* **135**, 337-345, doi:Doi 10.1016/S0167-2738(00)00462-8 (2000).
- 15 Mogensen, M., Jensen, K. V., Jorgensen, M. J. & Primdahl, S. Progress in understanding SOFC electrodes. *Solid State Ionics* **150**, 123-129, doi:Pii S0167-2738(02)00269-2, Doi 10.1016/S0167-2738(02)00269-2 (2002).
- 16 Vohs, J. M. & Gorte, R. J. High-Performance SOFC Cathodes Prepared by Infiltration. *Adv Mater* **21**, 943-956, doi:DOI 10.1002/adma.200802428 (2009).

- 17 Herbstritt, D., Weber, A. & Ivers-Tiffée, E. Modelling and DC-polarisation of a three dimensional electrode/electrolyte interface. *J Eur Ceram Soc* **21**, 1813-1816, doi:Doi 10.1016/S0955-2219(01)00121-2 (2001).
- 18 Kim, J. W., Virkar, A. V., Fung, K. Z., Mehta, K. & Singhal, S. C. Polarization effects in intermediate temperature, anode-supported solid oxide fuel cells. *J Electrochem Soc* **146**, 69-78, doi:Doi 10.1149/1.1391566 (1999).
- 19 Tanner, C. W., Fung, K. Z. & Virkar, A. V. The effect of porous composite electrode structure on solid oxide fuel cell performance .1. Theoretical analysis. *J Electrochem Soc* **144**, 21-30, doi:Doi 10.1149/1.1837360 (1997).
- 20 Ren, Y. Y., Kungas, R., Gorte, R. J. & Deng, C. S. The effect of A-site cation (Ln = La, Pr, Sm) on the crystal structure, conductivity and oxygen reduction properties of Sr-doped ferrite perovskites. *Solid State Ionics* **212**, 47-54, doi:DOI 10.1016/j.ssi.2012.02.028 (2012).
- 21 Sogaard, M., Hendriksen, P. V. & Mogensen, M. Oxygen nonstoichiometry and transport properties of strontium substituted lanthanum ferrite. *J Solid State Chem* **180**, 1489-1503, doi:DOI 10.1016/j.jssc.2007.02.012 (2007).
- 22 Waernhus, I., Grande, T. & Wiik, K. Electronic properties of polycrystalline LaFeO<sub>3</sub>. Part II: Defect modelling including Schottky defects. *Solid State Ionics* **176**, 2609-2616, doi:DOI 10.1016/j.ssi.2005.07.014 (2005).
- 23 Fergus, J. W. Lanthanum chromite-based materials for solid oxide fuel cell interconnects. *Solid State Ionics* **171**, 1-15, doi:DOI 10.1016/j.ssi.2004.04.010 (2004).

- 24 Zhu, W. Z. & Deevi, S. C. Development of interconnect materials for solid oxide fuel cells. *Mat Sci Eng a-Struct* **348**, 227-243, doi:Pii S0921-5093(02)00736-0, Doi 10.1016/S0921-5093(02)00736-0 (2003).
- 25 Tao, S. W. & Irvine, J. T. S. A redox-stable efficient anode for solid-oxide fuel cells. *Nat Mater* **2**, 320-323, doi:Doi 10.1038/Nmat871 (2003).
- 26 Tao, S. W., Irvine, J. T. S. & Plint, S. M. Methane oxidation at redox stable fuel cell electrode  $\text{La}_{0.75}\text{Sr}_{0.25}\text{Cr}_{0.5}\text{Mn}_{0.5}\text{O}_{3-\delta}$ . *J Phys Chem B* **110**, 21771-21776, doi:Doi 10.1021/Jp062376q (2006).
- 27 Huang, Y. Y., Vohs, J. M. & Gorte, R. J. Characterization of LSM-YSZ composites prepared by impregnation methods. *J Electrochem Soc* **152**, A1347-A1353, doi:Doi 10.1149/1.1926669 (2005).
- 28 Ji, Y., Kilner, J. A. & Carolan, M. F. Electrical properties and oxygen diffusion in yttria-stabilised zirconia (YSZ)- $\text{La}_{0.8}\text{Sr}_{0.2}\text{MnO}_{3-\delta}$  (LSM) composites. *Solid State Ionics* **176**, 937-943, doi:DOI 10.1016/j.ssi.2004.11.019 (2005).
- 29 Koh, J. H., Kang, B. S., Lim, H. C. & Yoo, Y. S. Thermodynamic analysis of carbon deposition and electrochemical oxidation of methane for SOFC anodes. *Electrochem Solid St* **4**, A12-A15, doi:Doi 10.1149/1.1339237 (2001).
- 30 Adler, S. B. Factors governing oxygen reduction in solid oxide fuel cell cathodes. *Chem Rev* **104**, 4791-4843, doi:Doi 10.1021/Cr020724o (2004).
- 31 Bidrawn, F., Kungas, R., Vohs, J. M. & Gorte, R. J. Modeling Impedance Response of SOFC Cathodes Prepared by Infiltration. *J Electrochem Soc* **158**, B514-B525, doi:Doi 10.1149/1.3565174 (2011).

- 32 Amado, R. S., Malta, L. F. B., Garrido, F. M. S. & Medeiros, M. E. Solid oxide fuel cells: Materials, components and configurations. *Quim Nova* **30**, 189-197 (2007).
- 33 Nesaraj, A. S. Recent developments in solid oxide fuel cell technology - a review. *J Sci Ind Res India* **69**, 169-176 (2010).
- 34 Tarancon, A. Strategies for Lowering Solid Oxide Fuel Cells Operating Temperature. *Energies* **2**, 1130-1150, doi:Doi 10.3390/En20401130 (2009).
- 35 Matsuzaki, Y. & Yasuda, I. The poisoning effect of sulfur-containing impurity gas on a SOFC anode: Part I. Dependence on temperature, time, and impurity concentration. *Solid State Ionics* **132**, 261-269 (2000).
- 36 Kim, H., Lu, C., Worrell, W. L., Vohs, J. M. & Gorte, R. J. Cu-Ni cermet anodes for direct oxidation of methane in solid-oxide fuel cells. *J Electrochem Soc* **149**, A247-A250, doi:10.1149/1.1445170 (2002).
- 37 Toebes, M. L., Bitter, J. H., van Dillen, A. J. & de Jong, K. P. Impact of the structure and reactivity of nickel particles on the catalytic growth of carbon nanofibers. *Catal Today* **76**, 33-42 (2002).
- 38 Toh, C. H., Munroe, P. R., Young, D. J. & Foger, K. High temperature carbon corrosion in solid oxide fuel cells. *Mater High Temp* **20**, 129-136 (2003).
- 39 Huang, Y. H., Dass, R. I., Denyszyn, J. C. & Goodenough, J. B. Synthesis and characterization of  $\text{Sr}_2\text{MgMoO}_{6-\delta}$  - An anode material for the solid oxide fuel cell. *J Electrochem Soc* **153**, A1266-A1272, doi:10.1149/1.2195882 (2006).

- 40 Sarantaridis, D. & Atkinson, A. Redox cycling of Ni-based solid oxide fuel cell anodes: A review. *Fuel Cells* **7**, 246-258, doi:DOI 10.1002/fuce.200600028 (2007).
- 41 Sfeir, J., van Herle, J. & McEvoy, A. J. Stability of calcium substituted lanthanum chromites used as SOFC anodes for methane oxidation. *J Eur Ceram Soc* **19**, 897-902 (1999).
- 42 Wachsman, E. D. & Lee, K. T. Lowering the Temperature of Solid Oxide Fuel Cells. *Science* **334**, 935-939, doi:DOI 10.1126/science.1204090 (2011).
- 43 Gross, M. D. *et al.* Redox Stability of  $\text{SrNb}_{(x)}\text{Ti}_{(1-x)}\text{O}_{(3)}$ -YSZ for Use in SOFC Anodes. *J Electrochem Soc* **156**, B540-B545, doi:10.1149/1.3078406 (2009).
- 44 Kim, G., Gross, M. D., Wang, W., Vohs, J. M. & Gorte, R. J. SOFC anodes based on LST-YSZ composites and on  $\text{Y}_{0.04}\text{Ce}_{0.48}\text{Zr}_{0.48}\text{O}_2$ . *J Electrochem Soc* **155**, B360-B366, doi:10.1149/1.2840473 (2008).
- 45 Lee, S., Kim, G., Vohs, J. M. & Gorte, R. J. SOFC anodes based on infiltration of  $\text{La}_{0.3}\text{Sr}_{0.7}\text{TiO}_3$ . *J Electrochem Soc* **155**, B1179-B1183, doi:Doi 10.1149/1.2976775 (2008).
- 46 Neagu, D. & Irvine, J. T. S. Structure and Properties of  $\text{La}_{(0.4)}\text{Sr}_{(0.4)}\text{TiO}_{(3)}$  Ceramics for Use as Anode Materials in Solid Oxide Fuel Cells. *Chem Mater* **22**, 5042-5053, doi:Doi 10.1021/Cm101508w (2010).
- 47 Vincent, A., Luo, J. L., Chuang, K. T. & Sanger, A. R. Effect of Ba doping on performance of LST as anode in solid oxide fuel cells. *J Power Sources* **195**, 769-774, doi:DOI 10.1016/j.jpowsour.2009.08.018 (2010).



- 48 Babaei, A., Zhang, L., Tan, S. L. & Jiang, S. P. Pd-promoted (La,Ca)(Cr,Mn)O<sub>3</sub>/GDC anode for hydrogen and methane oxidation reactions of solid oxide fuel cells. *Solid State Ionics* **181**, 1221-1228, doi:DOI 10.1016/j.ssi.2010.06.042 (2010).
- 49 Kim, G., Corre, G., Irvine, J. T. S., Vohs, J. M. & Gorte, R. J. Engineering composite oxide SOFC anodes for efficient oxidation of methane. *Electrochem Solid St* **11**, B16-B19, doi:10.1149/1.2817809 (2008).
- 50 van den Bossche, M., Matthews, R., Lichtenberger, A. & McIntosh, S. Insights Into the Fuel Oxidation Mechanism of La<sub>(0.75)</sub>Sr<sub>(0.25)</sub>Cr<sub>(0.5)</sub>Mn<sub>(0.5)</sub>O<sub>(3-delta)</sub> SOFC Anodes. *J Electrochem Soc* **157**, B392-B399, doi:Doi 10.1149/1.3288374 (2010).
- 51 Zhu, X. B. *et al.* A comparison of La<sub>(0.75)</sub>Sr<sub>(0.25)</sub>Cr<sub>(0.5)</sub>Mn<sub>(0.5)</sub>O<sub>(3-delta)</sub> and Ni impregnated porous YSZ anodes fabricated in two different ways for SOFCs. *Electrochim Acta* **55**, 3932-3938, doi:DOI 10.1016/j.electacta.2010.02.028 (2010).
- 52 Bierschenk, D. M. *et al.* Pd-substituted (La,Sr)CrO<sub>(3-delta)</sub>-Ce<sub>(0.9)</sub>Gd<sub>(0.1)</sub>O<sub>(2-delta)</sub> solid oxide fuel cell anodes exhibiting regenerative behavior. *J Power Sources* **196**, 3089-3094, doi:DOI 10.1016/j.jpowsour.2010.12.050 (2011).
- 53 Adjianto, L., Kungas, R., Park, J., Vohs, J. M. & Gorte, R. J. SOFC anodes based on infiltration of tungsten bronzes. *Int J Hydrogen Energ* **36**, 15722-15730, doi:DOI 10.1016/j.ijhydene.2011.09.059 (2011).
- 54 Smith, B. H. & Gross, M. D. A Highly Conductive Oxide Anode for Solid Oxide Fuel Cells. *Electrochem Solid St* **14**, B1-B5, doi:10.1149/1.3505101 (2011).
- 55 Adjianto, L., Padmanabhan, V. B., Holmes, K. J., Gorte, R. J. & Vohs, J. M. Physical and electrochemical properties of alkaline earth doped, rare earth

- vanadates. *J Solid State Chem* **190**, 12-17, doi:DOI 10.1016/j.jssc.2012.01.065 (2012).
- 56 Adijanto, L., Padmanabhan, V. B., Kungas, R., Gorte, R. J. & Vohs, J. M. Transition metal-doped rare earth vanadates: a regenerable catalytic material for SOFC anodes. *J Mater Chem* **22**, 11396-11402, doi:Doi 10.1039/C2jm31774e (2012).
- 57 Adijanto, L., Padmanabhan, V. B., Gorte, R. J. & Vohs, J. M. Polarization-Induced Hysteresis in CuCo-Doped Rare Earth Vanadates SOFC Anodes. *J Electrochem Soc* **159**, F751-F756, doi:Doi 10.1149/2.042211jes (2012).
- 58 Fang, X. H., Zhu, G. Y., Xia, C. R., Liu, X. Q. & Meng, G. Y. Synthesis and properties of Ni-SDC cermets for IT-SOFC anode by co-precipitation. *Solid State Ionics* **168**, 31-36 (2004).
- 59 Park, J. S. *et al.* A high-performance solid oxide fuel cell anode based on lanthanum strontium vanadate. *J Power Sources* **196**, 7488-7494, doi:DOI 10.1016/j.jpowsour.2011.05.028 (2011).
- 60 Zhu, W. Z. & Deevi, S. C. A review on the status of anode materials for solid oxide fuel cells. *Mat Sci Eng a-Struct* **362**, 228-239, doi:10.1016/S0921-5093(03)00620-8 (2003).
- 61 Gross, M. D., Vohs, J. M. & Gorte, R. J. A strategy for achieving high performance with SOFC ceramic anodes. *Electrochem Solid St* **10**, B65-B69, doi:10.1149/1.2432942 (2007).

- 62 Kim, G. *et al.* Investigation of the Structural and Catalytic Requirements for High-Performance SOFC Anodes Formed by Infiltration of LSCM. *Electrochem Solid St* **12**, B48-B52, doi:10.1149/1.3065971 (2009).
- 63 Kim, G., Vohs, J. M. & Gorte, R. J. Enhanced reducibility of ceria-YSZ composites in solid oxide electrodes. *J Mater Chem* **18**, 2386-2390, doi:Doi 10.1039/B718931a (2008).
- 64 Atkinson, A. *et al.* Advanced anodes for high-temperature fuel cells. *Nat Mater* **3**, 17-27, doi:10.1038/nmat1040 (2004).
- 65 He, H. P. *et al.* Low-temperature fabrication of oxide composites for solid-oxide fuel cells. *J Am Ceram Soc* **87**, 331-336 (2004).
- 66 Adijanto, L., Kungas, R., Bidrawn, F., Gorte, R. J. & Vohs, J. M. Stability and performance of infiltrated  $\text{La}_{0.8}\text{Sr}_{0.2}\text{Co}_x\text{Fe}_{1-x}\text{O}_3$  electrodes with and without  $\text{Sm}_{0.2}\text{Ce}_{0.8}\text{O}_{1.9}$  interlayers. *J Power Sources* **196**, 5797-5802, doi:DOI 10.1016/j.jpowsour.2011.03.022 (2011).
- 67 Huang, Y. Y., Vohs, J. M. & Gorte, R. J. Fabrication of Sr-doped  $\text{LaFeO}_{(3)}$ YSZ composite cathodes. *J Electrochem Soc* **151**, A646-A651, doi:10.1149/1.1652053 (2004).
- 68 Wang, W. S., Gross, M. D., Vohs, J. M. & Gorte, R. J. The stability of LSF-YSZ electrodes prepared by infiltration. *J Electrochem Soc* **154**, B439-B445, doi:Doi 10.1149/1.2709510 (2007).
- 69 Gorte, R. J., Park, S., Vohs, J. M. & Wang, C. H. Anodes for direct oxidation of dry hydrocarbons in a solid-oxide fuel cell. *Adv Mater* **12**, 1465-1469 (2000).

- 70 Kobsiriphat, W., Madsen, B. D., Wang, Y., Marks, L. D. & Barnett, S. A.  $\text{La}_{(0.8)}\text{Sr}_{(0.2)}\text{Cr}_{(1-x)}\text{Ru}_{(x)}\text{O}_{(3-\text{delta})}-\text{Gd}_{(0.1)}\text{Ce}_{(0.9)}\text{O}_{(1.95)}$  solid oxide fuel cell anodes: Ru precipitation and electrochemical performance. *Solid State Ionics* **180**, 257-264, doi:DOI 10.1016/j.ssi.2008.12.022 (2009).
- 71 Kim, J. S., Nair, V. V., Vohs, J. M. & Gorte, R. J. A study of the methane tolerance of LSCM-YSZ composite anodes with Pt, Ni, Pd and ceria catalysts. *Scripta Mater* **65**, 90-95, doi:DOI 10.1016/j.scriptamat.2010.06.016 (2011).
- 72 Bi, Z. H. & Zhu, J. H. Effect of Current Collecting Materials on the Performance of the Double-Perovskite  $\text{Sr}_{(2)}\text{MgMoO}_{(6-\text{delta})}$  Anode. *J Electrochem Soc* **158**, B605-B613, doi:10.1149/1.3569754 (2011).
- 73 Gross, M. D., Vohs, J. M. & Gorte, R. J. An examination of SOFC anode functional layers based on ceria in YSZ. *J Electrochem Soc* **154**, B694-B699, doi:10.1149/1.2736647 (2007).
- 74 Xiao, G. L., Jin, C., Liu, Q., Heyden, A. & Chen, F. L. Ni modified ceramic anodes for solid oxide fuel cells. *J Power Sources* **201**, 43-48, doi:DOI 10.1016/j.jpowsour.2011.10.103 (2012).
- 75 Wang, Y., Madsen, B. D., Kobsiriphat, W., Barnett, S. A. & Marks, L. D. Electron microscopy study of novel ru doped  $\text{La}_{(0.8)}\text{Sr}_{(0.2)}\text{CrO}_{(3)}$  as anode materials for Solid Oxide Fuel Cells (SOFCs). *Microsc Microanal* **13**, 100-101, doi:Doi 10.1017/S1431927607075125 (2007).
- 76 Madsen, B. D., Kobsiriphat, W., Wang, Y., Marks, L. D. & Barnett, S. A. Nucleation of nanometer-scale electrocatalyst particles in solid oxide fuel cell

anodes. *J Power Sources* **166**, 64-67, doi:DOI 10.1016/j.jpowsour.2006.12.080  
(2007).

## **Chapter 2. Experimental Techniques**

### **Summary**

This section will describe the experimental methods used for materials synthesis, as well as the methods used to characterize the properties of the candidate materials.

### **2.1 Materials Synthesis**

#### **2.1.1 Mixed Oxides**

The mixed oxides were prepared using the Pechini Method in order to produce the desired phases at lower temperatures. In this method, the appropriate amounts of each nitrate precursor are dissolved in an aqueous solution together with citric acid (Fisher Scientific) in a 1:1 molar ratio. Citric acid acts as a complexing agent to aid in the formation of a more homogeneous solid mixture of the constituent cations after precipitation from solution. Without the complexing agent, larger domains of the pure oxides are formed, requiring higher calcination temperatures in order to allow interdiffusion of the cations into the more thermodynamically stable, mixed oxide. After forming the solid mixture from solution, the precursor was dried and the resulting powder was calcined in air to the desired temperature.

#### **2.1.2 Pd@CeO<sub>2</sub> Core-Shell Nanostructures**

The synthesis of the Pd@CeO<sub>2</sub> core-shell structures is described in detail by Cargnello, et al.<sup>1,2</sup> and made use of Pd nanoparticles that were stabilized in tetrahydrofuran (THF) solvent via capping with 11-mercaptoundecanoic acid (MUA).

The ceria shells were formed by mixing the MUA-Pd/THF solution with a solution of cerium(IV)-tetrakis(decyloxiide) in THF, followed by the addition of a solution of dodecanoic acid in THF (equimolar to the Ce(IV)). Hydrolysis of cerium(IV)-tetrakis(decyloxiide) was carried out by slowly adding, over a period of 4 h, H<sub>2</sub>O dissolved in THF. This procedure resulted in Pd@Ceria core-shell structures with an average core diameter of 1.8 nm and shell thickness of 3 nm dispersed in the THF solution. Detailed structural characterization of the Pd@CeO<sub>2</sub> particles, including TEM analysis, has been reported in previous publications<sup>3</sup>.

## **2.2 Fuel Cell Preparation**

As mentioned in Section 1.2.4, our group has been preparing composite electrodes using infiltration methods in order to minimize the problems of low conductivity and solid-state reactions between components (Advantages of composites prepared by the infiltration method over the traditional method will be discussed in Section 2.2.6.)<sup>4-17</sup>. All of the fuel cells used for the work in this dissertation involves synthesizing a porous layer of the electrolyte that has been pre-sintered to the dense electrolyte, then infiltrating the catalytic and electronically conductive components into the porous scaffold as shown in Figure 2.1<sup>18,19</sup>. The tapes were prepared using organic solvents<sup>18,20,21</sup>. The tape-casting slurry composition and electrode materials, the fuel cell fabrication and the advantages of the infiltration method will be described in more detail in the next sections.

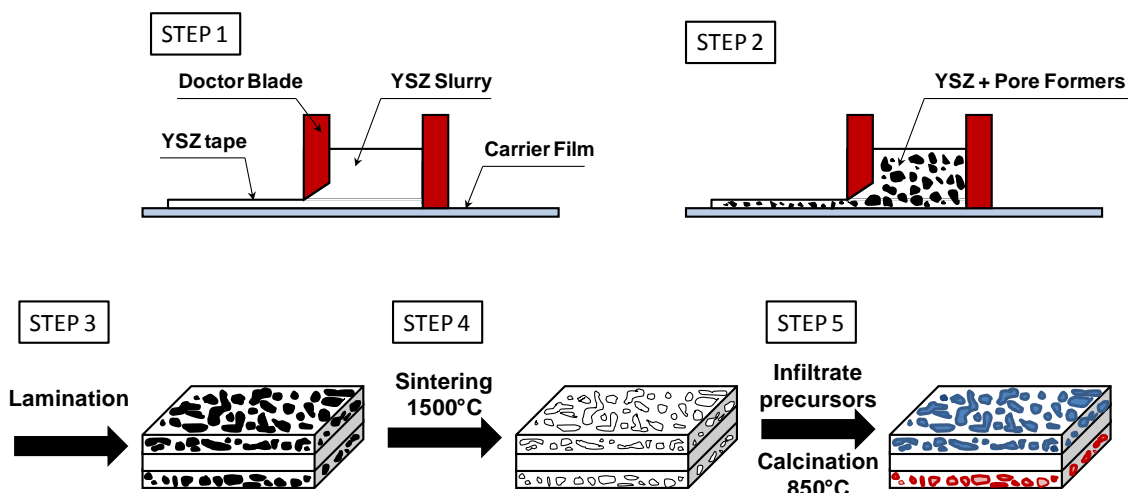


**Figure 2.1:** Cell fabrication by tape-casting and infiltration<sup>19</sup>.

### 2.2.1 Tape Casting

For the dense electrolyte layer, the tape-casting slurry was prepared using the following formulation:

| Material                   | Quantity (g)          | Purpose     | Supplier                |
|----------------------------|-----------------------|-------------|-------------------------|
| YSZ                        | 40                    |             | Tosoh                   |
| Menhaden fish oil          | 0.8                   | Dispersant  | Richard E. Mistler, Inc |
| Ethanol 100%               | 8.5+9<br>(17.5 total) | Solvent     | Fisher                  |
| Xylenes                    | 10                    | Solvent     | Sigma-Aldrich           |
| Polyvinyl butyral B-98     | 3                     | Binder      | Solutia                 |
| Polyethylene glycol 400 MW | 1.2                   | Plasticizer | Alfa Aesar              |
| Benzyl butyl phthalate     | 1.2                   | Plasticizer | Aldrich                 |



The YSZ powder was first added to a mixture of the ethanol and xylenes, in a weight ratio of 3:1, and a dispersant. After the slurry has been ball milled for 12 h, binder and plasticizers were then added to the solution, followed by another 24 h of ball milling. The dense electrolyte slurry was then cast onto a mylar carrier film using a doctor blade and a tape casting machine obtained from Richard E. Mistler, Inc to produce the dense electrolyte green tape. The thickness of the tape could be controlled by the settings of the doctor blade. The electrolyte tape was allowed to dry for at least 4 h before use.

For the porous electrode layer, the tape-casting slurry was prepared using a similar formulation, described in detail as follows:

| <b>Material</b>                  | <b>Quantity (g)</b> | <b>Purpose</b> | <b>Supplier</b>         |
|----------------------------------|---------------------|----------------|-------------------------|
| YSZ                              | 40                  |                | Tosoh                   |
| Menhaden fish oil                | 0.9                 | Dispersant     | Richard E. Mistler, Inc |
| Ethanol 100%                     | 12.6                | Solvent        | Fisher                  |
| Xylenes                          | 50.3                | Solvent        | Sigma-Aldrich           |
| Polyvinyl butyral B-79           | 16.2                | Binder         | Solutia                 |
| Polyethylene glycol 400 MW       | 6.95                | Plasticizer    | Alfa Aesar              |
| Benzyl butyl phthalate           | 6.95                | Plasticizer    | Aldrich                 |
| Graphite, synthetic, <20 $\mu$ m | 30.6                | Pore former    | Sigma-Aldrich           |

The porous electrode layer was prepared very similarly to that of the dense electrolyte layer, except that the ethanol to xylene ratio was different so as to allow the addition of a pore former, graphite (300 mesh). The porous YSZ layers on each side of the dense electrolyte layer had 60 % porosity with a BET surface area 0.3 m<sup>2</sup>g<sup>-1</sup>.

### 2.2.2 Cell Assembly Sintering

After both the dense electrolyte and the porous electrode tapes had been cast and allowed to dry, they were punched to produce dense electrolyte discs 1 cm in diameter and porous electrode discs 0.67 cm in diameter. The electrochemical cells used in this study were prepared from porous-dense-porous tri-layer YSZ wafers, in which a  $65\pm 2$   $\mu\text{m}$  dense electrolyte disc was sandwiched between two 50  $\mu\text{m}$  porous YSZ layers. The tri-layer wafers were fabricated by laminating three green tapes using a hydraulic press at 343 K and minimal pressure, followed by calcination at 1773 K for 4 h with a high temperature furnace (Deltech). The heating ramp rate was 2 K/min and the cooling rate was 3 K/min.

### 2.2.3 Cathode Preparation

For all the composite cathodes used in this dissertation, 40 wt. % Sr-doped lanthanum ferrite ( $\text{La}_{0.8}\text{Sr}_{0.2}\text{FeO}_3$  (LSF)) was added to one of the porous layers to form a cathode. Multiple infiltration cycles of an aqueous solution containing dissolved  $\text{La}(\text{NO}_3)_3 \cdot 6\text{H}_2\text{O}$  (Alfa Aesar, 99.9%),  $\text{Sr}(\text{NO}_3)_2$  (Alfa Aesar, 99%) and  $\text{Fe}(\text{NO}_3)_3 \cdot 9\text{H}_2\text{O}$  (Fisher Scientific), in the appropriate molar ratios, were required. This was followed by calcination in air at 723 K<sup>4,9,17</sup>. After the infiltration steps, the composite cathode was calcined to 1123 K for 4 h to form the perovskite structure. Previous studies have shown that cathodes of this design have an ASR of  $\sim 0.15 \Omega \text{ cm}^2$  in air at 973 K<sup>4,5</sup>.

### 2.2.4 Anode Preparation

The composite anode was fabricated using methods similar to that used to make the composite cathode. However, whether the anode was prepared before or after the

final calcination of the cathode depended on the anode composition and the temperature required for achieving the single-phase anodes that were used in the studies. The anode compositions used in various studies are described in detail in the experimental section in each chapter.

### **2.2.5 Preparation for Testing**

Upon completion of fuel cell fabrication, a loop made with Ag wire was attached to both porous electrodes on each side of the electrolyte and Ag paste was then applied and used as the current collector. The cells were mounted onto an alumina tube using a ceramic adhesive (Aremco, Ceramabond 552). All the cell tests were performed with the anode exposed to humidified H<sub>2</sub> (3% H<sub>2</sub>O) and the cathode to ambient air.

### **2.2.6 Advantages of the Infiltration Method over Tradition Method**

Electrodes prepared by the conventional processing methods involve co-sintering a mixture of the electrode material with YSZ powder onto the YSZ electrolyte at very high calcination temperatures, typically above 1473 K<sup>22,23</sup>. While high temperature sintering is required to prevent de-lamination of the electrode from the electrolyte and to form good ion-conducting channels (by sintering the YSZ particles in the electrode to the electrolyte), it can also cause serious problems such as the coarsening of the materials and can result in solid-state reactions between the YSZ and alternative electrode materials.

Composites fabricated by the infiltration method offer a number of advantages over composites prepared by the conventional methods. Using infiltration, the sintering temperature for the electrolyte component of the composite can be high so as to establish

good ion-conducting channels from the electrolyte into the electrode, without requiring that the conductive component of the composite be fired to those same high temperatures. Because the sintering steps to produce the YSZ scaffold and conductive composite electrode are separated, both the microstructure of the electrolyte scaffold and the active phase can be precisely controlled and engineered. In addition, the infiltration approach allows the measurement of the intrinsic properties of candidate electrode materials that are highly conductive but would otherwise have undergone solid-state reactions, have decomposed or possibly coarsened dramatically<sup>4-17</sup>.

Furthermore, composites formed by infiltration do not have a random structure, so that their conductivity can be significantly higher than that which would be obtained in random mixtures of conductive and insulating phases at the same loadings of the conducting phase<sup>24</sup>. The non-random structure also causes the coefficients of thermal expansion (CTE) of the composite to be closer to that of the electrolyte scaffold than to the weighted average of its components<sup>9,12</sup>. Finally, the effects of expansion due to oxidation and reduction of the electronic conductor are minimized in infiltrated composites<sup>25,26</sup> and catalytic components can be added separately if required<sup>5,6,14,27-32</sup>.

## 2.3 Cell Performance Measurements

The electrochemical performance of each fuel cell was usually characterized by the voltage-current polarization (V-i) curves and by impedance spectra. Examples for each of these are shown in Figure 2.2 and 2.3 respectively and will be described in more detail in the next sections. All the polarization curves shown in this dissertation were measured using a Gamry Instruments PC4/750 potentiostat with VFP600 software package. All the electrochemical impedance spectra were measured between 0.1 Hz and 300 kHz with a 1 mA AC perturbation using a Gamry Instruments potentiostat.

### 2.3.1 V-i Polarization Curves

The polarization curves show the voltage (y-axis) of the cell as a function of the current density (x-axis), with an example shown in Figure 2.2. At open-circuit-voltage (OCV) conditions, the voltages for SOFC are usually equal to the Nernst potential, the ideal thermodynamic voltage, when the electrolyte is a pure ion conductor, such as YSZ. For the hydrogen-oxidation reaction at 973 K, the OCV will be near 1.1 V. However, when the cell is polarized (when current is drawn), the voltage will drop due to energy losses associated with the electrodes and electrolyte. The total loss can be described by the area-specific resistance (ASR), the slope of the V-i curve. In a typical measurement, the V-i curve was measured starting from OCV, followed by ramping the potential to 0 V and back to OCV using a linear scan rate of  $0.025 \text{ Vs}^{-1}$  and sample rate of 5 Hz in both directions. In most cases, the polarization curves were nearly linear and reversible in both scan directions. In addition to the ASR, it is common to refer to the maximum power

density produced by the cell. This can be determined from the maximum in the product of the voltage and the current density.

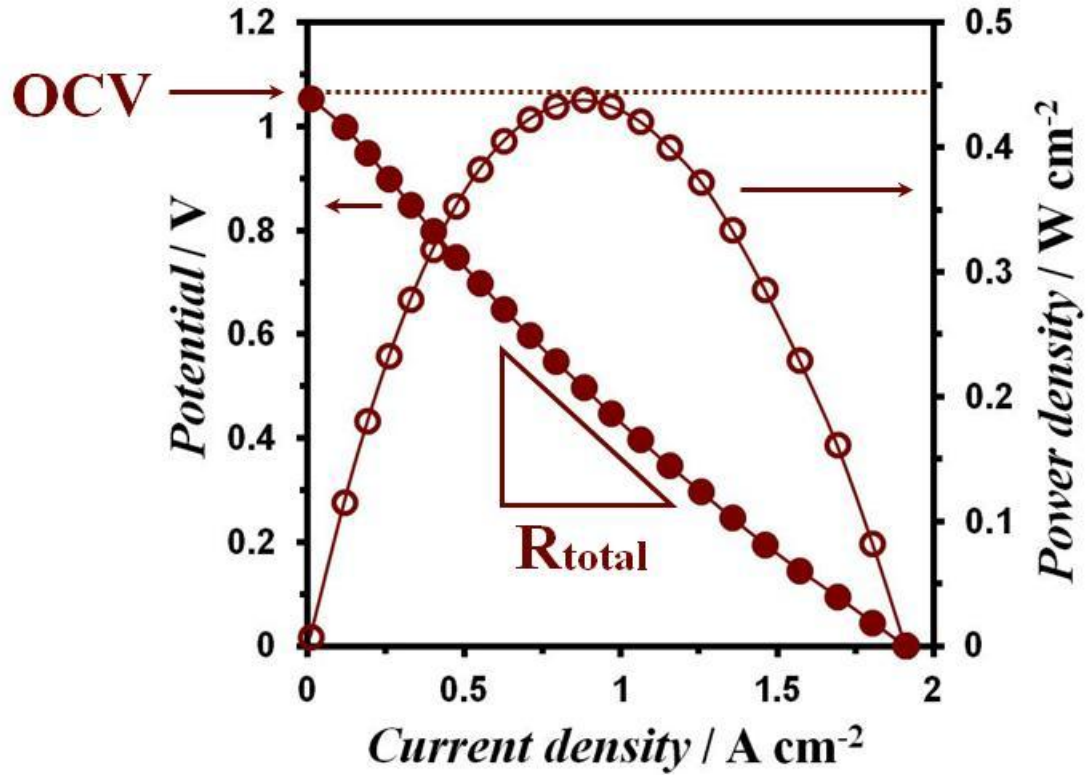


**Figure 2.2:** An example V-i polarization curve of an SOFC.

### 2.3.2 Electrochemical Impedance Spectroscopy

Although V-i curves can provide insight into fuel cell performance, they cannot be used to differentiate between the various sources of loss within the cell. Electrochemical impedance spectroscopy (EIS) was used to separate the overall ASR into electrolyte (ohmic) and electrode (non-ohmic) losses. Impedance measurements are usually made by applying a sinusoidal current perturbation (Equation 2.1) and measuring a corresponding phase shifted sinusoidal potential response (Equation 2.2). The

impedance (Equation 2.3), measured across a range of frequencies can then be presented as a Nyquist plot, with an example shown in Figure 2.3.

$$i(t)=i_0\cos(\omega t) \quad \text{Equation 2.1}$$

$$V(t)=V_0\cos(\omega t+\varphi) \quad \text{Equation 2.2}$$

$$Z=V(t)/i(t) \quad \text{Equation 2.3}$$

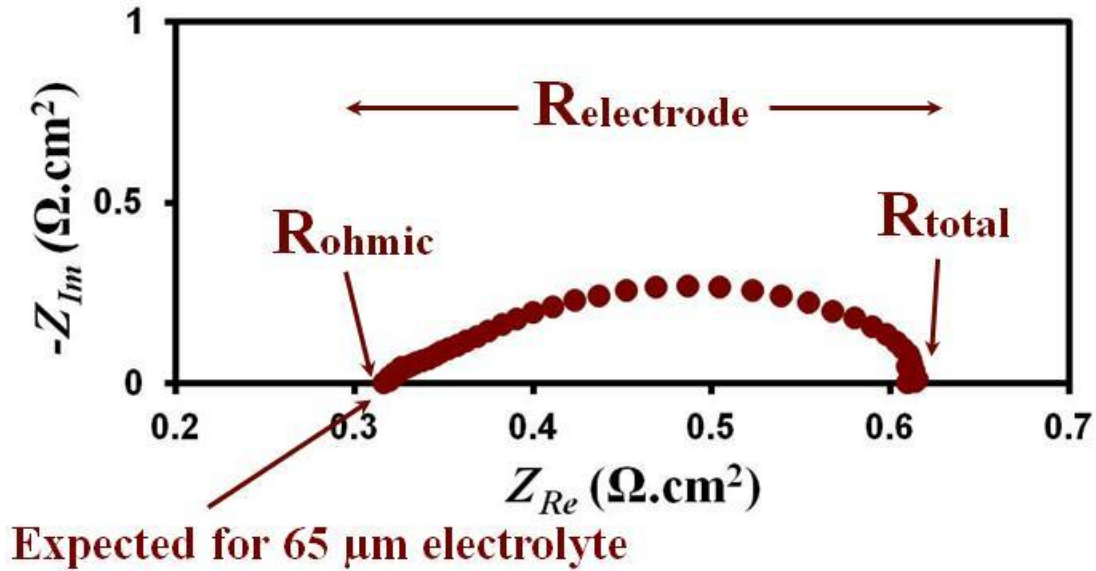


**Figure 2.3:** An example electrochemical impedance spectra from an SOFC.

The ohmic and non ohmic losses can be calculated by the high and low frequency intercepts with the real axis in the Nyquist plots. As mentioned previously, SOFC losses are due to energy losses in either the electrolyte or the electrodes. The ohmic losses are usually dominated by that  $iR$  drop associated with the diffusion of the oxygen anions across the electrolyte and are therefore directly proportional to the thicknesses of the electrolyte. Since the conduction of ions through the YSZ electrolyte is a time independent process, the ohmic resistance corresponds to the high frequency real-axis intercept. The low frequency real-axis intercept corresponds to the total resistance of the cell; and, therefore, the time dependent impedance of the electrodes can be determined by

the distance between the two intercepts. The non-ohmic (polarization) losses are usually associated with limited surface kinetics and electrochemical reactions at the electrodes.

## **2.4 Composite Slabs**

Porous YSZ slabs used for surface-area, hydrocarbon-stability and conductivity measurements were prepared by infiltration methods similar to that used in the preparation of the composite electrodes described in section 2.2.1. A porous electrode tape, 400- $\mu\text{m}$  thick, was tape cast and laminated in a layer-by-layer manner using xylene to produce a porous 8 mm x 8 mm x 20 mm YSZ slab. The slabs were then sintered to 1773 K for 4 h, and cut into small rectangular bars of 4 mm x 4 mm x 15 mm slabs. The resulting porous YSZ slabs were then infiltrated with the precursor solution and calcined in the same manner as described previously for the composite anode.

## **2.5 Surface Chemical Modification of Metal Oxide Powders or Planar Supports**

### **2.5.1 Liquid Silanization**

For the TEOOS-treated samples, 1-g of the oxide powders (YSZ, LSCM,  $\gamma\text{-Al}_2\text{O}_3$ ) were mixed in 20 mL of toluene followed by addition of TEOOS (0.55 mL). The resulting solution was refluxed at 384 K for 6 hrs and the precipitate powders were recovered by centrifugation. The powders were subsequently washed twice with toluene to remove unreacted TEOOS and byproducts and then dried overnight at 393 K.



### **2.5.2 Gas Silanization**

The YSZ(100) and sapphire(0001) single crystal substrates (5 mm x 5 mm) were cleaned using an O<sub>2</sub> plasma treatment prior to surface modification. Functionalization of the single crystal surface via reaction with triethoxy(octyl)silane (TEOOS) was performed using chemical vapor deposition (CVD) system. Prior to film deposition, the single crystal substrates were further cleaned in the CVD reactor by heating to 673 K and exposure to 400 torr of O<sub>2</sub> for 1 min. The samples were functionalized with TEOOS using ten deposition cycles consisting of a 1 min exposure to 0.5 torr of TEOOS with the sample at 323 K.

### **2.5.3 Liquid Phosphonation**

For the TDPA-treated sample,  $\gamma$ -Al<sub>2</sub>O<sub>3</sub> powder (1 g) was mixed in 30 mL of THF followed by addition of TDPA (0.20 g). The resulting solution was refluxed at 333 K for 6 hrs and the precipitate powder was recovered by centrifugation. The powder was subsequently washed twice with THF to remove unreacted TDPA and byproducts and was dried overnight at 393 K.

## 2.6 Materials Characterization Techniques

Several additional characterization techniques were used to characterize selected samples in this work. Some of these are described below.

### 2.6.1 Electrical Conductivity Measurements (4 Point DC-Probe)

The electrical conductivities of the conductive oxide-YSZ composites were determined using slabs (4 mm x 4 mm x 15 mm) prepared using methods described in Chapter 2.4. The conductive oxide was first pre-reduced at the desired temperature in humidified H<sub>2</sub> for 2 h before the conductivity measurements were performed. Four Ag wires were attached to the slab with Ag paste. One wire was wrapped around each end of the sample while two other were wrapped near the middle. The cross sectional area of the sample (A) and the distance (d) between the two middle Ag wires were measured. The conductivities were determined using 4-probe, DC measurements in humidified H<sub>2</sub> as a function of temperature. The current (i) was supplied through the two outer lead wires and the potential (V) was measured between the two inner lead wires. Based on the values measured, the electrical conductivity of the sample can then be calculated by the following Equation 2.4:

$$\sigma_e = \frac{i*d}{V*A} \quad \text{Equation 2.4}$$

### 2.6.2 X-Ray Diffraction (XRD)

The solubility limits of selected perovskite structures were determined by X-Ray Diffraction (XRD) based on both the appearance of secondary phases and the concentration at which a discontinuity was observed in plot of the lattice parameter

versus dopant concentration. The XRD instrument used for the work in this dissertation was a Rigaku D/Max-B Powder Diffractometer with a monochromated Cu K $\alpha$  radiation source. The scans were performed between 2 $\theta$  range of 20° to 60°, with a sampling interval of 0.02° and a scan speed of 2°/min. For some of the samples, a small amount of YSZ was physically mixed with the oxides to act as a reference.

### **2.6.3 Scanning Electron Microscopy (SEM)**

The morphological structure of the anode composites was determined using scanning electron microscopy (SEM) (FEI Quanta 600 ESEM).

### **2.6.4 BET Surface Area Measurements**

The surface areas of the porous oxides were measured by the BET method using Kr adsorption at 78 K. Prior to measurement, the samples were first preheated under vacuum at 473 K for 1 h to desorb surface impurities, followed by adsorption of Kr at 78 K. The surface area can be calculated from the volume of adsorbed Kr gas required to form a monolayer, as estimated using the BET measurements and the size of the Kr molecule.

### **2.6.5 Atomic Force Microscopy (AFM)**

The surface topography was measured in air using an AFM (Pacific Nanotechnology) operated in close-contact (tapping) mode.

### 2.6.6 Coulometric Titration

The redox properties for catalytic materials were measured electrochemically using a coulometric-titration cell. This technique measures the sample composition as a function of  $pO_2$  for the oxides and provides redox isotherms of the oxides as a function of oxygen fugacity from equilibrium constants.

For example, for a given redox reaction,



where M is a metal, the equilibrium constant is a function only of the oxygen fugacity since the activity of solids is equal to 1.

$$K_{eq} = \frac{a_{MO_{x+2}}}{a_{MO_x} \cdot P(O_2)} = P(O_2)^{-1} \quad \text{Equation 2.6}$$

The differential Gibbs free energy of the oxidation reaction can then be calculated using:

$$\Delta G = RT \ln(K_{eq}) \quad \text{Equation 2.7}$$

This can be calculated if the  $P(O_2)$  can be measured experimentally. As the experimental  $P(O_2)$  values are very low, that the oxygen fugacity must be established by an equilibrium of buffer gases, such as  $H_2$ - $H_2O$  and  $CO$ - $CO_2$ , as shown in following reactions:



If the values of the initial concentrations of the buffer gases are known, the  $P(O_2)$  can be determined by the following equations:

$$\log(P(O_2)) = -2\log(K_{eq}) + 2\log(P(H_2O)/P(H_2)) \quad \text{Equation 2.10}$$

$$\log(P(O_2)) = -2\log(K_{eq}) + 2\log(P(CO_2)/P(CO)) \quad \text{Equation 2.11}$$

The experimental setup used to measure the redox properties of materials used in this dissertation is shown in Figure 2.4<sup>33</sup>.

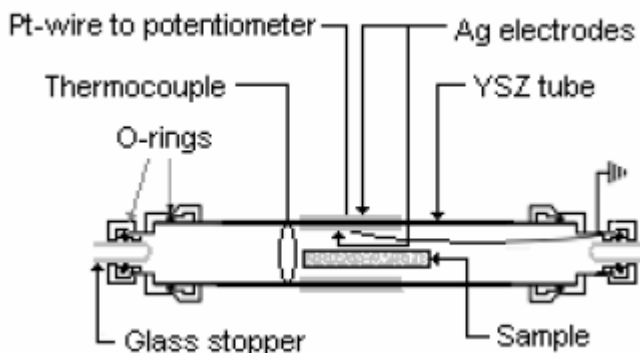


**Figure 2.4:** Schematic of Coulometric Titration apparatus<sup>33</sup>.

The cell consisted of a YSZ tube with Ag electrodes painted onto the inner and outer surfaces. Pt wire was attached to the inner electrode with a Ag gauze that was also pasted onto the inner electrode using Ag paste. The other end of the inner electrode connected Pt wire was then spot-welded to an Ultra-Torr fitting (Swagelok) which will eventually fit over the end of the tube. Approximately 0.1g of sample was placed in the cell and then pre-reduced in flowing 10% $H_2$ :90% $N_2$  at 973 K for 4 h. The  $H_2$  treatment insured that the measurements were started from the reduced state of the sample. After passing the gas buffer over the sample, the YSZ tube was immediately sealed using a glass stoppers into the Ultra-Torr fittings.

Precise amounts of oxygen were added to the cell in a stepwise fashion by pumping oxygen through the YSZ electrolyte by applying a voltage across the two electrodes using a Gamry Instruments potentiostat. After each  $O_2$  addition the sample was allowed to equilibrate (where the potential varied less than 0.1 mV/h which could take up

to two days), the  $pO_2$  in the cell was determined from the voltage across the two electrodes via the Nernst equation (equation 2.12).

$$OCV = -\frac{RT}{4F} * \ln \left( \frac{P(O_2)_{in}}{P(O_2)_{out}} \right) \quad \text{Equation 2.12}$$

The oxygen stoichiometry of the sample was determined from the known starting stoichiometry and the amount of  $O_2$  pumped into the cell. All coulometric titration experiments were performed with the sample at 973 K.

## 2.7 References

- 1 Cargnello, M. *et al.* Novel embedded Pd@CeO<sub>2</sub> catalysts: a way to active and stable catalysts. *Dalton T* **39**, 2122-2127, doi:Doi 10.1039/B916035c (2010).
- 2 Cargnello, M., Wieder, N. L., Montini, T., Gorte, R. J. & Fornasiero, P. Synthesis of Dispersible Pd@CeO<sub>2</sub> Core-Shell Nanostructures by Self-Assembly. *J Am Chem Soc* **132**, 1402-1409, doi:Doi 10.1021/Ja909131k (2010).
- 3 Cargnello, M. *et al.* Exceptional Activity for Methane Combustion over Modular Pd@CeO<sub>2</sub> Subunits on Functionalized Al<sub>2</sub>O<sub>3</sub>. *Science* **337**, 713-717, doi:DOI 10.1126/science.1222887 (2012).
- 4 Adijanto, L., Kungas, R., Bidrawn, F., Gorte, R. J. & Vohs, J. M. Stability and performance of infiltrated La<sub>0.8</sub>Sr<sub>0.2</sub>Co<sub>x</sub>Fe<sub>1-x</sub>O<sub>3</sub> electrodes with and without Sm<sub>0.2</sub>Ce<sub>0.8</sub>O<sub>1.9</sub> interlayers. *J Power Sources* **196**, 5797-5802, doi:DOI 10.1016/j.jpowsour.2011.03.022 (2011).
- 5 Adijanto, L., Kungas, R., Park, J., Vohs, J. M. & Gorte, R. J. SOFC anodes based on infiltration of tungsten bronzes. *Int J Hydrogen Energ* **36**, 15722-15730, doi:DOI 10.1016/j.ijhydene.2011.09.059 (2011).
- 6 Adijanto, L., Padmanabhan, V. B., Holmes, K. J., Gorte, R. J. & Vohs, J. M. Physical and electrochemical properties of alkaline earth doped, rare earth vanadates. *J Solid State Chem* **190**, 12-17, doi:DOI 10.1016/j.jssc.2012.01.065 (2012).
- 7 Adijanto, L., Padmanabhan, V. B., Kungas, R., Gorte, R. J. & Vohs, J. M. Transition metal-doped rare earth vanadates: a regenerable catalytic material for

- SOFC anodes. *J Mater Chem* **22**, 11396-11402, doi:Doi 10.1039/C2jm31774e (2012).
- 8 Adjianto, L., Padmanabhan, V. B., Gorte, R. J. & Vohs, J. M. Polarization-Induced Hysteresis in CuCo-Doped Rare Earth Vanadates SOFC Anodes. *J Electrochem Soc* **159**, F751-F756, doi:Doi 10.1149/2.042211jes (2012).
- 9 Vohs, J. M. & Gorte, R. J. High-Performance SOFC Cathodes Prepared by Infiltration. *Adv Mater* **21**, 943-956, doi:DOI 10.1002/adma.200802428 (2009).
- 10 Bidrawn, F., Kim, G., Aramrueang, N., Vohs, J. M. & Gorte, R. J. Dopants to enhance SOFC cathodes based on Sr-doped LaFeO<sub>3</sub> and LaMnO<sub>3</sub>. *J Power Sources* **195**, 720-728, doi:DOI 10.1016/j.jpowsour.2009.08.034 (2010).
- 11 Bidrawn, F., Lee, S., Vohs, J. M. & Gorte, R. J. The effect of Ca, Sr, and Ba doping on the ionic conductivity and cathode performance of LaFeO<sub>3</sub>. *J Electrochem Soc* **155**, B660-B665, doi:Doi 10.1149/1.2907431 (2008).
- 12 Huang, Y. Y., Ahn, K., Vohs, J. M. & Gorte, R. J. Characterization of Sr-doped LaCoO<sub>3</sub>-YSZ composites prepared by impregnation methods. *J Electrochem Soc* **151**, A1592-A1597, doi:Doi 10.1149/1.1789371 (2004).
- 13 Huang, Y. Y., Vohs, J. M. & Gorte, R. J. Fabrication of Sr-doped LaFeO<sub>3</sub>/YSZ composite cathodes. *J Electrochem Soc* **151**, A646-A651, doi:Doi 10.1149/1.1652053 (2004).
- 14 Kim, G., Corre, G., Irvine, J. T. S., Vohs, J. M. & Gorte, R. J. Engineering composite oxide SOFC anodes for efficient oxidation of methane. *Electrochem Solid St* **11**, B16-B19, doi:Doi 10.1149/1.2817809 (2008).



- 15 Kim, G., Vohs, J. M. & Gorte, R. J. Enhanced reducibility of ceria-YSZ composites in solid oxide electrodes. *J Mater Chem* **18**, 2386-2390, doi:Doi 10.1039/B718931a (2008).
- 16 Kungas, R., Bidrawn, F., Vohs, J. M. & Gorte, R. J. Doped-Ceria Diffusion Barriers Prepared by Infiltration for Solid Oxide Fuel Cells. *Electrochem Solid St* **13**, B87-B90, doi:Doi 10.1149/1.3432253 (2010).
- 17 Wang, W. S., Gross, M. D., Vohs, J. M. & Gorte, R. J. The stability of LSF-YSZ electrodes prepared by infiltration. *J Electrochem Soc* **154**, B439-B445, doi:Doi 10.1149/1.2709510 (2007).
- 18 Park, S., Gorte, R. J. & Vohs, J. M. Tape cast solid oxide fuel cells for the direct oxidation of hydrocarbons. *J Electrochem Soc* **148**, A443-A447 (2001).
- 19 Kungas, R., *Factors Governing the Performance and Stability of Solid Oxide Fuel Cell Cathodes Prepared by Infiltration*. Ph.D. Thesis. University of Pennsylvania: U.S.A. (2012).
- 20 Kungas, R., Kim, J. S., Vohs, J. M. & Gorte, R. J. Restructuring Porous YSZ by Treatment in Hydrofluoric Acid for Use in SOFC Cathodes. *J Am Ceram Soc* **94**, 2220-2224, doi:DOI 10.1111/j.1551-2916.2010.04359.x (2011).
- 21 R. E. Mistler and E. R. Twiname, *Tape Casting: Theory and Practice*, pp. 298. The American Ceramic Society: Westerville, OH, (2000).
- 22 Fukui, T., Ohara, S., Naito, M. & Nogi, K. Performance and stability of SOFC anode fabricated from NiO-YSZ composite particles. *J Power Sources* **110**, 91-95, doi:Pii S0378-7753(02)00218-5, Doi 10.1016/S0378-7753(02)00218-5 (2002).

- 23 Kim, S. D. *et al.* Ni-YSZ cermet anode fabricated from NiO-YSZ composite powder for high-performance and durability of solid oxide fuel cells. *Solid State Ionics* **178**, 1304-1309, doi:DOI 10.1016/j.ssi.2007.06.014 (2007).
- 24 He, H. P. *et al.* Low-temperature fabrication of oxide composites for solid-oxide fuel cells. *J Am Ceram Soc* **87**, 331-336 (2004).
- 25 Busawon, A. N., Sarantaridis, D. & Atkinson, A. Ni infiltration as a possible solution to the redox problem of SOFC anodes. *Electrochem Solid St* **11**, B186-B189, doi:10.1149/1.2959078 (2008).
- 26 Smith, B. H. & Gross, M. D. A Highly Conductive Oxide Anode for Solid Oxide Fuel Cells. *Electrochem Solid St* **14**, B1-B5, doi:10.1149/1.3505101 (2011).
- 27 Kim, G. *et al.* Investigation of the Structural and Catalytic Requirements for High-Performance SOFC Anodes Formed by Infiltration of LSCM. *Electrochem Solid St* **12**, B48-B52, doi:10.1149/1.3065971 (2009).
- 28 Gross, M. D., Vohs, J. M. & Gorte, R. J. An examination of SOFC anode functional layers based on ceria in YSZ. *J Electrochem Soc* **154**, B694-B699, doi:10.1149/1.2736647 (2007).
- 29 Kim, J. S., Nair, V. V., Vohs, J. M. & Gorte, R. J. A study of the methane tolerance of LSCM-YSZ composite anodes with Pt, Ni, Pd and ceria catalysts. *Scripta Mater* **65**, 90-95, doi:DOI 10.1016/j.scriptamat.2010.06.016 (2011).
- 30 Gorte, R. J., Kim, J. S., Nair, V. V. & Vohs, J. M. A study of the methane tolerance of LSCM-YSZ composite anodes with Pt, Ni, Pd and ceria catalysts. *Scripta Mater* **65**, 90-95, doi:10.1016/j.scriptamat.2010.06.016 (2011).

- 31 Kim, G., Gross, M. D., Wang, W., Vohs, J. M. & Gorte, R. J. SOFC anodes based on LST-YSZ composites and on  $Y_{0.04}Ce_{0.48}Zr_{0.48}O_2$ . *J Electrochem Soc* **155**, B360-B366, doi:10.1149/1.2840473 (2008).
- 32 Lee, S., Kim, G., Vohs, J. M. & Gorte, R. J. SOFC anodes based on infiltration of  $La_{0.3}Sr_{0.7}TiO_3$ . *J Electrochem Soc* **155**, B1179-B1183, doi:Doi 10.1149/1.2976775 (2008).
- 33 Baldychev, I., Gorte, R. J. & Vohs, J. M. The impact of redox properties on the reactivity of  $V_2O_5/Al_2O_3$  catalysts. *J Catal* **269**, 397-403, doi:DOI 10.1016/j.jcat.2009.11.022 (2010).

## Chapter 3. SOFC Anodes Based on Infiltration of Tungsten Bronze\*

### Summary

Several tungsten bronzes were investigated for use in solid oxide fuel cell (SOFC) anodes. Composite anodes were prepared by infiltration of the precursor salts into a porous yttria-stabilized zirconia (YSZ) scaffold to produce 40 wt. % composites with bronze compositions of  $\text{Na}_{0.8}\text{Nb}_y\text{W}_{1-y}\text{O}_{3-\delta}$  ( $y = 0, 0.3, 0.7, \text{ and } 1$ ),  $\text{K}_{0.5}\text{WO}_{3-\delta}$ ,  $\text{Cs}_{0.2}\text{WO}_{3-\delta}$ , and  $\text{Rb}_{0.2}\text{WO}_{3-\delta}$ . XRD data showed that the bronze structures were formed following reduction in humidified  $\text{H}_2$  at 873 K but that the bronzes were partially reduced to metallic W above 1073 K. Composite conductivities as high as 130 S/cm were observed at 973 K for the  $\text{Na}_{0.8}\text{WO}_{3-\delta}$ -YSZ composite but substitution of Nb significantly decreased the conductivity without increasing the temperature at which tungsten was reduced. The impedance of  $\text{Na}_{0.8}\text{WO}_{3-\delta}$ -YSZ anodes in humidified  $\text{H}_2$  at 973 K was greater than  $1.0 \Omega \text{ cm}^2$  but this decreased to approximately  $0.3 \Omega \text{ cm}^2$  upon the addition of 1 wt. % Pd for catalytic purposes. The possible use of anodes based on tungsten bronzes is discussed.

---

\* This chapter was published as a research paper in the International Journal of Hydrogen Energy, 36 (2011) 15722. Copyright: 2011, Elsevier.

### 3.1 Introduction

As discussed in Chapter 1, for SOFC based on yttria-stabilized zirconia (YSZ), the standard anode material is a composite of Ni and YSZ, a composition that works well under many conditions. However, Ni cermets have limitations and electrodes based on electronically conductive ceramics could provide a number of important advantages if they were able to provide comparable performance<sup>1,2</sup>. Ceramic electrodes are expected to be less susceptible to sintering and coking, could be redox stable, and could be more tolerant of impurities like sulfur<sup>3-7</sup>.

While some progress has been made in achieving this goal using mixed oxides based on titanates<sup>8-11</sup>, manganates<sup>12-17</sup>, and chromates<sup>18</sup> (e.g. (LaSr)TiO<sub>3</sub> and (La,Sr)<sub>x</sub>(Cr,Mn)<sub>y</sub>O<sub>3-δ</sub>) with the perovskite structure, these materials have only modest bulk electronic conductivities (< 5 S cm<sup>-1</sup>) under typical SOFC anode operating conditions. When used in a porous perovskite-YSZ composite anode, the overall conductivity is 1-2 orders of magnitude lower. Thus, for these materials to be used in SOFC anodes, the electrode must be very thin (<50 μm) in order to limit ohmic losses or the perovskite must be restricted to a thin functional layer near the electrolyte. For example, a 45 wt. % infiltrated, porous La<sub>0.8</sub>Sr<sub>0.2</sub>Cr<sub>0.5</sub>Mn<sub>0.5</sub>O<sub>3</sub>-YSZ composite has a electrical conductivity of only 0.1 S cm<sup>-1</sup> in humidified H<sub>2</sub> at 973 K<sup>12</sup>.

Another class of oxides, which has not been fully explored for use in SOFC anodes but whose members have very high electronic conductivities under reducing conditions, is the tungsten bronzes. Tungsten bronzes are well defined non-stoichiometric compounds of the general formula M<sub>x</sub>WO<sub>3</sub> where M is some other metal, most commonly an alkali, and x is less than one<sup>19-27</sup>. These materials became known as

bronzes after it was observed that heating sodium tungstate in dry hydrogen caused the formation of golden yellow crystals with metallic appearance. The range of colors and metallic luster of the bronzes are the result of high IR reflectivity (due to free electron interband transitions, as in a metal)<sup>28</sup>. In bronzes, this frequency occurs in the visible region of the spectrum, its exact position being dependent on the free electron concentration, and thus  $x$ ; therefore the color of the bronze is determined by  $x$ , as shown in Figure 3.1<sup>29</sup>.

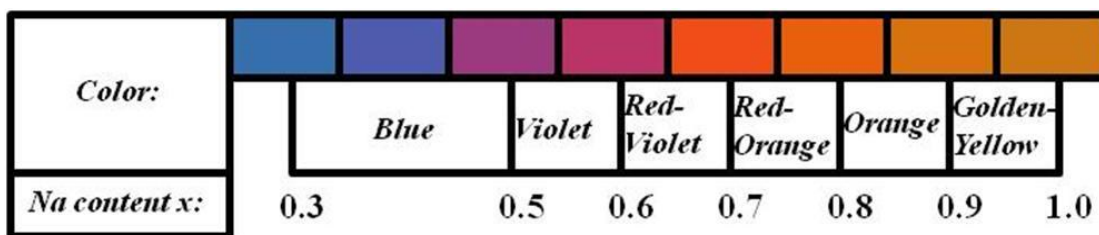


**Figure 3.1:** Colors of  $\text{Na}_x\text{WO}_3$  at different  $x$  values

Analogous compounds of Mo, V, Nb, and Ti have similar properties<sup>26</sup>. Bulk conductivities above  $10^4$  S/cm have been reported for a number of the tungsten bronzes<sup>20,22-25,27</sup>, but we are aware of only one study involving this class of compounds being used in SOFC anodes. Irvine, *et al.* investigated several oxide-bronze type phases and concluded that the most promising had the compositions of  $\text{Ba}_{0.6-x}\text{A}_x\text{Ti}_{0.2}\text{Nb}_{0.8}\text{O}_3$  (A=Sr, Ca). These materials were found to be stable under both air and reducing conditions, and exhibited bulk electronic conductivities of approximately 10 S/cm at low  $P(\text{O}_2)$  and 1203 K<sup>30</sup>. Perhaps because the electrodes in that study were prepared by conventional ceramics processing procedures, electrode performance was modest.

In this chapter, we set out to determine whether effective composite electrodes could be made from oxide bronzes using infiltration. We focused most of our attention on  $\text{Na}_{0.8}\text{WO}_{3-\delta}$  because of its very high conductivity but tungsten bronzes with Na replaced by K, Rb, and Cs were also investigated. Because these materials were reduced to metallic W above 1073 K, the effect of partial substitution of W for Nb ( $\text{Na}_{0.8}\text{Nb}_y\text{W}_{1-y}\text{O}_{3-\delta}$ ) was investigated to determine whether these materials would exhibit enhanced stability. Our results demonstrate that the tungsten bronzes are promising for SOFC applications at temperatures below 1073 K but that these bronzes are reduced to metallic W at higher temperatures.

### 3.2 Experimental

The  $\text{M}_x\text{WO}_{3-\delta}$  bronzes were prepared by mixing the amounts of  $(\text{NH}_4)_6\text{W}_{12}\text{O}_{39}$  (Alfa Aesar) with either  $\text{Na}_2\text{WO}_4 \cdot 2\text{H}_2\text{O}$  (Alfa Aesar, 95%),  $\text{K}_2\text{WO}_4$  (Alfa Aesar, 99.5%),  $\text{RbNO}_3$  (Alfa Aesar, 99%), or  $\text{Cs}_2\text{WO}_4$  (Alfa Aesar, 99.9%) in molar ratio of  $\text{M} : \text{W} = x : 1$ , in an aqueous solution. The mixed powders were then dried and calcined at 723 K in air before reduction in humidified  $\text{H}_2$  (3%  $\text{H}_2\text{O}$ ) to make the bronze. Since the non-stoichiometric compounds,  $\text{Na}_x\text{WO}_{3-\delta}$ , have the highest conductivity at  $x=0.8$ <sup>23,27</sup>, we chose this composition for most of our studies. For  $\text{K}_x\text{WO}_{3-\delta}$ , the range of stable structures exists only for  $0 < x < 0.6$ <sup>31</sup>, so that materials with K:W ratios of 0.5 were examined. Because the stability range for  $\text{Rb}_x\text{WO}_{3-\delta}$  and  $\text{Cs}_x\text{WO}_{3-\delta}$  are reported to be  $0 < x < 0.3$ , these materials were studied with  $x = 0.2$ <sup>21,32</sup>.

The stability of the alkali-tungsten bronzes in humidified  $\text{H}_2$  was found to be limited to temperatures below 1073 K due to reduction of the tungsten to its metallic

state. Therefore, we also investigated the effect of Nb doping for materials with compositions given by  $\text{Na}_{0.8}\text{Nb}_y\text{W}_{1-y}\text{O}_{3-\delta}$ , with  $y = 0, 0.3, 0.7,$  and  $1$  in an attempt to prevent the reduction of the metals. These Nb-based materials were prepared by adding the desired stoichiometric amount of  $\text{C}_4\text{H}_4\text{N}\cdot\text{NbO}_9$  (Aldrich, 99.99%) to the tungsten salts.

The button-sized fuel cells used in this study were fabricated from porous-dense-porous YSZ wafers that were produced by sintering of green YSZ (Tosoh Corp., 8 mol%  $\text{Y}_2\text{O}_3$ -doped  $\text{ZrO}_2$ ,  $0.2\mu\text{m}$ ) tapes formed by laminating layers that contained graphite pore formers to the electrolyte layer as described in Chapter 2<sup>33</sup>. For each cell, the dense electrolyte layer was  $80\ \mu\text{m}$  thick and  $1\ \text{cm}$  in diameter. The porous layers on each side of the electrolyte layer were  $50\ \mu\text{m}$  thick,  $0.67\ \text{cm}$  in diameter, and  $\sim 60\%$  porous, with a BET surface area  $0.3\ \text{m}^2\text{g}^{-1}$ .

The cathodes were prepared following the procedure detailed in Chapter 2. Once the perovskite loading was 40 wt. %, the cathode was calcined to  $1123\ \text{K}$  for 4 h to form the perovskite structure. After addition of the LSF cathode, the 30 wt. % of the oxide bronzes were added to the opposite side of the electrolyte, using methods similar to that used in preparing the bronze powders. In one cell, 1 wt. % Pd was added to the anode side by infiltration with an aqueous solution of  $(\text{NH}_3)_4\text{Pd}(\text{NO}_3)_2$ .

For fuel cell testing, silver paste was applied as a current collector for both the anode and cathode and the cells were mounted onto an alumina rod with a ceramic adhesive (Aremco, Ceramabond 552). All the cell testing was performed with the anode exposed to humidified (3%  $\text{H}_2\text{O}$ )  $\text{H}_2$  and the cathode to ambient air. The electrochemical impedance spectra and V-i polarization curves were measured using a Gamry Instruments

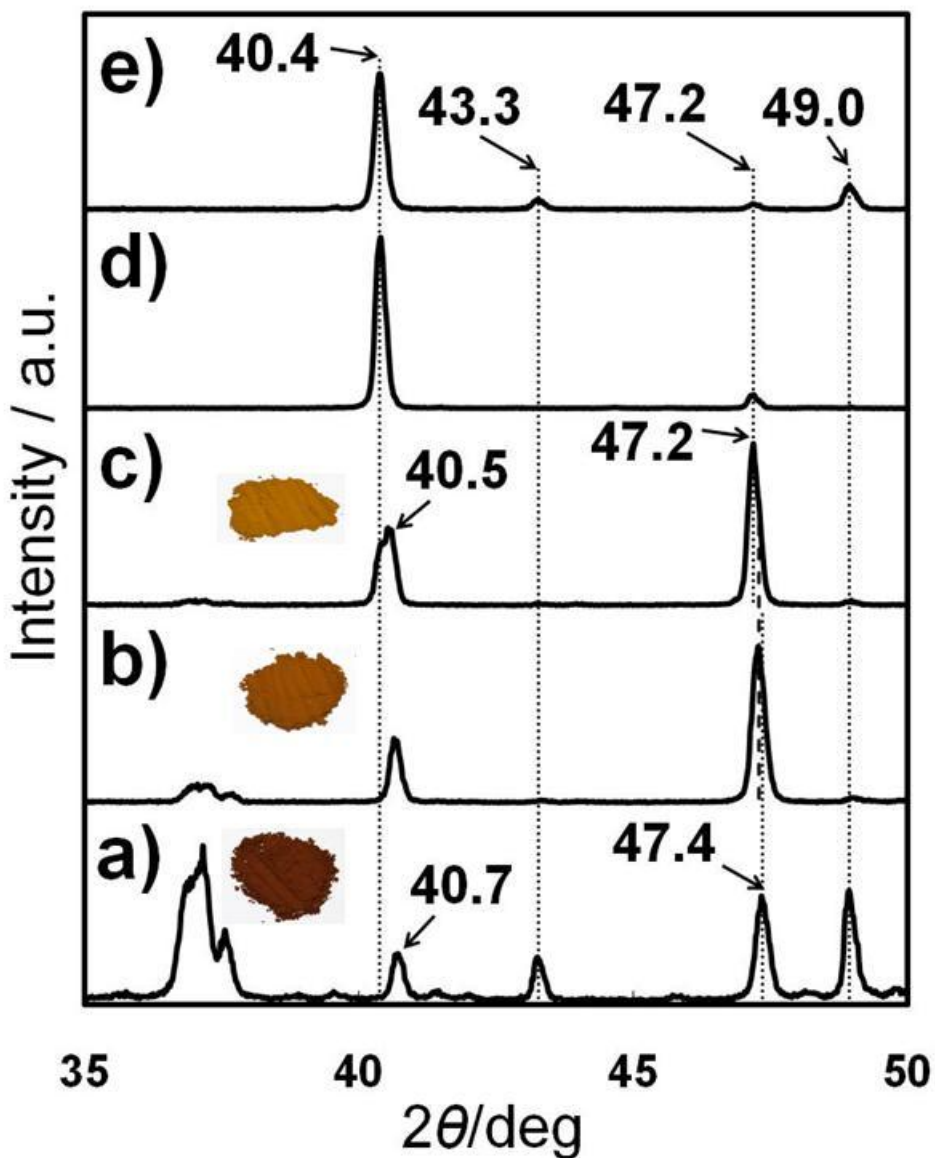


potentiostat. The electrochemical impedance spectrum was measured in the frequency range of 300 kHz to 0.01 Hz, with a 1-mA AC perturbation.

The conductivities of bronze-YSZ composites were determined using slabs (4 mm x 4 mm x 15 mm) prepared by infiltration of the bronzes into porous YSZ fabricated from the same slurry used in tape casting the porous layers. The conductivities were determined using 4-probe, DC measurements in controlled environments. The physical characterization of the anode composites were carried out using scanning electron microscopy (SEM) (FEI Quanta 600 ESEM) and X-ray diffraction (XRD), measured using Cu  $K_{\alpha}$  radiation at  $20^{\circ} \leq 2\theta \leq 60^{\circ}$ . In the work with bronze powders, YSZ was added as an internal standard to observe any shifts in the lattice parameters.

### 3.3 Results

To determine the conditions required to obtain the Na-W bronzes, we first examined the evolution of the bronze structures as a function of temperature from the precursors using XRD.



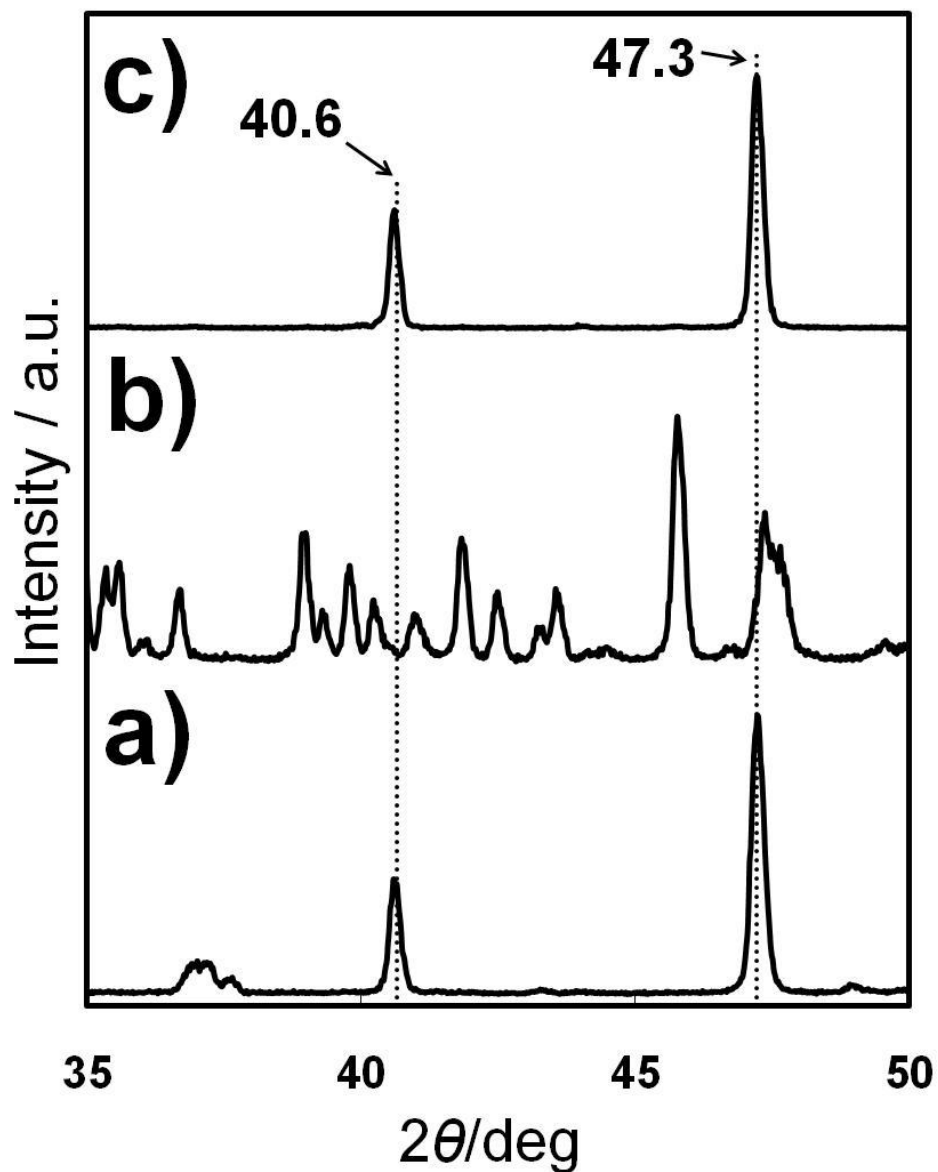
**Figure 3.2:** XRD patterns of  $\text{Na}_{0.8}\text{WO}_{3-\delta}$  synthesized in humidified (3%  $\text{H}_2\text{O}$ )  $\text{H}_2$  at following temperatures: a) 823 K b) 973 K c) 1023 K d) 1073 K, and e) 1123K.

Figure 3.2 shows diffraction patterns for mixtures of  $\text{Na}_2\text{WO}_4 \cdot 2\text{H}_2\text{O}$  and  $(\text{NH}_4)_6\text{W}_{12}\text{O}_{39} \cdot x\text{H}_2\text{O}$ , with a Na:W ratio of 0.8, upon heating to various temperatures in humidified (3%  $\text{H}_2\text{O}$ )  $\text{H}_2$ , after having been initially heated in air to 723 K. At 823 K, Figure 3.2a), Na-W bronzes started to form, as demonstrated by the presence of peaks at 40.7 and 47.4 degrees  $2\theta$ . Other features in the region of 37, and at 43.2 and 48.9, degrees  $2\theta$  are associated with the precursor oxides,  $\text{WO}_2$  and  $\text{Na}_2\text{WO}_4$ <sup>34</sup>. Increasing the reduction temperature to 973 K, Figure 3.2b), increased the conversion to the bronze significantly; further heating to 1023 K caused only minor additional changes, Figure 3.2c).

There was a slight shift in the position of the diffraction peaks for the bronze phase when the reduction temperature was increased from 823 to 1023 K, with the peak at 40.7 degrees  $2\theta$  shifting to 40.5 degrees  $2\theta$  and the peak at 47.4 shifting to 47.2. These shifts are consistent with an increase in the Na:W ratio of the bronze phase<sup>20,24</sup>, a conclusion that is also suggested by changes in the color of the sample. Following reduction at 873 K, the sample was a deep, reddish brown. It then turned to orange following reduction at 973 K and to a golden-yellow color at 1023 K. It has been reported that the color of Na-W bronzes changes with the Na:W ratio, with deep-red bronzes having a Na:W ratio of 0.6 to 0.7 and gold-colored bronzes having a Na:W ratio of 0.8 to 1<sup>20,35</sup>. Therefore, the color changes between 873 and 973 K suggest that there is incomplete mixing of the oxides at 873 K and that the Na:W ratio of the bronze phase only reaches the bulk composition at higher temperatures.

After reduction at 1073 K, Figure 3.2d), the diffraction pattern changed dramatically. In particular, the peak at 40.4 degrees  $2\theta$  is no longer associated with a bronze phase but is due to formation of metallic tungsten. The sample also took on a gray

color, consistent with formation of a metal phase. Further heating to 1123 K, Figure 3.2e), resulted in the restoration of some  $\text{Na}_2\text{WO}_4$ , associated with peaks at 43.3 and 48.9 degrees  $2\theta$ , in agreement with previous reports of Na-W bronzes following high-temperature reduction<sup>34</sup>. Furthermore, there was evidence that some of the powdered sample had melted after this treatment. It is noteworthy that  $\text{Na}_2\text{WO}_4$  has a melting point of 1011 K.



**Figure 3.3:** XRD patterns of  $\text{Na}_{0.8}\text{WO}_{3-\delta}$  that were a) reduced at 973 K under humidified (3%  $\text{H}_2\text{O}$ )  $\text{H}_2$ , b) oxidized at 973 K in air, and c) then re-reduced.

To determine the effect of oxidation and re-reduction of the Na-W bronze structure at SOFC operating temperatures, we examined the XRD patterns of the Na-W bronze after oxidation and reduction at 973 K, with the results shown in Figure 3.3. Figure 3.3a) is the diffraction pattern for the Na-W bronze formed by reduction in

humidified H<sub>2</sub> at 973 K, the same as that shown in Figure 3.2b). Oxidation of this bronze phase in air at 973 K produced the complex diffraction pattern in Figure 3.3b) that can be shown to be primarily Na<sub>2</sub>W<sub>2</sub>O<sub>7</sub>. Reduction at 973 K restored the bronze structure, Figure 3.3c), even removing peaks associated with impurity phases that were present in the initial sample.

To determine the compatibility of the Na-W bronzes with YSZ, we prepared a composite of the Na:W bronze (Na:W=0.8) with YSZ by aqueous infiltration of Na<sub>2</sub>WO<sub>4</sub>·2H<sub>2</sub>O and (NH<sub>4</sub>)<sub>6</sub>W<sub>12</sub>O<sub>39</sub>·xH<sub>2</sub>O into a porous YSZ slab, to a loading equivalent to 40 wt. % of the bronze. Multiple infiltration cycles were required to achieve this loading, with calcination to 723 K between cycles. After infiltration, the sample was reduced in humidified H<sub>2</sub> at 1023 K.

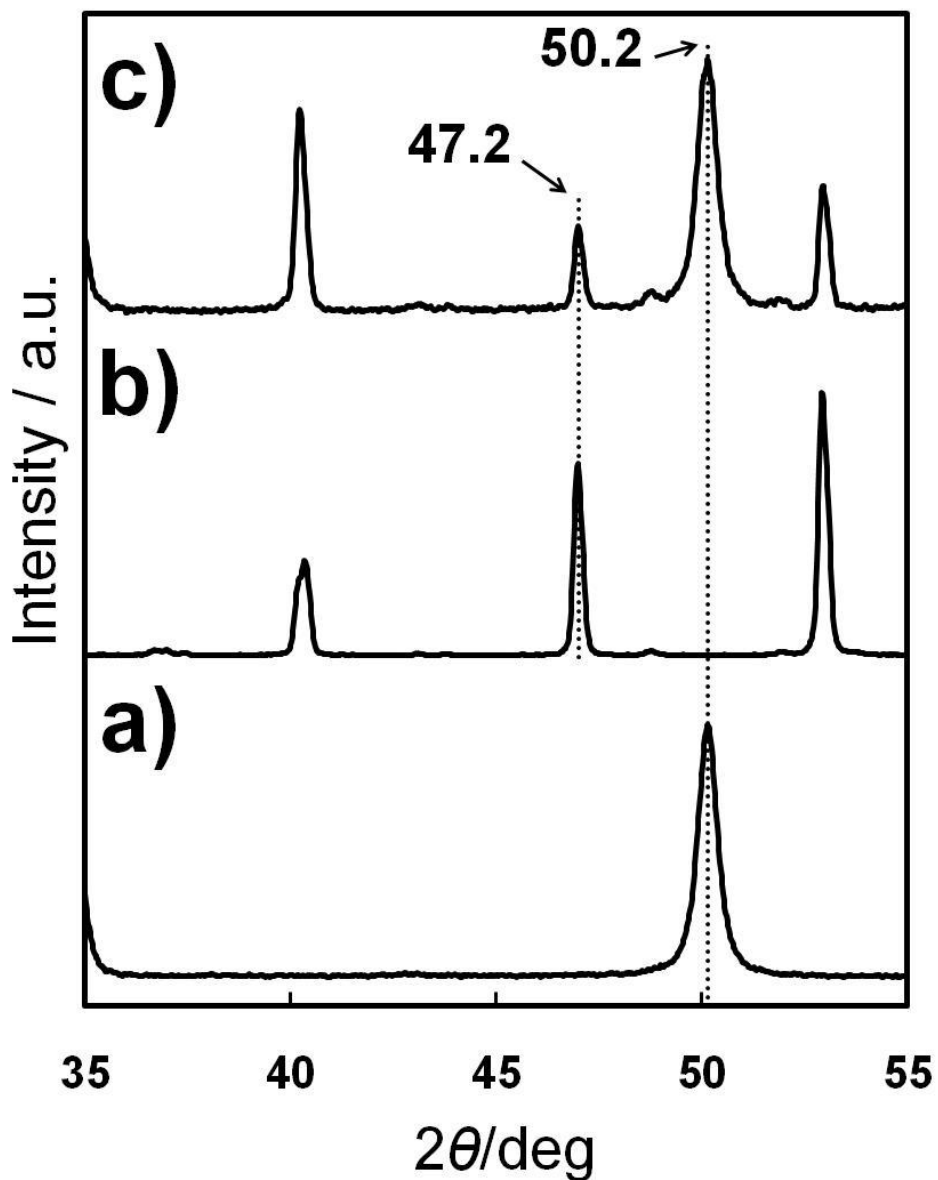


**Figure 3.4:** XRD patterns of a) YSZ, b) reduced  $\text{Na}_{0.8}\text{WO}_{3-\delta}$ , and c) mixed  $\text{Na}_{0.8}\text{WO}_{3-\delta}$  with YSZ reduced at 1023K under humidified (3%  $\text{H}_2\text{O}$ )  $\text{H}_2$ .

The XRD pattern of this sample is shown in Figure 3.4a), together with patterns of the pure Na-W bronze powder, Figure 3.4b) and the empty YSZ slab, Figure 3.4a). Small amounts of  $\text{Na}_2\text{WO}_4$  were observed in the composite after reduction, but the main features in the diffraction pattern of the composite were due to either YSZ or the Na-W

bronze. There was no evidence for solid-state reactions between the two components at this temperature. A previous study of SOFC anodes based on Nb-containing bronzes inferred that there were reactions with YSZ at 1573 K<sup>30</sup>; however, because 1573 K is above the temperature at which most cathode materials react with YSZ<sup>36</sup>, solid-state reactions with the YSZ electrolyte do not appear to be a serious problem for Na-W bronze anodes prepared by infiltration.

To determine whether tungsten bronzes formed from other alkali metals would show improved thermal stability under SOFC anode conditions, we prepared K-, Rb-, and Cs-tungsten bronzes according to the methods discussed in the Experimental section. XRD patterns were obtained for each sample after reduction in humidified H<sub>2</sub> at 973 and 1073 K, with results shown in Figure 3.5.



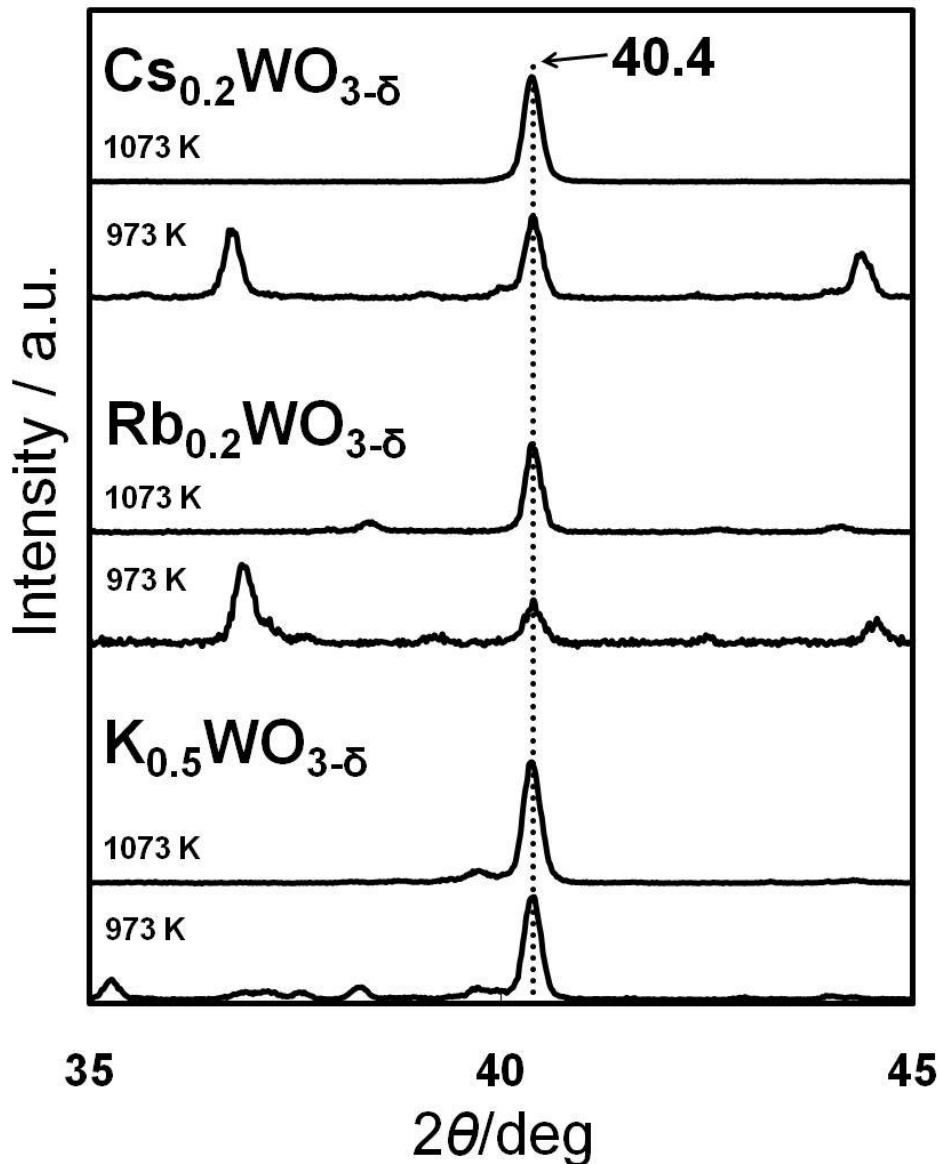


**Figure 3.5:** XRD patterns of a)  $\text{K}_{0.5}\text{WO}_{3-\delta}$ , b)  $\text{Rb}_{0.2}\text{WO}_{3-\delta}$ , and c)  $\text{Cs}_{0.2}\text{WO}_{3-\delta}$  synthesized in humidified (3%  $\text{H}_2\text{O}$ )  $\text{H}_2$  at 973 K and 1073K.

The diffraction patterns for these M-W bronzes are more complicated than that of the Na-W bronze, but the bronze phases were formed for each of the alkali cations at 973 K. Conversion to the bronze phase was nearly complete for Cs and Rb at 973 K; but diffraction peaks associated with the precursor oxides,  $\text{WO}_2$  and  $\text{K}_2\text{WO}_4$ , were still

observed at this temperature with K. The diffraction pattern for each of these samples also showed a peak for metallic tungsten at 40.4 degrees  $2\theta$ , even at 973 K, and this peak only grew larger after reduction at 1073 K. This suggests that the M-W bronzes are less stable than the Na-W bronze, due to the lower concentration of alkali cations. Since these materials did not show improved stability, we did not investigate them further.

Because Nb is much less reducible than W, we also investigated the stability of a series of bronzes with partial substitution of Nb for W,  $\text{Na}_{0.8}\text{Nb}_y\text{W}_{1-y}\text{O}_{3-\delta}$ . Following calcination of the mixed precursors in air to 723 K, each of the samples was reduced in humidified  $\text{H}_2$  at either 973 or 1123 K. XRD measurements were then performed on these samples, with the results shown in Figure 3.6. To determine the lattice parameters for each of the samples, a small amount of YSZ was physically mixed with the oxides to act as a reference.

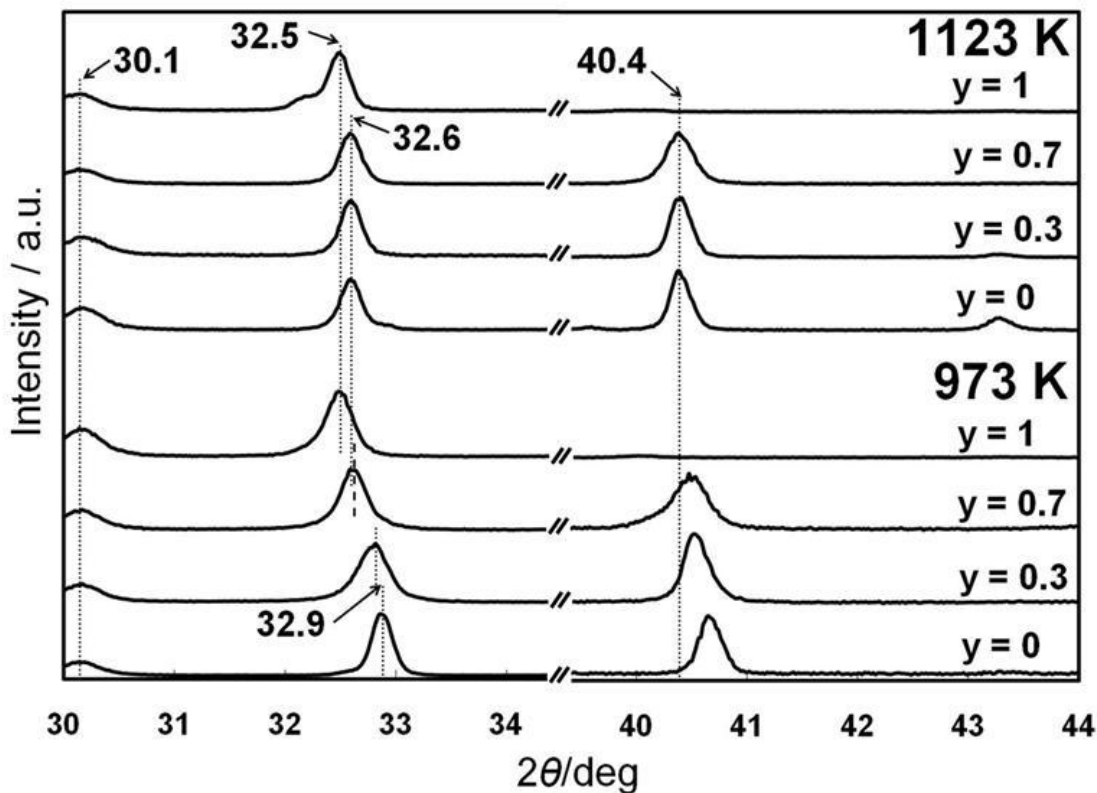


**Figure 3.6:** XRD patterns of  $\text{Na}_{0.8}\text{Nb}_y\text{W}_{1-y}\text{O}_{3-\delta}$  -YSZ composite with different Nb:W ratios ( $y = 0, 0.3, 0.7, 1$ ) synthesized in humidified (3%  $\text{H}_2\text{O}$ )  $\text{H}_2$  at following temperatures: a) 973 K, and b) 1123 K.

Reduction at 973 K removed peaks associated with  $\text{NaNbO}_3$  and  $\text{Na}_{0.8}\text{WO}_{3-\delta}$  from the diffraction pattern and formed peaks associated with bronze phases between 32 and 33 degrees  $2\theta$  and between 40 and 41 degrees  $2\theta$ . The position of these peaks varied with Nb content, from 32.9 degrees  $2\theta$  for  $\text{Na}_{0.8}\text{WO}_{3-\delta}$ , to 32.5 degrees  $2\theta$  for  $\text{NaNbO}_3$ , consistent with the lattice parameters expected for a single-phase species having the composition  $\text{Na}_{0.8}\text{Nb}_y\text{W}_{1-y}\text{O}_{3-\delta}$ . Additionally, there was no evidence for the formation of metallic tungsten at 973 K, as demonstrated by the positions of the peaks between 40 and 41 degrees  $2\theta$ , and the fact that peaks in this region shifted with Nb content. However, after reduction at 1123 K, changes were observed in the diffraction patterns for each of the W-containing samples that indicated formation of metallic tungsten. These samples all

exhibited peaks in their diffraction patterns at 32.6 and 40.4 degrees  $2\theta$ , independent of Nb content. Therefore, the partial substitution of Nb did not stabilize the bronze phase.

The electrical conductivities of several  $\text{Na}_x\text{Nb}_y\text{W}_{1-y}\text{O}_{3-\delta}$ -YSZ composites, with 40 wt. % of the bronze phase, are shown in Figure 3.7 as a function of temperature in humidified (3% $\text{H}_2\text{O}$ )  $\text{H}_2$ . All of the composites were prepared by aqueous infiltration of the bronze precursors into porous YSZ, with initial calcination in air at 723 K and then reduction at 973 K. Starting at 873 K, the conductivity measurements were then performed while raising the temperature progressively to 1123 K, and then lowering the temperature back to determine the effect of the higher reduction temperatures on the conductivity. In each case, the samples were held at the measurement temperature for 30 minutes to equilibrate.

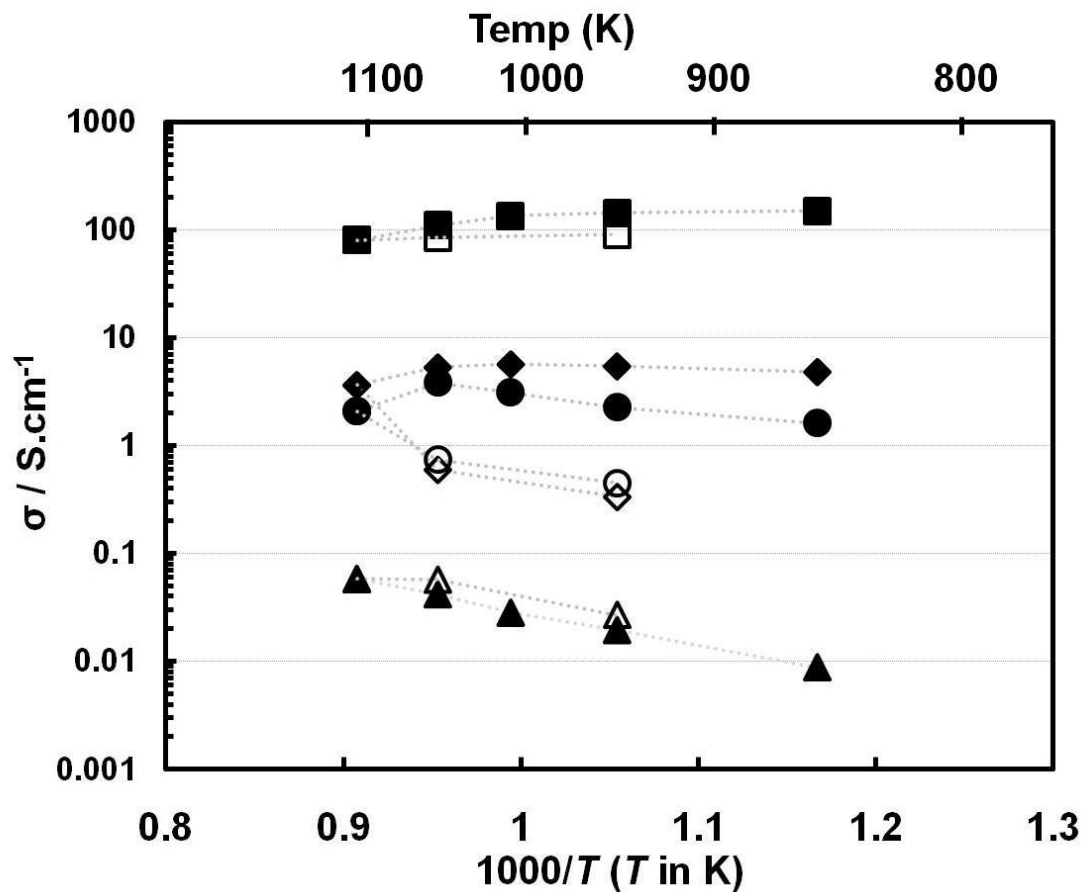


**Figure 3.7:** Electrical conductivities of the 40 wt. % (■)  $\text{Na}_{0.8}\text{WO}_{3-\delta}\text{-YSZ}$  (◆)  $\text{Na}_{0.8}\text{Nb}_{0.3}\text{W}_{0.7}\text{O}_{3-\delta}\text{-YSZ}$ , (●)  $\text{Na}_{0.8}\text{Nb}_{0.7}\text{W}_{0.3}\text{O}_{3-\delta}\text{-YSZ}$ , and (▲)  $\text{NaNbO}_{3-\delta}\text{-YSZ}$  composites in humidified (3%  $\text{H}_2\text{O}$ )  $\text{H}_2$  as a function of temperature. Data were obtained (■, ◆, ●, ▲) on heating and (□, ◇, ○, △) on cooling.

**Table 3.1:** Summary of the electronic conductivities of the bronze –YSZ composites used in this study reduced in H<sub>2</sub> (3% H<sub>2</sub>O).

| Compositions  | $\sigma_e$ of bronze-YSZ composite at 973 K (S/cm) |                           | Temperature at which decomposition was observed (K) |
|---|--|---------------------------|---|
|   | After reduction at 973 K                           | After reduction at 1123 K |   |
| Na <sub>0.8</sub> WO <sub>3</sub>                                   | 135  | 85                        | 1073  |
| K <sub>0.5</sub> WO <sub>3</sub>                                    | -  | -                         | 973   |
| Rb <sub>0.2</sub> WO <sub>3</sub>                                   | -  | -                         | 973   |
| Cs <sub>0.2</sub> WO <sub>3</sub>                                   | -  | -                         | 973   |
| Na <sub>0.8</sub> W <sub>0.7</sub> Nb <sub>0.3</sub> O <sub>3</sub> | 5.5  | 0.5                       | 1073  |
| Na <sub>0.8</sub> W <sub>0.3</sub> Nb <sub>0.7</sub> O <sub>3</sub> | 2.2  | 0.5                       | 1073  |
| Na <sub>0.8</sub> NbO <sub>3</sub>                                  | 0.03   | 0.03                      | stable  |

The electrical conductivity of the composite with the Na-W bronze ( $y = 0$ , Na:W = 0.8) was clearly the highest, with the maximum conductivity of 150 S/cm at 873 K and 135 S/cm at 973 K. The conductivity of the Na:W bronze decreased above 1073 K, but remained 80 S/cm at 1123 K. When this sample was cooled back to 973 K, the conductivity was 85 S/cm, likely due to partial decomposition of the Na-W bronze. The conductivities of the Nb-containing bronzes with  $y=0.3$  and  $0.7$  were lower but still well above the 1 S/cm target that has been proposed<sup>37,38</sup>. However, the conductivities for these samples fell significantly after reduction at 1123 K, to well under 1 S/cm at 973. Although the NaNbO<sub>3- $\delta$</sub> -YSZ composite was stable to higher temperature reduction, its conductivity was less than 0.1 S/cm at all temperatures. The conductivities of the various tungsten bronzes-YSZ composites are summarized in Table 3.1.

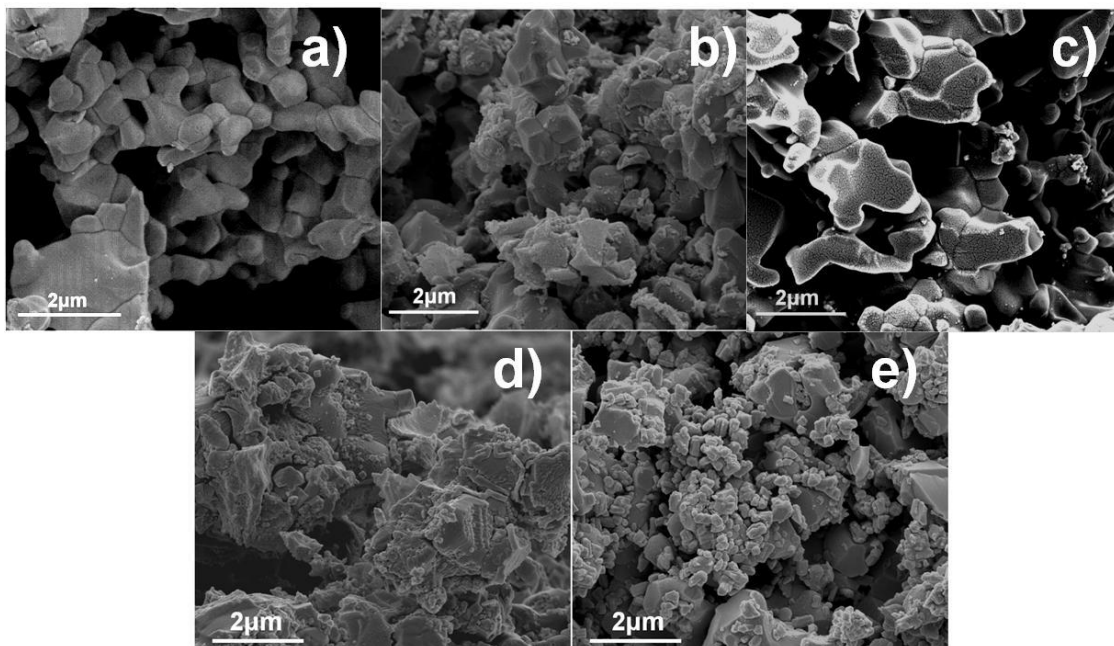


**Figure 3.8:** Microstructure of the (a) YSZ matrix,  $\text{Na}_{0.8}\text{WO}_{3-\delta}$ -YSZ composite reduced at following temperatures: (b) 973 K and (c) 1123 K, d)  $\text{Na}_{0.8}\text{Nb}_{0.3}\text{W}_{0.7}\text{O}_{3-\delta}$ -YSZ composite, and e)  $\text{Na}_{0.8}\text{Nb}_{0.7}\text{W}_{0.3}\text{O}_{3-\delta}$ -YSZ composite reduced at 1123 K in humidified (3%  $\text{H}_2\text{O}$ )  $\text{H}_2$ .

The microstructure of the bronze composites was investigated by SEM, with results shown in Figure 3.8. Figure 3.8a) shows the empty YSZ scaffold, which has a sponge-like morphology, with interconnecting pores that are roughly 2 to 3  $\mu\text{m}$  in size. The very low, BET surface area of the structure,  $0.3 \text{ m}^2\text{g}^{-1}$ , demonstrates that there is no microporosity within the YSZ channels. Figure 3.8b) is a micrograph after addition of 40 wt. % Na-W bronze, followed by reduction at 973 K. The YSZ pore structure is now covered by roughly shaped particles, approximately 0.1  $\mu\text{m}$  in size. Following reduction at 1123 K, Figure 3.8c), the Na-W appears to have melted and formed a uniform coating over the YSZ pores. It is noteworthy that  $\text{Na}_2\text{WO}_4$  has a melting point of 1011 K, so this partial melting is consistent with decomposition of the bronze at these higher temperatures. Furthermore, we observed that heating a sample of  $\text{Na}_2\text{WO}_4$  in humidified  $\text{H}_2$  at 1123 K also resulted in a gray structure with a melted appearance. Figures 3.8 d)

and 3.8e) are micrographs made from composites of YSZ with  $\text{Na}_{0.8}\text{Nb}_{0.3}\text{W}_{0.7}\text{O}_{3-\delta}$  and  $\text{Na}_{0.8}\text{Nb}_{0.7}\text{W}_{0.3}\text{O}_{3-\delta}$  after reduction at 1123 K. In the  $\text{Na}_{0.8}\text{Nb}_{0.3}\text{W}_{0.7}\text{O}_{3-\delta}$  composite, there appear to be larger platelets,  $\sim 1 \mu\text{m}$  in size, along with much smaller particles on the order of  $0.1 \mu\text{m}$  in diameter. In the  $\text{Na}_{0.8}\text{Nb}_{0.7}\text{W}_{0.3}\text{O}_{3-\delta}$  composite, only the smaller particles are observed.

To determine whether these tungsten bronzes could be used in SOFC anodes, button cells were prepared from  $\text{Na}_{0.8}\text{WO}_{3-\delta}$  and  $\text{Na}_{0.8}\text{Nb}_{0.7}\text{W}_{0.3}\text{O}_{3-\delta}$ . As described in the Experimental section, these cells had 80- $\mu\text{m}$  YSZ electrolytes with 40 wt. % LSF-YSZ cathodes. The anodes were prepared by infiltration of the bronze-phase, precursor salts to a loading of 40 wt. %, followed by calcination in air at 723 K and then reduction at the operating temperature, 973 K. In some cells, 1 wt. % Pd was also added to the anode by infiltration with aqueous solutions of  $(\text{NH}_3)_4\text{Pd}(\text{NO}_3)_2$ . Since the results for cells made from  $\text{Na}_{0.8}\text{WO}_{3-\delta}$  and  $\text{Na}_{0.8}\text{Nb}_{0.7}\text{W}_{0.3}\text{O}_{3-\delta}$  were essentially indistinguishable, only the V-i polarization curves and impedance spectra for the cells made from  $\text{Na}_{0.8}\text{WO}_{3-\delta}$  are shown in Figure 3.9, for operation at 973 K in humidified  $\text{H}_2$ .



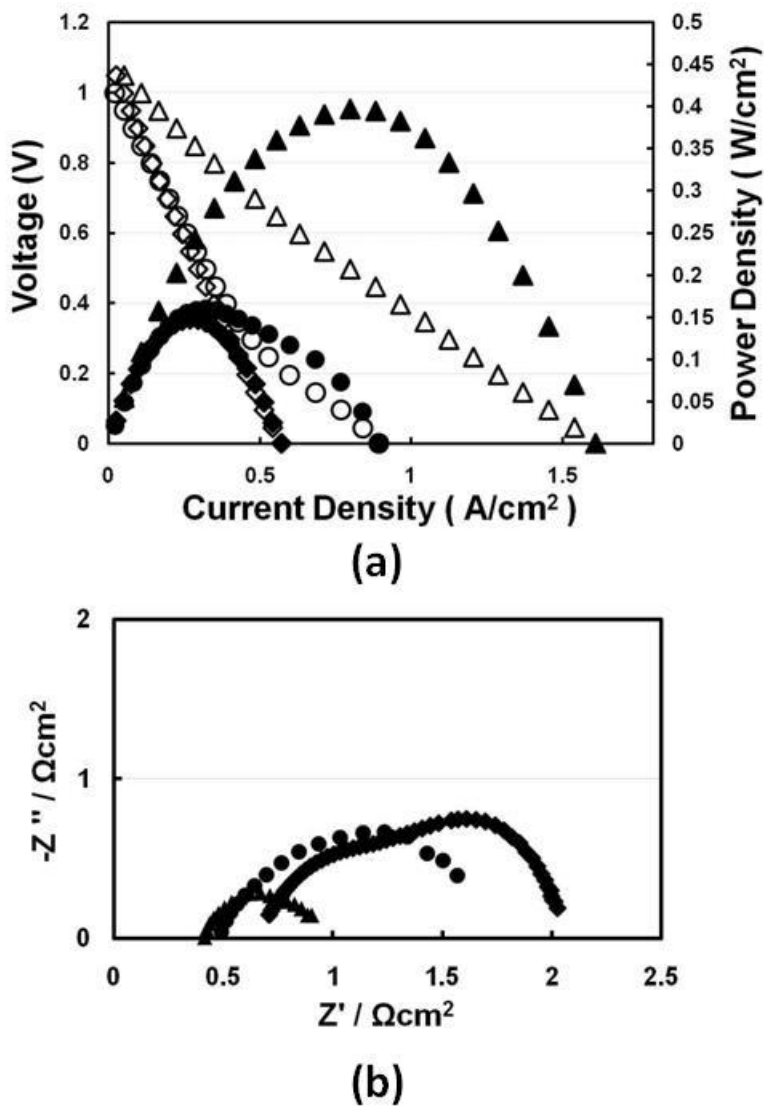


**Figure 3.9:** (a) V-i polarization curves and (b) electrochemical impedance spectra of cells with infiltrated  $\text{Na}_{0.8}\text{WO}_{3-\delta}$  anode ( $\blacktriangle$ ) with and ( $\bullet$ ) without Pd catalyst, and ( $\blacklozenge$ ) with Pd after exposure to humidified  $\text{H}_2$  at 1123 K, operated at 973 K under humidified (3%  $\text{H}_2\text{O}$ )  $\text{H}_2$ .

The V-i polarization curves demonstrate that cells made with or without added Pd have open-circuit potentials near the theoretical Nernst value of 1.1 V. While both cells also exhibited nearly linear V-i relationships, the slope was much lower for the cell with added Pd. As a result, the maximum power density for the cell with Pd was 0.4 W/cm<sup>2</sup>, while the cell without added Pd had a maximum power density of 0.17 W/cm<sup>2</sup>. The

impedance spectra demonstrate that the ohmic losses, calculated from the high-frequency intercept with the real axis in the open-circuit Nyquist plots in Figure 3.9b), were the same for cells with or without Pd,  $0.42 \Omega \text{ cm}^2$ . Since this is exactly the resistance expected for an 80- $\mu\text{m}$  YSZ with a conductivity of  $0.0189 \text{ S/cm}^{39}$ , the electrodes are not contributing to the ohmic losses in these cells. The major change upon the addition of Pd is in the non-ohmic losses, which were roughly  $0.5 \Omega \text{ cm}^2$  for the cell with 1 wt. % Pd and more than  $1.1 \Omega \text{ cm}^2$  for the cell without. Since LSF-YSZ cathodes identical to those used here have previously been shown to exhibit losses between  $0.1$  and  $0.2 \Omega \text{ cm}^2$ <sup>240,41</sup>, the anode losses must be  $0.3$  to  $0.4 \Omega \text{ cm}^2$  for the cell with Pd and  $0.9$  to  $1.1 \Omega \text{ cm}^2$  for the cell without. The addition of 1 wt. % Pd would be expected to affect only the catalyst properties of the anodes; thus, the fact that anode performance improved so dramatically upon the addition of Pd indicates that the tungsten bronzes are not sufficiently catalytic to exhibit outstanding fuel-cell performance at 973 K.

The performance of cells with anodes made from  $\text{Na}_{0.8}\text{WO}_{3.8}$  after exposure to humidified  $\text{H}_2$  at 1123 K was also examined. These cells exhibited a significant loss in performance due to increased ohmic resistances. For example, the ohmic resistance of the cell made with 1 wt. % Pd in Figure 3.9 increased to  $0.71 \Omega \text{ cm}^2$  at 973 K after the anode had been reduced in humidified  $\text{H}_2$  for 30 min at 1123 K. Even though the data in Figure 3.7 would suggest that the tungsten bronzes should remain sufficiently conductive after this pretreatment, there must be a loss of connectivity within the composite that causes the effective resistance of the cell to go up. This is similar to what was observed with infiltrated metallic anodes<sup>42</sup>, where the ohmic losses of the infiltrated electrodes also

increased after sintering, even though conductivity measurements suggested that the composite was still conductive.

### 3.4 Discussion

High electrode conductivities are important for reducing ohmic losses in SOFC. Typical conductivities for Ni ceramic-metallic (cermet) composites range from 100 to 1000 S/cm<sup>43,44</sup>, but few ceramic anode materials can match this. What we have demonstrated in the present study is that it is possible to achieve conductivities approaching that of Ni cermets using electrodes based on tungsten bronzes.

As with all other ceramic anodes that have been tested<sup>13,45,46</sup>, the tungsten bronzes are not sufficiently catalytic to achieve excellent electrode performance by themselves, as demonstrated by the fact that the anode impedances decreased significantly with the addition of catalytic amounts of Pd. This need for an added catalyst is probably true for all ceramic anode materials, due to the fact that no oxide has comparable activity for oxidation reactions to that of group VIII metals like Ni, Pt, or Pd. Although there had been reports that electrodes based on Sr<sub>2</sub>MgMoO<sub>6-δ</sub> have good catalytic properties, a recent report suggests that this was likely due to the use of Pt current collectors<sup>47</sup>. Because the catalytic metals can be added in very small amounts and only need to be present in the functional layer of the electrode, their addition to the electrode need not be prohibitive from a cost perspective, nor should their addition cause a loss in electrode redox stability<sup>48</sup>.

Although electrodes made using tungsten bronzes are capable of exhibiting very high electronic conductivities and good electrode performance at lower temperatures,

they undergo more deep reduction to metallic W at temperatures that are too low for most SOFC applications. Based on the fact that  $\text{Na}_2\text{WO}_4$  was not reduced under the conditions used in the present experiments and the fact that the bronzes with lower cation contents formed using K, Cs, and Rb cations reduced more easily, we suggest that the tungsten requires the presence of adjacent alkali cations to prevent total reduction. We were also not able to stabilize the structure by partial substitution with Nb.

The most important conclusion to be reached from the present study is that fabrication of electrodes by infiltration greatly increases the possible compositions that can be used in SOFC electrodes. It would be very difficult to attach a tungsten-bronze electrode to a YSZ electrolyte by normal fabrication procedures. Co-firing of the bronzes at temperatures required for making a dense electrolyte would likely lead to solid-state reactions. Reduction to form the bronze phase may also result in de-lamination of the electrode from the electrolyte. However, the infiltrated electrodes in the present study were capable of reasonably good performance 973 K. This is almost certainly due to the fact that high-temperature firing of the YSZ scaffold, prior to the addition of the tungsten bronzes and the catalyst, forms a well-connected, ion-conducting network within the electrode, so that there is a long three-phase boundary.

Because the requirements for the electronically conductive part of the anode are much less restrictive in composites formed by infiltration, many materials can play the role of the conductor. The search for the best ceramics for anode applications is still ongoing but infiltration procedures greatly simplify the search.

### **3.5 Conclusion**

Highly conductive, tungsten-bronze, SOFC anodes can be prepared by infiltration into a porous YSZ scaffold. These could find application at temperatures below 1073 K but tend to be reduced to metallic tungsten under reducing conditions at higher temperatures. Because the tungsten bronzes have only modest catalytic activity, good anode performance requires the addition of a catalytic component.

### 3.6 References

- 1 Huang, Y. H., Dass, R. I., Denyszyn, J. C. & Goodenough, J. B. Synthesis and characterization of  $\text{Sr}_2\text{MgMoO}_{6-\delta}$  - An anode material for the solid oxide fuel cell. *J Electrochem Soc* **153**, A1266-A1272, doi:10.1149/1.2195882 (2006).
- 2 Sfeir, J., van Herle, J. & McEvoy, A. J. Stability of calcium substituted lanthanum chromites used as SOFC anodes for methane oxidation. *J Eur Ceram Soc* **19**, 897-902 (1999).
- 3 Kim, H., Lu, C., Worrell, W. L., Vohs, J. M. & Gorte, R. J. Cu-Ni cermet anodes for direct oxidation of methane in solid-oxide fuel cells. *J Electrochem Soc* **149**, A247-A250, doi:10.1149/1.1445170 (2002).
- 4 Matsuzaki, Y. & Yasuda, I. The poisoning effect of sulfur-containing impurity gas on a SOFC anode: Part I. Dependence on temperature, time, and impurity concentration. *Solid State Ionics* **132**, 261-269 (2000).
- 5 Toebes, M. L., Bitter, J. H., van Dillen, A. J. & de Jong, K. P. Impact of the structure and reactivity of nickel particles on the catalytic growth of carbon nanofibers. *Catal Today* **76**, 33-42 (2002).
- 6 Toh, C. H., Munroe, P. R., Young, D. J. & Foger, K. High temperature carbon corrosion in solid oxide fuel cells. *Mater High Temp* **20**, 129-136 (2003).
- 7 Sarantaridis, D. & Atkinson, A. Redox cycling of Ni-based solid oxide fuel cell anodes: A review. *Fuel Cells* **7**, 246-258, doi:DOI 10.1002/fuce.200600028 (2007).

- 8 Lee, S., Kim, G., Vohs, J. M. & Gorte, R. J. SOFC anodes based on infiltration of  $\text{La}_{(0.3)}\text{Sr}_{(0.7)}\text{TiO}_{(3)}$ . *J Electrochem Soc* **155**, B1179-B1183, doi:Doi 10.1149/1.2976775 (2008).
- 9 Gross, M. D. *et al.* Redox Stability of  $\text{SrNb}_{(x)}\text{Ti}_{(1-x)}\text{O}_{(3)}$ -YSZ for Use in SOFC Anodes. *J Electrochem Soc* **156**, B540-B545, doi:10.1149/1.3078406 (2009).
- 10 Neagu, D. & Irvine, J. T. S. Structure and Properties of  $\text{La}_{(0.4)}\text{Sr}_{(0.4)}\text{TiO}_{(3)}$  Ceramics for Use as Anode Materials in Solid Oxide Fuel Cells. *Chem Mater* **22**, 5042-5053, doi:Doi 10.1021/Cm101508w (2010).
- 11 Vincent, A., Luo, J. L., Chuang, K. T. & Sanger, A. R. Effect of Ba doping on performance of LST as anode in solid oxide fuel cells. *J Power Sources* **195**, 769-774, doi:DOI 10.1016/j.jpowsour.2009.08.018 (2010).
- 12 Kim, G., Corre, G., Irvine, J. T. S., Vohs, J. M. & Gorte, R. J. Engineering composite oxide SOFC anodes for efficient oxidation of methane. *Electrochem Solid St* **11**, B16-B19, doi:10.1149/1.2817809 (2008).
- 13 Kim, G. *et al.* Investigation of the Structural and Catalytic Requirements for High-Performance SOFC Anodes Formed by Infiltration of LSCM. *Electrochem Solid St* **12**, B48-B52, doi:10.1149/1.3065971 (2009).
- 14 Tao, S. W. & Irvine, J. T. S. A redox-stable efficient anode for solid-oxide fuel cells. *Nat Mater* **2**, 320-323, doi:Doi 10.1038/Nmat871 (2003).
- 15 van den Bossche, M., Matthews, R., Lichtenberger, A. & McIntosh, S. Insights Into the Fuel Oxidation Mechanism of  $\text{La}_{(0.75)}\text{Sr}_{(0.25)}\text{Cr}_{(0.5)}\text{Mn}_{(0.5)}\text{O}_{(3-\delta)}$  SOFC Anodes. *J Electrochem Soc* **157**, B392-B399, doi:Doi 10.1149/1.3288374 (2010).

- 16 Babaei, A., Zhang, L., Tan, S. L. & Jiang, S. P. Pd-promoted (La,Ca)(Cr,Mn)O<sub>3</sub>/GDC anode for hydrogen and methane oxidation reactions of solid oxide fuel cells. *Solid State Ionics* **181**, 1221-1228, doi:DOI 10.1016/j.ssi.2010.06.042 (2010).
- 17 Zhu, X. B. *et al.* A comparison of La<sub>(0.75)</sub>Sr<sub>(0.25)</sub>Cr<sub>(0.5)</sub>Mn<sub>(0.5)</sub>O<sub>(3-delta)</sub> and Ni impregnated porous YSZ anodes fabricated in two different ways for SOFCs. *Electrochim Acta* **55**, 3932-3938, doi:DOI 10.1016/j.electacta.2010.02.028 (2010).
- 18 Kobsiriphat, W., Madsen, B. D., Wang, Y., Marks, L. D. & Barnett, S. A. La<sub>(0.8)</sub>Sr<sub>(0.2)</sub>Cr<sub>(1-x)</sub>Ru<sub>(x)</sub>O<sub>(3-delta)</sub>-Gd<sub>(0.1)</sub>Ce<sub>(0.9)</sub>O<sub>(1.95)</sub> solid oxide fuel cell anodes: Ru precipitation and electrochemical performance. *Solid State Ionics* **180**, 257-264, doi:DOI 10.1016/j.ssi.2008.12.022 (2009).
- 19 Conroy, L. E. Preparation and Characterization of a Sodium Tungsten Bronze - Inorganic Experiment. *J Chem Educ* **54**, 45-49 (1977).
- 20 Lekshmi, I. C., Gayen, A., Prasad, V., Subramanyam, S. V. & Hegde, M. S. Structure and electrical properties of sodium tungsten bronzes thin films. *Mater Res Bull* **37**, 1815-1823 (2002).
- 21 Leonova, L. S. *et al.* Electrochemical properties of systems with rubidium-tungsten-oxide bronze. *Russ J Electrochem+* **43**, 462-469, doi:10.1134/S1023193507040143 (2007).
- 22 Raub, C. J., Broadsto.S, Matthias, B. T., Jensen, M. A. & Sweedler, A. R. Superconductivity of Sodium Tungsten Bronzes. *Phys Rev Lett* **13**, 746-& (1964).
- 23 Ellerbeck, L., Danielson, G. C., Sidles, P. H. & Shanks, H. R. Electrical Resistivity of Cubic Sodium Tungsten Bronze. *J Chem Phys* **35**, 298-& (1961).



- 24 El-Sayed, A. M. & Mousa, S. M. A. Some properties of sodium tungsten bronzes as a function of sodium concentration. *Indian J Chem Techn* **12**, 304-308 (2005).
- 25 McNeill, W. & Conroy, L. E. Electrical Properties of Some Dilute Cubic Sodium Tungsten Bronzes. *J Chem Phys* **36**, 87-&, doi:Doi 10.1063/1.1732323 (1962).
- 26 Dickens, P. G., Jewess, M., Neild, D. J. & Rose, J. C. W. Thermochemistry of Oxide Bronzes .1. Sodium Vanadium Bronzes  $\text{Na}_x\text{V}_2\text{O}_5$  with X between 0.2 and 0.33. *J Chem Soc Dalton*, 30-33 (1973).
- 27 Weller, P. F., Taylor, B. E. & Mohler, R. L. Crystal Preparation of Doped Sodium Tungsten Bronze. *Mater Res Bull* **5**, 465-&, doi:Doi 10.1016/0025-5408(70)90086-3 (1970).
- 28 Lynch, D. W., Rosei, R., Weaver, J. H. & Olson, C. G. Optical Properties of Some Alkali-Metal Tungsten Bronzes from 0.1 to 38 Ev. *J Solid State Chem* **8**, 242-252, doi:Doi 10.1016/0022-4596(73)90092-3 (1973).
- 29 Dautremontsmith, W. C., Green, M. & Kang, K. S. Optical and Electrical-Properties of Thin-Films of  $\text{WO}_3$  Electrochemically Colored. *Electrochim Acta* **22**, 751-759, doi:Doi 10.1016/0013-4686(77)80031-5 (1977).
- 30 Kaiser, A., Bradley, J. L., Slater, P. R. & Irvine, J. T. S. Tetragonal tungsten bronze type phases  $(\text{Sr}_{1-x}\text{Ba}_x)_{(0.6)}\text{Ti}_{0.2}\text{Nb}_{0.8}\text{O}_{3-\text{delta}}$ : Material characterisation and performance as SOFC anodes. *Solid State Ionics* **135**, 519-524, doi:Doi 10.1016/S0167-2738(00)00432-X (2000).
- 31 Zivkovic, O., Yan, C. & Wagner, M. J. Tetragonal alkali metal tungsten bronze and hexagonal tungstate nanorods synthesized by alkalide reduction. *J Mater Chem* **19**, 6029-6033, doi:Doi 10.1039/B906888k (2009).

- 32 Brusetti, R., Haen, P. & Marcus, J. Concentration dependence of superconductivity and the order-disorder transition in the hexagonal rubidium tungsten bronze  $\text{Rb}_x\text{WO}_3$ : Interfacial and bulk properties. *Phys Rev B* **65**, doi:10.1103/PhysRevB.65.144528 (2002).
- 33 Park, S., Gorte, R. J. & Vohs, J. M. Tape cast solid oxide fuel cells for the direct oxidation of hydrocarbons. *J Electrochem Soc* **148**, A443-A447 (2001).
- 34 Kondo, W., Manabe, T., Kumagai, T. & Mizuta, S. Preparation of Sodium Tungsten Bronze (Cubic) by the Reduction of Tungstates with Hydrogen. *Nippon Kagaku Kaishi*, 1034-1040 (1993).
- 35 Xue, Y., Zhang, Y. & Zhang, P. H. Theory of the color change of  $\text{Na}_x\text{WO}_3$  as a function of Na-charge doping. *Phys Rev B* **79**, doi:Artn 205113, Doi 10.1103/Physrevb.79.205113 (2009).
- 36 He, H. P. *et al.* Low-temperature fabrication of oxide composites for solid-oxide fuel cells. *J Am Ceram Soc* **87**, 331-336 (2004).
- 37 Atkinson, A. *et al.* Advanced anodes for high-temperature fuel cells. *Nat Mater* **3**, 17-27, doi:10.1038/nmat1040 (2004).
- 38 Cowin, P. I., Petit, C. T. G., Lan, R., Irvine, J. T. S. & Tao, S. W. Recent Progress in the Development of Anode Materials for Solid Oxide Fuel Cells. *Adv Energy Mater* **1**, 314-332, doi:DOI 10.1002/aenm.201100108 (2011).
- 39 Sasaki, K. & Maier, J. Re-analysis of defect equilibria and transport parameters in  $\text{Y}_2\text{O}_3$ -stabilized  $\text{ZrO}_2$  using EPR and optical relaxation. *Solid State Ionics* **134**, 303-321 (2000).

- 40 Adjianto, L., Kungas, R., Bidrawn, F., Gorte, R. J. & Vohs, J. M. Stability and performance of infiltrated  $\text{La}_{0.8}\text{Sr}_{0.2}\text{Co}_x\text{Fe}_{1-x}\text{O}_3$  electrodes with and without  $\text{Sm}_{0.2}\text{Ce}_{0.8}\text{O}_{1.9}$  interlayers. *J Power Sources* **196**, 5797-5802, doi:DOI 10.1016/j.jpowsour.2011.03.022 (2011).
- 41 Wang, W. S., Gross, M. D., Vohs, J. M. & Gorte, R. J. The stability of LSF-YSZ electrodes prepared by infiltration. *J Electrochem Soc* **154**, B439-B445, doi:Doi 10.1149/1.2709510 (2007).
- 42 Jung, S. W. *et al.* Influence of composition and Cu impregnation method on the performance of Cu/CeO<sub>2</sub>/YSZ SOFC anodes. *J Power Sources* **154**, 42-50, doi:10.1016/j.jpowsour.2005.04.018 (2006).
- 43 Fang, X. H., Zhu, G. Y., Xia, C. R., Liu, X. Q. & Meng, G. Y. Synthesis and properties of Ni-SDC cermets for IT-SOFC anode by co-precipitation. *Solid State Ionics* **168**, 31-36 (2004).
- 44 Zhu, W. Z. & Deevi, S. C. A review on the status of anode materials for solid oxide fuel cells. *Mat Sci Eng a-Struct* **362**, 228-239, doi:10.1016/S0921-5093(03)00620-8 (2003).
- 45 Gross, M. D., Vohs, J. M. & Gorte, R. J. An examination of SOFC anode functional layers based on ceria in YSZ. *J Electrochem Soc* **154**, B694-B699, doi:10.1149/1.2736647 (2007).
- 46 Kim, J. S., Nair, V. V., Vohs, J. M. & Gorte, R. J. A study of the methane tolerance of LSCM-YSZ composite anodes with Pt, Ni, Pd and ceria catalysts. *Scripta Mater* **65**, 90-95, doi:DOI 10.1016/j.scriptamat.2010.06.016 (2011).

- 47 Bi, Z. H. & Zhu, J. H. Effect of Current Collecting Materials on the Performance of the Double-Perovskite  $\text{Sr}_{(2)}\text{MgMoO}_{(6-\delta)}$  Anode. *J Electrochem Soc* **158**, B605-B613, doi:10.1149/1.3569754 (2011).
- 48 Busawon, A. N., Sarantaridis, D. & Atkinson, A. Ni infiltration as a possible solution to the redox problem of SOFC anodes. *Electrochem Solid St* **11**, B186-B189, doi:10.1149/1.2959078 (2008).

## Chapter 4. Physical and Electrochemical Properties of Alkaline Earth Doped, Rare Earth Vanadates\*

### Summary

The effect of partial substitution of alkaline earth (AE) ions,  $\text{Sr}^{2+}$  and  $\text{Ca}^{2+}$ , for the rare earth (RE) ions,  $\text{La}^{3+}$ ,  $\text{Ce}^{3+}$ ,  $\text{Pr}^{3+}$ , and  $\text{Sm}^{3+}$ , on the physical properties of  $\text{REVO}_4$  compounds were investigated. The use of the Pechini method to synthesize the vanadates allowed for high levels of AE substitution to be obtained. Coulometric titration was used to measure redox isotherms for these materials and showed that the addition of the AE ions increased both reducibility and electronic conductivity under typical solid oxide fuel cell (SOFC) anode conditions, through the formation of compounds with mixed vanadium valence. In spite of their high electronic conductivity,  $\text{REVO}_4$ /yttria-stabilized zirconia (YSZ) composite anodes exhibited only modest performance when used in SOFCs operating with  $\text{H}_2$  fuel at 973 K due to their low catalytic activity. High performance was obtained, however, after the addition of a small amount of catalytically active Pd to the anode.

---

\* This chapter was published as a research paper in the Journal of Solid State Chemistry, 190 (2012) 12. Copyright: 2012, Elsevier.

## 4.1 Introduction

The standard anode in a SOFC is composed of a composite of Ni and the O<sup>2-</sup> anion conducting yttria-stabilized zirconia (YSZ) electrolyte. These Ni/YSZ cermet electrodes can be very efficient, but have low fuel flexibility and are restricted to use with H<sub>2</sub> or syngas fuels. The desire for anodes with increased fuel flexibility that will not deactivate via coke formation when exposed to hydrocarbons has motivated research into using conductive ceramics to replace the Ni components in SOFC anodes<sup>1-7</sup>. In the previous chapter (Chapter 3), more highly conductive oxide, Na<sub>x</sub>WO<sub>3-δ</sub> bronzes<sup>8</sup>, which have bulk conductivities approaching 1,000 S/cm, have been investigated for use in SOFC anodes; however, they appear to be chemically unstable under typical SOFC anode operating conditions.

Rare earth (RE) vanadates (REVO<sub>4</sub>), such as CeVO<sub>4</sub>, are another class of oxides that can have high electronic conductivities under some conditions and are chemically stable in a variety of fuels including H<sub>2</sub>, H<sub>2</sub>S, and CH<sub>4</sub><sup>9-11</sup>, and, therefore, show some promise for use in SOFC anodes. Cerium (III) orthovanadate, CeVO<sub>4</sub> has a zircon-type structure which consists of VO<sub>4</sub> tetrahedra sharing corners and edges with CeO<sub>8</sub> dodecahedra<sup>12</sup>. The tetragonal zircon structure stabilizes the Ce<sup>3+</sup> ion under oxidizing conditions<sup>13</sup>. Upon exposure to reducing environment, a zircon-to-perovskite phase transition occurs, forming CeVO<sub>3</sub><sup>9,14</sup>. Recently, Petit, et al. studied the redox and electrical properties of CeVO<sub>4</sub> under reducing conditions<sup>10,11,15,16</sup> and found that the substitution of a portion of the trivalent Ce ions with divalent alkaline earth (AE) ions significantly enhanced electronic conductivity, with a bulk conductivity as high as 12 S cm<sup>-1</sup> at 973 K being reported for Ce<sub>0.6</sub>Ca<sub>0.4</sub>VO<sub>3</sub><sup>10,16</sup>. The conductivity of the RE<sub>x</sub>AE<sub>1-x</sub>

$x\text{VO}_3$  ( $\text{REAEVO}_3$ ) compounds increases with increasing AE substitution up to the solubility limit. Petit, et al. and Watanabe, et al. reported the solubility limit of Ca and Sr in the parent  $\text{CeVO}_4$  corresponds to  $x$  values of 0.41 and 0.21, respectively, for materials synthesized by sintering the constituent binary oxides at 1273 K<sup>11,13,15</sup>. Secondary  $\text{Sr}_2\text{V}_2\text{O}_7$  and  $\text{Ca}_2\text{V}_2\text{O}_7$  phases are observed at higher AE concentrations<sup>11,15</sup>.

In this chapter, we have investigated the physical and electrochemical properties of a range of  $\text{RE}_x\text{AE}_{1-x}\text{VO}_{4-0.5x}$  ( $\text{REAEVO}_4$ ) where RE = La, Ce, Pr, and Sm, that have potential for use in SOFC anodes. In contrast to previous studies, a solution based Pechini method was used to synthesize the vanadates thereby allowing them to be produced at lower temperatures and with higher concentrations of AE (Ca, Sr) ions. The conductivity and the electrochemical performance of  $\text{REAEVO}_3$ -YSZ composites that were produced using wet infiltration of the vanadates into a pre-sintered porous YSZ electrode scaffold are also reported.

## 4.2 Experimental

The  $\text{REVO}_4$  materials were prepared using an aqueous precursor solution containing the appropriate amounts of  $\text{NH}_4\text{VO}_3$  (Aldrich, 99+ %) with either  $\text{La}(\text{NO}_3)_3 \cdot 6\text{H}_2\text{O}$  (Alfa Aesar, 99.9%),  $\text{Ce}(\text{NO}_3)_3 \cdot 6\text{H}_2\text{O}$  (Alfa Aesar, 99.5%),  $\text{Pr}(\text{NO}_3)_3 \cdot x\text{H}_2\text{O}$  (Alfa Aesar, 99.9%), or  $\text{Sm}(\text{NO}_3)_3 \cdot 6\text{H}_2\text{O}$  (Alfa Aesar, 99.9%). Citric acid (Fisher Scientific) was also added as a complexing agent to aid in the formation of a single phase at a lower temperature. The precursor solution was then dried and the resulting powder was calcined at 973 K in air to form the  $\text{REVO}_4$ . Perovskite  $\text{REVO}_3$  materials were produced by reducing the  $\text{REVO}_4$  in humidified  $\text{H}_2$  (3%  $\text{H}_2\text{O}$ ) at 973 K.

REAEVO<sub>4</sub> oxides were synthesized in the same way as the REVO<sub>4</sub>, with addition of Sr(NO<sub>3</sub>)<sub>2</sub> (Alfa Aesar, 99%), or Ca(NO<sub>3</sub>)<sub>2</sub>·4H<sub>2</sub>O (Alfa Aesar, 99%) to the precursor solution.

Porous YSZ slabs into which 30 wt. % of the REVO<sub>4</sub> had been infiltrated were used for conductivity measurements. The porous, 4 mm x 4 mm x 15 mm YSZ slabs were prepared using methods that have been described in detail previously<sup>17,18</sup>. The REVO<sub>4</sub> was added to the porous YSZ slabs by infiltrating the aqueous precursor solution followed by drying and annealing in air at 973 K. Multiple infiltration/annealing cycles were used to obtain the desired 30 wt. % loading. For conductivity measurements, the REVO<sub>4</sub>/YSZ composites were first pre-reduced at 973 K in humidified H<sub>2</sub> (3% H<sub>2</sub>O) for 2 h. The conductivity was measured using the 4-probe, DC method with the sample in humidified H<sub>2</sub> (3% H<sub>2</sub>O). Physical characterization of the anode composites were carried out using scanning electron microscopy (SEM) (FEI Quanta 600 ESEM) and X-ray diffraction (XRD) using Cu K<sub>α</sub> radiation. BET isotherms were measured using Kr adsorption at 78 K and were used to determine surface areas.

Redox isotherms (i.e. sample composition as a function of pO<sub>2</sub> for the REVO<sub>4</sub>/YSZ and REAEVO<sub>4</sub>/YSZ composites were measured using a coulometric-titration cell that has been previously described in detail<sup>19</sup>. The cell consisted of a YSZ tube with Ag electrodes painted onto the inner and outer surfaces. Approximately 0.1 g of sample was placed in the cell and then pre-reduced in flowing 10% H<sub>2</sub>:90% N<sub>2</sub> at 973 K for 4 h. The cell was then purged with CO and sealed. The H<sub>2</sub> treatment insured that the measurements were started from the reduced state of the sample. Precise amounts of oxygen were added to the cell in a stepwise fashion by pumping oxygen through the YSZ



electrolyte by applying a voltage across the two electrodes using a Gamry Instruments potentiostat. After each O<sub>2</sub> addition the sample was allowed to equilibrate (which could take up to two days) and then the pO<sub>2</sub> in the cell was determined from the voltage across the two electrodes via the Nernst equation. The oxygen stoichiometry of the sample was determined from the known starting stoichiometry and the amount of O<sub>2</sub> pumped into the cell. All coulometric titration experiments were performed with the sample at 973 K.

Button-sized cells were used in all fuel cell measurements. These cells were fabricated using porous-dense-porous tri-layer YSZ wafers that were produced using tape casting methods that have been described in detail previously<sup>17</sup>. For each cell, the dense electrolyte layer was 80 μm thick and 1 cm in diameter. The 60% porous YSZ layers on each side of the dense electrolyte layer were 50 μm thick with a BET surface area 0.3 m<sup>2</sup>g<sup>-1</sup>. Sr-doped lanthanum ferrite (La<sub>0.8</sub>Sr<sub>0.2</sub>FeO<sub>3</sub>, LSF) was added to one porous layer to form a cathode using multiple cycles of infiltration of an aqueous solution containing dissolved La(NO<sub>3</sub>)<sub>3</sub>·6H<sub>2</sub>O (Alfa Aesar, 99.9%), Sr(NO<sub>3</sub>)<sub>2</sub> (Alfa Aesar, 99%) and Fe(NO<sub>3</sub>)<sub>3</sub>·9H<sub>2</sub>O (Fisher Scientific) in the appropriate molar ratios, followed by calcination in air at 723 K<sup>20-22</sup>. These cycles were repeated until a 40% weight loading of LSF was obtained. After the infiltration steps the composite cathode was calcined to 1123 K for 4 h to form the perovskite structure. The Ce<sub>0.7</sub>Sr<sub>0.3</sub>VO<sub>3.85</sub> anode was synthesized in a similar manner except that a 30 wt. % loading was used and it was calcined to only 973 K. After forming the Ce<sub>0.7</sub>Sr<sub>0.3</sub>VO<sub>3.85</sub>-YSZ composite anode, it was reduced in humidified H<sub>2</sub> (3% H<sub>2</sub>O) at 973 K prior to cell testing. For one cell, 1 wt. % Pd was added to the anode side by infiltration with an aqueous solution of (NH<sub>3</sub>)<sub>4</sub>Pd(NO<sub>3</sub>)<sub>2</sub>.

For fuel cell testing, silver paste was applied to both electrodes and used as the current collector and the cells were mounted onto an alumina tube with a ceramic adhesive (Aremco, Ceramabond 552). All the cell tests were performed with the anode exposed to humidified H<sub>2</sub> (3% H<sub>2</sub>O) and the cathode to ambient air. Electrochemical impedance spectra were measured between 0.1 Hz and 300 kHz with a 1 mA AC perturbation, and V-i polarization curves were measured using a Gamry Instruments potentiostat.

### 4.3 Results and Discussion

The solubility limits of the alkaline earth dopants in the REVO<sub>4</sub> structure were determined by both the appearance of secondary phases as determined by XRD and the concentration at which a discontinuity was observed in plot of the REVO<sub>4</sub> lattice parameter versus alkaline earth concentration. For the sake of example, Sr- and Ca-doped CeVO<sub>4</sub> will be used to illustrate these methods. The Ce<sub>1-x</sub>Sr<sub>x</sub>VO<sub>4-0.5x</sub> zircon structure was confirmed by the presence of the expected diffraction peaks near 24.0, 32.4, 34.1, 36.4, 38.9, 43.2, 46.1, and 48.0 degrees 2θ<sup>13,15</sup>. Figure 4.1 shows the 21 to 31 degrees 2θ region of the powder XRD pattern for this material for several x values. This region of the spectrum contains the intense (200) peak of the zircon lattice of the vanadate and the 30.1 degrees 2θ peak of cubic YSZ which was added as a standard. The region between these two peaks is also where diffraction lines are expected for any secondary strontium vanadate phases that may form.

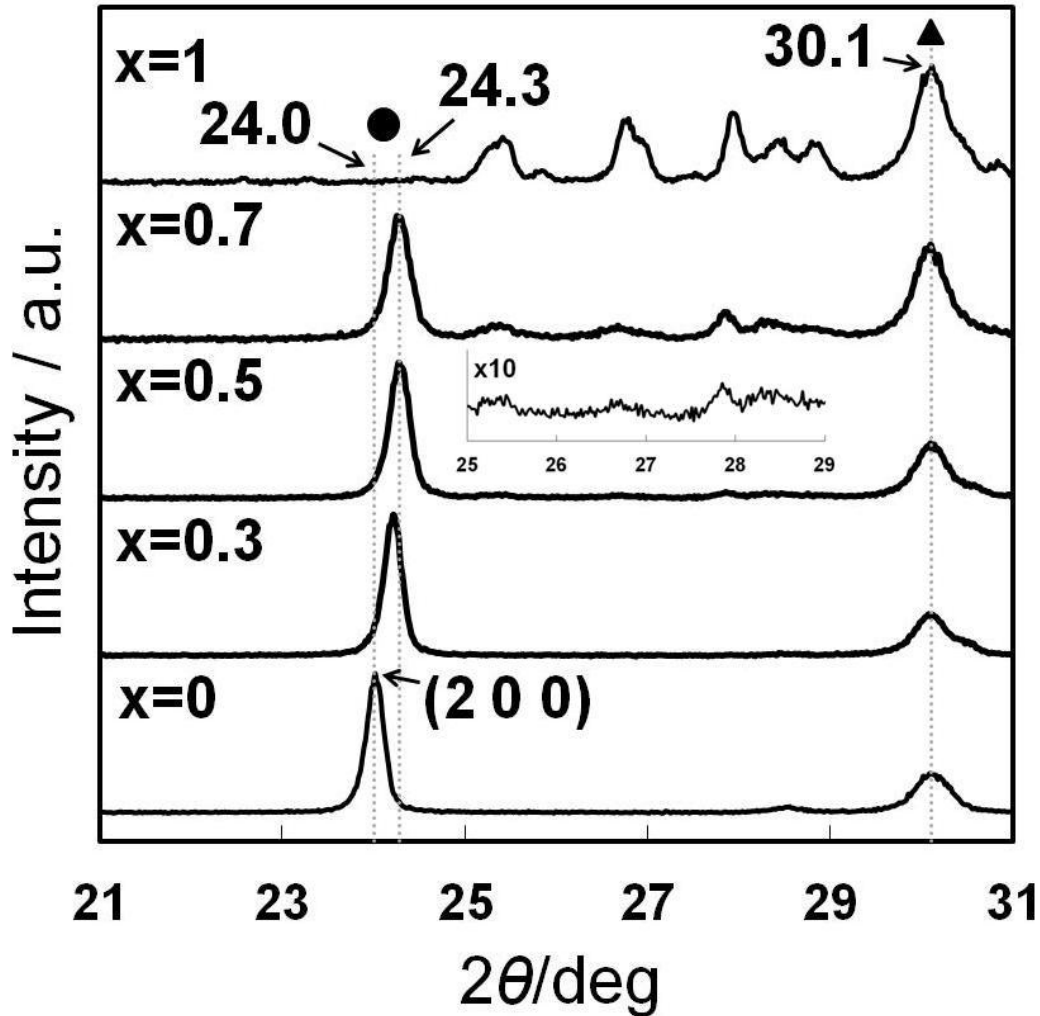


**Figure 4.1:** XRD patterns of  $\text{Ce}_{1-x}\text{Sr}_x\text{VO}_{4-0.5x}$ -YSZ composites with different Ce:Sr ratios ( $x=0, 0.3, 0.5, 0.7, 1$ ) that were calcined in air at 973 K. The peaks labeled ● and ▲ correspond to  $\text{Ce}_{1-x}\text{Sr}_x\text{VO}_{4-0.5x}$  and ▲, respectively.

The bottom spectrum in the figure corresponds to  $\text{CeVO}_4$  in which the (200) peak appears at 24.0 degrees  $2\theta$ . Note that this spectrum contains an additional small peak at 28.5 degrees  $2\theta$  which can be assigned to a small amount of  $\text{CeO}_2$  impurity. The spectrum for  $\text{Ce}_{0.7}\text{Sr}_{0.3}\text{VO}_{3.85}$  shows a single phase material with the (200) peak shifted to 24.2 degrees  $2\theta$  due to a decrease in the lattice parameter resulting from the substitution of the  $\text{Sr}^{+2}$  ion into the lattice. An additional shift to 24.3 degrees  $2\theta$  was observed for the

(200) peak for  $\text{Ce}_{0.5}\text{Sr}_{0.5}\text{VO}_{3.75}$ . Note that for this composition several additional peaks are also evident between 25 and 29 degrees  $2\theta$  which can be assigned to  $\text{Sr}_2\text{V}_2\text{O}_7$  (for comparison purposes the XRD pattern of  $\text{Sr}_2\text{V}_2\text{O}_7$  is also included in the figure); thus, the solubility limit for Sr in  $\text{Ce}_{1-x}\text{Sr}_x\text{VO}_{4-0.5x}$  occurs for an  $x$  value between 0.3 and 0.5. As shown by the spectrum of the sample with a nominal composition of  $\text{Ce}_{0.3}\text{Sr}_{0.7}\text{VO}_{3.65}$ , for  $x > 0.5$ , the  $\text{Sr}_2\text{V}_2\text{O}_7$  phase becomes more prominent and no additional shifts in the position of the (200) zircon peak are observed.

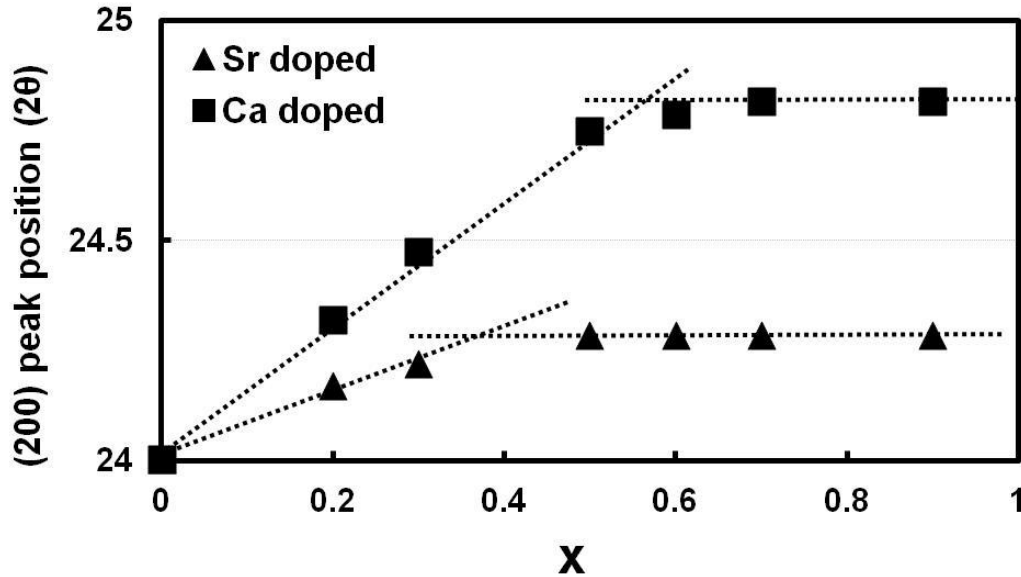


**Figure 4.2:** Plots of the position of the (200) diffraction peak as a function of  $x$  for both  $\text{Ce}_{1-x}\text{Sr}_x\text{VO}_{4-0.5x}$  and  $\text{Ce}_{1-x}\text{Ca}_x\text{VO}_{4-0.5x}$ .

A more accurate estimate of the solubility of Sr in  $\text{CeVO}_4$  can be obtained by applying Vegard's law<sup>13</sup> which predicts that the lattice constant for  $\text{Ce}_{1-x}\text{AE}_x\text{VO}_{4-0.5x}$  should be a linear function of  $x$ . Thus, a plot of the lattice constant (or the position of a characteristic diffraction peak) for  $\text{Ce}_{1-x}\text{AE}_x\text{VO}_{4-0.5x}$  should be linear up to the solubility limit of the alkaline earth ion. At higher nominal concentrations of the alkaline earth, the

lattice constant would remain fixed at the value for the saturated composition and secondary phases would be formed. Plots of the position of the (200) diffraction peak as a function of x for both  $Ce_{1-x}Sr_xVO_{4-0.5x}$  and  $Ce_{1-x}Ca_xVO_{4-0.5x}$  are shown in Figure 4.2. Note that the plots for both materials have the expected shape and are linear up to a critical x value at which point no additional shift in peak position is observed. Based on this data, the solubility limit for Sr and Ca in  $Ce_{1-x}AE_xVO_{4-0.5x}$  corresponds to x values of 0.37 and 0.57, respectively.

**Table 4.1:** AE solubility limit in various REAEVO<sub>4</sub> materials.

| <b>AE Solid Solubility Limit</b> |             |             |             |             |
|----------------------------------|-------------|-------------|-------------|-------------|
| <b>Dopants/RE</b>                | <b>La</b>   | <b>Ce</b>   | <b>Pr</b>   | <b>Sm</b>   |
| <b>Sr</b>                        | <b>0.30</b> | <b>0.37</b> | <b>0.28</b> | <b>0.00</b> |
| <b>Ca</b>                        | <b>0.30</b> | <b>0.57</b> | <b>0.35</b> | <b>0.00</b> |

The same methods were used to determine the solid solubility limits for Sr and Ca in the La, Pr, and Sm vanadates with the resulting values reported in Table 4.1. (Note that LaVO<sub>4</sub> has a monazite-like, monoclinic structure which is similar to the zircon structure<sup>23,24</sup>). For the vanadates that were studied, the highest solubility of the alkaline earth dopant was obtained for CeVO<sub>4</sub>, and the lowest for SmVO<sub>4</sub> in which it was not possible to substitute the alkaline earths for Sm. The higher solubility observed for Ca compared to Sr in CeVO<sub>4</sub> and PrVO<sub>4</sub> is likely due to the fact that the Ca<sup>2+</sup> ionic radius (1.12 Å) is closer to that for Ce<sup>+3</sup> (1.14 Å) and Pr<sup>+3</sup> (1.13 Å) than Sr<sup>2+</sup> (1.26 Å)<sup>13,25</sup>.

Cerium vanadate is the most well investigated of the rare earth vanadates<sup>9-11,13-16,26</sup>, and in previous studies of the solubility limits of alkaline earth ions in this material, values somewhat less than those obtained here have been reported. For example based on

XRD data, Petit, et al. found that the x values at the solubility limits for Sr<sup>15</sup> and Ca<sup>11</sup> in Ce<sub>1-x</sub>AE<sub>x</sub>VO<sub>4-0.5x</sub> were 0.175 and 0.413, respectively, for samples that were synthesized via annealing mixtures of the constituent oxides in air at 1273 K. For samples produced using the same technique but annealed at 1123 K, Watanabe<sup>13</sup> found that the Sr and Ca solubility limits corresponded to x values of 0.21 and 0.41, respectively. The higher values of 0.4 and 0.6 obtained in the present study are likely due to the use of the Pechini synthesis method for which annealing in air at only 973 K was required to produce the zircon (or monazite) phase; thus, a lower temperature region of the phase diagram is being explored in the present study compared to the earlier work. Together these studies suggest that the solubility of the alkaline earth ions in the REVO<sub>4</sub> materials may decrease with temperature. Since it is expected that the electronic conductivity will increase with the concentration of the alkaline earth dopant, the lower temperature synthesis route may have advantages when using these materials in electrode applications, such as anodes or cathodes in SOFC.

Next, the redox properties and conductivity of REVO<sub>4</sub> with the levels of alkaline earth substitution in the present work will be presented. Since high electronic conductivity in these materials is typically only obtained upon partial reduction<sup>10,16</sup>, it is useful to determine at what pO<sub>2</sub> reduction takes place and what are the resulting phases. We have used coulometric titration along with XRD to explore these properties.

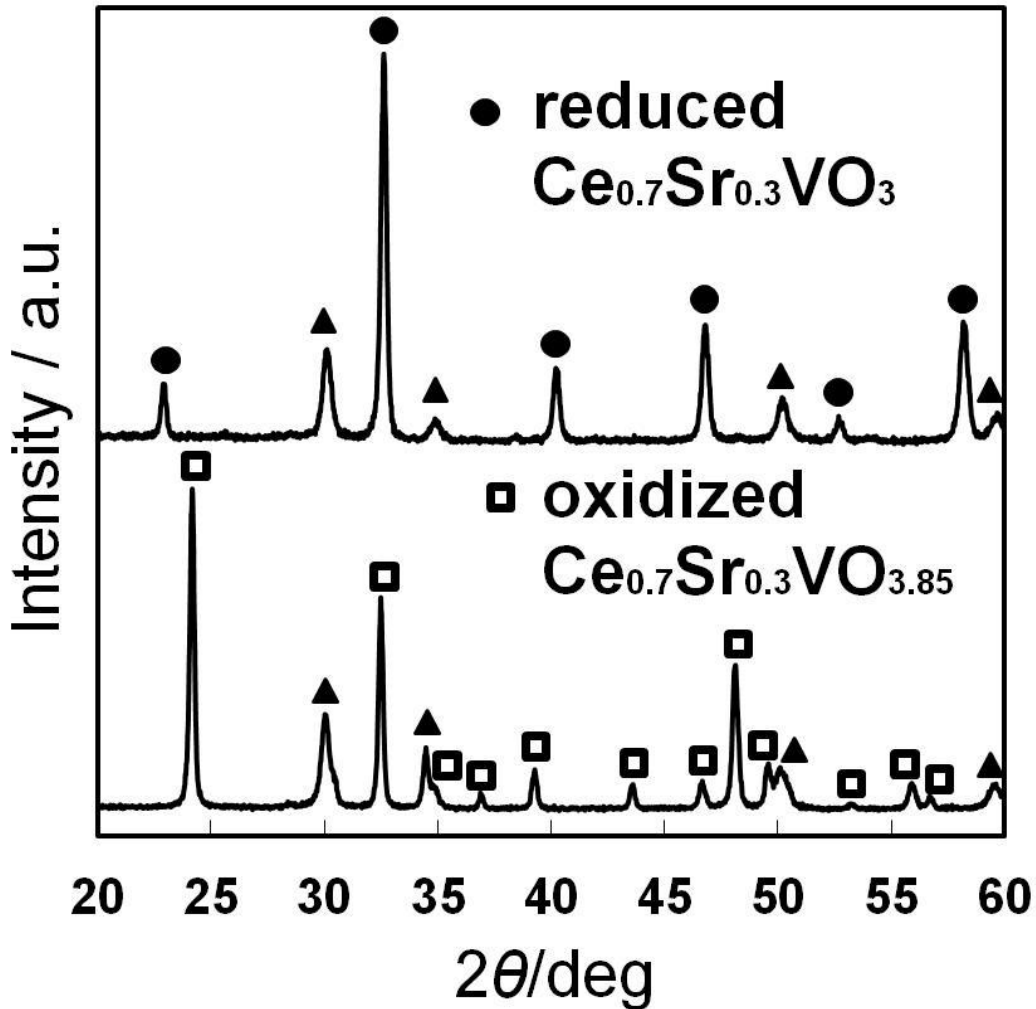


**Figure 4.3:** XRD patterns of oxidized and reduced cerium-strontium vanadate: The peaks are labeled as follows: (□) zircon  $\text{Ce}_{0.7}\text{Sr}_{0.3}\text{VO}_{3.85}$ , (●) perovskite  $\text{Ce}_{0.7}\text{Sr}_{0.3}\text{VO}_{3.0}$ , and (▲) cubic YSZ.

For all of the AE-doped  $\text{REVO}_4$  listed in Table 4.1, reduction in flowing  $\text{H}_2$  at 973 K resulted in the production of single phase materials with the perovskite structure (i.e.  $\text{REAEVO}_3$ ) as determined by XRD and shown in Figure 4.3 for  $\text{Ce}_{0.7}\text{Sr}_{0.3}\text{VO}_{3.85}$ . This was also the case for the undoped analogs.

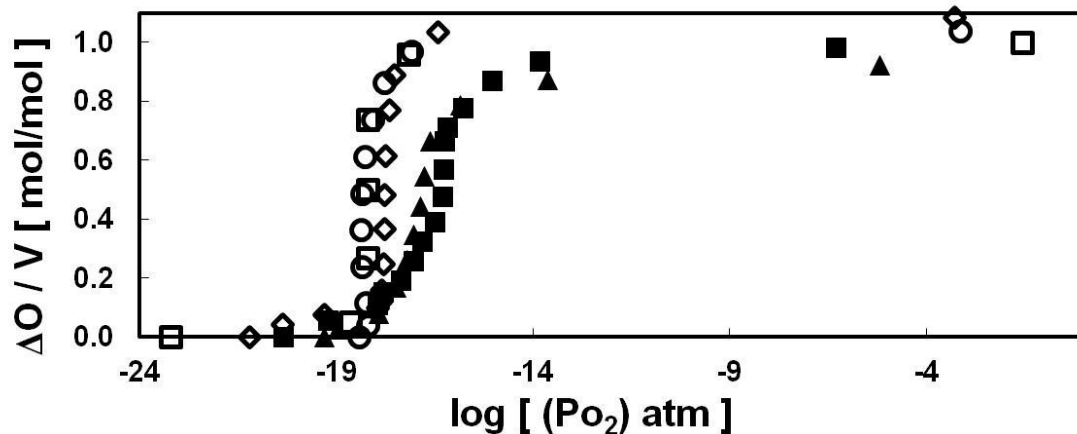


**Figure 4.4:** Coulometric titration isotherms for (□)  $\text{LaVO}_4$ , (○)  $\text{PrVO}_4$ , (◇)  $\text{CeVO}_4$ , (▲)  $\text{Ce}_{0.7}\text{Sr}_{0.3}\text{VO}_{3.85}$ , and (■)  $\text{Ce}_{0.7}\text{Ca}_{0.3}\text{VO}_{3.85}$ , at 973 K.

Figure 4.4 displays redox isotherms at 973 K obtained using the coulometric method for all of the bulk  $\text{REVO}_4$  samples and for  $\text{Ce}_{0.7}\text{Sr}_{0.3}\text{VO}_{3.85}$  and  $\text{Ce}_{0.7}\text{Ca}_{0.3}\text{VO}_{3.85}$  which were used as representatives of the alkaline earth substituted materials. In this set of experiments the samples were initially reduced in flowing  $\text{H}_2$  at 973 K for 4 h to produce the perovskite phase, and then the oxygen stoichiometry of the sample was measured as a function of  $p\text{O}_2$ . In Figure 4.4, the equilibrium amount of oxygen added to the sample per V ion is plotted as a function of the  $p\text{O}_2$ .

The data in Figure 4.4 show that the redox isotherms at 973 K for the undoped  $\text{REVO}_4$  samples are nearly identical, containing a single, well-defined, transition at a  $p\text{O}_2$  of  $10^{-18}$  atm corresponding to the addition/removal of one oxygen per vanadium to the lattice. The data for  $\text{CeVO}_4$  and  $\text{LaVO}_4$  are in agreement with those reported previously<sup>19</sup>. The similarity of the isotherms for  $\text{CeVO}_4$ ,  $\text{LaVO}_4$ ,  $\text{PrVO}_4$  and the fact that only a single redox step is observed, indicates that only the V cation, which is common to all of the materials, is involved in the redox reaction. This conclusion is also consistent with the structures of the starting and ending phases in which the RE ion is known to be in the +3



oxidation state<sup>19,27-30</sup>. Based on the isotherm and XRD results, the step in the redox isotherms can therefore be assigned to  $V^{3+}$  to  $V^{5+}$  transition corresponding to the perovskite to zircon (or monazite in the case of  $LaVO_4$ ) phase transition.

Note that the  $V^{3+}$  to  $V^{5+}$  transition occurs in a single step without the formation of an intermediate phase containing any  $V^{4+}$  cations. The fact that the phase transition occurs at the same  $pO_2$  indicates a similar chemical environment for the vanadium ions in all of these materials. It is also noteworthy that rare earth vanadates are much less reducible than transition metal analogs. For example  $CrVO_4$  undergoes reduction to  $CrVO_3$  at 973 K at a  $pO_2$  of only  $10^{-6}$  atm<sup>19</sup>.

As illustrated by the isotherm data for  $Ce_{0.7}Sr_{0.3}VO_{3.85}$  and  $Ce_{0.7}Ca_{0.3}VO_{3.85}$ , doping the  $REVO_4$  compounds with alkaline earth ions significantly alters their redox properties. The redox isotherms for both of these materials were similar with reduction/oxidation occurring near  $10^{-16}$  atm. This process also takes place over a much wider  $pO_2$  range compared to the undoped compounds and appears to occur in stages. Starting with the fully oxidized materials,  $Ce_{0.7}AE_{0.3}VO_{3.85}$ , the onset of reduction occurs near  $10^{-15}$  atm of  $O_2$  with a sharp transition at  $10^{-16}$  atm which ends after 0.47 oxygens per vanadium have been removed from the lattice. Further reduction occurs less abruptly between  $pO_2$  values of  $10^{-16}$  and  $10^{-18}$  atm, producing a material with a final stoichiometry of  $Ce_{0.7}AE_{0.3}VO_{3.85}$  which has the perovskite structure as determined by XRD. Note that the abrupt transition at  $10^{-16}$  atm corresponds to the reduction of  $Ce_{0.7}AE_{0.3}VO_{3.85}$  to  $Ce_{0.7}AE_{0.3}VO_{3.38}$ , which is near the expected stoichiometry for a material containing only  $V^{4+}$  cations, allowing this transition to be assigned to reduction of  $V^{5+}$  to  $V^{4+}$ . The structure of this  $V^{4+}$  containing phase was not determined in the

present study. The slower reduction that occurs for lower  $pO_2$  values results in the formation of a range of mixed valent materials that contain both  $V^{4+}$  and  $V^{3+}$ , ultimately producing perovskite  $Ce_{0.7}AE_{0.3}VO_{3.0}$  (which also contains  $V^{4+}$  and  $V^{3+}$ ). Thus, these redox isotherm data demonstrate that doping  $REVO_4$  with alkaline earths produces compounds which upon reduction have mixed vanadium valence. The formation of these mixed valence compounds is likely responsible for the high electronic conductivity exhibited by these materials under reducing conditions at intermediate to high temperatures.

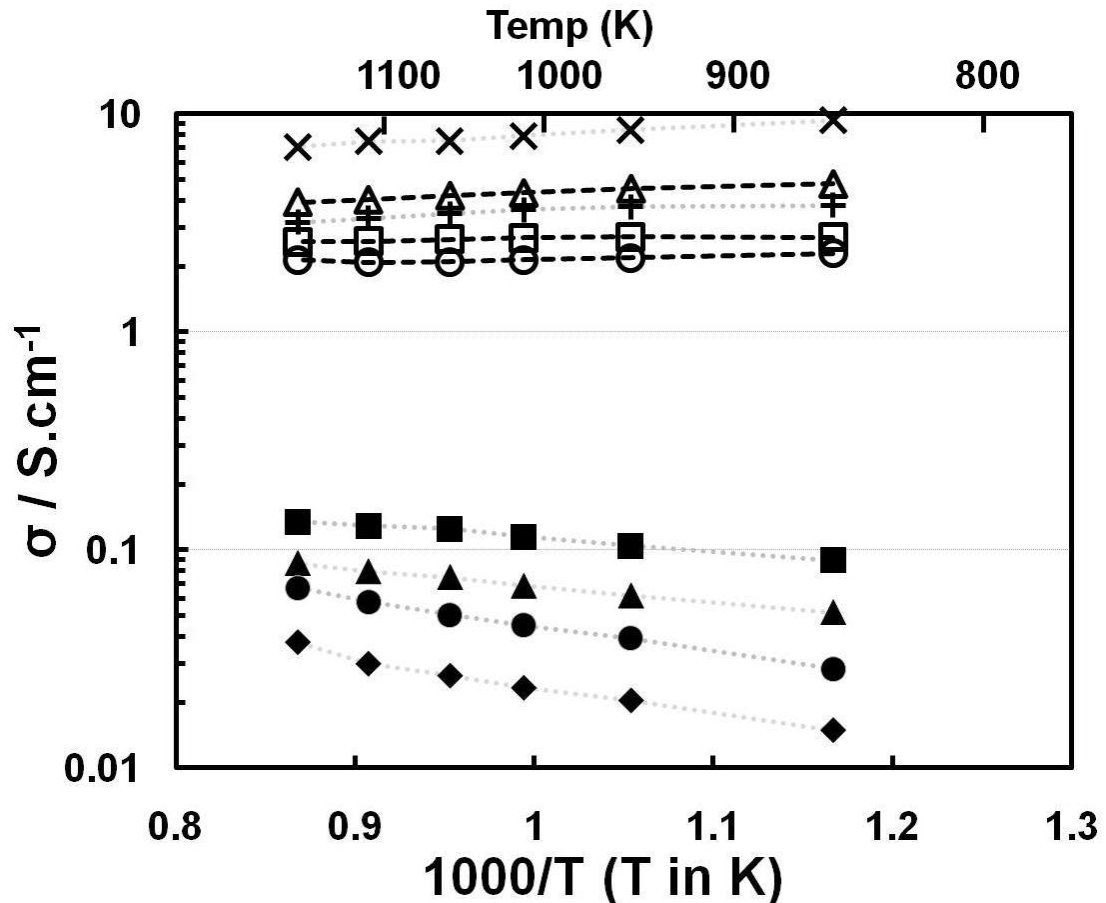


**Figure 4.5:** Electronic conductivities of 30 wt. % (■)  $LaVO_3^-$ , (▲)  $CeVO_3^-$ , (●)  $PrVO_3^-$ , (◆)  $SmVO_3^-$ , (+)  $La_{0.7}Sr_{0.3}VO_3^-$ , (×)  $Ce_{0.7}Sr_{0.3}VO_3^-$ , (□)  $La_{0.7}Ca_{0.3}VO_3^-$ , (Δ)  $Ce_{0.7}Ca_{0.3}VO_3^-$ , (○)  $Pr_{0.7}Ca_{0.3}VO_3$  - YSZ composites in humidified  $H_2$  as a function of temperature.

The electrical conductivities of composites of both reduced alkaline earth doped and undoped REVO<sub>4</sub> compounds in humidified H<sub>2</sub> (3 % H<sub>2</sub>O) were also investigated and are reported in Figure 4.5. The samples used in this series of experiments consisted of porous slabs of YSZ (60% porosity) into which 30 wt. % REVO<sub>4</sub> was infiltrated using the method described in the experimental section. The use of composites manufactured in this way simplified sample preparation compared to that for bulk samples since high-temperature sintering was not required to produce dense bodies. The porous composites also had structures that closely approximate those used in actual electrochemical devices, such as a SOFC, allowing the conductivity numbers to be used to predict the properties of real electrodes. For the alkaline earth doped materials the RE:AE ratio was held fixed at 0.7:0.3 in order to allow materials with similar compositions to be compared.

As has been reported previously<sup>11,15</sup>, the undoped-REVO<sub>3</sub> materials all exhibited semiconducting behavior with the conductivity increasing with temperature in humidified hydrogen. Except for the LaVO<sub>3</sub>-YSZ composite which had a conductivity slightly higher than 0.1 S/cm above 973 K, the electrical conductivities of the other REVO<sub>3</sub>-YSZ composites were significantly less than 0.1 S/cm at all temperatures studied. The data show that the conductivities increase in the following order LaVO<sub>3</sub> > CeVO<sub>3</sub> > PrVO<sub>3</sub> > SmVO<sub>3</sub>. This trend indicates that the conductivity of REVO<sub>3</sub> compounds increases with increasing size of the rare earth ion. Unfortunately, the conductivities of these composites are all too low to allow them to be used as electrodes in practical electrochemical devices.

The alkaline-earth doped, REVO<sub>3</sub>-YSZ composites all exhibited conductivities that were at least an order of magnitude higher than those for the corresponding composites with the undoped material. The highest conductivities at 973 K were 9 S/cm

and 4 S/cm for the  $\text{Ce}_{0.7}\text{Sr}_{0.3}\text{VO}_{3.0}\text{-YSZ}$  and  $\text{Ce}_{0.7}\text{Ca}_{0.3}\text{VO}_{3.0}\text{-YSZ}$ , respectively. Note that these values are sufficient for these composites to be useful in practical electrochemical devices, as will be demonstrated below. As noted in the introduction, the conductivities of the bulk REAEVO<sub>3</sub> materials would be expected to be at least an order of magnitude higher than those of the composites. Also note that all of the alkaline-earth doped materials exhibited metallic behavior with the conductivity decreasing with increasing temperature.

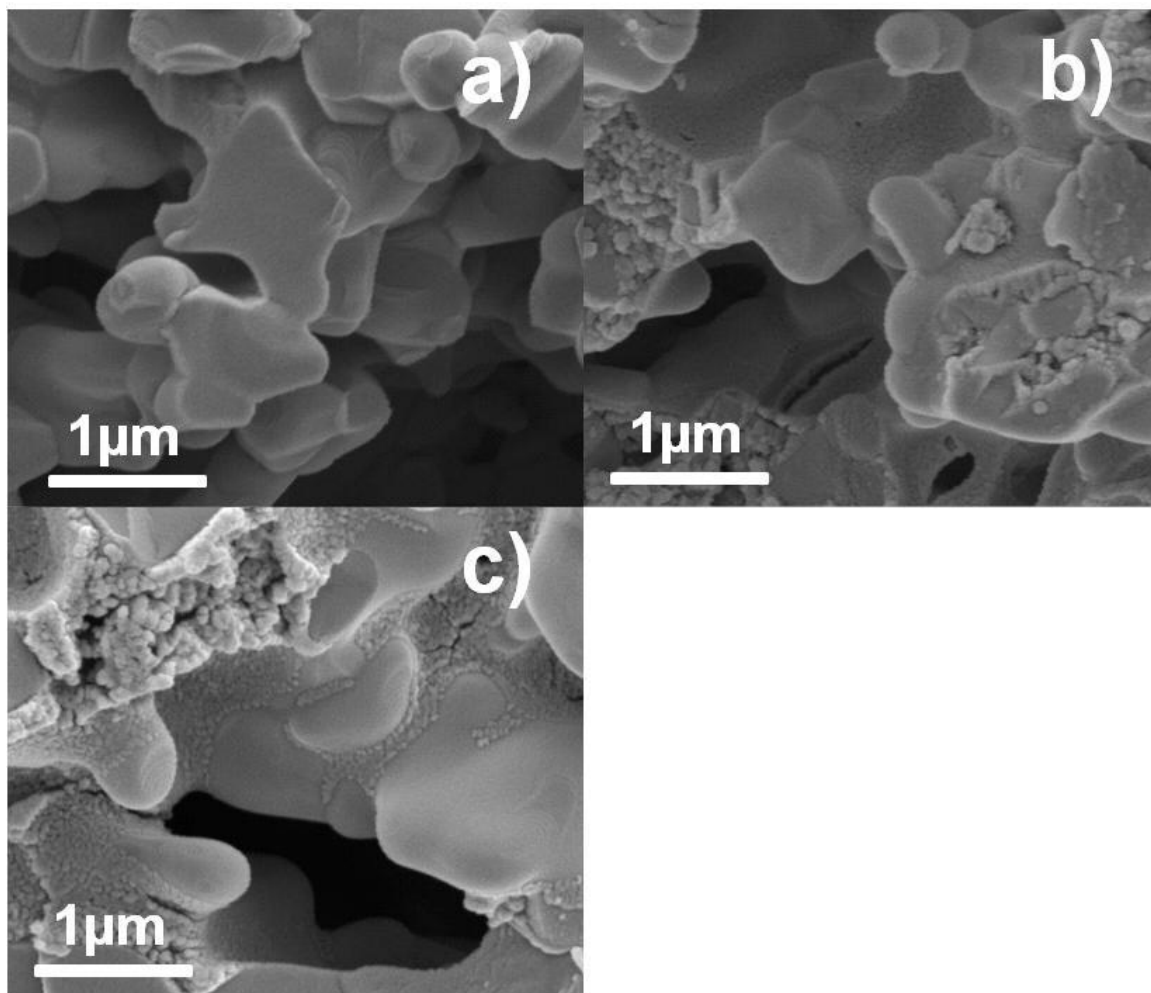


**Figure 4.6:** SEM micrographs of (a) the bare YSZ scaffold, and the Ce<sub>0.7</sub>Sr<sub>0.3</sub>VO<sub>3.85</sub>-YSZ composite calcined at 973 K (b) before and (c) after reduction in humidified H<sub>2</sub> at 973 K.

**Table 4.2:** Specific surface areas of Ce<sub>0.7</sub>Sr<sub>0.3</sub>VO<sub>3.85</sub>-YSZ composites fabricated at 973 K, before and after reduction.

| Fabrication Temp. (K) | Surface Area (m <sup>2</sup> g <sup>-1</sup> ) |  |  |
|-----------------------|--|--|--|
|                       | Blank YSZ                                      | Ce <sub>0.7</sub> Sr <sub>0.3</sub> VO <sub>3.85</sub> -YSZ before reduction | Ce <sub>0.7</sub> Sr <sub>0.3</sub> VO <sub>3.0</sub> -YSZ after reduction |
| 973                   | 0.30   | 0.48   | 1.85   |

The microstructural evolution of a porous  $\text{Ce}_{0.7}\text{Sr}_{0.3}\text{VO}_{3.85}$ -YSZ composite was investigated by SEM, with results shown in Figure 4.6. Figure 4.6a displays the YSZ scaffold prior to the addition of the vanadate and shows a sponge-like morphology with interconnecting pores that are roughly 2 to 3  $\mu\text{m}$  in diameter. Figure 4.6b shows the structure after the infiltration of 30 wt. %  $\text{Ce}_{0.7}\text{Sr}_{0.3}\text{VO}_{3.85}$  followed by calcination in air at 973 K. While a few particles of  $\text{Ce}_{0.7}\text{Sr}_{0.3}\text{VO}_{3.85}$  are visible in the image, the majority of the  $\text{Ce}_{0.7}\text{Sr}_{0.3}\text{VO}_{3.85}$  is present in the form of a textured, relatively dense film that coats the surface of the YSZ scaffold. As shown in Table 4.2, the BET surface areas for the bare and  $\text{Ce}_{0.7}\text{Sr}_{0.3}\text{VO}_{3.85}$ -infiltrated YSZ samples were 0.30 and 0.48  $\text{m}^2\text{g}^{-1}$ , respectively. This similarity in surface areas supports the conclusion that the  $\text{Ce}_{0.7}\text{Sr}_{0.3}\text{VO}_{3.85}$  forms a relatively dense film upon calcination in air.

As shown in Figure 4.6c, reduction of the  $\text{Ce}_{0.7}\text{Sr}_{0.3}\text{VO}_{3.85}$ -infiltrated YSZ sample in humidified  $\text{H}_2$  at 973 K caused significant changes in the structure of the vanadate film which appears to have been transformed from a dense film into a more porous structure composed of interconnected nanoparticles. This structural transformation was accompanied by an increase in the BET surface area from 0.48 to 1.85  $\text{m}^2\text{g}^{-1}$ . Similar morphological changes have been reported upon reduction of  $\text{La}_{0.7}\text{Sr}_{0.3}\text{VO}_{3.85}$ <sup>23</sup> and  $\text{La}_{0.8}\text{Sr}_{0.2}\text{Cr}_{0.5}\text{Mn}_{0.5}\text{O}_{3-\delta}$  (LSCM)<sup>31</sup> films coating a YSZ substrate. For these materials it has been argued that these morphological changes produce structures that have a high concentration of three-phase boundary sites thereby making them better suited for electrode applications.

To investigate the electrochemical performance of the vanadates in SOFC anodes, button cells were prepared with an 80  $\mu\text{m}$  thick YSZ electrolyte, an infiltrated 30 wt. %

$\text{Ce}_{0.7}\text{Sr}_{0.3}\text{VO}_{3.85}$ -YSZ composite anode, and a 40 wt. % LSF-YSZ composite cathode. In order to produce the conductive phase, the  $\text{Ce}_{0.7}\text{Sr}_{0.3}\text{VO}_{3.85}$  was initially reduced in humidified  $\text{H}_2$  at the cell operating temperature of 973 K. For one cell, to enhance the catalytic activity, 1 wt. % Pd was added to the  $\text{Ce}_{0.7}\text{Sr}_{0.3}\text{VO}_{3.85}$  anode by infiltration with aqueous solution of  $(\text{NH}_3)_4\text{Pd}(\text{NO}_3)_2$ . V-i polarization curves and impedance spectra for the cells with and without the added Pd oxidation catalyst operating at 973 K in humidified  $\text{H}_2$  are shown in Figure 4.7.

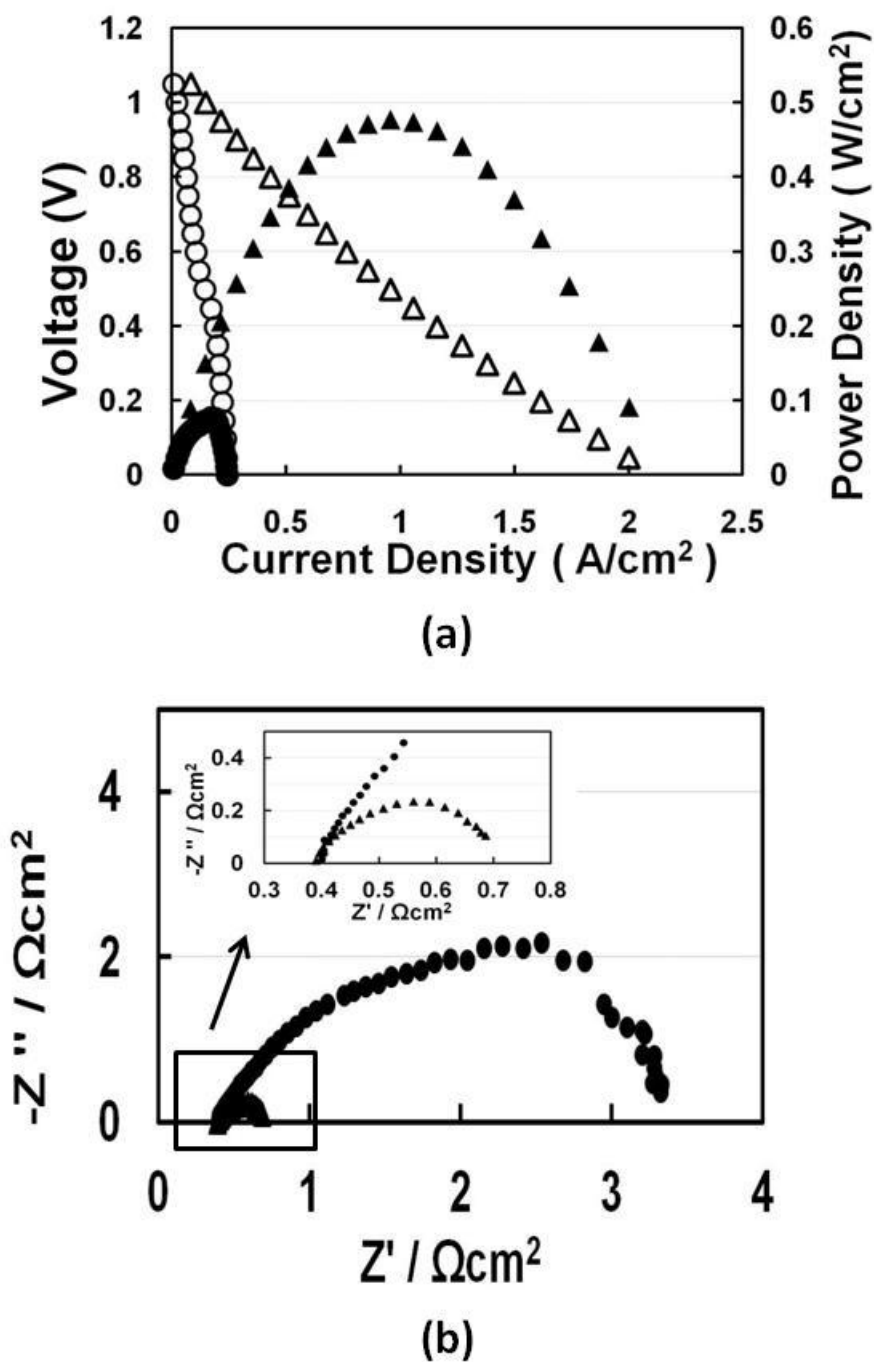


**Figure 4.7:** (a) V-i polarization curves and (b) electrochemical impedance spectra of cells with infiltrated 30 wt. % of  $\text{Ce}_{0.7}\text{Sr}_{0.3}\text{VO}_{3.85}$ -YSZ anodes with ( $\Delta$ ) and without ( $\blacktriangle$ ) Pd catalyst. The cells were operated at 973 K with humidified  $\text{H}_2$  fuel.



The V-i polarization curves (Figure 4.7a) show that the cells with and without added Pd had open-circuit potentials near the theoretical Nernst value of 1.1 V. The V-i curves for both cells were also nearly linear with maximum power densities of 0.08 and 0.47 W cm<sup>-2</sup> for the cells with and without the Pd catalyst, respectively. The Nyquist plots of the impedance spectra collected at open circuit (Figure 4.7b) show that the ohmic losses, calculated from the high-frequency intercept with the real axis, were the same, 0.42 Ω cm<sup>2</sup>, for both cells. Since this value is consistent with area specific resistance expected for an 80 μm thick YSZ electrolyte layer, the electrodes are not contributing significantly to the ohmic losses in these cells. This further demonstrates that the conductivity of the Ce<sub>0.7</sub>Sr<sub>0.3</sub>VO<sub>3.0</sub> is sufficient to produce a high performance electrode. The importance of enhancing the catalytic activity of the Ce<sub>0.7</sub>Sr<sub>0.3</sub>VO<sub>3.0</sub>-YSZ anode is also demonstrated by the impedance data which shows that the area specific resistance of the electrodes decreases from 2.9 to 0.3 Ω cm<sup>2</sup> upon addition of the Pd catalyst. The need to enhance catalytic activity is consistent with nearly all previous studies of SOFC anodes in which a ceramic material has been used to supply electronic conductivity. Nonetheless, the high performance of the cell with the Pd-Ce<sub>0.7</sub>Sr<sub>0.3</sub>VO<sub>3.0</sub>-YSZ composite anode is very encouraging and further demonstrates the promise of doped rare-earth vanadates as conducting components in SOFC anodes, and that these types of ceramic-based anodes can be practical.

#### 4.4 Conclusion

In this study we have shown that the Pechini method can be used to synthesize REAEVO<sub>4</sub> oxides with higher concentrations of the alkaline earth ions compared to those prepared using conventional solid-state synthesis routes. The redox properties for both REVO<sub>4</sub> and REAEVO<sub>4</sub> compounds were characterized and it was found that the addition of the alkaline earth ions, Sr<sup>2+</sup> and Ca<sup>2+</sup>, to LaVO<sub>4</sub>, CeVO<sub>4</sub>, and PrVO<sub>4</sub> produced compounds that were more easily reduced and had significantly higher electronic conductivities compared to the pure REVO<sub>4</sub> compounds. Redox isotherms indicate that the higher conductivities upon reduction are due to the formation of compounds with mixed valency on the V ions. In spite of their high electronic conductivity, porous REAEVO<sub>3</sub>-YSZ composite anodes in SOFCs were found to exhibit only modest performance due to their low catalytic activity. High performance was obtained, however, when dopant amounts of a catalytic metal, such as Pd, were added to the electrode.

## 4.5 References

- 1 Huang, Y. H., Dass, R. I., Denyszyn, J. C. & Goodenough, J. B. Synthesis and characterization of  $\text{Sr}_2\text{MgMoO}_{6-\delta}$  - An anode material for the solid oxide fuel cell. *J Electrochem Soc* **153**, A1266-A1272, doi:10.1149/1.2195882 (2006).
- 2 Kim, H., Lu, C., Worrell, W. L., Vohs, J. M. & Gorte, R. J. Cu-Ni cermet anodes for direct oxidation of methane in solid-oxide fuel cells. *J Electrochem Soc* **149**, A247-A250, doi:10.1149/1.1445170 (2002).
- 3 Matsuzaki, Y. & Yasuda, I. The poisoning effect of sulfur-containing impurity gas on a SOFC anode: Part I. Dependence on temperature, time, and impurity concentration. *Solid State Ionics* **132**, 261-269 (2000).
- 4 Sarantaridis, D. & Atkinson, A. Redox cycling of Ni-based solid oxide fuel cell anodes: A review. *Fuel Cells* **7**, 246-258, doi:DOI 10.1002/fuce.200600028 (2007).
- 5 Sfeir, J., van Herle, J. & McEvoy, A. J. Stability of calcium substituted lanthanum chromites used as SOFC anodes for methane oxidation. *J Eur Ceram Soc* **19**, 897-902 (1999).
- 6 Toebes, M. L., Bitter, J. H., van Dillen, A. J. & de Jong, K. P. Impact of the structure and reactivity of nickel particles on the catalytic growth of carbon nanofibers. *Catal Today* **76**, 33-42 (2002).
- 7 Toh, C. H., Munroe, P. R., Young, D. J. & Foger, K. High temperature carbon corrosion in solid oxide fuel cells. *Mater High Temp* **20**, 129-136 (2003).

- 8 Adjianto, L., Kungas, R., Park, J., Vohs, J. M. & Gorte, R. J. SOFC anodes based on infiltration of tungsten bronzes. *Int J Hydrogen Energ* **36**, 15722-15730, doi:DOI 10.1016/j.ijhydene.2011.09.059 (2011).
- 9 Danilovic, N., Luo, J. L., Chuang, K. T. & Sanger, A. R.  $\text{Ce}_{(0.9)}\text{Sr}_{(0.1)}\text{VO}_{(x)}$  ( $x=3, 4$ ) as anode materials for  $\text{H}_{(2)}\text{S}$ -containing  $\text{CH}_{(4)}$  fueled solid oxide fuel cells. *J Power Sources* **192**, 247-257, doi:DOI 10.1016/j.jpowsour.2009.03.045 (2009).
- 10 Petit, C. T. G., Lan, R., Cowin, P. I., Irvine, J. T. S. & Tao, S. W. Novel redox reversible oxide, Sr-doped cerium orthovanadate to metavanadate. *J Mater Chem* **21**, 525-531, doi:Doi 10.1039/C0jm02669g (2011).
- 11 Petit, C. T. G., Lan, R., Cowin, P. I., Kraft, A. & Tao, S. W. Structure, conductivity and redox stability of solid solution  $\text{Ce}_{1-x}\text{Ca}_x\text{VO}_4$  ( $0 \leq x \leq 0.4125$ ). *J Mater Sci* **46**, 316-326, doi:DOI 10.1007/s10853-010-4812-x (2011).
- 12 Chakoumakos, B. C., Abraham, M. M. & Boatner, L. A. Crystal-Structure Refinements of Zircon-Type  $\text{MVO}_4$  ( $\text{M}=\text{Sc}, \text{Y}, \text{Ce}, \text{Pr}, \text{Nd}, \text{Tb}, \text{Ho}, \text{Er}, \text{Tm}, \text{Yb}, \text{Lu}$ ). *J Solid State Chem* **109**, 197-202, doi:DOI 10.1006/jssc.1994.1091 (1994).
- 13 Watanabe, A. Highly conductive oxides,  $\text{CeVO}_4$ ,  $\text{Ce}_{1-x}\text{M}_x\text{VO}_{4-0.5x}$  ( $\text{M}=\text{Ca}, \text{Sr}, \text{Pb}$ ) and  $\text{Ce}_{1-y}\text{Bi}_y\text{VO}_4$ , with zircon-type structure prepared by solid-state reaction in air. *J Solid State Chem* **153**, 174-179, doi:DOI 10.1006/jssc.2000.8773 (2000).
- 14 Tsipis, E. V., Kharton, V. V., Vyshatko, N. P., Shaula, A. L. & Frade, J. R. Stability and oxygen ionic conductivity of zircon-type  $\text{Ce}_{(1-x)}\text{A}_{(x)}\text{VO}_{(4+\delta)}$  ( $\text{A}=\text{Ca}, \text{Sr}$ ). *J Solid State Chem* **176**, 47-56, doi:Doi 10.1016/S0022-4596(03)00342-6 (2003).

- 15 Petit, C. T. G., Lan, R., Cowin, P. I. & Tao, S. W. Structure and conductivity of strontium-doped cerium orthovanadates  $Ce_{1-x}Sr_xVO_4$  ( $0 \leq x \leq 0.175$ ). *J Solid State Chem* **183**, 1231-1238, doi:DOI 10.1016/j.jssc.2010.03.032 (2010).
- 16 Petit, C. T. G., Lan, R., Cowin, P. I., Irvine, J. T. S. & Tao, S. W. Structure, conductivity and redox reversibility of Ca-doped cerium metavanadate. *J Mater Chem* **21**, 8854-8861, doi:Doi 10.1039/C1jm10960j (2011).
- 17 Park, S., Gorte, R. J. & Vohs, J. M. Tape cast solid oxide fuel cells for the direct oxidation of hydrocarbons. *J Electrochem Soc* **148**, A443-A447 (2001).
- 18 Kungas, R., Kim, J. S., Vohs, J. M. & Gorte, R. J. Restructuring Porous YSZ by Treatment in Hydrofluoric Acid for Use in SOFC Cathodes. *J Am Ceram Soc* **94**, 2220-2224, doi:DOI 10.1111/j.1551-2916.2010.04359.x (2011).
- 19 Shah, P. R., Khader, M. M., Vohs, J. M. & Gorte, R. J. A comparison of the redox properties of vanadia-based mixed oxides. *J Phys Chem C* **112**, 2613-2617, doi:Doi 10.1021/Jp710516d (2008).
- 20 Adijanto, L., Kungas, R., Bidrawn, F., Gorte, R. J. & Vohs, J. M. Stability and performance of infiltrated  $La_{0.8}Sr_{0.2}Co_xFe_{1-x}O_3$  electrodes with and without  $Sm_{0.2}Ce_{0.8}O_{1.9}$  interlayers. *J Power Sources* **196**, 5797-5802, doi:DOI 10.1016/j.jpowsour.2011.03.022 (2011).
- 21 Wang, W. S., Gross, M. D., Vohs, J. M. & Gorte, R. J. The stability of LSF-YSZ electrodes prepared by infiltration. *J Electrochem Soc* **154**, B439-B445, doi:Doi 10.1149/1.2709510 (2007).
- 22 Vohs, J. M. & Gorte, R. J. High-Performance SOFC Cathodes Prepared by Infiltration. *Adv Mater* **21**, 943-956, doi:DOI 10.1002/adma.200802428 (2009).

- 23 Park, J. S. *et al.* A high-performance solid oxide fuel cell anode based on lanthanum strontium vanadate. *J Power Sources* **196**, 7488-7494, doi:DOI 10.1016/j.jpowsour.2011.05.028 (2011).
- 24 Ge, X. M. & Chan, S. H. Lanthanum Strontium Vanadate as Potential Anodes for Solid Oxide Fuel Cells. *J Electrochem Soc* **156**, B386-B391, doi:Doi 10.1149/1.3058585 (2009).
- 25 Shannon, R. D. Revised Effective Ionic-Radii and Systematic Studies of Interatomic Distances in Halides and Chalcogenides. *Acta Crystallogr A* **32**, 751-767, doi:Doi 10.1107/S0567739476001551 (1976).
- 26 Shen, Y. Q. *et al.* Nanocrystals of CeVO<sub>4</sub> Doped by Metallic Heteroions. *Inorg Chem* **50**, 6189-6194, doi:Doi 10.1021/Ic200459t (2011).
- 27 Reidy, R. F. & Swider, K. E. Determination of the Cerium Oxidation-State in Cerium Vanadate. *J Am Ceram Soc* **78**, 1121-1122, doi:DOI 10.1111/j.1151-2916.1995.tb08453.x (1995).
- 28 Da Silva, J. L. F., Ganduglia-Pirovano, M. V. & Sauer, J. Formation of the cerium orthovanadate CeVO<sub>4</sub> : DFT+U study. *Phys Rev B* **76**, doi:Artn 125117 Doi 10.1103/Physrevb.76.125117 (2007).
- 29 Hirata, T. & Watanabe, A. A Comparison between the Raman Spectra of Ce<sub>1-x</sub>Ca<sub>x</sub>VO<sub>4-0.5x</sub> (0 ≤ x ≤ 0.41) and Ce<sub>1-x</sub>Bi<sub>x</sub>VO<sub>4</sub> (0 ≤ x ≤ 0.68). *J Solid State Chem* **158**, 264-267, doi:DOI 10.1006/jssc.2001.9104 (2001).
- 30 Tshipis, E. V., Patrakeev, M. V., Kharton, V. V., Vyshatko, N. P. & Frade, J. R. Ionic and p-type electronic transport in zircon-type Ce<sub>(1-x)</sub>A<sub>(x)</sub>VO<sub>(4 +/-delta)</sub> (A = Ca, Sr). *J Mater Chem* **12**, 3738-3745, doi:Doi 10.1039/B206004c (2002).

- 31 Kim, G., Corre, G., Irvine, J. T. S., Vohs, J. M. & Gorte, R. J. Engineering composite oxide SOFC anodes for efficient oxidation of methane. *Electrochem Solid St* **11**, B16-B19, doi:10.1149/1.2817809 (2008).

## Chapter 5. Transition Metal-Doped Rare Earth Vanadates: A Regenerable Catalytic Material for SOFC Anodes\*

### Summary

The physical and electrochemical properties of cerium vanadates in which a portion of the cerium cations have been substituted with transition metals ( $\text{Ce}_{1-x}\text{TM}_x\text{VO}_{4-0.5x}$ , TM = Ni, Co, Cu) were investigated and their suitability for use in solid oxide fuel cell (SOFC) anodes was assessed. Similar to other transition metal doped perovskites, the metals were found to move out of and into the oxide lattice in response to exposure to reducing and oxidizing conditions at elevated temperatures. This process produces nanoparticle metal catalysts that decorate the surface of the conductive cerium vanadate. Solid oxide fuel cells (SOFC) with  $\text{Ce}_{1-x}\text{TM}_x\text{VO}_3$ -YSZ composite anodes exhibited high electrochemical activity. It was also demonstrated that doping with the alkaline earth ions,  $\text{Ca}^{2+}$  and  $\text{Sr}^{2+}$  enhances the electronic conductivity of the vanadate and  $\text{Ce}_{0.7}\text{Sr}_{0.1}\text{Ni}_{0.2}\text{VO}_3$ -YSZ composite SOFC anodes were found to have both high electrochemical activity and unusually high redox stability.

---

\* This chapter was published as a research paper in the Journal of Materials Chemistry, 22 (2012) 11396. Copyright: 2012, The Royal Society of Chemistry.



## 5.1 Introduction

In the previous chapters, we demonstrated there are a variety of conducting oxides that have been extensively studied to replace Ni-YSZ cermets as SOFC anodes, and they are mostly in the perovskite family such as titanates<sup>1-4</sup>, manganates<sup>5-8</sup>, chromates<sup>9</sup> and bronzes<sup>10,11</sup>. In almost all the cases, these materials have relatively low catalytic activity for oxidation reactions resulting in high electrode overpotentials. Their performance improves significantly, however, upon the addition of nanoparticles of highly catalytic metals (e.g. Ni, Pt, or Pd) to the surface of the oxide<sup>2,6,9-20</sup>.

The catalytic metals are generally added onto the surface of the oxide using standard wet infiltration techniques. Recent work from the Barnett group, however, has shown that the catalytic metal nanoparticles can also be produced in situ via exsolution from an electronically conducting ceramic host<sup>9,17-19,21</sup>. This approach is similar to that used in so called “intelligent” catalysts which were first developed by researchers at Daihatsu for use in automotive emissions control systems<sup>22-26</sup>. One of the key insights in the Daihatsu work was the realization that while precious metals, such as Pd, were soluble on the B-site in perovskite oxides under oxidizing conditions, they had only limited solubility under reducing conditions. Thus, by changing between reducing and oxidizing conditions the metal could be substituted into and out of the perovskite lattice. This process is shown schematically in Figure 5.1.

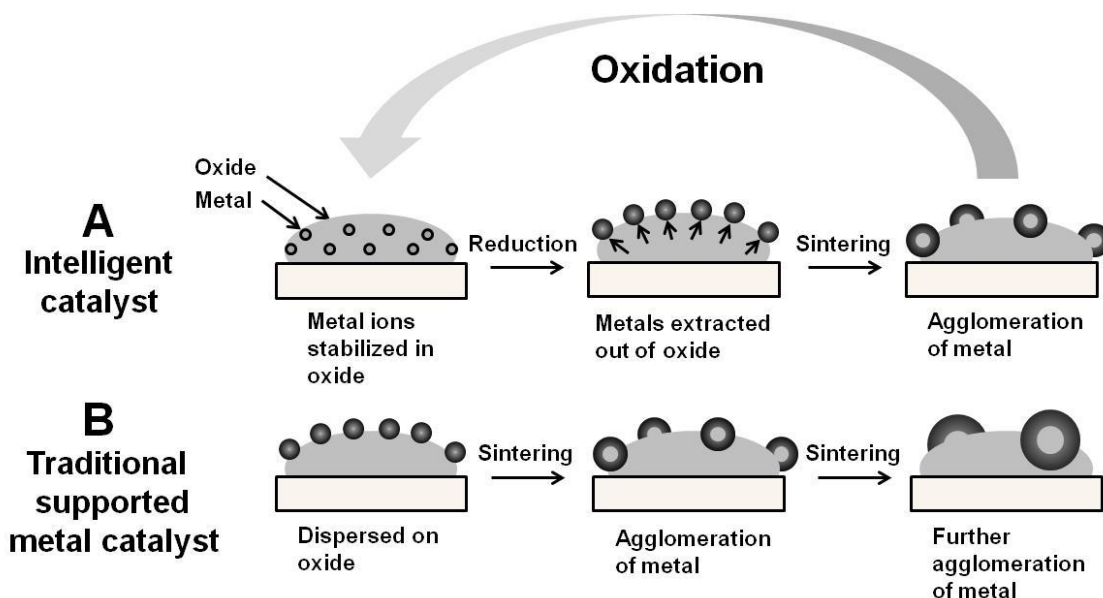


**Figure 5.1:** Panel A: Schematic of an intelligent catalyst in which metals move out of and into an oxide host lattice in response to exposure to reducing and oxidizing conditions, respectively. Panel B: Sintering of metal nanoparticles on an oxide which occurs over time for most traditional supported metal catalysts.

Barnett's initial studies of the use of this phenomena in SOFC anodes focused on the mixed conducting perovskite,  $\text{La}_{0.8}\text{Sr}_{0.2}\text{Cr}_{1-x}\text{Ru}_x\text{O}_{3-x}$ , and showed that upon reduction Ru nanoparticles  $< 5$  nm in diameter were formed via exsolution of Ru from the perovskite lattice<sup>9,19</sup>. Anodes composed of composites of  $\text{La}_{0.8}\text{Sr}_{0.2}\text{Cr}_{1-x}\text{Ru}_x\text{O}_{3-x}$  and gadolinia-doped ceria (GDC) electrolyte were found to exhibit excellent performance after activation in  $\text{H}_2$ . They have subsequently expanded their studies to include the exsolution of Ni and Pd particles from electronically conducting  $(\text{La,Sr})\text{CrO}_3$ <sup>17,21</sup>.

The work from the Barnett group provides an exciting new paradigm for both optimizing the catalytic properties of ceramic anodes for SOFC for specific fuels and for maintaining long term performance. In order to obtain high performance anodes, this approach does require, however, the use of host oxides that have a high electronic conductivity. We and others have shown that alkaline earth (AE) doped rare earth (RE)

vanadates ( $\text{RE}_{1-x}\text{AE}_x\text{VO}_4$ ), such as  $\text{Ce}_{1-x}\text{Sr}_x\text{VO}_4$  and  $\text{La}_{1-x}\text{Sr}_x\text{VO}_4$ , have electronic conductivities approaching  $1000 \text{ S cm}^{-1}$  under some conditions, and are chemically stable in a variety of fuels including  $\text{H}_2$ ,  $\text{H}_2\text{S}$ , and  $\text{CH}_4$ <sup>27-34</sup>. In the last chapter, we have demonstrated that these materials have a zircon structure under oxidizing conditions but undergo a phase change to the perovskite structure upon reduction<sup>27,35</sup>. It is unclear, however, whether transition metals can be substituted into these materials, and whether they will undergo exsolution phenomena such as that described above.

In this chapter, the goal of the work presented here was to investigate the suitability of transition metal substituted  $\text{RE}_{1-x}\text{AE}_x\text{VO}_4$  materials for use in SOFC anodes and to specifically determine whether the metal can be moved out of and into the lattice by redox cycling, and if this phenomenon can be used to tailor catalytic properties.

## 5.2 Experimental

$\text{Ce}_{1-x}\text{TM}_x\text{VO}_{4-0.5x}$  materials (where  $\text{TM} = \text{Ni}, \text{Co}, \text{Cu}$ ) were prepared using an aqueous precursor solution containing the appropriate amounts of  $\text{Ce}(\text{NO}_3)_3 \cdot 6\text{H}_2\text{O}$  (Alfa Aesar, 99.5%),  $\text{NH}_4\text{VO}_3$  (Aldrich, 99+ %), and with either  $\text{Ni}(\text{NO}_3)_3 \cdot 6\text{H}_2\text{O}$ ,  $\text{Co}(\text{NO}_3)_3 \cdot 6\text{H}_2\text{O}$ , or  $\text{Cu}(\text{NO}_3)_3 \cdot 6\text{H}_2\text{O}$  (Alfa Aesar, 99.9%). Citric acid (Fisher Scientific) was also added as a complexing agent to aid in the formation of a single phase at a lower temperature. The precursor solution was then dried and the resulting powder was calcined at 973 K in air to form the zircon phase. Perovskite  $\text{Ce}_{1-x}\text{TM}_x\text{VO}_3$  materials were produced by reducing the  $\text{Ce}_{1-x}\text{TM}_x\text{VO}_{4-0.5x}$  in humidified  $\text{H}_2$  (3%  $\text{H}_2\text{O}$ ) at 973 K. Materials in which alkaline earth (AE) ions,  $\text{Sr}^{2+}$  and  $\text{Ca}^{2+}$ , were substituted for a portion

of the cerium cations were also synthesized in a similar manner using  $\text{Sr}(\text{NO}_3)_2$  and  $\text{Ca}(\text{NO}_3)_2 \cdot 4\text{H}_2\text{O}$  (Alfa Aesar, 99.9%) in the precursor solution.

Porous YSZ slabs into which 30 wt. %  $\text{Ce}_{1-x}\text{TM}_x\text{VO}_{4-0.5x}$  or  $\text{Ce}_{1-y-x}\text{AE}_y\text{TM}_x\text{VO}_{4-0.5y-0.5x}$  (for simplicity we will refer to the latter compound as  $\text{Ce}_{1-x-y}\text{AE}_y\text{TM}_x\text{VO}_{4-\delta}$  throughout the remainder of the chapter) had been infiltrated were used for hydrocarbon stability and conductivity measurements. The porous, 4 mm x 4 mm x 15 mm YSZ slabs were prepared using methods that have been described in Chapter 2<sup>36,37</sup>. The vanadates were added to the porous YSZ slabs by infiltrating the aqueous precursor solution followed by drying and annealing in air at 973 K. Multiple infiltration/annealing cycles were used to obtain the desired 30 wt. % loading. For conductivity measurements, the  $\text{Ce}_{1-x-y}\text{AE}_y\text{TM}_x\text{VO}_{4-\delta}/\text{YSZ}$  composites were first pre-reduced at 973 K in humidified  $\text{H}_2$  (3%  $\text{H}_2\text{O}$ ) for 2 h. The conductivity was measured using the 4-probe, DC method with the sample in humidified  $\text{H}_2$  as a function of temperature. The stability of the vanadates in hydrocarbons was assessed by exposing  $\text{Ce}_{1-x-y}\text{AE}_y\text{TM}_x\text{VO}_{4-\delta}/\text{YSZ}$  composites to dry methane at 973 K for 3 h and measuring the weight gain resulting from carbon deposition. The morphological structure of the anode composites was determined using scanning electron microscopy (SEM) (FEI Quanta 600 ESEM) and X-ray diffraction (XRD) using  $\text{Cu K}_\alpha$  radiation. Powder samples were used for the XRD measurements and a small amount of YSZ was physically mixed with the vanadate powder to act as a reference. Surface areas of the composites were measured by the BET method using Kr adsorption at 78 K.

Cells 1 cm in diameter were used in all fuel cell measurements. These cells were fabricated using porous-dense-porous tri-layer YSZ wafers that were produced using tape

casting methods that have been described in Chapter 2<sup>36</sup>. For each cell, the dense electrolyte layer was 80  $\mu\text{m}$  thick and 1 cm in diameter. The 60% porous YSZ layers on each side of the dense electrolyte layer were 50  $\mu\text{m}$  thick with a BET surface area 0.3  $\text{m}^2\text{g}^{-1}$ . The cathodes were prepared following the procedure detailed in Chapter 2. Once the perovskite loading was 40 wt. %, the cathode was calcined to 1123 K for 4 h to form the perovskite structure. The  $\text{Ce}_{1-x-y}\text{AE}_y\text{TM}_x\text{VO}_{4-\delta}$  anode was synthesized in a similar manner except that a 30 wt. % loading was used and it was calcined to only 973 K and was reduced in humidified  $\text{H}_2$  (3%  $\text{H}_2\text{O}$ ) at 973 K prior to cell testing. Silver paste was applied to both electrodes and used as the current collector and the cells were mounted onto an alumina tube using a ceramic adhesive (Aremco, Ceramabond 552). All the cell tests were performed with the anode exposed to humidified  $\text{H}_2$  (3%  $\text{H}_2\text{O}$ ) and the cathode to ambient air. Electrochemical impedance spectra were measured between 0.1 Hz and 300 kHz with a 1 mA AC perturbation and V-i polarization curves were measured using a Gamry Instruments potentiostat.

### 5.3 Results and Discussion

Initial studies focused on using XRD of the powder samples to determine the solubility limits of the transition metal dopants (Ni, Co, or Cu) within the zircon,  $\text{CeVO}_4$  structure. XRD allowed changes in the lattice parameter as a function of dopant concentration to be determined and the presence of secondary phases to be detected. Ni-doped  $\text{CeVO}_4$  will be used as an example to illustrate these methods. The zircon structure of  $\text{Ce}_{1-x}\text{Ni}_x\text{VO}_{4-0.5x}$  was confirmed by the presence of the expected diffraction peaks near 24.0, 32.4, 34.1, 36.4, 38.9, 43.2, 46.1, and 48.0 degrees  $2\theta$ <sup>33,38</sup>. Powder XRD patterns in

the range 30 to 35 degrees  $2\theta$ , which contains the intense (112) peak of the zircon lattice between 32.39 and 32.42 degrees  $2\theta$  are shown in Figure 5.2 for this material for several  $x$  values. Note that the peak at 30.1 degrees  $2\theta$  corresponds to the YSZ that was added as a standard.

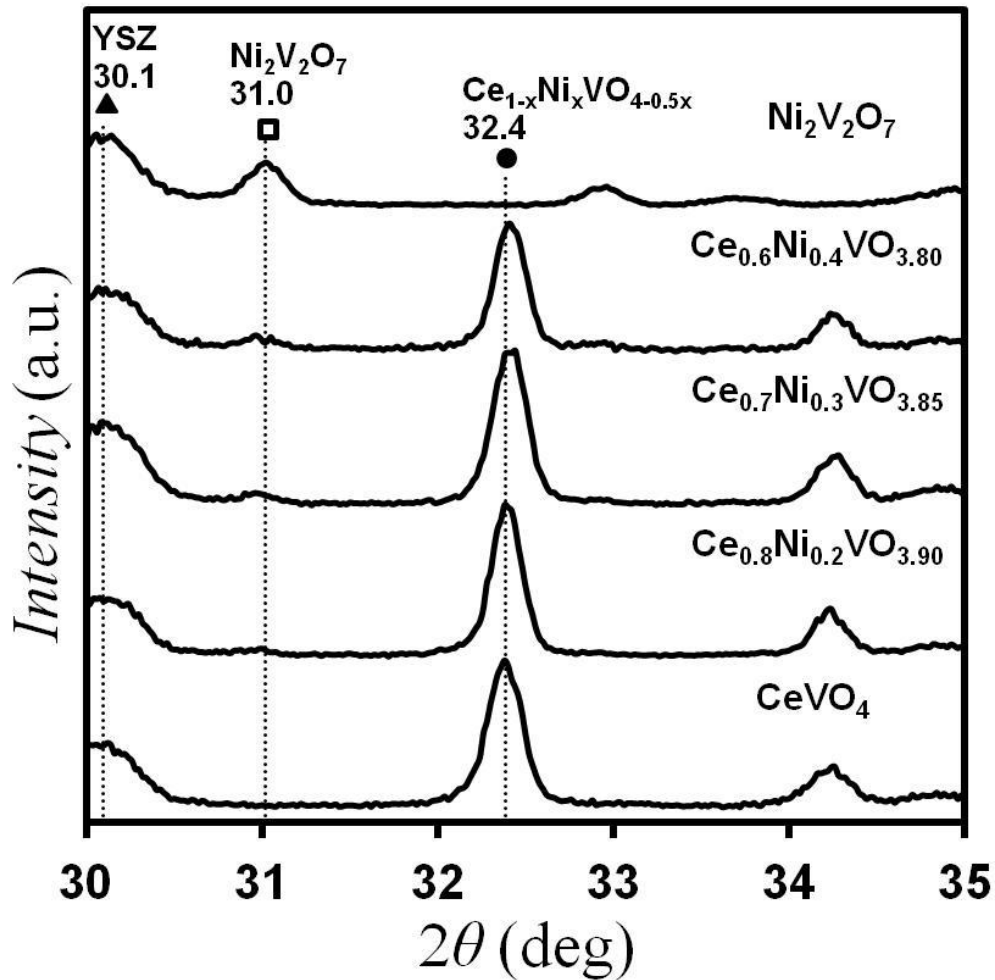


**Figure 5.2:** XRD patterns of  $\text{Ce}_{1-x}\text{Ni}_x\text{VO}_{4-0.5x}$ -YSZ composites that were calcined in air at 973 K for  $x$  values of 0, 0.2, 0.3, 0.4, 1. The peaks labeled  $\blacktriangle$ ,  $\square$  and  $\bullet$  correspond to YSZ,  $\text{Ni}_2\text{V}_2\text{O}_7$  and  $\text{Ce}_{1-x}\text{Ni}_x\text{VO}_{4-0.5x}$ , respectively.

In the bottom pattern in the figure, corresponding to  $\text{CeVO}_4$ , the (112) peak of the zircon lattice appears at 32.39 degrees  $2\theta$ . Substitution of 20 mol % of Ce cations with Ni cations ( $\text{Ce}_{0.8}\text{Ni}_{0.2}\text{VO}_{3.90}$ ) resulted in a shift of the (112) peak to 32.41 degrees  $2\theta$  due to a

decrease in the lattice parameter. Assuming the formation of a single phase material with the zircon structure, Vegard's law<sup>38</sup> predicts that the lattice parameter (or the position of a characteristic diffraction peak) should be a linear function of the Ni concentration up to the solubility limit. At higher Ni concentrations the zircon lattice constant should remain fixed with secondary Ni-rich phases being formed.

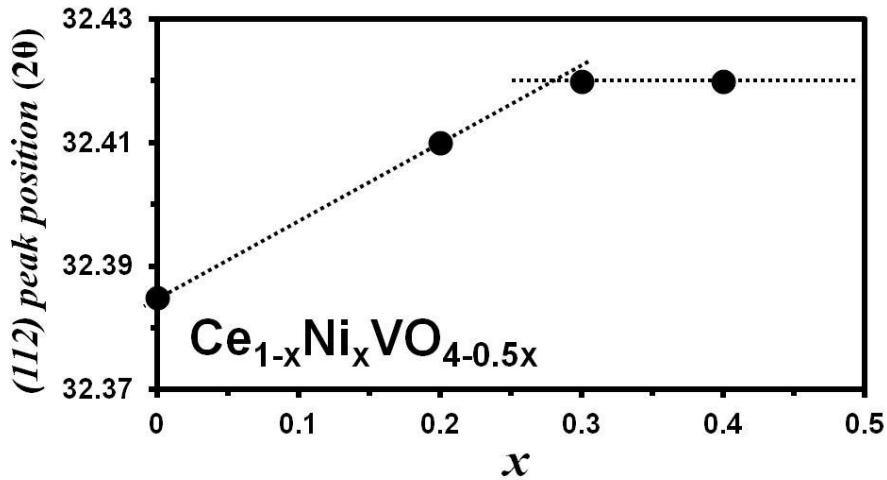


**Figure 5.3:** Plot of the position of the (112) diffraction peak as a function of  $x$  for  $Ce_{1-x}Ni_xVO_{4-0.5x}$ .

**Table 5.1:** Transition metal solubility limit in  $Ce_{1-x}TM_xVO_{4-0.5x}$ .

| Solid Solubility Limit    |      |      |      |
|---------------------------|------|------|------|
| $Ce_{1-x}TM_xVO_{4-0.5x}$ | Ni   | Co   | Cu   |
| $x$                       | 0.28 | 0.25 | 0.28 |

The plot of the position of the (112) diffraction peak as a function of  $x$  in  $Ce_{1-x}Ni_xVO_{4-0.5x}$  in Figure 5.3 shows this characteristic behavior and indicates that the limiting value of  $x$  is 0.28. This result is consistent with the XRD data in Figure 5.2 which show that for  $x$  values  $\geq 0.3$  an additional peak appears in the diffraction pattern at 31.0 degrees  $2\theta$  which can be assigned to  $Ni_2V_2O_7$  (for comparison purposes the XRD pattern of this compound

is also included in the figure). The solubility limits for Co and Cu in  $\text{CeVO}_4$  were determined in an analogous manner and are reported in Table 5.1. Note that the solubility limits were nearly the same for all three metal cations,  $x = \sim 0.28$ , which is consistent with the fact that the ionic radii of these cations,  $\text{Ni}^{2+}$  (0.83 Å),  $\text{Co}^{2+}$  (0.79 Å),  $\text{Cu}^{2+}$  (0.87 Å), are similar<sup>39</sup>. In the remainder of the study in order to allow materials with similar compositions to be compared, a Ce:transition metal ratio of 0.8:0.2 was used.

To establish that the transition metal can reversibly move out of/into the oxide lattice in response to changes in the reducing/oxidizing atmospheres, a series of XRD measurements were performed for a  $\text{Ce}_{0.8}\text{Ni}_{0.2}\text{VO}_{3.90}$  sample that was exposed to both oxidizing (air) and reducing ( $\text{H}_2 + 3\% \text{H}_2\text{O}$ ) environments at 973 K for 2 h.



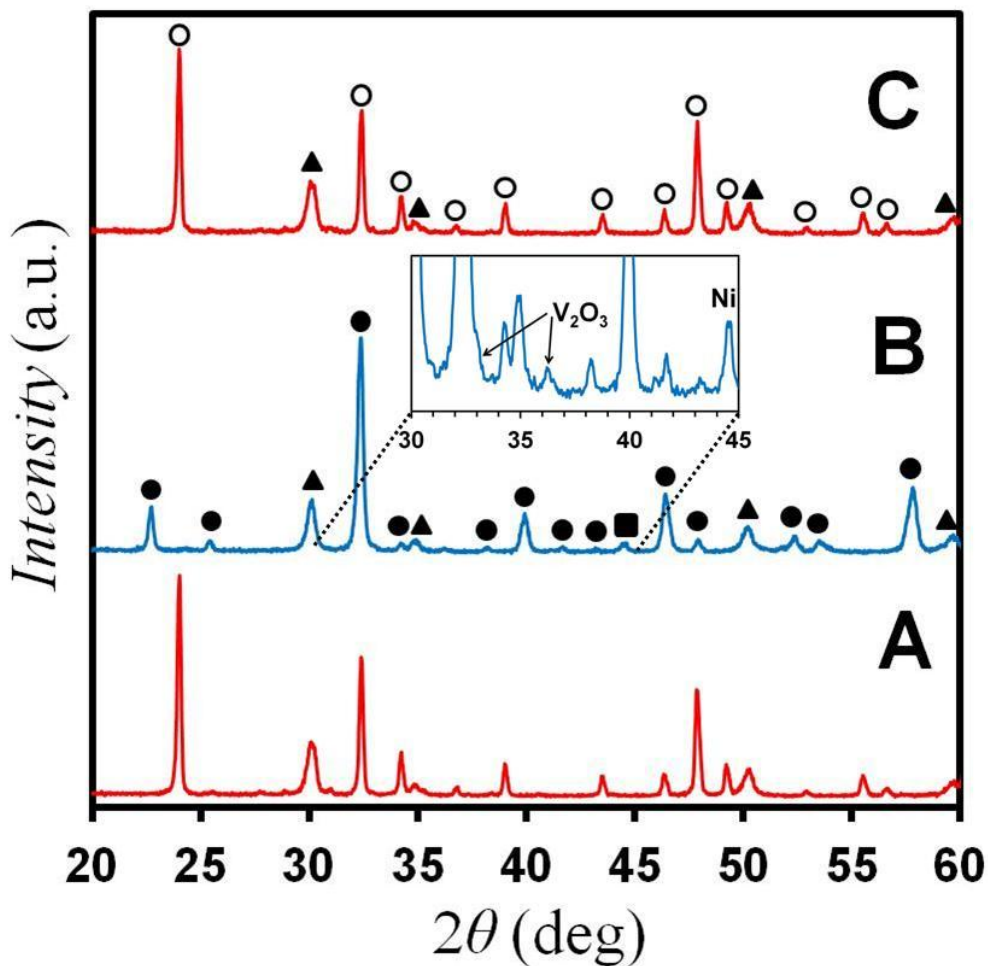


**Figure 5.4:** XRD patterns from a  $\text{Ce}_{0.8}\text{Ni}_{0.2}\text{VO}_{3.90}$  sample that was (A) oxidized at 973 K in air, (B) reduced at 973 K in humidified  $\text{H}_2$ , and (C) re-oxidized in air at 973 K. The peaks are labeled as follows: (▲) cubic YSZ, (○) zircon  $\text{Ce}_{0.8}\text{Ni}_{0.2}\text{VO}_{3.90}$ , (●) perovskite  $\text{Ce}_{1-x}\text{Ni}_x\text{VO}_3$ , and (■) metallic Ni.

Pattern A in Figure 5.4 corresponds to the oxidized sample and contains peaks for the zircon lattice. As shown by pattern B in this figure, significant changes in the diffraction pattern occurred upon reduction of the sample in humidified  $\text{H}_2$ . As expected for reducing conditions, this diffraction pattern contains peaks indicative of a perovskite phase (labeled with ● symbols in the figure). The positions of the peaks for this phase are close to those reported previously for  $\text{CeVO}_3$ <sup>27,35</sup>. As shown in the inset in the figure, small peaks indicative of metallic Ni (44.5 degrees  $2\theta$ ) and  $\text{V}_2\text{O}_3$  (32.9 and 36.2 degrees  $2\theta$ ) are

also present in the diffraction pattern for the reduced sample. These results therefore demonstrate that for cerium nickel vanadate the zircon to perovskite transition which occurs upon exposure to reducing conditions is accompanied by exsolution of at least a portion of the Ni from the lattice. Furthermore, pattern C in Figure 5.4, which was obtained after annealing the reduced sample in air, only contains peaks characteristic of zircon  $\text{Ce}_{0.8}\text{Ni}_{0.2}\text{VO}_{3.90}$  and does not contain peaks indicative of Ni, NiO, or  $\text{Ni}_2\text{V}_2\text{O}_7$ ; thus, demonstrating that the exsolution of the transition metal is reversible upon re-oxidation.

The microstructure of the porous  $\text{Ce}_{0.8}\text{TM}_{0.2}\text{VO}_3$ -YSZ composite electrodes was investigated by SEM with resulting images shown in Figure 5.5.

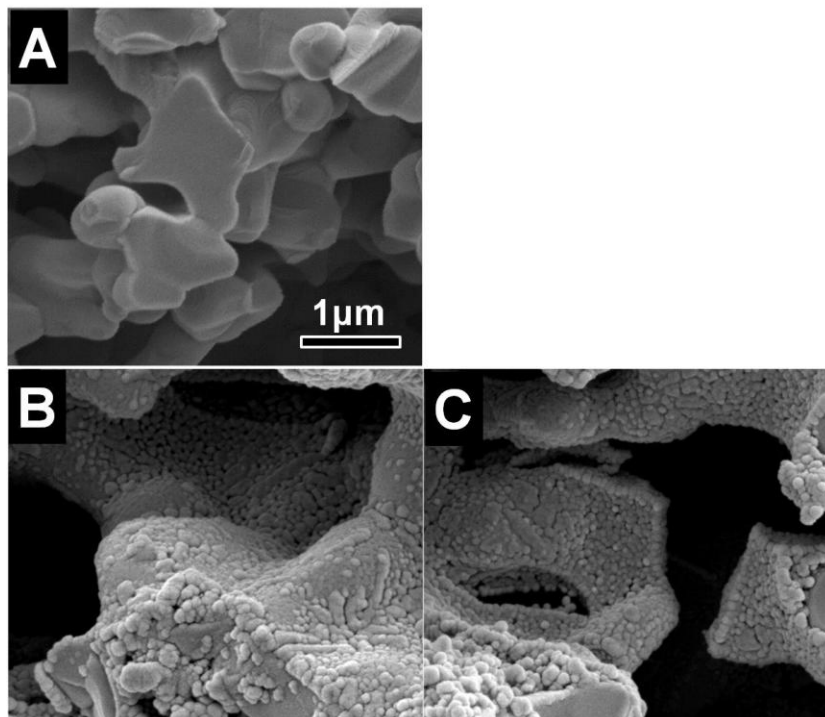


**Figure 5.5:** SEM images of (a) the bare YSZ matrix, and the  $\text{Ce}_{0.8}\text{Ni}_{0.2}\text{VO}_{3.90}$ -YSZ composite (b) oxidized in air at 973 K, and (c) reduced in humidified  $\text{H}_2$  at 973 K.

Panel A in this figure is a micrograph of the porous YSZ prior to infiltration of the vanadate and shows that the YSZ matrix has a sponge-like appearance, with smooth pores ranging in size from 2 to 3  $\mu\text{m}$ . The micrograph in Panel B was obtained after addition of 30 wt. % of  $\text{Ce}_{0.8}\text{Ni}_{0.2}\text{VO}_{3.90}$ , followed by calcination in air at 973 K. The  $\text{Ce}_{0.8}\text{Ni}_{0.2}\text{VO}_{3.90}$  phase consists of what appears to be a relatively dense film composed of individual, interconnected  $\text{Ce}_{0.8}\text{Ni}_{0.2}\text{VO}_{3.90}$  particles that range in size from 10 to 20 nm.

**Table 5.2:** BET surface areas of  $\text{Ce}_{0.8}\text{Ni}_{0.2}\text{VO}_{3.90}$ -YSZ composites.

| <b>Redox Cycle</b> |                 | <b>Surface Area (<math>\text{m}^2\text{g}^{-1}</math>)</b> |
|--------------------|-----------------|--|
| <b>1</b>           | <b>oxidized</b> | <b>0.30</b>  |
|                    | <b>reduced</b>  | <b>1.07</b>  |
| <b>2</b>           | <b>oxidized</b> | <b>0.31</b>  |
|                    | <b>reduced</b>  | <b>1.11</b>  |

The BET surface area for the YSZ scaffold before infiltration of  $\text{Ce}_{0.8}\text{Ni}_{0.2}\text{VO}_{3.90}$  was  $0.22 \text{ m}^2\text{g}^{-1}$ . As shown in Table 5.2, which lists of the BET surface area of the  $\text{Ce}_{0.8}\text{Ni}_{0.2}\text{VO}_{3.90}$ -YSZ composite as a function of oxidation and reduction treatments, the surface area of the freshly-prepared  $\text{Ce}_{0.8}\text{Ni}_{0.2}\text{VO}_{3.90}$ -YSZ composite (redox cycle 1) was  $0.30 \text{ m}^2\text{g}^{-1}$ . The similarity in surface areas of the bare YSZ scaffold ( $0.22 \text{ m}^2\text{g}^{-1}$ ) and the composite is consistent with the infiltrated  $\text{Ce}_{0.8}\text{Ni}_{0.2}\text{VO}_{3.90}$  film being relatively dense.

The SEM image of the  $\text{Ce}_{0.8}\text{Ni}_{0.2}\text{VO}_{3.90}$ -YSZ composite obtained after reduction in humidified  $\text{H}_2$  at 973 K (Panel C, Figure 5.5) was similar to that of the oxidized sample and no significant changes in the microstructure of the vanadate film are readily apparent. In particular, the SEM image does not provide any evidence for the formation

of Ni particles; however, as shown in Table 5.2, reduction did result in a more than three-fold increase in the BET surface area from 0.30 to 1.07 m<sup>2</sup>g<sup>-1</sup>. This result suggests that the Ni that is exsolved during the transition of the vanadate from the zircon to the perovskite phase must be in the form of high surface area nanoparticles that are too small to be resolved in the SEM image.

To further confirm that the transition metal is being exsolved from the lattice under reducing conditions, Ce<sub>0.8</sub>TM<sub>0.2</sub>VO<sub>3</sub>-YSZ composite samples were exposed to dry methane at 973 K for 3 h. Since most transition metals, including Ni and Co, are known to catalyze the formation of carbon filaments (i.e. multi-walled carbon nanotubes), this treatment would be expected to produce such filaments if metal nanoparticles are present on the surface of the vanadate. SEM images obtained after this treatment for CeVO<sub>3</sub>, Ce<sub>0.8</sub>Ni<sub>0.2</sub>VO<sub>3</sub>, Ce<sub>0.8</sub>Co<sub>0.2</sub>VO<sub>3</sub>, and Ce<sub>0.8</sub>Cu<sub>0.2</sub>VO<sub>3</sub> are displayed in Figure 5.6 and the % weight gain for each sample is listed in Table 5.3.

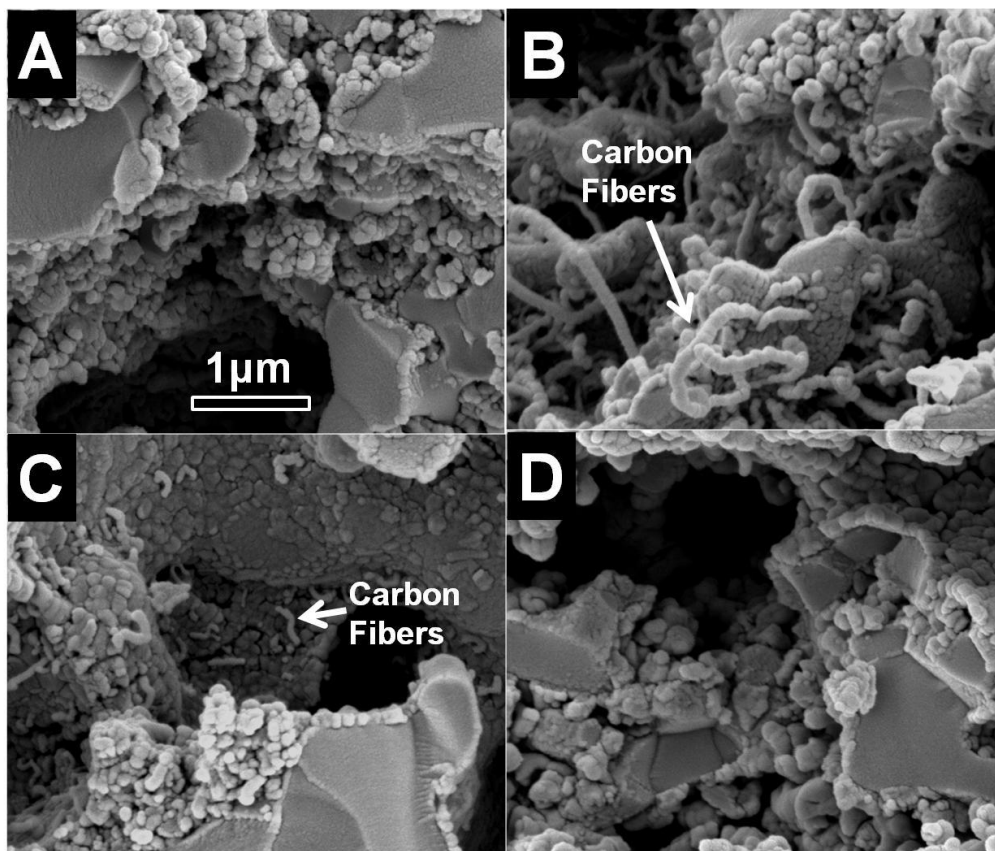


**Figure 5.6:** SEM images of of the (a)  $\text{CeVO}_3$ -, (b)  $\text{Ce}_{0.8}\text{Ni}_{0.2}\text{VO}_3$ -, (c)  $\text{Ce}_{0.8}\text{Co}_{0.2}\text{VO}_3$ -, (d)  $\text{Ce}_{0.8}\text{Cu}_{0.2}\text{VO}_3$  - YSZ composites that had been exposed to dry methane at 973 K for 3 h.

**Table 5.3:** The percentage weight changes measured after reducing the samples in humidified  $\text{H}_2$  at 973 K for 2 h before exposing them to dry methane at 973 K for 3 h.

| Sample                                      | % weight gain after exposure to dry $\text{CH}_4$ at 973 K |
|---|--|
| $\text{Ce}_{0.8}\text{Ni}_{0.2}\text{VO}_3$ | 27   |
| $\text{Ce}_{0.8}\text{Co}_{0.2}\text{VO}_3$ | 10   |
| $\text{Ce}_{0.8}\text{Cu}_{0.2}\text{VO}_3$ | <1   |
| $\text{CeVO}_3$                             | <1   |
| $\text{Ce}_{0.7}\text{Sr}_{0.3}\text{VO}_3$ | <1   |

Panel A in Figure 5.6 corresponds to the CH<sub>4</sub>-treated CeVO<sub>3</sub>-YSZ composite. This image is essentially identical to that obtained prior to CH<sub>4</sub> exposure and does not contain any evidence for carbon deposition. This conclusion is supported by the fact that the weight of this sample changed by less than 1 % after CH<sub>4</sub> exposure.

A significantly different result was obtained for the Ce<sub>0.8</sub>Ni<sub>0.2</sub>VO<sub>3</sub>- (panel B, Fig. 5.6) and Ce<sub>0.8</sub>Co<sub>0.2</sub>VO<sub>3</sub>-YSZ (panel C, Fig. 5.6) composites. For these samples, worm-like features corresponding to carbon filaments are clearly evident in the micrographs. The weight gains for the Ce<sub>0.8</sub>Ni<sub>0.2</sub>VO<sub>3</sub> and Ce<sub>0.8</sub>Co<sub>0.2</sub>VO<sub>3</sub> samples were also 27 and 10 %, respectively, further confirming that carbon deposition has occurred. These results clearly demonstrate the presence of Ni and Co nanoparticles on the surface of these reduced samples. For Ce<sub>0.8</sub>Cu<sub>0.2</sub>VO<sub>3</sub> (panel D, Fig. 5.6), carbon filament formation was not observed, nor was there any weight gain following exposure to CH<sub>4</sub>. As has previously been shown<sup>12,40,41</sup>, Cu is relatively non-catalytic and does not promote carbon filament growth for the conditions used in these experiments; thus, it is likely that Cu nanoparticles were also formed upon reduction of this material.

To investigate the electrochemical performance of the transition-metal doped CeVO<sub>3</sub> in SOFC anodes, button cells were prepared with an 80 μm thick YSZ electrolyte, an infiltrated 30 wt. % Ce<sub>0.8</sub>TM<sub>0.2</sub>VO<sub>3,85</sub>-YSZ composite anode, and a 40 wt. % LSF-YSZ composite cathode. For comparison purposes, cells with an infiltrated CeVO<sub>3</sub> anode were also fabricated. For one of these cell the catalytic activity of the anode was enhanced by the addition of 1 wt. % Pd by infiltration with aqueous solution of (NH<sub>3</sub>)<sub>4</sub>Pd(NO<sub>3</sub>)<sub>2</sub>. In order to produce the conductive phase of the vanadate, the anodes were initially reduced in humidified H<sub>2</sub> at 973 K. V-i polarization curves and impedance spectra for these cells

operated at 973 K in humidified H<sub>2</sub> are shown in Figure 5.7, with the electrochemical performances summarized in Table 5.4.

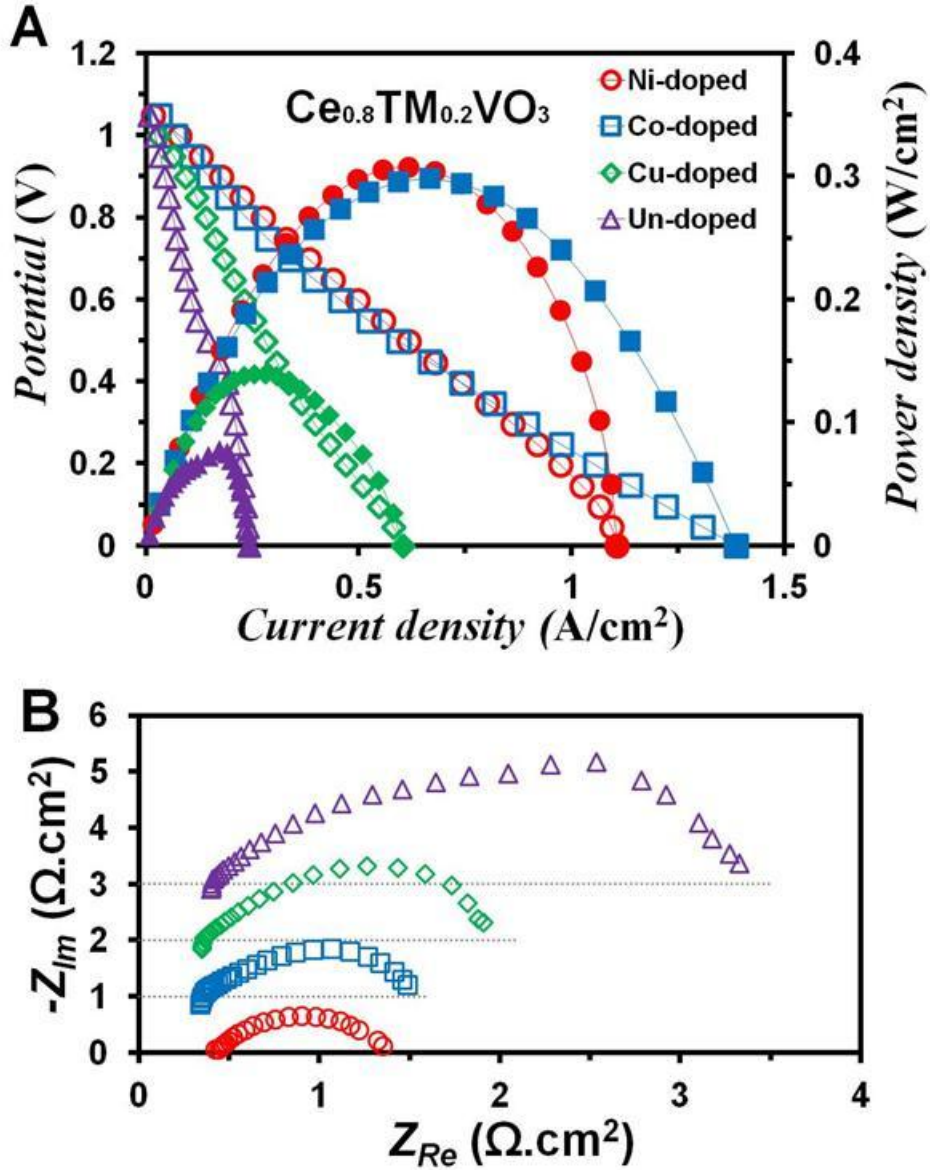


**Figure 5.7:** (a) V-i polarization curves and (b) electrochemical impedance spectra of cells with infiltrated 30 wt. % of (●)  $\text{Ce}_{0.8}\text{Ni}_{0.2}\text{VO}_3$ -, (■)  $\text{Ce}_{0.8}\text{Co}_{0.2}\text{VO}_3$ -, (◆)  $\text{Ce}_{0.8}\text{Cu}_{0.2}\text{VO}_3$ -, and (▲)  $\text{CeVO}_3$ -YSZ anodes. The cells were operated at 973 K with humidified H<sub>2</sub> fuel.

**Table 5.4:** Maximum power density and anode ASR.

| <b>Anode material</b>   | <b>Maximum Power Density<br/>(W cm<sup>-2</sup>)</b> | <b>Anode ASR<br/>(Ω cm<sup>2</sup>)</b> |
|---|--|---|
| <b>Ce<sub>0.8</sub>Ni<sub>0.2</sub>VO<sub>3</sub></b>                 | <b>0.31</b>  | <b>0.8</b>                              |
| <b>Ce<sub>0.8</sub>Co<sub>0.2</sub>VO<sub>3</sub></b>                 | <b>0.30</b>  | <b>0.9</b>                              |
| <b>Ce<sub>0.8</sub>Cu<sub>0.2</sub>VO<sub>3</sub></b>                 | <b>0.14</b>  | <b>1.4</b>                              |
| <b>CeVO<sub>3</sub></b>   | <b>0.07</b>  | <b>2.7</b>                              |
| <b>Ce<sub>0.7</sub>Sr<sub>0.1</sub>Ni<sub>0.2</sub>VO<sub>3</sub></b> | <b>0.31</b>  | <b>0.8</b>                              |

The V-i polarization (Figure 5.7a) curves show that the cells each had an open-circuit potential near the theoretical Nernst value of 1.1 V. The Nyquist plots of the impedance spectra collected at open circuit (Figure 5.7b) also show that the ohmic loss for each cell, calculated from the high-frequency intercept with the real axis, was  $\sim 0.4 \Omega \text{ cm}^2$ , which is close to the expected value for the 80  $\mu\text{m}$  thick YSZ electrolyte layer. This demonstrates that the vanadates provide adequate conductivity for the 50  $\mu\text{m}$  thick anodes used here. As will be discussed below, enhancements in electronic conductivity may be needed, however, if thicker electrodes are used. Since LSF-YSZ cathodes identical to those used here have previously been shown to have an ASR of  $\sim 0.2 \Omega \text{ cm}^2$ <sup>242,43</sup>, the anode ASR can be obtained by subtracting from the total resistance the ohmic ( $0.4 \Omega \text{ cm}^2$ ) and cathode ( $0.2 \Omega \text{ cm}^2$ ) contributions.

Note the relatively poor electrochemical performance obtained from the cells with the CeVO<sub>3</sub>- and Ce<sub>0.8</sub>Cu<sub>0.2</sub>VO<sub>3</sub>-YSZ composite anodes which had maximum current densities (Table 5.4) of only 0.07 and 0.14 W cm<sup>-2</sup> and anode area specific resistances (ASR) of 2.7 and 1.4  $\Omega \text{ cm}^2$ , respectively. This poor performance is indicative of the low



catalytic activity of both  $\text{CeVO}_3$  and Cu. Much better performance was obtained for the cells with  $\text{Ce}_{0.8}\text{Ni}_{0.2}\text{VO}_3$ - and  $\text{Ce}_{0.8}\text{Co}_{0.2}\text{VO}_3$ -YSZ composite anodes. These cells both had maximum power densities of  $0.30 \text{ W cm}^{-2}$  and anode ASR of  $0.9 \Omega \text{ cm}^2$ . This result is consistent with the presence of Ni or Co nanoparticles on the surface of the anode, both of which have high catalytic activity for  $\text{H}_2$  oxidation. It is noteworthy that nearly the same maximum power density was obtained from a cell with a  $\text{CeVO}_3$ -YSZ anode to which 1 wt. % Pd had been added.

While the cell performance and impedance data indicate that for the relatively thin anodes used in this study the  $\text{Ce}_{0.8}\text{TM}_{0.2}\text{VO}_3$ -YSZ composites have adequate electronic conductivity, our previous studies of  $\text{CeVO}_3$ -YSZ composites<sup>34</sup> in Chapter 4 suggest that this may not be the case if thicker anodes, such as those in an anode supported cell, are used. In Chapter 4, we showed that  $\text{CeVO}_3$ -YSZ composites with a structure similar to those used in the present study had an electronic conductivity of only  $0.1 \text{ S/cm}$  at  $973 \text{ K}$ . It was found, however, that doping the cerium vanadate with +2 alkaline earth ions produced compounds with mixed vanadium valence which had much higher electronic conductivity<sup>34</sup>. For example, the conductivity of a  $\text{Ce}_{0.7}\text{Sr}_{0.3}\text{VO}_3$ -YSZ composite was  $9 \text{ S cm}^{-1}$  at  $973 \text{ K}$ . In order to determine if this method of enhancing the electronic conductivity would also work for the transition metal substituted cerium vanadates, we investigated the effect of substituting  $\text{Sr}^{2+}$  and  $\text{Ca}^{2+}$  for a portion of the  $\text{Ce}^{3+}$  in  $\text{Ce}_{0.8}\text{Ni}_{0.2}\text{VO}_3$ .

XRD analysis indicated that upon reduction the Ca- and Sr-substituted vanadates also formed the perovskite phase. The electrical conductivities of reduced  $\text{Ce}_{0.7}\text{AE}_{0.1}\text{Ni}_{0.2}\text{VO}_3$ -YSZ composites in humidified  $\text{H}_2$  are reported in Figure 5.8 as a

function of temperature. For comparison purposes, data for vanadates without Ni substitution are also included in the figure. The samples used in this series of experiments consisted of porous slabs of YSZ (60% porosity) into which 30 wt. % of the vanadate was infiltrated using the method described in the Chapter 2. The use of composites manufactured in this way simplified sample preparation compared to that for bulk samples since high-temperature sintering was not required to produce dense bodies. The porous composites also had structures that closely approximate those used in actual electrochemical devices, such as a SOFC, allowing the conductivity values to be used to predict the properties of real electrodes. Note that the conductivities of the bulk materials would be expected to be at least an order of magnitude higher than those of the composites<sup>30,44,45</sup>. In each case, the samples were held at the measurement temperature for 30 minutes to equilibrate.

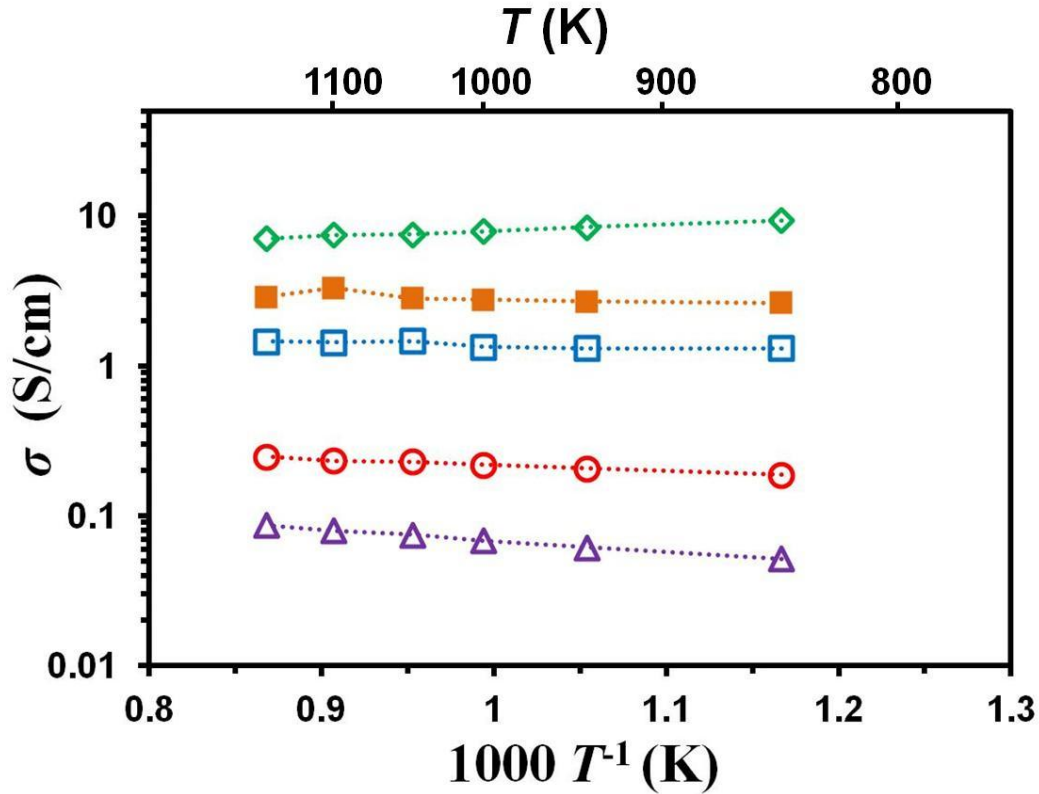


**Figure 5.8:** Electronic conductivities of infiltrated 30 wt. % ( $\Delta$ )  $\text{CeVO}_3$ -, ( $\circ$ )  $\text{Ce}_{0.8}\text{Ni}_{0.2}\text{VO}_3$ -, ( $\square$ )  $\text{Ce}_{0.7}\text{Sr}_{0.1}\text{Ni}_{0.2}\text{VO}_3$ -, ( $\blacksquare$ )  $\text{Ce}_{0.7}\text{Ca}_{0.1}\text{Ni}_{0.2}\text{VO}_3$ -, ( $\diamond$ )  $\text{Ce}_{0.7}\text{Sr}_{0.3}\text{VO}_3$ -YSZ composites in humidified  $\text{H}_2$  as a function of temperature.

As expected, the alkaline earth doped  $\text{Ce}_{0.7}(\text{Sr}/\text{Ca})_{0.1}\text{Ni}_{0.2}\text{VO}_3$ -YSZ composites all exhibited conductivities that were at least an order of magnitude higher than those for the non-calcium or strontium containing analogs. The conductivities at 973 K for the  $\text{Ce}_{0.7}\text{Sr}_{0.1}\text{Ni}_{0.2}\text{VO}_3$ - the  $\text{Ce}_{0.7}\text{Ca}_{0.1}\text{Ni}_{0.2}\text{VO}_3$ -YSZ composites were 2.0 and 3.0  $\text{S cm}^{-1}$ , respectively.

One potential advantage of using transition-metal doped cerium vanadate in SOFC anodes is that these materials may exhibit high redox stability, since the metal reversibly moves in and out of the lattice upon exposure to oxidizing and reducing conditions. In order to test this possibility, a fuel cell with a  $\text{Ce}_{0.7}\text{Sr}_{0.1}\text{Ni}_{0.2}\text{VO}_3$ -YSZ anode was tested and subjected to redox cycling.

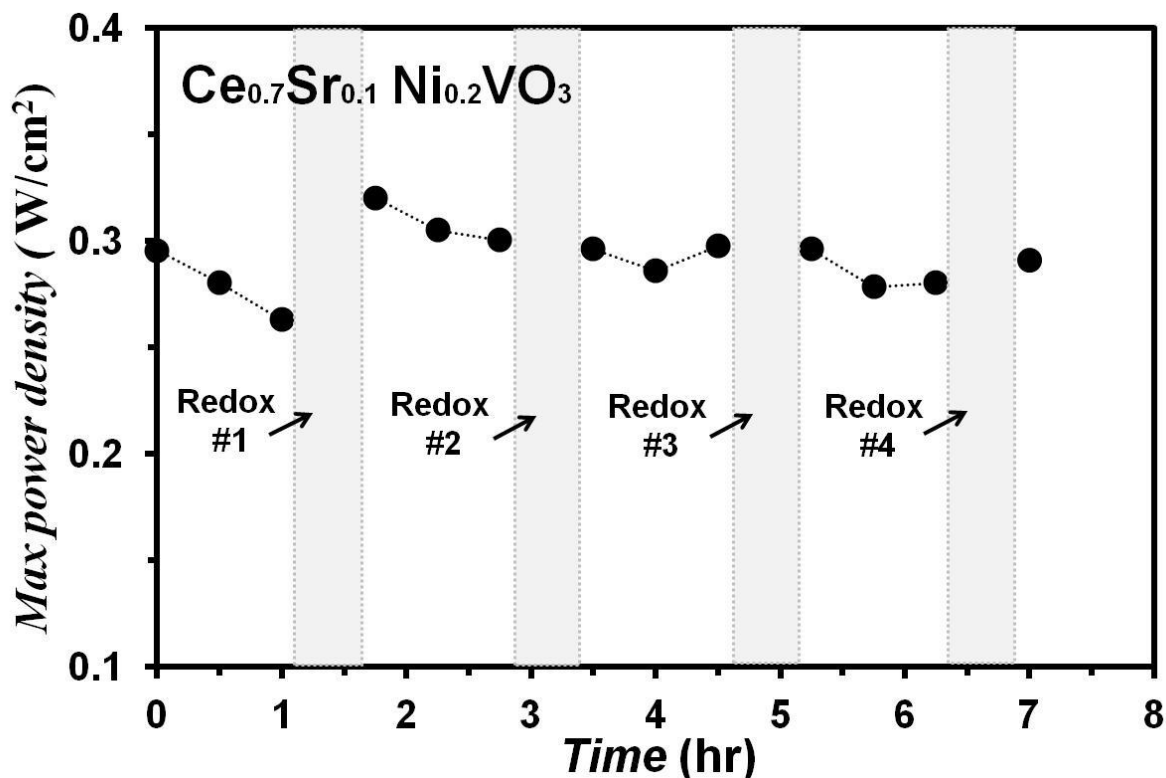


**Figure 5.9:** Maximum power density for a cell with an infiltrated 30 wt. % of  $\text{Ce}_{0.7}\text{Sr}_{0.1}\text{Ni}_{0.2}\text{VO}_3$ -YSZ anode as a function of time at 973 K with humidified  $\text{H}_2$  (3%  $\text{H}_2\text{O}$ ) fuel. The cell was periodically subjected to a redox treatment consisting of oxidation in air for 30 min followed by reduction in humidified  $\text{H}_2$  for 15 min, both at 973 K.

This cell had a maximum power density of  $0.31 \text{ W cm}^{-2}$  at 0.5 V while operating on humidified  $\text{H}_2$  at 973 K. Figure 5.9 displays the maximum power density of this cell as a function of time on stream. During the first hour of operation some degradation in performance is evident with the maximum current density decreasing to  $0.26 \text{ W cm}^{-2}$ . This degradation may be due at least in part to sintering of the exsolved metal nanoparticles. The cell was then subjected to an oxidation treatment which consisted of exposing the anode to air for 30 min followed by reduction in humidified  $\text{H}_2$  for 15 min, both at 973 K. As shown in the figure, this oxidation treatment had no adverse affect on the cell performance with the maximum current density increasing to  $0.33 \text{ W cm}^{-2}$ . The

cell performance was also found to remain relatively stable after several additional redox cycles.

## 5.4 Summary and Conclusion

In this chapter it was demonstrated that upon reduction in humidified hydrogen at 973 K zircon-type  $\text{Ce}_{1-x}\text{TM}_x\text{VO}_{4-0.5x}$  oxides undergo a phase transition to the perovskite structure which is accompanied by exsolution of a portion of the transition metal from the lattice. The exsolved metal forms nanoparticles that decorate the surface of the oxide. Furthermore, this process was demonstrated to be reversible with the metal moving back into the oxide lattice upon exposure to an oxidizing environment at 973 K, resulting in reformation of zircon  $\text{Ce}_{1-x}\text{TM}_x\text{VO}_{4-0.5x}$ . The movement of the transition metal into and out of the lattice upon redox cycling is analogous to previously described intelligent perovskite-based catalysts<sup>9,17-19,21-26</sup>.

The metal exsolution process coupled with the high electronic conductivity of the alkaline earth-doped cerium vanadates makes them particularly attractive for use in SOFC anodes. The electronic conductivity of  $\text{Ce}_{0.7}\text{Sr}_{0.1}\text{Ni}_{0.2}\text{VO}_3$ -YSZ anodes that were synthesized using wet infiltration were found to be in excess of  $1 \text{ S cm}^{-1}$  at 973 K under reducing conditions. The exsolved Ni nanoparticles exhibited high catalytic activity for  $\text{H}_2$  oxidation and a cell with an anode of this design with a 50  $\mu\text{m}$  thick YSZ electrolyte and LSF-YSZ composite anode exhibited a maximum power density of  $0.31 \text{ W cm}^{-2}$  at 973 K. More importantly, the anode in this cell had unusually high redox stability with exposure to air at 973 K not resulting in any performance degradation or mechanical instabilities. These properties suggest that one may be able to use redox cycling to

regenerate any activity loss exhibited by these anodes over time. For example, sintering of the catalytic metal nanoparticles causing loss of reactive surface area and performance degradation could be reversed by an oxidation/reduction cycle in which the metal is re-dissolved into the vanadate during the oxidation treatment, followed by metal nanoparticles being reformed when the anode is exposed to the H<sub>2</sub>-rich reactant stream (shown schematically in Figure 5.1).

It should be noted that while most of the anodes studied in the present investigation were not hydrocarbon tolerant due to the fact that both Co and Ni catalyze the formation of carbon filaments when exposed to hydrocarbons under reducing conditions, the results of this study do suggest a strategy for using the cerium vanadate-based materials to produce hydrocarbon tolerant electrodes. As we have reported previously, SOFC anodes that use Cu-rich, Ni-Cu alloys for both the catalyst and electronically conductive component exhibit high activity and relatively high hydrocarbon tolerance<sup>46-48</sup>. Even higher hydrocarbon tolerance has been obtained for anodes using mixtures of Cu and Co where stable performance while operating on dry methane at 1073 K has been reported<sup>47,49-51</sup>. In this latter case the two metals do not form an alloy, but rather due to copper's low surface free energy, the surface of the metal particles in the anode is enriched in the relatively un-reactive Cu, although enough Co atoms remain exposed to maintain high catalytic activity<sup>47,49-51</sup>. Since in the present investigation we have demonstrated that Cu, Ni, and Co can be substituted into the alkaline earth doped cerium vanadates, it may be possible to synthesize vanadates that contain a mixture of Cu and Co or Cu and Ni. For these materials exsolution of the metals

under reducing conditions may produce catalyst particles with high hydrocarbon tolerance as shown in the next Chapter.

## 5.5 References

- 1 Gross, M. D. *et al.* Redox Stability of  $\text{SrNb}_{(x)}\text{Ti}_{(1-x)}\text{O}_{(3)}$ -YSZ for Use in SOFC Anodes. *J Electrochem Soc* **156**, B540-B545, doi:10.1149/1.3078406 (2009).
- 2 Lee, S., Kim, G., Vohs, J. M. & Gorte, R. J. SOFC anodes based on infiltration of  $\text{La}_{0.3}\text{Sr}_{0.7}\text{TiO}_3$ . *J Electrochem Soc* **155**, B1179-B1183, doi:10.1149/1.2976775 (2008).
- 3 Neagu, D. & Irvine, J. T. S. Structure and Properties of  $\text{La}_{(0.4)}\text{Sr}_{(0.4)}\text{TiO}_{(3)}$  Ceramics for Use as Anode Materials in Solid Oxide Fuel Cells. *Chem Mater* **22**, 5042-5053, doi:10.1021/Cm101508w (2010).
- 4 Vincent, A., Luo, J. L., Chuang, K. T. & Sanger, A. R. Effect of Ba doping on performance of LST as anode in solid oxide fuel cells. *J Power Sources* **195**, 769-774, doi:10.1016/j.jpowsour.2009.08.018 (2010).
- 5 Kim, G., Corre, G., Irvine, J. T. S., Vohs, J. M. & Gorte, R. J. Engineering composite oxide SOFC anodes for efficient oxidation of methane. *Electrochem Solid St* **11**, B16-B19, doi:10.1149/1.2817809 (2008).
- 6 Kim, G. *et al.* Investigation of the Structural and Catalytic Requirements for High-Performance SOFC Anodes Formed by Infiltration of LSCM. *Electrochem Solid St* **12**, B48-B52, doi:10.1149/1.3065971 (2009).
- 7 Tao, S. W. & Irvine, J. T. S. A redox-stable efficient anode for solid-oxide fuel cells. *Nat Mater* **2**, 320-323, doi:10.1038/Nmat871 (2003).
- 8 van den Bossche, M., Matthews, R., Lichtenberger, A. & McIntosh, S. Insights Into the Fuel Oxidation Mechanism of  $\text{La}_{(0.75)}\text{Sr}_{(0.25)}\text{Cr}_{(0.5)}\text{Mn}_{(0.5)}\text{O}_{(3-\delta)}$  SOFC Anodes. *J Electrochem Soc* **157**, B392-B399, doi:10.1149/1.3288374 (2010).



- 9 Kobsiriphat, W., Madsen, B. D., Wang, Y., Marks, L. D. & Barnett, S. A.  $\text{La}_{(0.8)}\text{Sr}_{(0.2)}\text{Cr}_{(1-x)}\text{Ru}_{(x)}\text{O}_{(3-\text{delta})}-\text{Gd}_{(0.1)}\text{Ce}_{(0.9)}\text{O}_{(1.95)}$  solid oxide fuel cell anodes: Ru precipitation and electrochemical performance. *Solid State Ionics* **180**, 257-264, doi:DOI 10.1016/j.ssi.2008.12.022 (2009).
- 10 Adijanto, L., Kungas, R., Park, J., Vohs, J. M. & Gorte, R. J. SOFC anodes based on infiltration of tungsten bronzes. *Int J Hydrogen Energ* **36**, 15722-15730, doi:DOI 10.1016/j.ijhydene.2011.09.059 (2011).
- 11 Smith, B. H. & Gross, M. D. A Highly Conductive Oxide Anode for Solid Oxide Fuel Cells. *Electrochem Solid St* **14**, B1-B5, doi:10.1149/1.3505101 (2011).
- 12 Gorte, R. J., Park, S., Vohs, J. M. & Wang, C. H. Anodes for direct oxidation of dry hydrocarbons in a solid-oxide fuel cell. *Adv Mater* **12**, 1465-1469 (2000).
- 13 Gross, M. D., Vohs, J. M. & Gorte, R. J. An examination of SOFC anode functional layers based on ceria in YSZ. *J Electrochem Soc* **154**, B694-B699, doi:10.1149/1.2736647 (2007).
- 14 Kim, J. S., Nair, V. V., Vohs, J. M. & Gorte, R. J. A study of the methane tolerance of LSCM-YSZ composite anodes with Pt, Ni, Pd and ceria catalysts. *Scripta Mater* **65**, 90-95, doi:DOI 10.1016/j.scriptamat.2010.06.016 (2011).
- 15 Bi, Z. H. & Zhu, J. H. Effect of Current Collecting Materials on the Performance of the Double-Perovskite  $\text{Sr}_{(2)}\text{MgMoO}_{(6-\text{delta})}$  Anode. *J Electrochem Soc* **158**, B605-B613, doi:10.1149/1.3569754 (2011).
- 16 Babaei, A., Zhang, L., Tan, S. L. & Jiang, S. P. Pd-promoted  $(\text{La,Ca})(\text{Cr,Mn})\text{O}_{(3)}/\text{GDC}$  anode for hydrogen and methane oxidation reactions of

- solid oxide fuel cells. *Solid State Ionics* **181**, 1221-1228, doi:DOI 10.1016/j.ssi.2010.06.042 (2010).
- 17 Bierschenk, D. M. *et al.* Pd-substituted  $(\text{La,Sr})\text{CrO}_{(3-\delta)}\text{-Ce}_{(0.9)}\text{Gd}_{(0.1)}\text{O}_{(2-\delta)}$  solid oxide fuel cell anodes exhibiting regenerative behavior. *J Power Sources* **196**, 3089-3094, doi:DOI 10.1016/j.jpowsour.2010.12.050 (2011).
- 18 Madsen, B. D., Kobsiriphat, W., Wang, Y., Marks, L. D. & Barnett, S. A. Nucleation of nanometer-scale electrocatalyst particles in solid oxide fuel cell anodes. *J Power Sources* **166**, 64-67, doi:DOI 10.1016/j.jpowsour.2006.12.080 (2007).
- 19 Wang, Y., Madsen, B. D., Kobsiriphat, W., Barnett, S. A. & Marks, L. D. Electron microscopy study of novel ru doped  $\text{La}_{(0.8)}\text{Sr}_{(0.2)}\text{CrO}_{(3)}$  as anode materials for Solid Oxide Fuel Cells (SOFCs). *Microsc Microanal* **13**, 100-101, doi:Doi 10.1017/S1431927607075125 (2007).
- 20 Xiao, G. L., Jin, C., Liu, Q., Heyden, A. & Chen, F. L. Ni modified ceramic anodes for solid oxide fuel cells. *J Power Sources* **201**, 43-48, doi:DOI 10.1016/j.jpowsour.2011.10.103 (2012).
- 21 Kobsiriphat, W. *et al.* Nickel- and Ruthenium-Doped Lanthanum Chromite Anodes: Effects of Nanoscale Metal Precipitation on Solid Oxide Fuel Cell Performance. *J Electrochem Soc* **157**, B279-B284, doi:Doi 10.1149/1.3269993 (2010).
- 22 Nishihata, Y. *et al.* Self-regeneration of a Pd-perovskite catalyst for automotive emissions control. *Nature* **418**, 164-167, doi:Doi 10.1038/Nature00893 (2002).

- 23 Tan, I. *et al.* The self-regenerative "intelligent" catalyst for automotive emissions control. *Science of Engineering Ceramics Iii* **317-318**, 833-836 (2006).
- 24 Tanaka, H. *et al.* Self-regenerating Rh- and Pt-based perovskite catalysts for automotive-emissions control. *Angew Chem Int Edit* **45**, 5998-6002, doi:DOI 10.1002/anie.200503938 (2006).
- 25 Tanaka, H. *et al.* Intelligent catalyst having the self-regenerative function of Pd, Rh and Pt for automotive emissions control. *Catal Today* **117**, 321-328, doi:DOI 10.1016/j.cattod.2006.05.029 (2006).
- 26 Taniguchi, M. *et al.* The self-regenerative Pd-, Rh-, and Pt-perovskite catalysts. *Top Catal* **42-43**, 367-371, doi:DOI 10.1007/s11244-007-0207-x (2007).
- 27 Danilovic, N., Luo, J. L., Chuang, K. T. & Sanger, A. R. Ce<sub>(0.9)</sub>Sr<sub>(0.1)</sub>VO<sub>(x)</sub> (x=3, 4) as anode materials for H<sub>(2)</sub>S-containing CH<sub>(4)</sub> fueled solid oxide fuel cells. *J Power Sources* **192**, 247-257, doi:DOI 10.1016/j.jpowsour.2009.03.045 (2009).
- 28 Cooper, M., Channa, K., De Silva, R. & Bayless, D. J. Comparison of LSV/YSZ and LSV/GDC SOFC Anode Performance in Coal Syngas Containing H<sub>(2)</sub>S. *J Electrochem Soc* **157**, B1713-B1718, doi:Doi 10.1149/1.3489380 (2010).
- 29 Peng, C., Luo, J. L., Sanger, A. R. & Chuang, K. T. Sulfur-Tolerant Anode Catalyst for Solid Oxide Fuel Cells Operating on H<sub>(2)</sub>S-Containing Syngas. *Chem Mater* **22**, 1032-1037, doi:Doi 10.1021/Cm901910p (2010).
- 30 Park, J. S. *et al.* A high-performance solid oxide fuel cell anode based on lanthanum strontium vanadate. *J Power Sources* **196**, 7488-7494, doi:DOI 10.1016/j.jpowsour.2011.05.028 (2011).

- 31 Cheng, Z., Zha, S. W., Aguilar, L. & Liu, M. L. Chemical, electrical, and thermal properties of strontium doped lanthanum vanadate. *Solid State Ionics* **176**, 1921-1928, doi:DOI 10.1016/j.ssi.2005.05.009 (2005).
- 32 Petit, C. T. G., Lan, R., Cowin, P. I., Kraft, A. & Tao, S. W. Structure, conductivity and redox stability of solid solution  $Ce_{1-x}Ca_xVO_4$  ( $0 \leq x \leq 0.4125$ ). *J Mater Sci* **46**, 316-326, doi:DOI 10.1007/s10853-010-4812-x (2011).
- 33 Petit, C. T. G., Lan, R., Cowin, P. I., Irvine, J. T. S. & Tao, S. W. Novel redox reversible oxide, Sr-doped cerium orthovanadate to metavanadate. *J Mater Chem* **21**, 525-531, doi:Doi 10.1039/C0jm02669g (2011).
- 34 Adijanto, L., Balaji Padmanabhan, V., Holmes, K. J., Gorte, R. J. & Vohs, J. M. Physical and electrochemical properties of alkaline earth doped, rare earth vanadates. *J Solid State Chem*, doi:doi:10.1016/j.jssc.2012.01.065 (2012).
- 35 Tsipis, E. V., Kharton, V. V., Vyshatko, N. P., Shaula, A. L. & Frade, J. R. Stability and oxygen ionic conductivity of zircon-type  $Ce_{(1-x)}A_{(x)}VO_{(4+\delta)}$  ( $A = Ca, Sr$ ). *J Solid State Chem* **176**, 47-56, doi:Doi 10.1016/S0022-4596(03)00342-6 (2003).
- 36 Park, S., Gorte, R. J. & Vohs, J. M. Tape cast solid oxide fuel cells for the direct oxidation of hydrocarbons. *J Electrochem Soc* **148**, A443-A447 (2001).
- 37 Kungas, R., Kim, J. S., Vohs, J. M. & Gorte, R. J. Restructuring Porous YSZ by Treatment in Hydrofluoric Acid for Use in SOFC Cathodes. *J Am Ceram Soc* **94**, 2220-2224, doi:DOI 10.1111/j.1551-2916.2010.04359.x (2011).

- 38 Watanabe, A. Highly conductive oxides,  $\text{CeVO}_4$ ,  $\text{Ce}_{1-x}\text{M}_x\text{VO}_{4-0.5x}$  ( $\text{M} = \text{Ca}, \text{Sr}, \text{Pb}$ ) and  $\text{Ce}_{1-y}\text{Bi}_y\text{VO}_4$ , with zircon-type structure prepared by solid-state reaction in air. *J Solid State Chem* **153**, 174-179, doi:DOI 10.1006/jssc.2000.8773 (2000).
- 39 Devan, R. S., Kolekar, Y. D. & Chougule, B. K. Effect of cobalt substitution on the properties of nickel-copper ferrite. *J Phys-Condens Mat* **18**, 9809-9821, doi:Doi 10.1088/0953-8984/18/43/004 (2006).
- 40 McIntosh, S. & Gorte, R. J. Direct hydrocarbon solid oxide fuel cells. *Chem Rev* **104**, 4845-4865, doi:Doi 10.1021/Cr020725g (2004).
- 41 Gorte, R. J., Vohs, J. M. & McIntosh, S. Recent developments on anodes for direct fuel utilization in SOFC. *Solid State Ionics* **175**, 1-6, doi:DOI 10.1016/j.ssi.2004.09.036 (2004).
- 42 Wang, W. S., Gross, M. D., Vohs, J. M. & Gorte, R. J. The stability of LSF-YSZ electrodes prepared by infiltration. *J Electrochem Soc* **154**, B439-B445, doi:10.1149/1.2709510 (2007).
- 43 Vohs, J. M., Adijanto, L., Kungas, R., Bidrawn, F. & Gorte, R. J. Stability and performance of infiltrated  $\text{La}_{(0.8)}\text{Sr}_{(0.2)}\text{Co}_{(x)}\text{Fe}_{(1-x)}\text{O}_{(3)}$  electrodes with and without  $\text{Sm}_{(0.2)}\text{Ce}_{(0.8)}\text{O}_{(1.9)}$  interlayers. *J Power Sources* **196**, 5797-5802, doi:10.1016/j.jpowsour.2011.03.022 (2011).
- 44 Fang, X. H., Zhu, G. Y., Xia, C. R., Liu, X. Q. & Meng, G. Y. Synthesis and properties of Ni-SDC cermets for IT-SOFC anode by co-precipitation. *Solid State Ionics* **168**, 31-36 (2004).

- 45 Zhu, W. Z. & Deevi, S. C. A review on the status of anode materials for solid oxide fuel cells. *Mat Sci Eng a-Struct* **362**, 228-239, doi:Doi 10.1016/S0921-5093(03)00620-8 (2003).
- 46 Jung, S., Gross, M. D., Gorte, R. J. & Vohs, J. M. Electrodeposition of Cu into a highly porous Ni/YSZ cermet. *J Electrochem Soc* **153**, A1539-A1543, doi:Doi 10.1149/1.2208908 (2006).
- 47 Lee, S. I., Vohs, J. M. & Gorte, R. J. A study of SOFC anodes based on Cu-Ni and Cu-Co bimetallics in CeO<sub>2</sub>-YSZ. *J Electrochem Soc* **151**, A1319-A1323, doi:Doi 10.1149/1.1774184 (2004).
- 48 Kim, H., Lu, C., Worrell, W. L., Vohs, J. M. & Gorte, R. J. Cu-Ni cermet anodes for direct oxidation of methane in solid-oxide fuel cells. *J Electrochem Soc* **149**, A247-A250, doi:10.1149/1.1445170 (2002).
- 49 Lee, S. I., Ahn, K., Vohs, J. M. & Gorte, R. J. Cu-Co bimetallic anodes for direct utilization of methane in SOFCs. *Electrochem Solid St* **8**, A48-A51, doi:Doi 10.1149/1.1833678 (2005).
- 50 Jung, S. W., Vohs, J. M. & Gorte, R. J. Preparation of SOFC anodes by Electrodeposition. *J Electrochem Soc* **154**, B1270-B1275, doi:Doi 10.1149/1.2790280 (2007).
- 51 Gross, M. D., Vohs, J. M. & Gorte, R. J. A study of thermal stability and methane tolerance of Cu-based SOFC anodes with electrodeposited Co. *Electrochim Acta* **52**, 1951-1957, doi:DOI 10.1016/j.electacta.2006.08.005 (2007).

## Chapter 6. Polarization-Induced Hysteresis in (CuCo)-Doped Rare Earth Vanadates SOFC Anodes\*

### Summary

The physical and electrochemical properties of strontium substituted cerium vanadates in which a portion of the cerium cations have been substituted with transition metals ( $\text{Ce}_{0.8}\text{Sr}_{0.1}\text{Cu}_{0.05}\text{TM}_{0.05}\text{VO}_{4-0.5x}$ , TM = Ni or Co) were investigated and their suitability for use in solid oxide fuel cell (SOFC) anodes was assessed. Upon reduction at elevated temperature, Cu and Co or Cu and Ni were exsolved from the electronically conductive  $\text{Ce}_{1-x}\text{Sr}_x\text{VO}_4$  lattice to produce Cu-Ni and Cu-Co catalytic nanoparticles. The  $\text{Ce}_{0.8}\text{Sr}_{0.1}\text{Cu}_{0.05}\text{Co}_{0.05}\text{VO}_3$  appears to have high activity and relatively high hydrocarbon tolerance, suggesting that intimate contact between the exsolved Cu and Co and that the majority of the Co nanoparticles must be at least partially coated with the Cu. The electrochemical performance when used in anodes operating on hydrogen has been characterized, and the results demonstrate the exsolution of both metals from the host lattice; but observed dynamic changes in the structure of the resulting metal nanoparticles as a function of SOFC operating conditions complicate their use in SOFC anodes.

---

\* This chapter was published as a research paper in the Journal of the Electrochemical Society, 159(11) (2012) F751. Copyright: 2012, The Electrochemical Society.

## 6.1 Introduction

In the previous chapter (chapter 5), we demonstrated that enhanced catalytic activity of ceramic-based anodes can be achieved by using materials for which the metal nanoparticle catalysts can be generated *in situ* through their exsolution from a conducting perovskite host<sup>1-12</sup>. Under mildly reducing conditions the easily reduced noble metal cations are exsolved from the lattice and precipitate as nanoparticles that decorate the surface of the perovskite. This in turn greatly enhanced the performance of electrodes based on this material since redox cycling could be used in an SOFC to regenerate any metal surface area loss due to sintering. Therefore, this approach provides a novel strategy for both optimizing the catalytic properties of ceramic anodes for SOFC for specific fuels and for maintaining long-term performance.

$\text{RE}_{1-x}\text{AE}_x\text{VO}_4$  anodes doped with Co or Ni (used as a composite with YSZ) have been shown to exhibit high electrochemical activity and unusually high redox stability, with the latter property being partially due to the exsolution/dissolution of the catalytic metals. These anodes, however, are not hydrocarbon stable since both Ni and Co catalyze carbon formation<sup>1</sup>. It has previously been shown in studies of anodes with a more conventional design that the propensity for Ni and Co to catalyze coke deposition can be ameliorated by alloying with a less reactive metal, such as Cu, while still maintaining high oxidation activity<sup>13-19</sup>. Particles composed of Ni and Cu, form a solid solution so that both Cu and Ni remain at the surface. Based on previous work, Cu-Ni alloys exposed to dry methane still formed significant amounts of carbon up to alloy compositions of 20 % Ni. Unlike Cu-Ni alloys, the Cu and Co in Cu-Co mixtures remain as separate phases, with the surface enriched in Cu due to its lower surface free energy. The low activity for



C-C bond breaking and forming on Cu causes these particles to have a lower activity for coke formation, even for compositions with high Co:Cu ratios. Enough of the more active metal remains exposed, however, to allow relatively high catalytic activity for oxidation reactions to be maintained.

In this chapter, we have explored the possibility of doping  $RE_{1-x}AE_xVO_4$  with both Cu and Co or Cu and Ni and using the exsolution phenomena described above as an *in situ* means to synthesize Cu-Ni and Cu-Co catalytic nanoparticles, with the goal of using these materials to produce high-performance, highly robust SOFC anodes that can directly utilize hydrocarbon-based fuels. Specific materials that have been studied include  $Ce_{0.8}Sr_{0.1}Cu_{0.05}Co_{0.05}VO_3$  and  $Ce_{0.8}Sr_{0.1}Cu_{0.05}Ni_{0.05}VO_3$ . The exsolution of the metals from these materials and their electrochemical performance when used in anodes operating on hydrogen have been characterized. Preliminary studies of their hydrocarbon stability are also reported. The results obtained in this study demonstrate the exsolution of both metals from the host lattice, but observed dynamic changes in the structure of the resulting metal nanoparticles as a function of SOFC operating conditions complicate their use in SOFC anodes.

## 6.2 Experimental

Bulk  $Ce_{0.8}Sr_{0.1}Cu_{0.05}TM_{0.05}VO_{4-\delta}$  powders were used for XRD analysis and (where TM = Ni, Co) were prepared using an aqueous precursor solution containing the appropriate amounts of  $Ce(NO_3)_3 \cdot 6H_2O$  (Alfa Aesar, 99.5%),  $Sr(NO_3)_2$  (Alfa Aesar, 99.9%),  $NH_4VO_3$  (Aldrich, 99+ %), and either  $Ni(NO_3)_2 \cdot 6H_2O$ ,  $Co(NO_3)_2 \cdot 6H_2O$ , or  $Cu(NO_3)_2 \cdot 3H_2O$  (Alfa Aesar, 99.9%). Citric acid (Fisher Scientific) was also added as a

complexing agent to aid in the formation of a more homogeneous mixture. The precursor solution was dried and the resulting powder was calcined at 973 K in air to form the zircon phase. Perovskite  $\text{Ce}_{0.8}\text{Sr}_{0.1}\text{Cu}_{0.05}\text{TM}_{0.05}\text{VO}_3$  materials were produced by reducing the  $\text{Ce}_{0.8}\text{Sr}_{0.1}\text{Cu}_{0.05}\text{TM}_{0.05}\text{VO}_{4-\delta}$  in humidified  $\text{H}_2$  (3%  $\text{H}_2\text{O}$ ) at 973 K.

Porous YSZ slabs into which 30 wt. %  $\text{Ce}_{0.8}\text{Sr}_{0.1}\text{Cu}_{0.05}\text{TM}_{0.05}\text{VO}_{4-\delta}$  had been infiltrated were used for hydrocarbon stability measurements. The porous, 4 mm x 4 mm x 15 mm YSZ slabs were prepared using methods that have been described in Chapter 2<sup>20,21</sup>. The vanadates were added to the porous YSZ slabs by infiltrating the aqueous precursor solution followed by drying and annealing in air at 973 K. Multiple infiltration/annealing cycles were used to obtain the desired 30 wt. % loading. The stability of the vanadates in hydrocarbons was assessed by exposing  $\text{Ce}_{0.8}\text{Sr}_{0.1}\text{Cu}_{0.05}\text{TM}_{0.05}\text{VO}_3/\text{YSZ}$  composites under humidified  $\text{H}_2$  (3%  $\text{H}_2\text{O}$ ) for 3 h at 1073 K before exposing them to dry methane at 1073 K for 3 h and measuring their weight gain resulting from carbon deposition. The morphological structure of the porous composites was determined using scanning electron microscopy (SEM) (FEI Quanta 600 ESEM) and X-ray diffraction (XRD) using  $\text{Cu K}_\alpha$  radiation. For the XRD measurements, a small amount of YSZ was physically mixed with the oxides to act as a reference.

Solid oxide fuel cells 1-cm in diameter were used in all fuel cell measurements. These cells were fabricated using porous-dense-porous tri-layer YSZ wafers that were produced using tape casting methods that have been described in Chapter 2<sup>20</sup>. For each cell, the dense electrolyte layer was 65- $\mu\text{m}$  thick and 1-cm in diameter. The 60 % porous YSZ layers on each side of the dense electrolyte layer were 50- $\mu\text{m}$  thick with a BET surface area 0.3  $\text{m}^2\text{g}^{-1}$ . The cathodes were prepared following the procedure detailed in

Chapter 2. Once the perovskite loading was 40 wt. %, the cathode was calcined to 1123 K for 4 h to form the perovskite structure. Previous studies have shown that cathodes of this design have an ASR of  $\sim 0.15 \Omega \text{ cm}^2$  in air at 973 K<sup>22,23</sup>. The  $\text{Ce}_{0.8}\text{Sr}_{0.1}\text{Cu}_{0.05}\text{TM}_{0.05}\text{VO}_3$  anode was synthesized in a similar manner except that a 30 wt. % loading was used and it was calcined to only 973 K. The anode was reduced in humidified  $\text{H}_2$  (3%  $\text{H}_2\text{O}$ ) at 973 K prior to cell testing. Silver paste current collectors were applied to both electrodes and the cells were mounted onto an alumina tube using a ceramic adhesive (Aremco, Ceramabond 552). All the cell tests were performed with the cathode exposed to ambient air and the anode exposed to humidified  $\text{H}_2$ . Electrochemical impedance spectra were measured between 0.1 Hz and 300 kHz with a 1 mA AC perturbation. Both impedance spectra and V-i polarization curves were measured using a Gamry Instruments potentiostat.

### 6.3 Results and Discussion

XRD was used to determine the phase composition of the Cu and Co or Cu and Ni vanadates following various pretreatments. XRD patterns for (A)  $\text{Ce}_{0.8}\text{Sr}_{0.1}\text{Cu}_{0.05}\text{Co}_{0.05}\text{VO}_{4-\delta}$  and (B)  $\text{Ce}_{0.8}\text{Sr}_{0.1}\text{Cu}_{0.05}\text{Ni}_{0.05}\text{VO}_{4-\delta}$  samples that were calcined in air at 973 K for 2 h are presented in Figure 6.1.

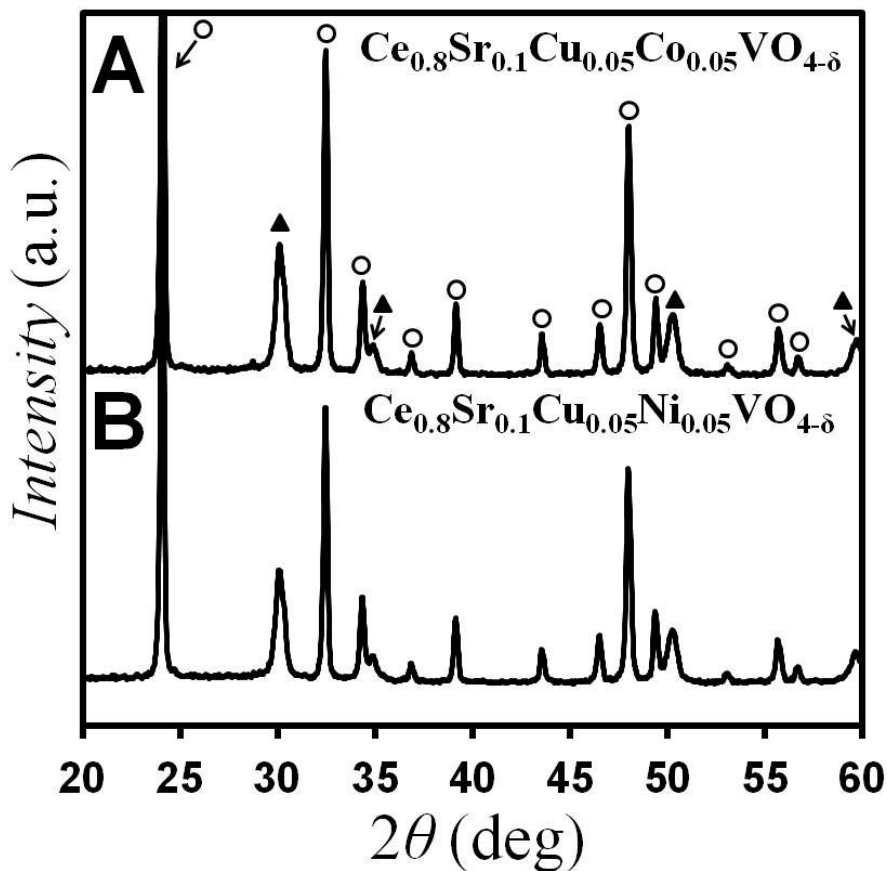


**Figure 6.1:** XRD patterns of (A)  $\text{Ce}_{0.8}\text{Sr}_{0.1}\text{Cu}_{0.05}\text{Co}_{0.05}\text{VO}_{4-\delta}$ , and (B)  $\text{Ce}_{0.8}\text{Sr}_{0.1}\text{Cu}_{0.05}\text{Ni}_{0.05}\text{VO}_{4-\delta}$  oxidized at 973 K in air. The peaks are labeled as follows: (▲) cubic YSZ, (○) zircon  $\text{Ce}_{0.8}\text{Sr}_{0.1}\text{Cu}_{0.05}\text{Co}_{0.05}\text{VO}_{4-\delta}$  and  $\text{Ce}_{0.8}\text{Sr}_{0.1}\text{Cu}_{0.05}\text{Ni}_{0.05}\text{VO}_{4-\delta}$ .

The zircon structure of  $\text{Ce}_{0.8}\text{Sr}_{0.1}\text{Cu}_{0.05}\text{Co}_{0.05}\text{VO}_{4-\delta}$  and  $\text{Ce}_{0.8}\text{Sr}_{0.1}\text{Cu}_{0.05}\text{Ni}_{0.05}\text{VO}_{4-\delta}$  was confirmed by the presence of the expected diffraction peaks near 24.0, 32.4, 34.1, 36.4, 38.9, 43.2, 46.1, and 48.0 degrees  $2\theta$ <sup>24,25</sup>. The XRD patterns are comprised of peaks that correspond only to  $\text{Ce}_{0.8}\text{Sr}_{0.1}\text{Cu}_{0.05}\text{Co}_{0.05}\text{VO}_{4-\delta}$  and  $\text{Ce}_{0.8}\text{Sr}_{0.1}\text{Cu}_{0.05}\text{Ni}_{0.05}\text{VO}_{4-\delta}$  and do not contain any peaks indicative of other oxide phases including  $\text{TM}_2\text{V}_2\text{O}_7$  (where TM = Ni, Co, or Cu), thus demonstrating that the single phase vanadates were formed.

As noted above, the transition metal doped vanadates undergo a phase change from the zircon structure to the perovskite structure upon reduction, with a portion of the metals being exsolved from the lattice<sup>1</sup>. This is demonstrated by the XRD patterns in

Figure 6.2 for (A)  $\text{Ce}_{0.8}\text{Sr}_{0.1}\text{Cu}_{0.05}\text{Co}_{0.05}\text{VO}_3$  and (B)  $\text{Ce}_{0.8}\text{Sr}_{0.1}\text{Cu}_{0.05}\text{Ni}_{0.05}\text{VO}_3$  samples that were reduced in humidified  $\text{H}_2$  at 973 K. For comparison purposes, XRD patterns for reduced vanadates that contain only one of the transition metals ((C)  $\text{Ce}_{0.8}\text{Sr}_{0.1}\text{Ni}_{0.1}\text{VO}_3$ , (D)  $\text{Ce}_{0.8}\text{Sr}_{0.1}\text{Co}_{0.1}\text{VO}_3$ , and (E)  $\text{Ce}_{0.8}\text{Sr}_{0.1}\text{Cu}_{0.1}\text{VO}_3$ ) are also included in the figure.

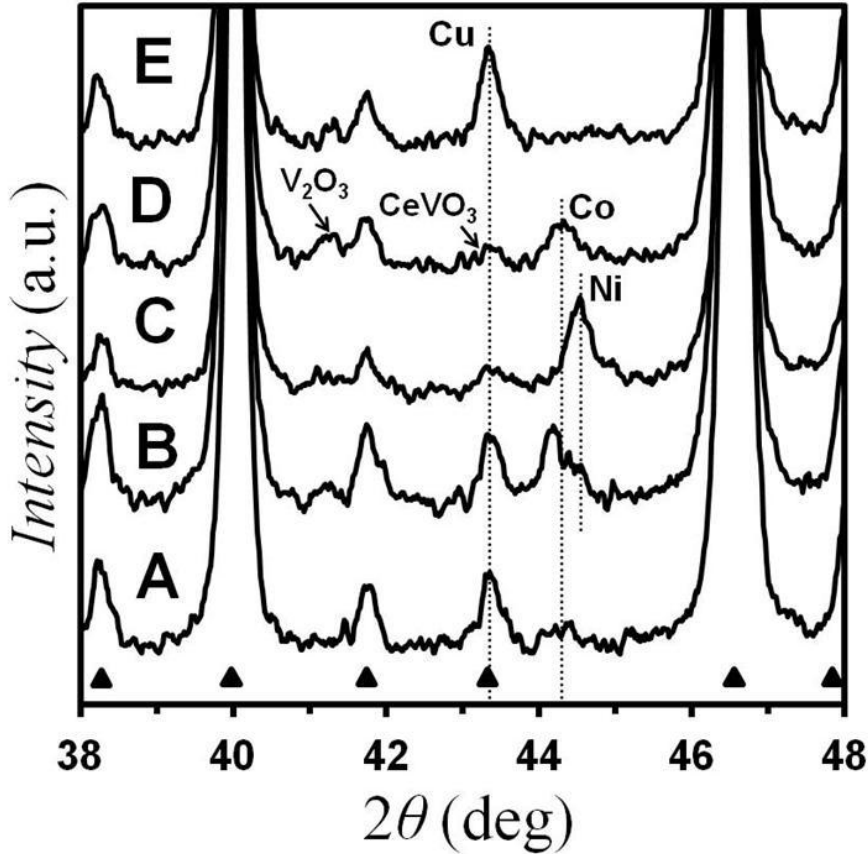


**Figure 6.2:** XRD patterns of (A)  $\text{Ce}_{0.8}\text{Sr}_{0.1}\text{Cu}_{0.05}\text{Co}_{0.05}\text{VO}_3$ , (B)  $\text{Ce}_{0.8}\text{Sr}_{0.1}\text{Cu}_{0.05}\text{Ni}_{0.05}\text{VO}_3$ , (C)  $\text{Ce}_{0.8}\text{Sr}_{0.1}\text{Ni}_{0.1}\text{VO}_3$ , (D)  $\text{Ce}_{0.8}\text{Sr}_{0.1}\text{Co}_{0.1}\text{VO}_3$ , and (E)  $\text{Ce}_{0.8}\text{Sr}_{0.1}\text{Cu}_{0.1}\text{VO}_3$  reduced under humidified  $\text{H}_2$  at 973 K. The dotted lines indicate the position of the Ni, Co, and Cu metal peaks. The (▲) peaks correspond to Sr doped-CeVO<sub>3</sub>.

The large peaks at 40.1 and 46.7 degrees  $2\theta$  are indicative of the perovskite phase. Peaks corresponding to the bulk transition metals are also apparent between 43 and 45 degrees  $2\theta$  for each sample. The positions of the expected peak for each metal are indicated in the figure. Note that the Cu diffraction peak overlaps with one of the minor peaks for the perovskite vanadate. The presence of peaks indicative of the transition metals in each

pattern further demonstrates that the phase transition from zircon to perovskite is accompanied by the exsolution of the transition metals from the lattice.

Note that the XRD pattern for  $\text{Ce}_{0.8}\text{Sr}_{0.1}\text{Cu}_{0.05}\text{Co}_{0.05}\text{VO}_3$  (pattern A) contains peaks indicative of both Cu and Co, thereby demonstrating that both metals have been exsolved from the host oxide lattice upon reduction. Similarly, the pattern for  $\text{Ce}_{0.8}\text{Sr}_{0.1}\text{Cu}_{0.05}\text{Ni}_{0.05}\text{VO}_3$  (pattern B) contains peaks for both Cu and Ni. For this sample an additional peak is also present at 44.2 degrees  $2\theta$ . Unlike Cu and Co, Cu and Ni are miscible<sup>14,17,18</sup>. We therefore assign the peak at 44.2 degrees  $2\theta$  to the formation of Cu-Ni alloy particles. Although particles with a range of compositions are likely to have been formed, the 44.2 degrees  $2\theta$  peak position is consistent with a 50:50 Cu:Ni alloy composition<sup>18</sup>.

While the exsolved metals would be expected to enhance the catalytic activity of an SOFC anode made with these materials, as discussed in the introduction, intimate contact between the Cu and the Co or Ni will be required to produce catalysts that do not undergo severe coking upon exposure to hydrocarbons. To assess whether this can be achieved for transition metal decorated surfaces produced by reduction of  $\text{Ce}_{0.8}\text{Sr}_{0.1}\text{Cu}_{0.05}\text{Co}_{0.05}\text{VO}_3$  and  $\text{Ce}_{0.8}\text{Sr}_{0.1}\text{Cu}_{0.05}\text{Ni}_{0.05}\text{VO}_3$ , we exposed porous composites of these materials with YSZ to dry methane at 1073 K for 3 h. SEM images of these samples after this treatment are displayed in Figure 6.3. For comparison purposes, images obtained from reduced  $\text{Ce}_{0.8}\text{Sr}_{0.1}\text{Cu}_{0.1}\text{VO}_3$ -YSZ and  $\text{Ce}_{0.8}\text{Sr}_{0.1}\text{Co}_{0.1}\text{VO}_3$ -YSZ composites subjected to the same treatment are also included in the figure. The weight gain for each sample after the hydrocarbon treatment is listed in Table 6.1.

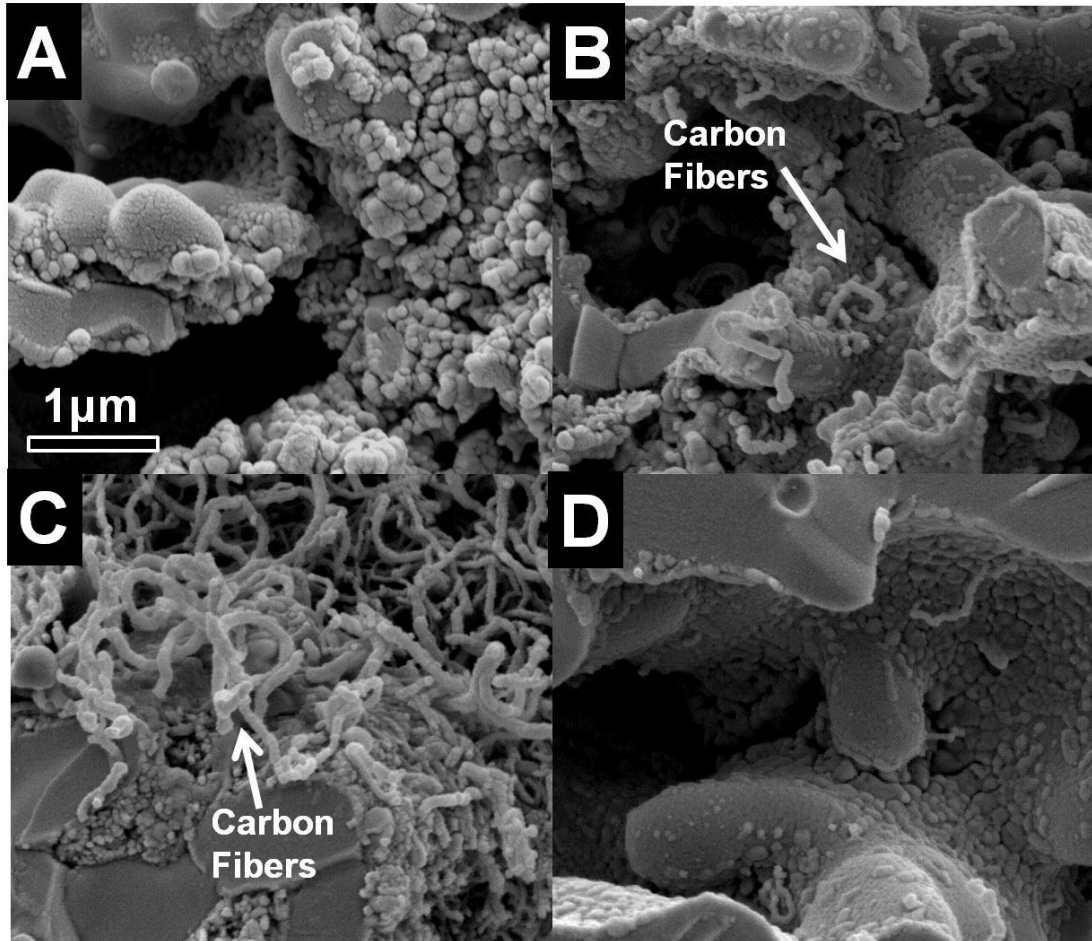


**Figure 6.3:** SEM images of the (A)  $\text{Ce}_{0.8}\text{Sr}_{0.1}\text{Cu}_{0.1}\text{VO}_3^-$ , (B)  $\text{Ce}_{0.8}\text{Sr}_{0.1}\text{Co}_{0.1}\text{VO}_3^-$ , (C)  $\text{Ce}_{0.8}\text{Sr}_{0.1}\text{Cu}_{0.05}\text{Ni}_{0.05}\text{VO}_3^-$ , (D)  $\text{Ce}_{0.8}\text{Sr}_{0.1}\text{Cu}_{0.05}\text{Co}_{0.05}\text{VO}_3^-$ -YSZ composites that had been exposed to dry methane at 1073 K for 3 h.

**Table 6.1:** Percentage weight changes after exposure to dry  $\text{CH}_4$  at 1073 K for 3 h.

| Sample  | % weight gain |
|---|---------------|
| $\text{Ce}_{0.8}\text{Sr}_{0.1}\text{Cu}_{0.1}\text{VO}_3$                  | < 1           |
| $\text{Ce}_{0.8}\text{Sr}_{0.1}\text{Co}_{0.1}\text{VO}_3$                  | 12            |
| $\text{Ce}_{0.8}\text{Sr}_{0.1}\text{Cu}_{0.05}\text{Co}_{0.05}\text{VO}_3$ | 2             |
| $\text{Ce}_{0.8}\text{Sr}_{0.1}\text{Cu}_{0.05}\text{Ni}_{0.05}\text{VO}_3$ | 61            |

Panel A in Figure 6.3 corresponds to the  $\text{CH}_4$ -treated  $\text{Ce}_{0.8}\text{Sr}_{0.1}\text{Cu}_{0.1}\text{VO}_3$ -YSZ composite. Cu is a relatively unreactive metal and does not catalyze carbon fiber formation from hydrocarbons<sup>1,18</sup>. As expected, this image does not contain any evidence for carbon deposition, and this sample exhibited only a negligible weight gain. In contrast, for the reduced  $\text{Ce}_{0.8}\text{Sr}_{0.1}\text{Co}_{0.1}\text{VO}_3$ -YSZ sample whose surfaces are decorated with Co nanoparticles, worm-like carbon fibers are readily apparent in the SEM image obtained after exposure to  $\text{CH}_4$  (panel B, Fig. 6.3) and this sample exhibited a 12 % weight gain. Unfortunately, similar results were obtained from the  $\text{Ce}_{0.8}\text{Sr}_{0.1}\text{Cu}_{0.05}\text{Ni}_{0.05}\text{VO}_3$ -YSZ composite. The SEM image for this sample (panel C, Fig. 6.3) shows the presence of a high concentration of carbon fibers and the weight of the sample increased by 61 %. The high activity of this sample for carbon fiber formation is consistent with previous results for Cu-Ni alloys<sup>19</sup>. Although one would expect some suppression of the carbon formation in Cu-Ni alloys, carbon formation with a 50:50 Cu-Ni alloy is still significant. More promising results were obtained for the  $\text{Ce}_{0.8}\text{Sr}_{0.1}\text{Cu}_{0.05}\text{Co}_{0.05}\text{VO}_3$ -YSZ composite. The SEM image of this sample after exposure to  $\text{CH}_4$  (panel D, Fig. 6.3) is nearly devoid of carbon fibers and the weight gain for the sample was only 2 %. Since Co is highly active for carbon fiber formation, this result indicates that there is intimate contact between the exsolved Cu and Co and that the majority of the Co nanoparticles must be at least partially coated with the Cu.

Based on the hydrocarbon stability tests, the Cu-Co substituted vanadates were considered more promising for use in SOFC anodes and were therefore the focus of electrochemical testing. This was done using SOFC button cells that with a 65- $\mu\text{m}$  thick YSZ electrolyte, an infiltrated 30 wt. %  $\text{Ce}_{0.8}\text{Sr}_{0.1}\text{Cu}_{0.05}\text{Co}_{0.05}\text{VO}_3$ -YSZ composite anode,



and a 40 wt. % LSF-YSZ composite cathode<sup>26-29</sup>. For comparison purposes, cells with  $\text{Ce}_{0.8}\text{Sr}_{0.1}\text{Cu}_{0.1}\text{VO}_3\text{-YSZ}$ ,  $\text{Ce}_{0.8}\text{Sr}_{0.1}\text{Co}_{0.1}\text{VO}_3\text{-YSZ}$ , and  $\text{CeVO}_3\text{-YSZ}$  composite anodes were also used in some experiments. The fuel-cell measurements reported here focused on characterizing stability of the  $\text{Ce}_{0.8}\text{Sr}_{0.1}\text{Cu}_{0.05}\text{Co}_{0.05}\text{VO}_3\text{-YSZ}$  anode while operating with humidified  $\text{H}_2$  (3 %  $\text{H}_2\text{O}$ ) fuel.

Polarization curves for each cell at 973 K using humidified  $\text{H}_2$  as fuel are shown in Figure 6.4. Each curve was measured starting from OCV, followed by ramping the potential to 0 V and back to OCV using a linear scan rate of  $0.025 \text{ Vs}^{-1}$  in both directions. The polarization curves for the cells with the  $\text{CeVO}_3\text{-YSZ}$  (dashed black curve) and  $\text{Ce}_{0.8}\text{Sr}_{0.1}\text{Cu}_{0.1}\text{VO}_3\text{-YSZ}$  (dashed blue curve) and  $\text{Ce}_{0.8}\text{Sr}_{0.1}\text{Co}_{0.1}\text{VO}_3\text{-YSZ}$  (dotted red curve) were all nearly linear and reversible, showing the same behavior in both scan directions. As will be discussed below, more complex hysteretic behavior was observed for the cell with the  $\text{Ce}_{0.8}\text{Sr}_{0.1}\text{Cu}_{0.05}\text{Co}_{0.05}\text{VO}_3\text{-YSZ}$  anode. Each cell had an open-circuit potential near the theoretical Nernst value of 1.1 V.

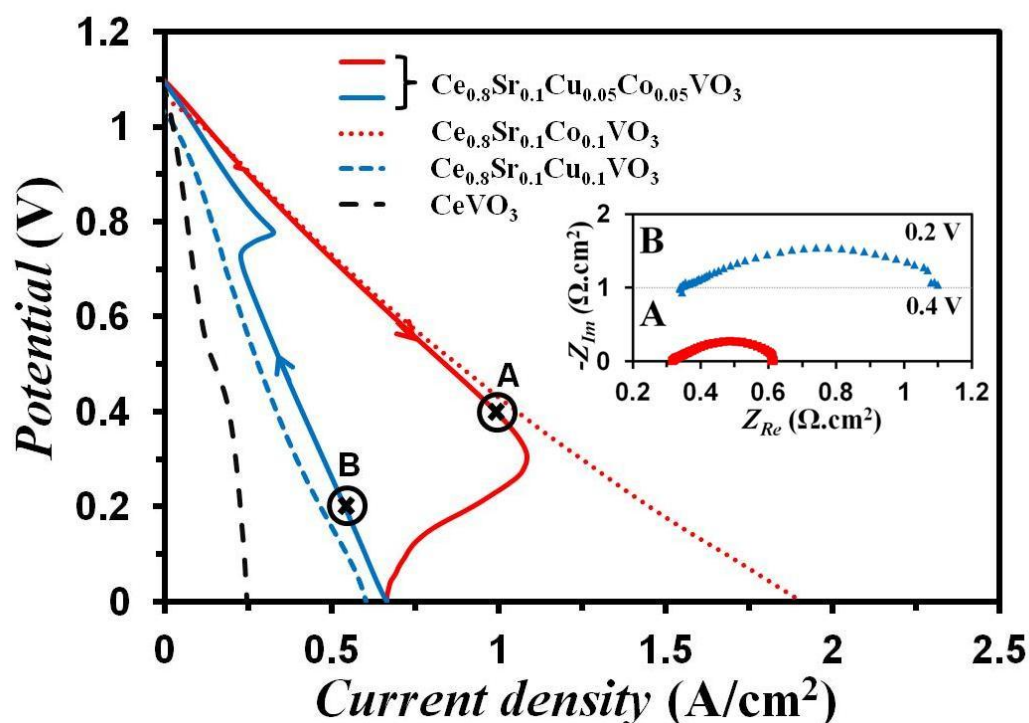


**Figure 6.4:** V-i polarization curves for cells with infiltrated 30 wt. % of (—, —)  $\text{Ce}_{0.8}\text{Sr}_{0.1}\text{Cu}_{0.05}\text{Co}_{0.05}\text{VO}_3$ , (- -)  $\text{Ce}_{0.8}\text{Sr}_{0.1}\text{Co}_{0.1}\text{VO}_3$ , (- -)  $\text{Ce}_{0.8}\text{Sr}_{0.1}\text{Cu}_{0.1}\text{VO}_3$ , and (—)  $\text{CeVO}_3$  -YSZ anodes. Inset: Electrochemical impedance spectra of  $\text{Ce}_{0.8}\text{Sr}_{0.1}\text{Cu}_{0.05}\text{Co}_{0.05}\text{VO}_3$  cell measured at (A) 0.4 V and (B) 0.2 V. The cells were operated at 973 K with humidified  $\text{H}_2$  fuel.

As reported previously, relatively poor electrochemical performance was obtained from the cell with the  $\text{CeVO}_3$ -YSZ composite anode ( $\text{ASR}_{\text{anode}} = 2.70 \Omega \text{ cm}^2$ ) due to the low catalytic activity of this material<sup>1,30</sup>. Only slightly better performance was obtained for the cell with the  $\text{Ce}_{0.8}\text{Sr}_{0.1}\text{Cu}_{0.1}\text{VO}_3$ -YSZ anode ( $\text{ASR}_{\text{anode}} = 0.65 \Omega \text{ cm}^2$ ) which is consistent with the low catalytic activity of both Cu and the vanadate. Excellent performance was obtained from the cell with the  $\text{Ce}_{0.8}\text{Sr}_{0.1}\text{Co}_{0.1}\text{VO}_3$ -YSZ anode which had an  $\text{ASR}_{\text{anode}}$  of only  $0.1 \Omega \text{ cm}^2$  (This assumes that the cathode ASR  $0.15 \Omega \text{ cm}^2$ , as determined in other work<sup>22,23</sup>). This result is consistent with the surface of the

$\text{Ce}_{0.8}\text{Sr}_{0.1}\text{Co}_{0.1}\text{VO}_3$  being decorated with highly catalytic Co nanoparticles under reducing conditions as demonstrated above.

Unusually complex behavior was exhibited by the cell with the  $\text{Ce}_{0.8}\text{Sr}_{0.1}\text{Cu}_{0.05}\text{Co}_{0.05}\text{VO}_3$ -YSZ composite anode, including hysteresis in the polarization curve, with abrupt changes in performance occurring at several voltages (Figure 6.4). The initial portion of the polarization curve for this cell, starting from OCV and ramping to  $\sim 0.3$  V (solid red curve in Fig. 6.4), closely follows that of the cell with the  $\text{Ce}_{0.8}\text{Sr}_{0.1}\text{Co}_{0.1}\text{VO}_3$ -YSZ anode. As shown by the impedance spectrum obtained at point A (see figure insert), the anode ASR in this portion of the polarization curve is  $0.15 \Omega \text{ cm}^2$  after subtracting off the cathode ASR,  $0.15 \Omega \text{ cm}^2$ . The hydrocarbon stability tests described above indicated that the Co nanoparticles exsolved from the  $\text{Ce}_{0.8}\text{Sr}_{0.1}\text{Cu}_{0.05}\text{Co}_{0.05}\text{VO}_3$  lattice under reducing conditions are primarily coated with Cu. The similarity in the initial performance of the two anode formulations containing Co, however, demonstrates that, for the  $\text{Ce}_{0.8}\text{Sr}_{0.1}\text{Cu}_{0.05}\text{Co}_{0.05}\text{VO}_3$ -YSZ anode, enough Co remains exposed to impart high catalytic activity for  $\text{H}_2$  oxidation.

Near 0.3 V, an abrupt change in the electrochemical properties of the  $\text{Ce}_{0.8}\text{Sr}_{0.1}\text{Cu}_{0.05}\text{Co}_{0.05}\text{VO}_3$ -YSZ anode takes place, causing a rapid decrease in cell performance as the voltage is ramped from 0.3 to 0 V. As shown by the solid blue curve in Figure 6.4, the polarization curve for the  $\text{Ce}_{0.8}\text{Sr}_{0.1}\text{Cu}_{0.05}\text{Co}_{0.05}\text{VO}_3$  cell exhibited hysteresis and was not immediately reversible, with low performance persisting upon reversal of the sweep direction from 0 to  $\sim 0.78$  V. In this region of the polarization curve the cell performance was close to that of the cell with the  $\text{Ce}_{0.8}\text{Sr}_{0.1}\text{Cu}_{0.1}\text{VO}_3$ -YSZ anode. As shown by the impedance spectrum collected at point B, the anode ASR in this region of the polarization

curve was  $0.65 \Omega \text{ cm}^2$  (the estimated cathode ASR of  $0.15 \Omega \text{ cm}^2$  has again been taken into account here). At 0.78 V on the increasing voltage sweep, another abrupt change occurs, with the cell performance switching from the low-activity state back to the high-activity state exhibited by the fresh cell. This high-activity state then persists up to OCV. The hysteretic behavior exhibited by this cell was stable and occurred for repeated polarization curve measurements at a variety of scan rates. Similar results were obtained with multiple cells and the changes in performance occurred at nearly the same voltages ( $\sim 0.3$  and  $\sim 0.8$  V) in all cases.

It is important to note that the impedance spectra show that the ohmic contribution remained fixed at  $0.3 \Omega \text{ cm}^2$  in both the high- and low-performance regions of the polarization curve. This value is consistent with that expected for the 65  $\mu\text{m}$  thick YSZ electrolyte layer, ruling out the possibility that the change in cell performance is due to a change in the electronic conductivity of the vanadate phase or the formation of an insulating layer at the YSZ-vanadate interface.

*In situ* characterization of the phase composition and structure of the  $\text{Ce}_{0.8}\text{Sr}_{0.1}\text{Cu}_{0.05}\text{Co}_{0.05}\text{VO}_3$ -YSZ composite anode in both the high- and low-activity states, in the region near the electrolyte-anode interface, would be required to provide a definitive explanation for the observed hysteresis in electrochemical properties. However, the results here provide important clues as to its possible origin. It is useful to first consider the structure of the Cu and Co nanoparticles that are exsolved from the  $\text{Ce}_{0.8}\text{Sr}_{0.1}\text{Cu}_{0.05}\text{Co}_{0.05}\text{VO}_3$  lattice under reducing conditions. The hydrocarbon stability tests (Figure 6.3) demonstrate that the anode has relatively low catalytic activity for the production of carbon fibers from hydrocarbons. Since Co by itself has high activity for

this reaction, Co nanoparticles must be in intimate contact with Cu on the reduced electrode. Since Cu and Co are nearly immiscible and do not form bulk alloys, the nanoscale mixtures of these metals that are produced by the exsolution process would be expected to phase separate; furthermore, due to the lower surface free energy of Cu, one would expect this process to produce Cu-coated Co particles.

A previous study of a Cu-CeO<sub>2</sub>-YSZ composite electrode (the Cu and CeO<sub>2</sub> were added using wet infiltration) that was coated with a thin layer of Co using electrodeposition demonstrated that Cu does indeed segregate to a Co surface<sup>51</sup>. Under typical SOFC operating conditions, this anode was found to have high hydrocarbon stability and did not catalyze carbon fiber formation. In this study X-ray photoelectron spectroscopy (XPS) was used to characterize a 250-nm Co film that had been electrodeposited onto a Cu foil as a function of temperature in ultra-high vacuum (a reducing environment). It was found that, at temperatures above 800 K, Cu migrated through the Co film, ultimately coating its surface. Furthermore, analysis of the XPS peak intensities during sputter depth-profile measurements indicated that the equilibrium thickness of the Cu coating was only 1-2 monolayers. Applying these results to the reduced Ce<sub>0.8</sub>Sr<sub>0.1</sub>Cu<sub>0.05</sub>Co<sub>0.05</sub>VO<sub>3</sub> electrode used in the present study, the exsolved Co nanoparticles will also become coated with a 1-2 monolayers of Cu.

While coating of the Co particles with a thin layer of Cu could explain the low activity of the reduced Ce<sub>0.8</sub>Sr<sub>0.1</sub>Cu<sub>0.05</sub>Co<sub>0.05</sub>VO<sub>3</sub> anode for carbon deposition, some Co must still be exposed since the catalytic activity of the anode for H<sub>2</sub> oxidation at high cell potentials is essentially the same as that for an electrode that contains only Co nanoparticles. Based on these observations, we propose that, for the

$\text{Ce}_{0.8}\text{Sr}_{0.1}\text{Cu}_{0.05}\text{Co}_{0.05}\text{VO}_3$  anode, some Co is present in the thin Cu layer that coats the Co nanoparticles, as shown schematically in Figure 6.5.

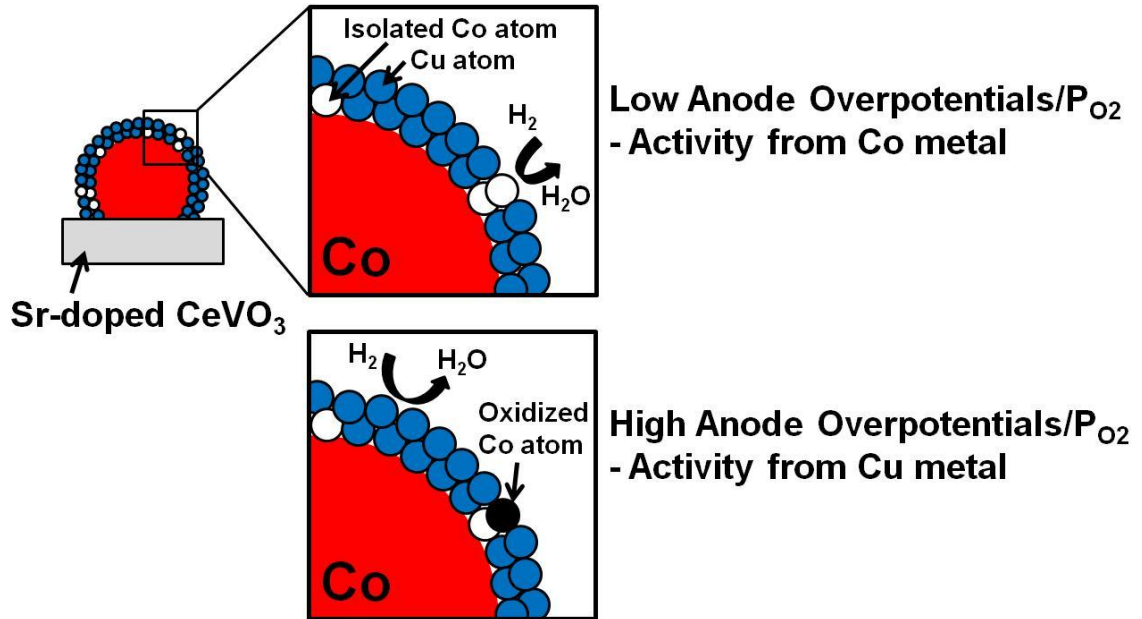


**Figure 6.5:** Schematic of the structure of the Cu-Co particles and the effect of polarization.

Note that the mechanism for transition metal catalyzed formation of carbon fibers from hydrocarbons involves the dissolution of carbon into the metal and the precipitation of a metal carbide particle that is lifted off the surface of the original metal particle by the growing carbon fiber<sup>31,32</sup>. This process would not occur for the isolated Co atoms in the surface Cu layer shown in Figure 6.5, but these atoms would be expected to retain their catalytic activity for oxidation reactions.

It is interesting to estimate the anode overpotentials corresponding to the critical points in the V-i curve for the cell with the  $\text{Ce}_{0.8}\text{Sr}_{0.1}\text{Cu}_{0.05}\text{Co}_{0.05}\text{VO}_3$  anode. Based on the estimated anode ASR for the high- and low-activity regions of curve ( $0.15 \text{ } \Omega \text{ cm}^2$  and  $0.65 \text{ } \Omega \text{ cm}^2$ ), the anode overpotentials at the points where the performance jumps occur are  $0.165 \text{ V}$  ( $0.15 \text{ } \Omega \text{ cm}^2 \cdot 1.1 \text{ Acm}^{-2}$ ) and  $0.163 \text{ V}$  ( $0.65 \text{ } \Omega \text{ cm}^2 \cdot 0.25 \text{ Acm}^{-2}$ ), respectively. This in turn can be related to an increase in the  $\text{P}_{\text{O}_2}$  in the three-phase boundary (TPB) region relative to the anode compartment gas phase, from  $10^{-24}$  atm in the anode compartment to approximately  $10^{-20}$  atm at the TPB.

Although the  $\text{P}_{\text{O}_2}$  at the TPB remains well below that needed to oxidize either bulk Co ( $\sim 10^{-18}$  atm<sup>33</sup>) or Cu ( $\sim 10^{-11}$  atm<sup>34</sup>), we suggest that the switch in catalytic performance of the  $\text{Ce}_{0.8}\text{Sr}_{0.1}\text{Cu}_{0.05}\text{Co}_{0.05}\text{VO}_3$ -YSZ anode from that characteristic of a Co catalyst to one characteristic of a Cu catalyst at low cell potentials is due to oxidation of the Co that is exposed in the Cu-coated, Co particles on the electrode surface. It would not be surprising if these isolated cobalt atoms have thermodynamic properties that vary somewhat from that of the bulk material. Indeed, it has been suggested that small Co nanoparticles are more easily oxidized than bulk Co and can become oxidized at a significantly lower  $\text{P}_{\text{O}_2}$ <sup>35,36</sup>. Support and promoter effects have also been reported to alter the redox properties of small Co particles<sup>33</sup>. Since CoO does not exhibit the high oxidation activity of metallic Co, when the Co becomes oxidized the catalytic activity would decrease. The observed switching behavior for the Cu-Co system is therefore likely to be due to oxidation/reduction of the surface Co in the Cu-Co particles at the  $\text{P}_{\text{O}_2}$  corresponding to an anode overpotential of  $\sim 0.164 \text{ V}$ . Based on this scenario, the exposed

Co provides the catalytic activity at low anode overpotentials (low  $P_{O_2}$ ) and Cu provides the catalytic activity at high overpotentials as shown schematically in Figure 6.5.

The performance of the anodes made with Cu-Co mixtures is very intriguing and provides another example of the use of exsolution from an oxide host under reducing conditions as an *in situ* means to synthesize catalytic metal nanoparticles on SOFC electrode surfaces and also shows how the anode overpotential and the local  $P_{O_2}$  can affect the structure and catalytic properties of bimetallic metal catalyst particles. Since  $Ce_{0.8}Sr_{0.1}Cu_{0.05}Co_{0.05}VO_3$ -YSZ composite anodes appear to be hydrocarbon tolerant and exhibit good performance at low overpotentials in  $H_2$  fuel these materials hold some promise for use in SOFC. The performance and stability of these anodes while operating with hydrocarbon fuels, and whether similar hysteresis phenomena occur with hydrocarbons, will be the subject of a future study.

#### **6.4 Conclusion**

In this chapter it was demonstrated that upon reduction in humidified hydrogen at 973 K zircon-type  $Ce_{0.8}Sr_{0.1}Cu_{0.05}TM_{0.05}VO_{4-0.5x}$  oxides (TM = Ni or Co) undergo a phase transition to the perovskite structure which is accompanied by exsolution of a portion of the transition metals from the lattice. The exsolved metals form Cu-Ni and Cu-Co mixtures with the surface of the mixture enriched with Cu due to its lower surface energy (note that Ni and Cu form an alloy, while Co and Cu form separate phases), which decorate the surface of the oxide. The hydrocarbon stability tests and the electrochemical performance measurement demonstrated that majority of the Co nanoparticles must be at least partially coated with the Cu, with some isolated Co atoms in the surface Cu layer



providing the catalytic activity for H<sub>2</sub> oxidation. However, an unusually complex behavior was exhibited by the cell with the Ce<sub>0.8</sub>Sr<sub>0.1</sub>Cu<sub>0.05</sub>Co<sub>0.05</sub>VO<sub>3</sub>-YSZ composite anode including hysteresis in the polarization curve with abrupt changes in performance occurring at several voltages. The switch in the performance of the Ce<sub>0.8</sub>-Sr<sub>0.1</sub>Cu<sub>0.05</sub>Co<sub>0.05</sub>VO<sub>3</sub>-YSZ anode from that characteristic of one with a Co catalyst to one with a Cu catalyst at low cell voltages indicates that the isolated cobalt sites are being oxidized at higher anode overpotentials.

## 6.5 References

- 1 Adijanto, L., Padmanabhan, V. B., Kungas, R., Gorte, R. J. & Vohs, J. M. Transition metal-doped rare earth vanadates: a regenerable catalytic material for SOFC anodes. *J Mater Chem* 22, 11396-11402, doi:Doi 10.1039/C2jm31774e (2012).
- 2 Babaei, A., Zhang, L., Tan, S. L. & Jiang, S. P. Pd-promoted (La,Ca)(Cr,Mn)O<sub>3</sub>/GDC anode for hydrogen and methane oxidation reactions of solid oxide fuel cells. *Solid State Ionics* 181, 1221-1228, doi:DOI 10.1016/j.ssi.2010.06.042 (2010).
- 3 Bierschenk, D. M. *et al.* Pd-substituted (La,Sr)CrO<sub>(3-delta)</sub>-Ce<sub>(0.9)</sub>Gd<sub>(0.1)</sub>O<sub>(2-delta)</sub> solid oxide fuel cell anodes exhibiting regenerative behavior. *J Power Sources* 196, 3089-3094, doi:DOI 10.1016/j.jpowsour.2010.12.050 (2011).
- 4 Kobsiriphat, W., Madsen, B. D., Wang, Y., Marks, L. D. & Barnett, S. A. La<sub>(0.8)</sub>Sr<sub>(0.2)</sub>Cr<sub>(1-x)</sub>Ru<sub>(x)</sub>O<sub>(3-delta)</sub>-Gd<sub>(0.1)</sub>Ce<sub>(0.9)</sub>O<sub>(1.95)</sub> solid oxide fuel cell anodes: Ru precipitation and electrochemical performance. *Solid State Ionics* 180, 257-264, doi:DOI 10.1016/j.ssi.2008.12.022 (2009).
- 5 Kobsiriphat, W. *et al.* Nickel- and Ruthenium-Doped Lanthanum Chromite Anodes: Effects of Nanoscale Metal Precipitation on Solid Oxide Fuel Cell Performance. *J Electrochem Soc* 157, B279-B284, doi:Doi 10.1149/1.3269993 (2010).
- 6 Kurzman, J. A. *et al.* Pd<sup>2+</sup>/Pd<sup>0</sup> Redox Cycling in Hexagonal YMn<sub>0.5</sub>Fe<sub>0.5</sub>O<sub>3</sub>: Implications for Catalysis by PGM-Substituted Complex Oxides. *Inorg Chem* 50, 8073-8084, doi:Doi 10.1021/Ic200455a (2011).

- 7 Madsen, B. D., Kobsiriphat, W., Wang, Y., Marks, L. D. & Barnett, S. A. Nucleation of nanometer-scale electrocatalyst particles in solid oxide fuel cell anodes. *J Power Sources* 166, 64-67, doi:DOI 10.1016/j.jpowsour.2006.12.080 (2007).
- 8 Nishihata, Y. *et al.* Self-regeneration of a Pd-perovskite catalyst for automotive emissions control. *Nature* 418, 164-167, doi:Doi 10.1038/Nature00893 (2002).
- 9 Singh, U. G. *et al.* A Pd-doped perovskite catalyst,  $\text{BaCe}_{1-x}\text{Pd}_x\text{O}_{3-\text{delta}}$ , for CO oxidation. *J Catal* 249, 349-358, doi:DOI 10.1016/j.jcat.2007.04.023 (2007).
- 10 Tan, I. *et al.* The self-regenerative "intelligent" catalyst for automotive emissions control. *Science of Engineering Ceramics Iii* 317-318, 833-836 (2006).
- 11 Tanaka, H. *et al.* Self-regenerating Rh- and Pt-based perovskite catalysts for automotive-emissions control. *Angew Chem Int Edit* 45, 5998-6002, doi:DOI 10.1002/anie.200503938 (2006).
- 12 Tanaka, H. *et al.* Intelligent catalyst having the self-regenerative function of Pd, Rh and Pt for automotive emissions control. *Catal Today* 117, 321-328, doi:DOI 10.1016/j.cattod.2006.05.029 (2006).
- 13 Gross, M. D., Vohs, J. M. & Gorte, R. J. Recent progress in SOFC anodes for direct utilization of hydrocarbons. *J Mater Chem* 17, 3071-3077, doi:Doi 10.1039/B702633a (2007).
- 14 Gross, M. D., Vohs, J. M. & Gorte, R. J. A study of thermal stability and methane tolerance of Cu-based SOFC anodes with electrodeposited Co. *Electrochim Acta* 52, 1951-1957, doi:DOI 10.1016/j.electacta.2006.08.005 (2007).

- 15 Jung, S. W., Vohs, J. M. & Gorte, R. J. Preparation of SOFC anodes by Electrodeposition. *J Electrochem Soc* 154, B1270-B1275, doi:Doi 10.1149/1.2790280 (2007).
- 16 Jung, S., Gross, M. D., Gorte, R. J. & Vohs, J. M. Electrodeposition of Cu into a highly porous Ni/YSZ cermet. *J Electrochem Soc* 153, A1539-A1543, doi:Doi 10.1149/1.2208908 (2006).
- 17 Lee, S. I., Ahn, K., Vohs, J. M. & Gorte, R. J. Cu-Co bimetallic anodes for direct utilization of methane in SOFCs. *Electrochem Solid St* 8, A48-A51, doi:Doi 10.1149/1.1833678 (2005).
- 18 Lee, S. I., Vohs, J. M. & Gorte, R. J. A study of SOFC anodes based on Cu-Ni and Cu-Co bimetallics in CeO<sub>2</sub>-YSZ. *J Electrochem Soc* 151, A1319-A1323, doi:Doi 10.1149/1.1774184 (2004).
- 19 Kim, H., Lu, C., Worrell, W. L., Vohs, J. M. & Gorte, R. J. Cu-Ni cermet anodes for direct oxidation of methane in solid-oxide fuel cells. *J Electrochem Soc* 149, A247-A250, doi:Doi 10.1149/1.1445170 (2002).
- 20 Park, S., Gorte, R. J. & Vohs, J. M. Tape cast solid oxide fuel cells for the direct oxidation of hydrocarbons. *J Electrochem Soc* 148, A443-A447 (2001).
- 21 Kungas, R., Kim, J. S., Vohs, J. M. & Gorte, R. J. Restructuring Porous YSZ by Treatment in Hydrofluoric Acid for Use in SOFC Cathodes. *J Am Ceram Soc* 94, 2220-2224, doi:DOI 10.1111/j.1551-2916.2010.04359.x (2011).
- 22 Adijanto, L., Kungas, R., Bidrawn, F., Gorte, R. J. & Vohs, J. M. Stability and performance of infiltrated La<sub>0.8</sub>Sr<sub>0.2</sub>Co<sub>x</sub>Fe<sub>1-x</sub>O<sub>3</sub> electrodes with and without

- $\text{Sm}_{0.2}\text{Ce}_{0.8}\text{O}_{1.9}$  interlayers. *J Power Sources* 196, 5797-5802, doi:DOI 10.1016/j.jpowsour.2011.03.022 (2011).
- 23 Adjianto, L., Kungas, R., Park, J., Vohs, J. M. & Gorte, R. J. SOFC anodes based on infiltration of tungsten bronzes. *Int J Hydrogen Energ* 36, 15722-15730, doi:DOI 10.1016/j.ijhydene.2011.09.059 (2011).
- 24 Petit, C. T. G., Lan, R., Cowin, P. I., Irvine, J. T. S. & Tao, S. W. Novel redox reversible oxide, Sr-doped cerium orthovanadate to metavanadate. *J Mater Chem* 21, 525-531, doi:Doi 10.1039/C0jm02669g (2011).
- 25 Watanabe, A. Highly conductive oxides,  $\text{CeVO}_4$ ,  $\text{Ce}_{1-x}\text{M}_x\text{VO}_{4-0.5x}$  (M= Ca, Sr, Pb) and  $\text{Ce}_{1-y}\text{Bi}_y\text{VO}_4$ , with zircon-type structure prepared by solid-state reaction in air. *J Solid State Chem* 153, 174-179, doi:DOI 10.1006/jssc.2000.8773 (2000).
- 26 Wang, W. S., Gross, M. D., Vohs, J. M. & Gorte, R. J. The stability of LSF-YSZ electrodes prepared by infiltration. *J Electrochem Soc* 154, B439-B445, doi:10.1149/1.2709510 (2007).
- 27 Vohs, J. M., Adjianto, L., Kungas, R., Bidrawn, F. & Gorte, R. J. Stability and performance of infiltrated  $\text{La}_{(0.8)}\text{Sr}_{(0.2)}\text{Co}_{(x)}\text{Fe}_{(1-x)}\text{O}_{(3)}$  electrodes with and without  $\text{Sm}_{(0.2)}\text{Ce}_{(0.8)}\text{O}_{(1.9)}$  interlayers. *J Power Sources* 196, 5797-5802, doi:10.1016/j.jpowsour.2011.03.022 (2011).
- 28 Gorte, R. J. & Vohs, J. M. High-Performance SOFC Cathodes Prepared by Infiltration. *Adv Mater* 21, 943-956, doi:10.1002/adma.200802428 (2009).
- 29 Vohs, J. M. & Gorte, R. J. High-Performance SOFC Cathodes Prepared by Infiltration. *Adv Mater* 21, 943-956, doi:DOI 10.1002/adma.200802428 (2009).

- 30 Adjianto, L., Padmanabhan, V. B., Holmes, K. J., Gorte, R. J. & Vohs, J. M. Physical and electrochemical properties of alkaline earth doped, rare earth vanadates. *J Solid State Chem* 190, 12-17, doi:DOI 10.1016/j.jssc.2012.01.065 (2012).
- 31 Toebes, M. L., Bitter, J. H., van Dillen, A. J. & de Jong, K. P. Impact of the structure and reactivity of nickel particles on the catalytic growth of carbon nanofibers. *Catal Today* 76, 33-42 (2002).
- 32 Teo, K. B. K., Singh, C., Chhowalla, M. & Milne, W. I. Catalytic Synthesis of Carbon Nanotubes and Nanofibers. *Encyclopedia of Nanoscience and Nanotechnology X*, 1-22 (2003).
- 33 Bakhmutsky, K., Wieder, N. L., Baldassare, T., Smith, M. A. & Gorte, R. J. A thermodynamic study of the redox properties of supported Co particles. *Appl Catal a-Gen* 397, 266-271, doi:DOI 10.1016/j.apcata.2011.03.013 (2011).
- 34 Shah, P. R., Kim, T., Zhou, G., Fornasiero, P. & Gorte, R. J. Evidence for entropy effects in the reduction of ceria-zirconia solutions. *Chem Mater* 18, 5363-5369, doi:Doi 10.1021/Cm061374f (2006).
- 35 Navrotsky, A., Ma, C. C., Lilova, K. & Birkner, N. Nanophase Transition Metal Oxides Show Large Thermodynamically Driven Shifts in Oxidation-Reduction Equilibria. *Science* 330, 199-201, doi:DOI 10.1126/science.1195875 (2010).
- 36 van Steen, E. *et al.* Stability of nanocrystals: Thermodynamic analysis of oxidation and re-reduction of cobalt in water/hydrogen mixtures. *J Phys Chem B* 109, 3575-3577, doi:Doi 10.1021/Jp05136o (2005).

## **Chapter 7. Exceptional Thermal Stability of Pd@CeO<sub>2</sub> Core-Shell Catalyst Nanostructures Grafted onto an Oxide Surface\***

### **Summary**

Monolayer films of highly catalytically active, Pd@CeO<sub>2</sub> core-shell nanocomposites were grafted onto a planar YSZ(100) (yttria-stabilized zirconia, YSZ) single crystal support which was functionalized with a CVD-deposited layer of triethoxy(octyl)silane (TEOOS). The resulting monolayer films were found to exhibit exceptionally high thermal stability compared to bare Pd nanoparticles, with the Pd@CeO<sub>2</sub> nanostructures remaining intact and highly dispersed upon calcining in air at temperatures in excess of 1000 K. The CeO<sub>2</sub> shells were also shown to be more easily reduced than bulk CeO<sub>2</sub> which may partially explain their unique activity as oxidation catalysts. The use of both TEOOS and tetradecylphosphonic acid (TDPA) as coupling agents for dispersing Pd@CeO<sub>2</sub> core-shell nanocomposites onto a high surface area  $\gamma$ -Al<sub>2</sub>O<sub>3</sub> support is also demonstrated.

---

\* This chapter was published as a research paper in the Journal of the NanoLetters, 13 (2013) 2252. Copyright: 2013, ACS.

## 7.1 Introduction

For many technologically important chemical processes which employ supported noble metal catalysts, loss of metal surface area due to sintering limits catalyst lifetime and efficiency. Encapsulating the metal nanoparticles in a thin porous oxide shell has been proposed as one means to alleviate this problem and improve catalyst lifetime<sup>1-12</sup>, although methods to disperse these core-shell structures onto high surface area oxide supports still presents a challenge. In this study we demonstrate the growth of highly dispersed, monolayer films of catalytically active Pd@CeO<sub>2</sub> core-shell nanocomposites onto a planar, single crystal YSZ(100) (yttria stabilized zirconia) support using an alkylsilane coupling agent, and that these films exhibit exceptional thermal stability with high Pd dispersion being maintained even after calcination in air at temperatures in excess of 1000 K. The general utility of this approach for the synthesis of dispersed core-shell catalysts on high surface area oxide supports is also demonstrated.

## 7.2 Experimental

### *Materials:*

Triethoxy(octyl)silane (TEOOS, Sigma Aldrich 97.5 %), Pd(NO<sub>3</sub>)<sub>2</sub>·2H<sub>2</sub>O (40 % as Pd), (NH<sub>4</sub>)<sub>2</sub>Ce(NO<sub>3</sub>)<sub>6</sub> (99.99 %). n-Tetradecylphosphonic acid (TDPA, ≥97 %) was purchased from Strem Chemicals. Al<sub>2</sub>O<sub>3</sub> Puralox TH100/150 (90 m<sup>2</sup> g<sup>-1</sup>) was purchased from Sasol and calcined at 1173 K for 24 h. Pd@CeO<sub>2</sub> structures (at 1:9 Pd/Ce weight ratios) were prepared according to the procedure described in detail elsewhere<sup>10,13</sup>. YSZ(100) single crystal substrates with dimensions of 5 mm x 5 mm were purchased



from MTI corporation. All of the solvents were reagent grade from Sigma-Aldrich and used as received.

*Preparation of samples:*

The YSZ(100) single crystal substrates (5 mm x 5 mm) were cleaned using an O<sub>2</sub> plasma treatment prior to surface modification. Functionalization of the YSZ(100) surface via reaction with triethoxy(octyl)silane (TEOOS) was performed using chemical vapor deposition (CVD) system. Prior to film deposition, the YSZ(100) substrate was further cleaned in the CVD reactor by heating to 673 K and exposure to 400 torr of O<sub>2</sub> for 1 min. The sample was functionalized with TEOOS using ten deposition cycles consisting of a 1 min exposure to 0.5 torr of TEOOS with the sample at 323 K. The Pd@CeO<sub>2</sub> particles were added (in excess of that required for a monolayer) to the clean and TEOOS-functionalized YSZ(100) surfaces using ten cycles of placing a 0.1 ml drop of the 1.5x10<sup>-3</sup> M Pd@CeO<sub>2</sub>/THF solution onto the YSZ(100), waiting 2 minutes, and then rinsing with THF. The samples were then calcined to 723 K in air for 4 h to remove the alkyl groups.

For the TEOOS treated sample,  $\gamma$ -Al<sub>2</sub>O<sub>3</sub> powder (1 g) was mixed in 20 mL of toluene followed by addition of TEOOS (0.55 mL). The resulting solution was refluxed at 384 K for 6 h and the precipitate powder was recovered by centrifugation. For the TDPA-treated sample,  $\gamma$ -Al<sub>2</sub>O<sub>3</sub> powder (1 g) was mixed in 30 mL of THF followed by addition of TDPA (0.20 g). The resulting solution was refluxed at 333 K for 6 h and the precipitate powder was recovered by centrifugation. The powder was subsequently

washed twice with toluene/THF to remove unreacted TEOOS/TDPA and byproducts and was dried overnight at 393 K.

The appropriate amount of Pd@CeO<sub>2</sub> structures was added to the hydrophobic  $\gamma$ -Al<sub>2</sub>O<sub>3</sub> well dispersed in THF (15 mL). Although a complete adsorption occurred almost immediately when using loadings of Pd and ceria of 1 and 9 wt. % or less, respectively, the mixture was left stirring overnight. The solid residue was recovered by centrifugation and washed twice with THF. Finally, the powder was dried at 403 K overnight, ground to a particle size below 150  $\mu$ m and calcined in air at 1123 K for 6 h using a heating ramp of 3 K min<sup>-1</sup>.

*Characterization techniques:*

The surface topography was measured in air using an AFM (Pacific Nanotechnology) operated in close-contact (tapping) mode. XPS and TPD measurements were conducted in an ultra-high vacuum (UHV) surface analysis chamber with a base pressure of  $2 \times 10^{-10}$  Torr. Sample heating in UHV was accomplished through conduction from a resistively heated tantalum foil sample holder, and the temperature was monitored using a type K thermocouple that was attached to the back surface of the YSZ crystal using a ceramic adhesive (Aremco). Samples were exposed to adsorbates through a dosing needle with the sample positioned directly in front to maintain a low base pressure. The hydrophobicity of the YSZ(100) substrate before and after TEOOS deposition was measured by pendant drop Tensiometry (Attension, Theta), and the thickness of the TEOOS/Pd@CeO<sub>2</sub> layer was measured using an Alpha-SE ellipsometer (J.A. Woollam).

### *Catalytic tests:*

Methane oxidation experiments were performed in a 6.4 mm diameter, tubular quartz reactor, using ~0.10 g of catalyst. The reactants (0.5 % CH<sub>4</sub>, 5 % O<sub>2</sub>, balance N<sub>2</sub>) at 1 atm were flowed over the catalyst at a rate 120 mL/min. The CH<sub>4</sub> conversion was kept below 10% so that differential conditions could be assumed. Products were analyzed using an on-line gas chromatograph. Prior to measuring rates, each catalyst was pressed into wafers, heated to 693 K under flowing He and cleaned under a flow of 20% O<sub>2</sub>/80% He at 120mL/min for 30min.

## **7.3 Results and Discussion**

Pd@CeO<sub>2</sub> nanostructures were chosen as the subject of this investigation because synergistic interactions between Pd and CeO<sub>2</sub> are known to enhance catalytic activity for industrially important reactions ranging from water gas shift to hydrocarbon oxidation. The Pd@CeO<sub>2</sub> nanostructures consisted of a 2 nm diameter Pd core surrounded by a 3 nm thick, porous CeO<sub>2</sub> shell, and were synthesized in THF solution using the procedure developed by Cargnello et al.<sup>9,10,13</sup>. The surface of the Pd@CeO<sub>2</sub> particles was functionalized with dodecanoic acid in order to both control particle size during synthesis and inhibit particle agglomeration in solution. Unfortunately, this hydrophobic alkyl capping layer is repelled by the hydrophilic surface of most oxide supports, including the YSZ(100) single crystal and high surface area  $\gamma$ -Al<sub>2</sub>O<sub>3</sub> supports used here. Due to this repulsive particle-surface interaction, the core-shell particles assemble into large agglomerates when they are deposited by incipient wetness onto high surface area metal oxide powders or by drop casting onto planar supports. We have overcome this problem

by functionalizing the surface of the oxide support with hydrophobic long-chain alkyl groups via deposition of a monolayer of triethoxy(octyl)silane (TEOOS) or n-tetradecylphosphonic acid (TDPA). As will be shown below, monolayer films of Pd@CeO<sub>2</sub> particles can be grafted onto the alkyl-functionalized oxide surfaces.

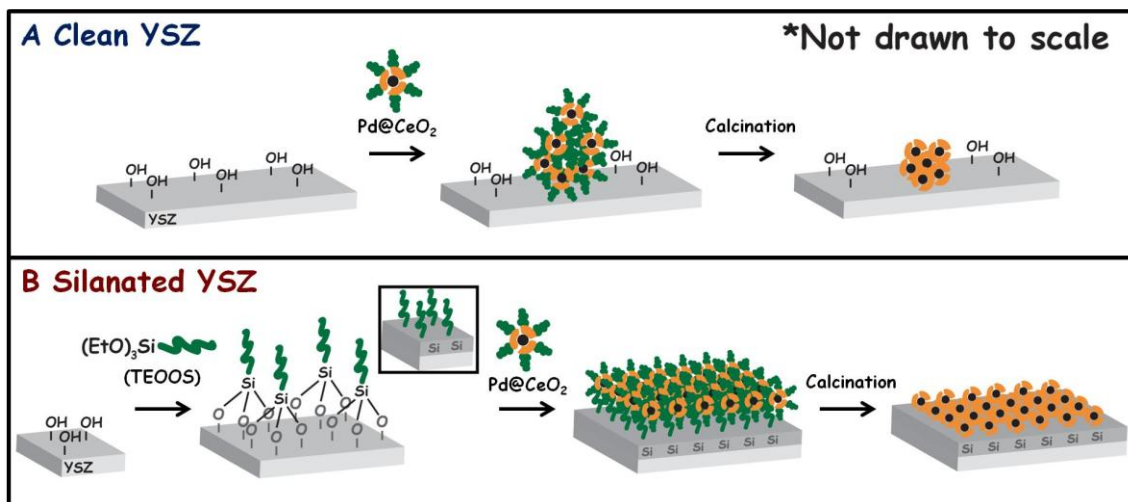


**Figure 7.1:** Overview of the deposition of Pd@CeO<sub>2</sub> nanostructures on (A) clean YSZ(100) and (B) alkyl-siloxane functionalized YSZ(100). On clean YSZ the hydrophobic, alkyl-capped Pd@CeO<sub>2</sub> particles are repelled by the hydrophilic OH-terminated YSZ surface, resulting in the formation of agglomerates during deposition, with further agglomeration occurring upon calcination in air. On the alky-siloxane functionalized YSZ surface, the Van der Waals interactions between the capping alkyl groups on the surface and the core-shell particles directs the formation of a monolayer film of the Pd@CeO<sub>2</sub> particles. This Pd@CeO<sub>2</sub> layer is highly stable and remains highly dispersed upon calcination in air.

Figure 7.1 provides an overview of the preparation of the planar Pd@CeO<sub>2</sub>/YSZ(100) samples used in this study. Following CVD of a TEOOS layer, the Pd@CeO<sub>2</sub> nanostructures were added to the YSZ(100) surface using several deposition cycles consisting of placing a 0.1 ml drop of the 1.5x10<sup>-3</sup> M Pd@ CeO<sub>2</sub>/THF solution onto the YSZ(100), waiting 2 minutes, and then rinsing with THF to remove weakly adsorbed particles. The sample was then calcined at 723 K in air for 4 h in order to

oxidatively remove the alkyl groups on both the support and core-shell particles. A Pd@CeO<sub>2</sub>/YSZ(100) sample for which the YSZ(100) substrate was not functionalized with TEOOS prior to deposition of the nanoparticles was also prepared in a similar manner. For comparison purposes, a sample consisting of Pd nanoparticles without a CeO<sub>2</sub> shell supported on YSZ(100) was also prepared. The synthesis procedure for this sample was identical to that of the Pd@CeO<sub>2</sub>/YSZ(100) sample except dodecanethiol-capped 2 nm Pd particles were used.

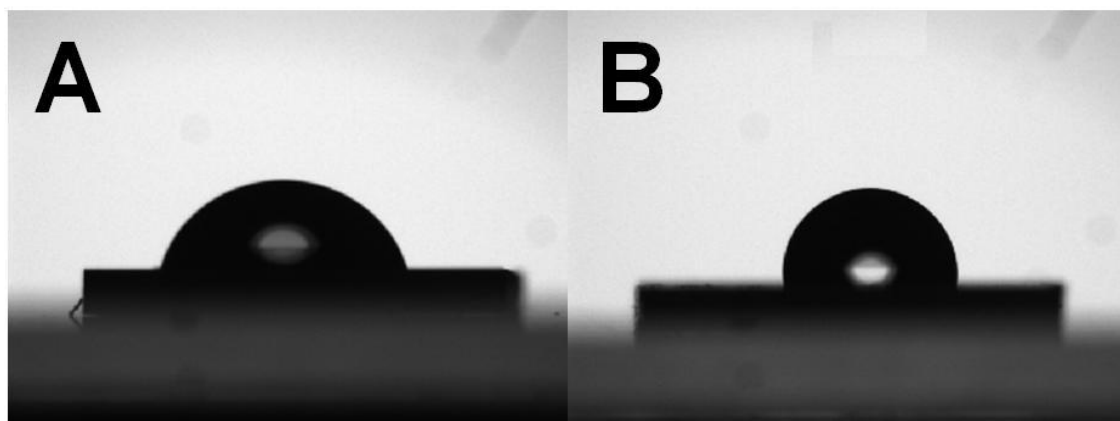


**Figure 7.2:** Contact angle measurements. Image of 1  $\mu\text{L}$  water droplet placed on clean YSZ(100) substrate (Panel A) and silanated YSZ(100) substrate (Panel B) with tensiometry. Deposition of the TEOOS layer using the CVD process resulted in an increase in the water contact angle from  $70^\circ$  to  $100^\circ$ .

Water contact angle measurements were used to assess the hydrophobicity of the TEOSS-treated surface and to confirm that the capping octyl groups were retained throughout the CVD process. The contact angle was measured by tensiometry using a 1  $\mu\text{L}$  water droplet. Cross-sectional images of the water droplets on the TEOSS-free (Panel A) and TEOSS-coated YSZ(100) (Panel B) samples are displayed in Figure 7.2 and the contact angles for each sample are listed in Table 7.1. Deposition of the TEOOS layer

resulted in an increase in the water contact angle from  $70^\circ$  to  $100^\circ$ . This difference is readily apparent in the images in the figure. This change from a moderately hydrophilic surface to a hydrophobic surface is consistent with the TEOOS-treated surface being predominantly terminated with the non-polar (i.e. hydrophobic) octyl groups.

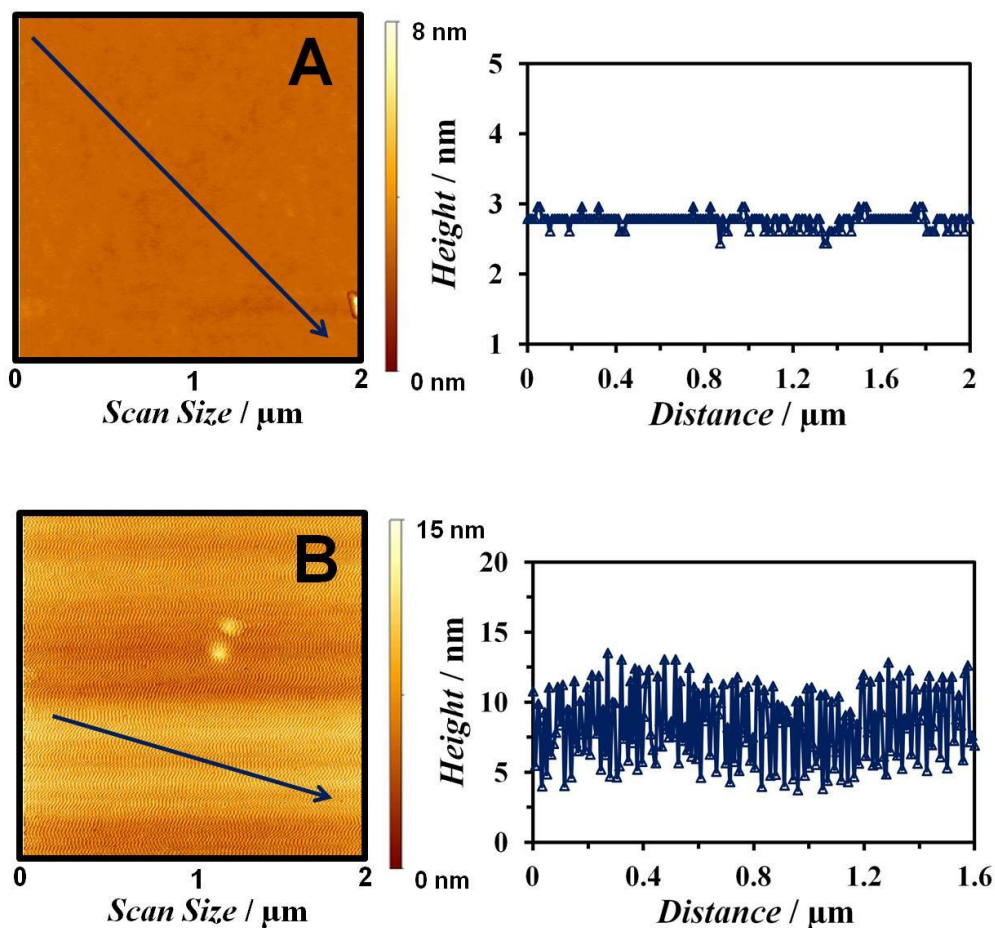


**Figure 7.3:** AFM characterization of clean and TEOOS-treated YSZ(100). AFM topography images with representative line scans for clean (A) YSZ(100) and (B) TEOOS-treated YSZ(100) samples. The AFM image of the plasma-cleaned YSZ(100) substrate prior to silane deposition (A) shows it to be featureless with a rms roughness of 0.07 nm which is consistent with a nearly atomically flat surface. A relatively uniform image was also obtained for the silanated/YSZ(100) sample (B), but it contained small wave-like features and had a rms roughness of 2.4 nm.

The uniformity of the silane film on the silanated-YSZ(100) sample was investigated by AFM, with the images and line analysis shown in Figure 7.3. The AFM

image of the plasma-cleaned YSZ(100) substrate prior to silane deposition (panel A) shows it to be featureless with a rms roughness of 0.07 nm which is consistent with a nearly atomically flat surface. A relatively uniform image was also obtained for the TEOSS-treated YSZ(100) sample (panel B), but it contained small wave-like features and had a rms roughness of 2.4 nm. As shown by the high noise level in the line scan, the wave-like features and resulting high rms roughness are likely artifacts due to a tip-surface instability which is perhaps caused by complex interactions between the tip and the “soft” easily reconfigured octyl-group capping layer. Regardless of the origin of these features, the image indicates that the CVD process produced a relatively uniform layer of the silane.

AFM was used to characterize the distribution of the Pd@CeO<sub>2</sub> structures that were deposited onto the pristine and functionalized YSZ(100) surfaces. As a base case for comparison, the interaction of the Pd@CeO<sub>2</sub> nanostructures with the pristine YSZ(100) surface will initially be considered.

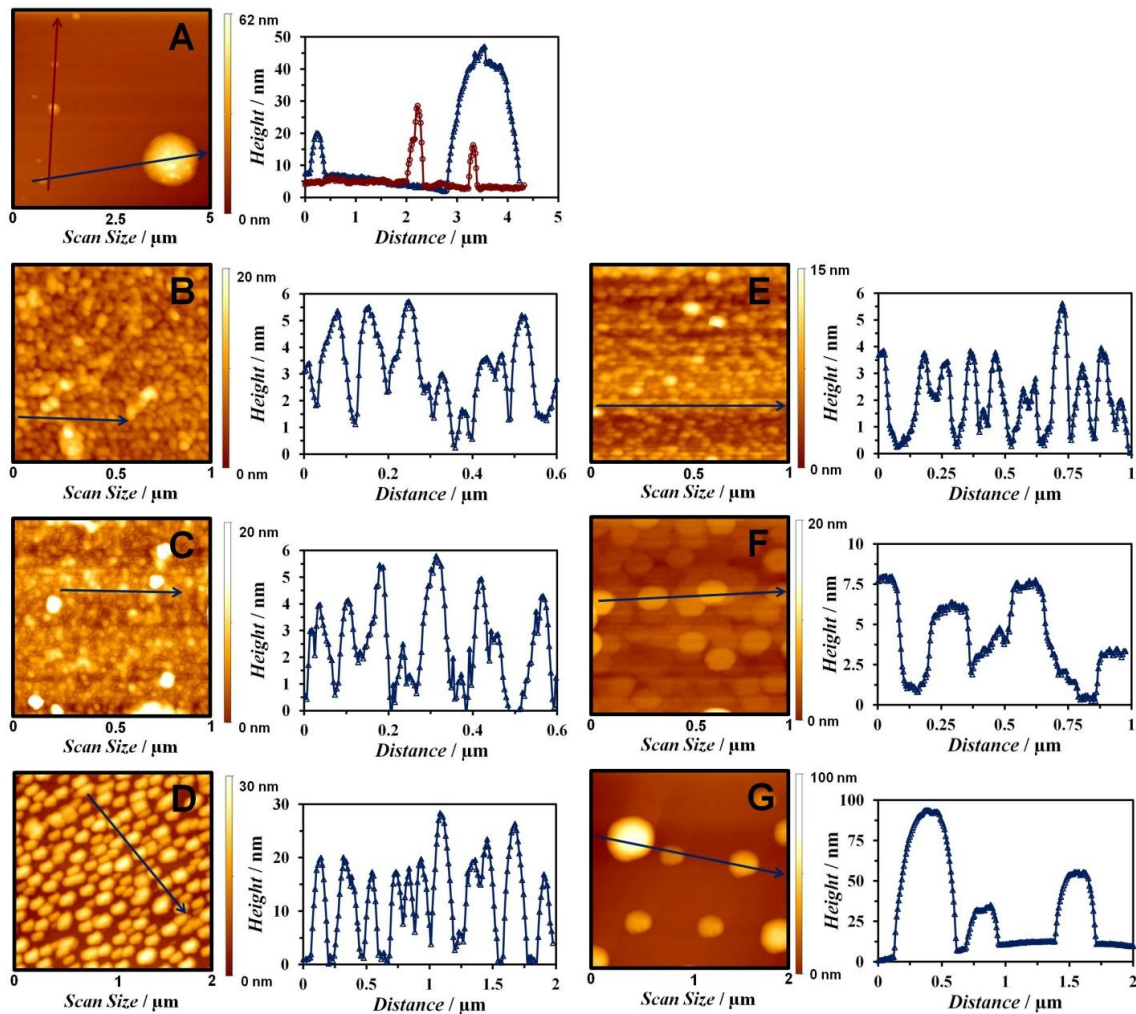


**Figure 7.4:** AFM topography images with representative line scans for Pd@CeO<sub>2</sub> and Pd nanoparticles deposited on clean and alkyl-silanated YSZ(100). Panel A corresponds to Pd@CeO<sub>2</sub> deposited on pristine YSZ(100) calcined in air 723 K. Panels B, C, D, corresponds to Pd@CeO<sub>2</sub> deposited on alkyl-siloxane functionalized YSZ(100) after calcination in air at 723 K (B), 973 K (C) and 1373 K (D). Panels E, F, and G corresponds to Pd nanoparticles deposited on pristine YSZ(100) after calcination in air at 723 K (E), 973 K (F) and 1373 K (G). Comparison of the images for the Pd@CeO<sub>2</sub> and Pd nanoparticles clearly demonstrates the high thermal stability of the Pd@CeO<sub>2</sub> nanoparticles.



A 5  $\mu\text{m}$  by 5  $\mu\text{m}$  topographic AFM image of the surface of this sample, along with several representative line scans are shown in Figure 7.4A. Note that the image is relatively free of features except for several randomly distributed, large structures that are 0.5 to 1.5  $\mu\text{m}$  in lateral dimension and 20 to 50 nm in height. These features were not observed prior to exposure to the Pd@CeO<sub>2</sub>/THF solution and are much larger than an individual Pd@CeO<sub>2</sub> particle; we, therefore, attribute them to large agglomerates of the Pd@CeO<sub>2</sub> particles. This result is consistent with repulsive interactions between hydrophobic alkyl-group capped Pd@CeO<sub>2</sub> particles in the deposition solution and the hydrophilic YSZ(100) surface, and illustrates the difficulty in obtaining a high dispersion of metal-metal oxide, core-shell catalysts on an oxide support using standard infiltration techniques.

As shown by the 1  $\mu\text{m}$  by 1  $\mu\text{m}$  AFM image in Figure 7.4B, significantly different results were obtained for the TEOOS-treated YSZ(100) surface. For this sample following calcination at 723 K in air to remove the alkyl groups, the AFM image contains a relatively uniform, well-dispersed layer of nanoparticles. Analysis of the line scans shows that the height of the particles is between 4-6 nm, which compares favorably with the diameter of the Pd@CeO<sub>2</sub> nanostructures of ~8 nm as determined by high-angle annular dark field, scanning transmission electron microscopy (STEM) and X-Ray Diffraction (XRD)<sup>9</sup>, demonstrating that the majority of the surface is covered by a single layer of the particles, although a few small agglomerates are also present in the image. (Note that the apparent lateral dimension of the particles in the AFM image represents a convolution of the diameter of each particle and that of the AFM tip and is therefore not representative of the actual particle diameter.)

**Table 7.1:** Ellipsometry thicknesses and water contact angle measurements

| Sample   | Thickness (nm) | RMS Roughness (nm) | Contact angle ( $^{\circ}$ , Water) |
|--|----------------|--------------------|-------------------------------------|
| Clean YSZ(100)   | -              | 0.07               | 70                                  |
| Silanated YSZ(100)   | 2.4            | 2.4                | 100                                 |
| Pd@CeO <sub>2</sub> on silanated YSZ(100) (973 K in air 4 h) | 7.4            | -                  | -                                   |

The thickness of the core-shell particle film was also estimated to be 7 nm by ellipsometry (Table 7.1), further corroborating this conclusion. These AFM results clearly show that the dodecanoic acid-capped Pd@CeO<sub>2</sub> nanostructures can be grafted onto the octyl-siloxane coated YSZ(100) surface, and that the distribution of the nanostructures can be maintained upon calcination in air at 723 K.

To investigate the thermal stability of the dispersed Pd@CeO<sub>2</sub> layer, the sample in Figure 7.4B was annealed in air to a series of successively higher temperatures and reexamined by AFM. The 1 μm by 1 μm image in Figure 7.4C was obtained after calcining in air at 973 K for 4 h. The features in this image are similar to those in the image of the 723 K calcined sample. There is no evidence of significant agglomeration of the Pd@CeO<sub>2</sub> particles and the line scans still give an average particle diameter of ~5 nm. As shown by the 2 μm by 2 μm AFM image in Figure 7.4D, calcination in air at 1373 K did cause some changes in the structure of the Pd@CeO<sub>2</sub> film. For this severe calcination temperature, the line scans indicate that the surface is covered with structures that are approximately 15 to 25 nm in height. Assuming that the individual Pd@CeO<sub>2</sub> particles retain their shape (~5 nm per particle), these structures consist of agglomerates containing 5 to 8 Pd@CeO<sub>2</sub> particles. It is noteworthy that while some agglomeration of the Pd@CeO<sub>2</sub> particles has clearly occurred, the overall dispersion of the Pd remains high.

The exceptional thermal stability of the Pd@CeO<sub>2</sub> nanostructures and their resistance to sintering on TEOOS-treated surfaces becomes readily apparent when one compares the AFM images of the Pd@CeO<sub>2</sub>/YSZ(100) sample in Figure 7.4B-7.4D to those obtained from the TEOOS-treated YSZ(100) surface on which Pd nanoparticles without a ceria coating were deposited, Figure 7.4E-7.4G. Note that for the latter sample after calcining in air at 723 K to remove the capping alkyl groups, the surface is covered with a high dispersion of particles that are ~3 nm in height (Figure 7.4E). The as-synthesized Pd particles are only 2 nm in diameter so the larger size observed here is either due to a volume expansion that occurs upon oxidation of the Pd or to partial

sintering upon heating to 723 K. Extensive sintering of the Pd particles is observed, however, upon heating to 973 K (Figure 7.4F), where the average Pd particle size has increased to ~6 nm in height with a lateral dimension approaching 0.25  $\mu\text{m}$ , indicating the agglomeration of the as-deposited, 2 nm diameter Pd nanoparticles into extended two-dimensional raft structures. Note that for these conditions little to no sintering of the Pd@CeO<sub>2</sub> particles was observed. Upon calcining to 1373 K additional sintering of the Pd particles is readily apparent with the 2  $\mu\text{m}$  by 2  $\mu\text{m}$  AFM image in Figure 7.4G showing only a few particles that are 0.25 to 0.5  $\mu\text{m}$  in diameter.

The chemical and thermal stability of the ceria shell in the Pd@CeO<sub>2</sub> particles was also investigated using x-ray photoelectron spectroscopy (XPS). C(1s) and Ce(3d) XP spectra of a Pd@CeO<sub>2</sub>/YSZ(100) sample calcined in air at 723 K and 973 K, and then subsequently annealed in ultra-high vacuum (UHV) at 700 K were collected.

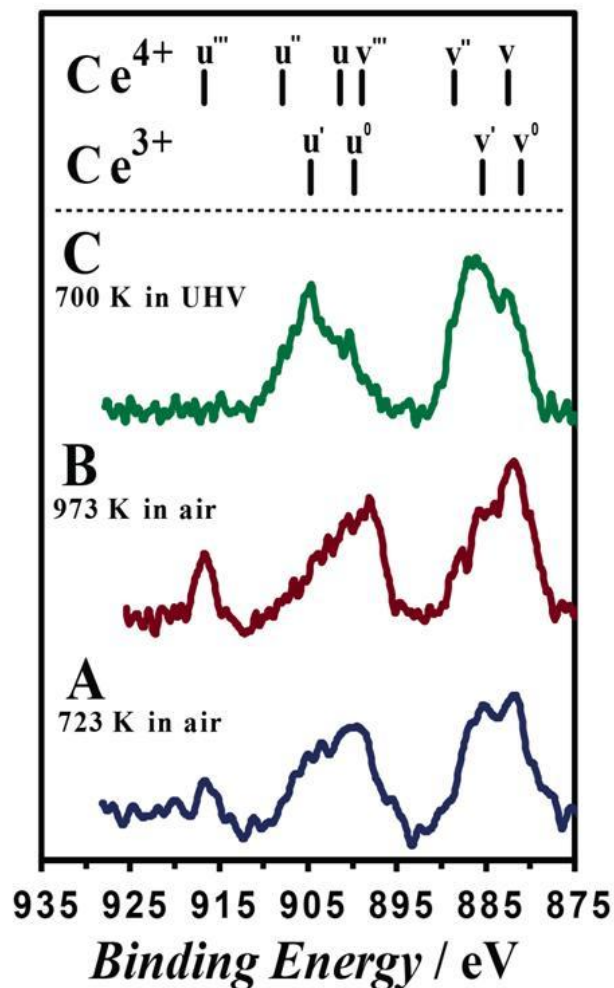


**Figure 7.5:** Ce(3d) XP spectra obtained from Pd@CeO<sub>2</sub> deposited on alkyl-siloxane functionalized YSZ(100) after calcination under different conditions. The sample was calcined in air at 723 K (A) and 973 K (B), and in ultra-high vacuum at 700 K (C).

No C(1s) signal was detected, confirming the oxidative removal of the capping alkyl groups. The Ce(3d) spectra in Figure 7.5 contains peaks labeled u and v which correspond to the 3d<sub>3/2</sub> and 3d<sub>5/2</sub> spin-orbit states of the cerium cations, respectively, with the u''/v'' doublet being due to the primary photoemission from Ce<sup>4+</sup> cations, and the associated u'/v' and u<sup>0</sup>/v<sup>0</sup> doublets being shakedown features resulting from transfer of electrons during photoemission from filled O(2p) orbitals to empty Ce(4f) orbitals<sup>14</sup>. Ce<sup>3+</sup> cations give rise to the u'/v' (primary photoemission) and u<sup>0</sup>/v<sup>0</sup> (shakedown) doublets.

The spectrum of the 723 K, air calcined sample (Figure 7.5A) contains a mixture of  $\text{Ce}^{3+}$  and  $\text{Ce}^{4+}$ . Based on the reported thermodynamic properties of bulk and polycrystalline ceria, for the conditions used in these experiments the  $\text{CeO}_2$  would be expected to be fully oxidized (i.e.  $\text{Ce}^{4+}$ )<sup>15-17</sup>. The appearance of both  $\text{Ce}^{3+}$  and  $\text{Ce}^{4+}$  in the spectrum of this sample, therefore, indicates that the nano-structured ceria shells in the  $\text{Pd@CeO}_2$  particles in this sample are more reducible than normal catalytic forms of  $\text{CeO}_2$ . In contrast, the XP spectrum of the 973 K, air calcined sample (Figure 7.5B) contains primarily  $\text{Ce}^{4+}$ , demonstrating that this treatment makes the ceria less reducible and more bulk like. This result is noteworthy since reactivity studies of supported  $\text{Pd@CeO}_2$  catalysts have shown that high oxidation activity is obtained only after calcining in air to temperatures in excess of 1123 K<sup>9</sup>. More study is needed to determine the origin of this effect, but it may be due to a change from an amorphous to more crystalline ceria shell upon high-temperature air calcination.

While the 973 K air-calcined sample appears to be less reducible than the 723 K air-calcined sample, it is still more easily reduced than that of bulk  $\text{CeO}_2$ . This is demonstrated by spectrum C in Figure 7.5C which shows that heating this sample to 700 K in UHV was sufficient to reduce all the  $\text{Ce}^{4+}$  to  $\text{Ce}^{3+}$  (i.e. reduction of  $\text{CeO}_2$  to  $\text{Ce}_2\text{O}_3$ ) in spite of the fact that under UHV conditions, bulk  $\text{CeO}_2$  is thermodynamically stable at this temperature<sup>15-17</sup>. Furthermore, CO temperature-programmed desorption (TPD) measurements indicate that significant structural rearrangement of the oxide shell occurs upon reduction. CO desorption spectra obtained from the 973 K air calcined and 700 K

UHV annealed samples dosed with 50 L of CO at 260 K are shown in Figure 7.6.

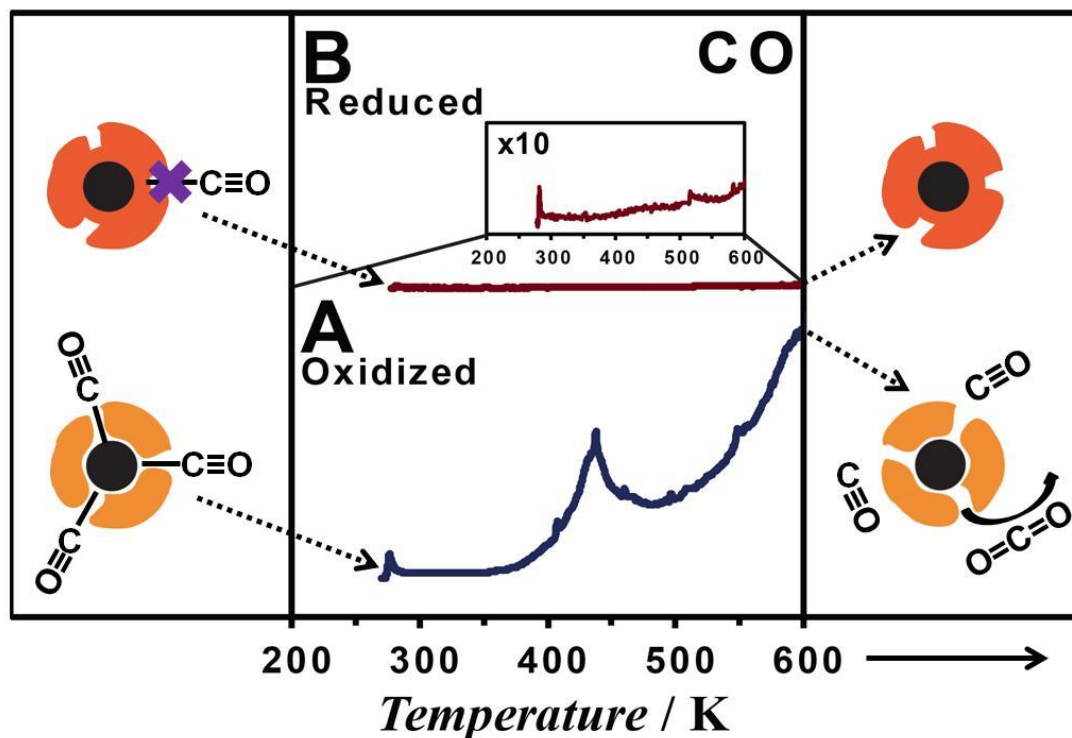


**Figure 7.6:** CO-TPD data and schematic representation of changes in shell morphology for oxidized and reduced Pd@CeO<sub>2</sub>/YSZ(100) catalysts. The CO-TPD results obtained after 50 L CO dose at 260 K on Pd@CeO<sub>2</sub> deposited on silanated YSZ(100) calcined at 973 K in air (A) and 700 K in vacuum (B). The y-axis in the figure corresponds to the m/e 28 mass spectrometer signal in arbitrary units. The two spectra have been offset to facilitate comparison.

For the air calcined sample, CO and a smaller amount of CO<sub>2</sub> (not shown in the figure) desorb at 440 K, which is the expected temperature for CO desorption from Pd<sup>18</sup>. In contrast, CO was found not to adsorb on the 700 K vacuum annealed sample. This demonstrates that the metal is not accessible in this sample and suggests that, upon reduction, the ceria shell loses its porosity and completely encapsulates the underlying Pd nanoparticle as shown schematically in Figure 7.6. This result is in concordance with previous studies of CO adsorption on high surface area supported Pd@CeO<sub>2</sub> catalysts<sup>11</sup>.

While the AFM results presented above vividly demonstrate the high thermal stability of Pd@CeO<sub>2</sub> particles grafted onto a TEOOS-coated YSZ(100) surface, one must recognize that this method for dispersing the particles results in a siloxane interlayer between the support and the core-shell particles that may alter catalytic properties. For example, Rocchini et al. have shown that Si impurities can significantly enhance the reducibility of ceria<sup>19</sup>. For some applications, such as electrodes in solid oxide fuel cells, the siloxane layer may also interfere with other properties such as oxygen ion transport through the electrolyte<sup>20-22</sup>. In order to investigate the influence of the SiO<sub>x</sub> layer on catalytic properties, we compared the rates of methane oxidation over catalysts consisting of Pd@CeO<sub>2</sub> particles grafted onto a high surface area  $\gamma$ -Al<sub>2</sub>O<sub>3</sub> support that was pre-treated with either TEOSS or TDPA. Like TEOSS, TDPA reacts with hydroxyl groups on the oxide surface to form a hydrophobic, alkyl-functionalized phosphonate layer onto which the Pd@CeO<sub>2</sub> particles can be grafted; however, unlike the siloxane linkage, the phosphate group is removed upon calcination in air at 1123 K resulting in the Pd@CeO<sub>2</sub> particles being directly adsorbed on the  $\gamma$ -Al<sub>2</sub>O<sub>3</sub> surface.



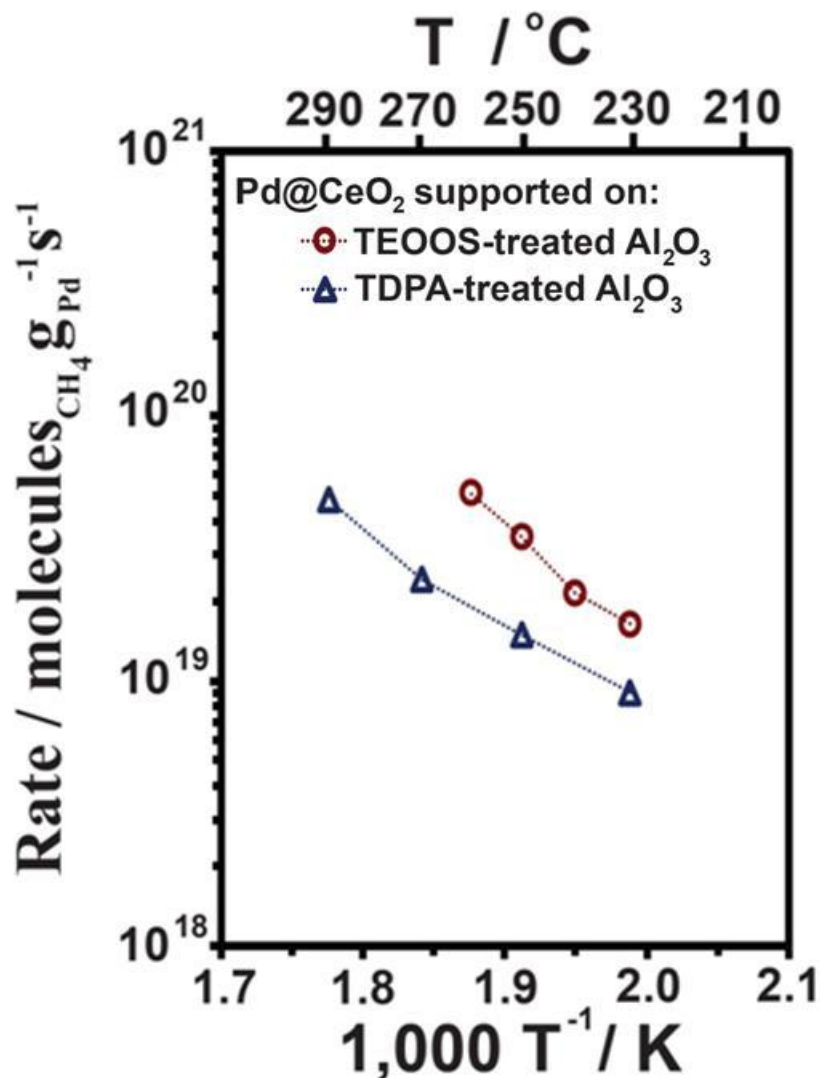


**Figure 7.7:** Reaction rate data for CH<sub>4</sub> oxidation. Pd@CeO<sub>2</sub> core-shell catalyst supported on (○) TEOOS-treated  $\gamma$ -Al<sub>2</sub>O<sub>3</sub> and (Δ) TDPA-treated  $\gamma$ -Al<sub>2</sub>O<sub>3</sub> calcined in air at 1123 K for 6 hrs prior to rate measurements. The Pd weight loading in each catalyst was 1 %.

Figure 7.7 shows rate data for CH<sub>4</sub> oxidation over the Pd@CeO<sub>2</sub>/TEOSS/Al<sub>2</sub>O<sub>3</sub> and Pd@CeO<sub>2</sub>/TDPA/Al<sub>2</sub>O<sub>3</sub> samples that had previously been calcined in air at 1123 K. Note that similar rates were obtained for both samples indicating that the siloxane layer does not influence the catalytic properties of the supported Pd@CeO<sub>2</sub> particles and is also not required to maintain their high dispersion. Thus, it appears that direct interaction of

CeO<sub>2</sub> shell with the support, possibly through the formation of Al-O-Ce linkages is sufficient to prevent sintering upon high-temperature calcination. It is also noteworthy that, consistent with previous reports for Pd@CeO<sub>2</sub>, the rates from these catalysts were found to be an order of magnitude higher than that obtained from a conventional 1 wt. % Pd/CeO<sub>2</sub> catalyst<sup>9</sup>.

#### **7.4 Conclusion**

In conclusion, the results of this study demonstrate that monolayer films of Pd@CeO<sub>2</sub> core-shell, nanocomposites can be produced on a planar YSZ(100) support using alkyl coupling agents, and that these films exhibit exceptionally high thermal stability and resistance to sintering compared to bare Pd particles on the same support. The AFM images provide a direct measure of dispersion and show little to no sintering of the Pd@CeO<sub>2</sub> particles occurs for temperatures up to 973 K, with only moderate sintering at temperatures as high as 1373 K. The high activity of Pd@CeO<sub>2</sub> nanostructures grafted onto  $\gamma$ -Al<sub>2</sub>O<sub>3</sub> following calcination to 1123 K also demonstrates that this stability is maintained even when high surface area supports are employed. Additionally it was shown that the ceria shells in these nanostructures have unique properties being more reducible than bulk ceria which may play a role in the high activity of these materials for some reactions, such as methane combustion.

## 7.5 References

- 1 Bakhmutsky, K. *et al.* A Versatile Route to Core-Shell Catalysts: Synthesis of Dispersible M@Oxide (M=Pd, Pt; Oxide=TiO<sub>2</sub>, ZrO<sub>2</sub>) Nanostructures by Self-Assembly. *Chemsuschem* **5**, 140-148, doi:DOI 10.1002/cssc.201100491 (2012).
- 2 Kim, J. S. *et al.* Highly Active and Thermally Stable Core-Shell Catalysts for Solid Oxide Fuel Cells. *J Electrochem Soc* **158**, B596-B600, doi:Doi 10.1149/1.3571039 (2011).
- 3 De Rogatis, L. *et al.* Embedded Phases: A Way to Active and Stable Catalysts. *Chemsuschem* **3**, 24-42, doi:DOI 10.1002/cssc.200900151 (2010).
- 4 Yeung, C. M. Y. *et al.* Engineering Pt in ceria for a maximum metal-support interaction in catalysis. *J Am Chem Soc* **127**, 18010-18011, doi:Doi 10.1021/Ja056102c (2005).
- 5 Tedsree, K. *et al.* Hydrogen production from formic acid decomposition at room temperature using a Ag-Pd core-shell nanocatalyst. *Nat Nanotechnol* **6**, 302-307, doi:Doi 10.1038/Nnano.2011.42 (2011).
- 6 Joo, S. H. *et al.* Thermally stable Pt/mesoporous silica core-shell nanocatalysts for high-temperature reactions. *Nat Mater* **8**, 126-131, doi:Doi 10.1038/Nmat2329 (2009).
- 7 Park, J. N. *et al.* Highly Active and Sinter-Resistant Pd-Nanoparticle Catalysts Encapsulated in Silica. *Small* **4**, 1694-1697, doi:DOI 10.1002/sml.200800895 (2008).

- 8 Arnal, P. M., Comotti, M. & Schuth, F. High-temperature-stable catalysts by hollow sphere encapsulation. *Angew Chem Int Edit* **45**, 8224-8227, doi:DOI 10.1002/anie.200603507 (2006).
- 9 Cargnello, M. *et al.* Exceptional Activity for Methane Combustion over Modular Pd@CeO<sub>2</sub> Subunits on Functionalized Al<sub>2</sub>O<sub>3</sub>. *Science* **337**, 713-717, doi:DOI 10.1126/science.1222887 (2012).
- 10 Cargnello, M., Wieder, N. L., Montini, T., Gorte, R. J. & Fornasiero, P. Synthesis of Dispersible Pd@CeO<sub>2</sub> Core-Shell Nanostructures by Self-Assembly. *J Am Chem Soc* **132**, 1402-1409, doi:Doi 10.1021/Ja909131k (2010).
- 11 Wieder, N. L. *et al.* Study of the Water-Gas-Shift Reaction on Pd@CeO<sub>2</sub>/Al<sub>2</sub>O<sub>3</sub> Core-Shell Catalysts. *J Phys Chem C* **115**, 915-919, doi:Doi 10.1021/Jp102965e (2011).
- 12 Yoon, K. *et al.* A Highly Reactive and Sinter-Resistant Catalytic System Based on Platinum Nanoparticles Embedded in the Inner Surfaces of CeO<sub>2</sub> Hollow Fibers. *Angew Chem Int Edit* **51**, 9543-9546, doi:DOI 10.1002/anie.201203755 (2012).
- 13 Cargnello, M. *et al.* Novel embedded Pd@CeO<sub>2</sub> catalysts: a way to active and stable catalysts. *Dalton T* **39**, 2122-2127, doi:Doi 10.1039/B916035c (2010).
- 14 Fujimori, A. 4f-Level and Core-Level Photoemission Satellites in Cerium Compounds. *Phys Rev B* **27**, 3992-4001, doi:DOI 10.1103/PhysRevB.27.3992 (1983).

- 15 Zhou, G., Hanson, J. & Gorte, R. J. A thermodynamic investigation of the redox properties of ceria-titania mixed oxides. *Appl Catal a-Gen* **335**, 153-158, doi:DOI 10.1016/j.apcata.2007.11.011 (2008).
- 16 Zhou, G., Shah, P. R., Montini, T., Fornasiero, P. & Gorte, R. J. Oxidation enthalpies for reduction of ceria surfaces. *Surf Sci* **601**, 2512-2519, doi:DOI 10.1016/j.susc.2007.04.238 (2007).
- 17 Zhou, G., Shah, P. R., Kim, T., Fornasiero, P. & Gorte, R. J. Oxidation entropies and enthalpies of ceria-zirconia solid solutions. *Catal Today* **123**, 86-93, doi:DOI 10.1016/j.cattod.2007.01.013 (2007).
- 18 Guo, X. C. & Yates, J. T. Dependence of Effective Desorption Kinetic-Parameters on Surface Coverage and Adsorption Temperature - Co on Pd(111). *J Chem Phys* **90**, 6761-6766, doi:Doi 10.1063/1.456294 (1989).
- 19 Rocchini, E. *et al.* Relationships between structural/morphological modifications and oxygen storage-redox behavior of silica-doped ceria. *J Catal* **194**, 461-478, doi:DOI 10.1006/jcat.2000.2954 (2000).
- 20 Zhang, T. S. *et al.* Different conduction behaviors of grain boundaries in SiO<sub>2</sub>-containing 8YSZ and CGO20 electrolytes. *Solid State Ionics* **177**, 1227-1235, doi:DOI 10.1016/j.ssi.2006.05.006 (2006).
- 21 Lankin, M., Du, Y. H. & Finnerty, C. A Review of the Implications of Silica in Solid Oxide Fuel Cells. *J Fuel Cell Sci Tech* **8**, doi:Artn 054001, Doi 10.1115/1.4003980 (2011).

- 22 Hauch, A., Jensen, S. H., Bilde-Sorensen, J. B. & Mogensen, M. Silica segregation in the Ni/YSZ electrode. *J Electrochem Soc* **154**, A619-A626, doi:Doi 10.1149/1.2733861 (2007).

## **Chapter 8. Synthesis and Stability of Pd@CeO<sub>2</sub> Core-Shell Catalyst Films in Solid Oxide Fuel Cell Anodes\***

### **Summary**

Sub-monolayer films of highly catalytically active Pd@CeO<sub>2</sub> nanocomposites were deposited onto porous solid oxide fuel cells (SOFC) anodes which were functionalized with triethoxy(octyl)silane (TEOOS). SEM results show that in contrast to bare Pd particles, Pd@CeO<sub>2</sub> particles grafted onto the surface of the ceramic anode remained highly dispersed even after calcination in air at 1373 K. SOFC with anodes that were modified with very low loadings (0.01 wt. %) of the Pd@CeO<sub>2</sub> nanocomposites were shown to exhibit good electrochemical performance when operating with either H<sub>2</sub> or CH<sub>4</sub> fuels at 973 K. This performance was also maintained after annealing the anode in air at 1173 K. These results demonstrate a strategy for using very low loadings of highly active metal catalysts to enhance the activity of ceramic anodes while maintaining long-term stability.

---

\* This chapter has been submitted for publication.

## 8.1 Introduction

Several of us have previously demonstrated the use of Pd@CeO<sub>2</sub> nanocomposites to significantly enhance the catalytic oxidation activity of an SOFC anode consisting of a porous YSZ scaffold coated with a thin film of LSCM<sup>1</sup>. In this work, the catalyst was deposited into the anode using infiltration of a Pd@CeO<sub>2</sub> dispersion in tetrahydrofuran (THF) solution. While this produced a high-performance anode that did not undergo significant deactivation due to loss of catalyst surface area upon calcination at 1173 K, a high 10 wt. % loading of the Pd@CeO<sub>2</sub> (1 wt. % Pd and 9 wt. % CeO<sub>2</sub>) was required in order to obtain a sufficient concentration of the catalyst particles in the electrochemically active zone near the electrode-electrolyte interface. SEM analysis also indicated that this synthesis method produced large agglomerates of the Pd@CeO<sub>2</sub> particles. Given the relatively high cost of Pd, much more efficient use of the catalyst will be required for this method of enhancing anode activity to be practical. This could be achieved by producing a highly-dispersed layer of individual Pd@CeO<sub>2</sub> particles on the surface of the anode.

In order to address this issue and obtain high catalyst dispersion, we have recently developed a method to graft individual Pd@CeO<sub>2</sub> particles onto an oxide surface<sup>2</sup>. This method relies on initially coating the surface of the oxide support (or anode) with hydrophobic alkyl groups via reaction with triethoxy(octyl)silane (TEOOS) as surface modifier. The Pd@CeO<sub>2</sub> particles are also functionalized with hydrophobic groups in order to stabilize them in organic solvents such as THF. Upon infiltration, Van der Waals interactions between the hydrophobic groups on both the YSZ surface and the Pd@CeO<sub>2</sub> particles help them stick to the surface and prevents their agglomeration. The organic groups are then subsequently oxidatively removed by calcination in air. Characterization



of the deposition of Pd@CeO<sub>2</sub> particles on model planar YSZ single crystal supports has demonstrated that this procedure produces a sub-monolayer coverage of individual Pd@CeO<sub>2</sub> particles<sup>2</sup>.

While this approach produces a highly dispersed catalyst layer, the functionalization of the oxide surface using an organosilane coupling agent may be problematic for use with SOFC electrodes, since Si is known to migrate to the grain boundaries in YSZ (the electrolyte of choice for most SOFCs) and this may detrimentally affect oxygen ion transport, reducing the overall performance<sup>3-5</sup>. We anticipate that the amount of SiO<sub>x</sub> deposited is quite small (monolayer coverage), therefore its effect on transport properties will be negligible.

In the present study we have used the deposition method outlined above to control both the loading and dispersion of Pd@CeO<sub>2</sub> catalytic nanoparticles in SOFC composite anodes which use a conductive LSCM layer for electron transport. The results of this study demonstrate that a highly-dispersed and thermally stable layer of Pd@CeO<sub>2</sub> nanostructures can be produced in the porous electrode and that electrodes incorporating less than 0.01 wt. % Pd@CeO<sub>2</sub> exhibit excellent performance.

## 8.2 Experimental

Solid oxide fuel cells 1-cm in diameter were used in all fuel cell measurements. These cells were fabricated using porous-dense-porous tri-layer YSZ wafers that were produced using tape casting methods that have been described in detail previously.<sup>6</sup> For each cell, the dense electrolyte layer was 65 μm thick and 1cm in diameter. The 60 %

porous YSZ layers on each side of the dense electrolyte layer were 50  $\mu\text{m}$  thick with a BET surface area  $0.3 \text{ m}^2\text{g}^{-1}$ .

45 wt. % of Sr-doped lanthanum chromium manganate,  $\text{La}_{0.8}\text{Sr}_{0.2}\text{Cr}_{0.5}\text{Mn}_{0.5}\text{O}_3$  (LSCM) anode was added to one porous layer using multiple cycles of infiltration of an aqueous solution containing dissolved  $\text{La}(\text{NO}_3)_3 \cdot 6\text{H}_2\text{O}$  (Alfa Aesar, 99.9%),  $\text{Sr}(\text{NO}_3)_2$  (Alfa Aesar, 99%),  $\text{Cr}(\text{NO}_3)_3 \cdot 9\text{H}_2\text{O}$  (Alfa Aesar, 98.5%) and  $\text{Mn}(\text{NO}_3)_3 \cdot 4\text{H}_2\text{O}$  (Alfa Aesar, 99.98%) in the appropriate molar ratios, followed by calcination in air at 873 K. After the infiltration steps the composite anode was calcined to 1473 K for 4 h to form the perovskite structure. 40 wt. % of Sr-doped lanthanum ferrite,  $\text{La}_{0.8}\text{Sr}_{0.2}\text{FeO}_3$  (LSF), was added to the other porous layer to form a cathode using multiple cycles of infiltration of an aqueous solution containing dissolved  $\text{La}(\text{NO}_3)_3 \cdot 6\text{H}_2\text{O}$  (Alfa Aesar, 99.9%),  $\text{Sr}(\text{NO}_3)_2$  (Alfa Aesar, 99%) and  $\text{Fe}(\text{NO}_3)_3 \cdot 9\text{H}_2\text{O}$  (Fisher Scientific) in the appropriate molar ratios, followed by calcination in air at 723 K. Citric acid (Fisher Scientific) was also added as a complexing agent to aid in the formation of a more homogeneous mixture. The composite cathode was then calcined to 1123 K for 4 h to form the perovskite structure. Previous studies have shown that cathodes of this design have an ASR of  $\sim 0.2 \text{ } \Omega \text{ cm}^2$  in air at 973 K<sup>7,8</sup>.

The synthesis of the Pd@CeO<sub>2</sub> core-shell structures (1:9 Pd/Ce weight ratios) is described in detail in previous publications<sup>9,10</sup>. For most cells prior to the addition of the catalyst, the surface of the anode (45 wt. % of LSCM) was functionalized with long-chain alkyl groups via reaction with Triethoxy(octyl)silane (TEOOS, Sigma Aldrich 97.5 %). The TEOOS (0.1 ml drop) was added to the porous anode layer by infiltration followed by calcination to 403 K for 4 h which was found to be sufficient to induce reaction. The

catalyst was then added via infiltration of an amount of a  $1.5 \times 10^{-3}$  M Pd@CeO<sub>2</sub>/THF solution which contained the theoretical number of core-shell particles required to form a monolayer over the TEOOS-treated LSCM surface in the LSCM/YSZ composite anode. A similar procedure was also used to deposit un-coated 2 nm Pd particles. The samples were then calcined to 723 K and 1123 K in air for 4 h to remove the stabilizing organic ligands. For some cells, an aqueous solution of (NH<sub>3</sub>)<sub>4</sub>Pd(NO<sub>3</sub>)<sub>2</sub> (Alfa Aesar, 99.9%) was used to deposit Pd.

The anodes were reduced in humidified H<sub>2</sub> (3% H<sub>2</sub>O) at 973 K prior to cell testing with humidified H<sub>2</sub> or dry CH<sub>4</sub>. Silver current collectors (paste and wires) were applied to both electrodes for electrical connections and the cells were mounted onto an alumina tube using a ceramic adhesive (Aremco, Ceramabond 552). All the cell tests were performed with the cathode exposed to ambient air. Electrochemical impedance spectra were measured between 0.1 Hz and 300 kHz with a 1 mA AC perturbation. Both impedance spectra and V-i polarization curves were measured using a Gamry Instruments potentiostat.

For scanning electron microscopy (SEM) studies, the sample preparation was similar to that used for the fuel cell anodes as described above, except that the surface of the 60 % porous YSZ electrode (without 45 wt. % of LSCM) was functionalized with TEOOS prior to addition of the THF solution of Pd@CeO<sub>2</sub> and 2nm un-coated Pd particles. The samples were then calcined to 973 K and 1373 K in air for 4 h. The morphological structure of the porous composites was determined using an FEI Quanta 600 SEM.

### 8.3 Results and Discussion

#### *SEM characterization of Pd@CeO<sub>2</sub> on porous YSZ*

As reported previously and described above, nearly monolayer films of highly catalytically active, Pd@CeO<sub>2</sub> core-shell nanocomposites can be grafted onto a high surface area metal oxide powders or planar supports which have previously been functionalized with TEOOS<sup>2,9,11-13</sup>. SEM was used to assess whether this approach can be used to deposit sub-monolayer films of Pd@CeO<sub>2</sub> onto the surface of a porous SOFC electrode. Since an LSCM thin film is known to undergo microstructural changes upon reduction<sup>14</sup>, in these studies YSZ was used as the substrate rather than LSCM-coated YSZ in order to more easily differentiate between the Pd@CeO<sub>2</sub> particles and the support. As described in the experimental section, the surface of a 60 % porous YSZ electrode was initially functionalized by reaction with TEOOS and then infiltrated with a THF solution of Pd@CeO<sub>2</sub> that contained the theoretical number of core-shell particles to form a monolayer. The sample was then calcined at 973 K in air for 4 h to remove the organic groups. An SEM image of this sample is displayed in Figure 8.1. For comparison purposes, SEM images of a TEOOS-treated porous YSZ electrode which was infiltrated with 2 nm Pd particles (i.e. Pd particles without the CeO<sub>2</sub> shell), and a porous YSZ electrode that was not treated with TEOOS prior to deposition of the Pd@CeO<sub>2</sub> particles are also included in the figure.

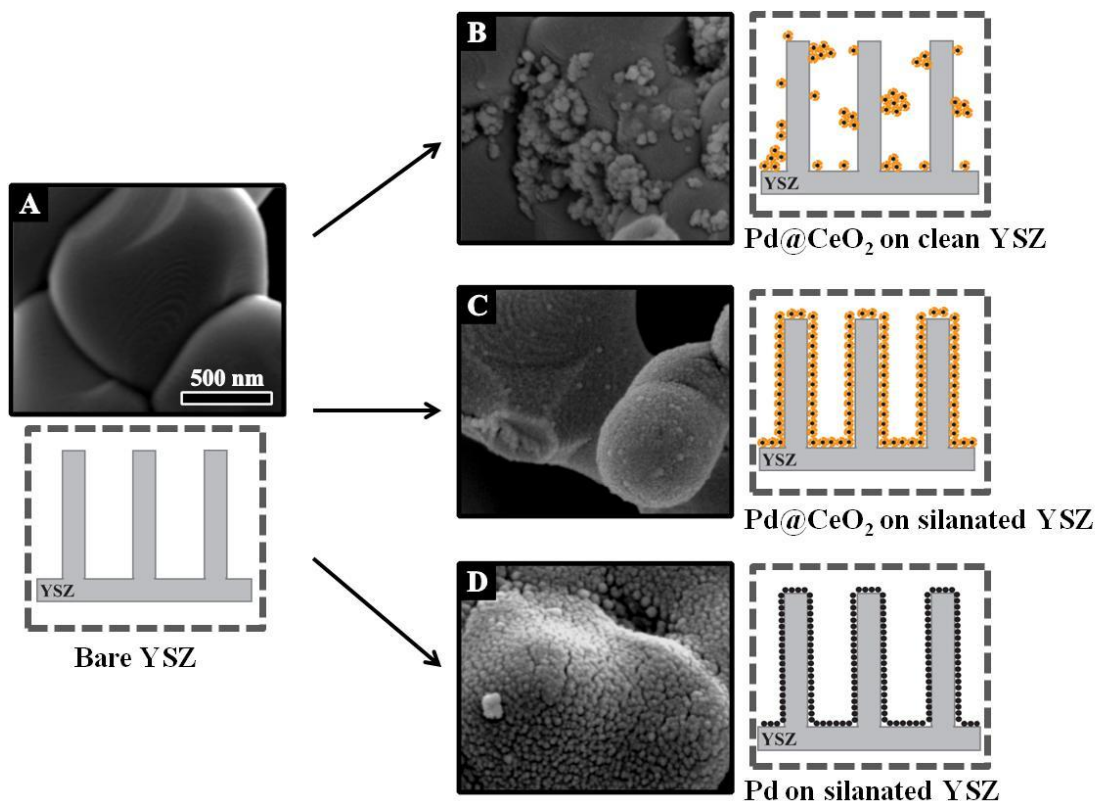


**Figure 8.1:** SEM images, with the schematic representation of bare YSZ matrix (Panel A), Pd@CeO<sub>2</sub> nanoparticles deposited on: clean YSZ porous electrode (Panel B) and silanated YSZ porous electrode (Panel C). 2 nm un-coated Pd nanoparticles deposited on silanated YSZ porous electrode (Panel D). All samples calcined at 973 K in air.

As we have demonstrated previously<sup>2</sup>, the hydrophobic, alkyl-capped Pd@CeO<sub>2</sub> particles interact only weakly with the hydrophilic, untreated YSZ substrate which results in the formation of agglomerates of the core-shell particles during the infiltration and subsequent calcination processes. This is demonstrated by the SEM image of the pristine YSZ substrate infiltrated with the Pd@CeO<sub>2</sub>/THF solution and then calcined at 973 K in air displayed in Figure 8.1 (image B). Note that large regions of the substrate are devoid of features while others contain assemblies of the core-shell particles which are not present in the image of the YSZ surface prior to infiltration (image A).

As expected, a significantly different result was obtained when the Pd@CeO<sub>2</sub> nanostructures were deposited onto the TEOOS-treated porous YSZ electrode surface. The TEOOS treatment produces a siloxane layer with attached long alkyl chains rendering the surface hydrophobic. The hydrophobic Pd@CeO<sub>2</sub> particles can have at this point favorable interactions via Van der Waals forces with the treated YSZ which helps disperse them and prevent agglomeration during deposition. As shown in image C in Figure 8.1, this high dispersion of the Pd@CeO<sub>2</sub> particles is maintained after calcination in air at 973 K to oxidatively remove the organic byproducts. In contrast, agglomeration was obtained for a sample prepared using 2 nm Pd particles that were not coated with CeO<sub>2</sub>. These particles were also capped with alkyl groups to stabilize them in the THF solution and would therefore be expected to form a well-dispersed layer upon infiltration into the TEOOS-treated YSZ in a manner similar to that for Pd@CeO<sub>2</sub>. Calcination in air at 973 K, however, was sufficient to cause partial agglomeration and sintering of the Pd nanoparticles as evidenced by the more highly textured surface (larger particles) in the SEM image (image D).

The exceptionally high thermal stability of the Pd@CeO<sub>2</sub> catalyst compared to uncoated Pd particles is more readily apparent in Figure 8.2 which displays SEM images obtained after heating samples similar to those in Figure 8.1 to a much higher temperature (1373 K) in air for 4 h.

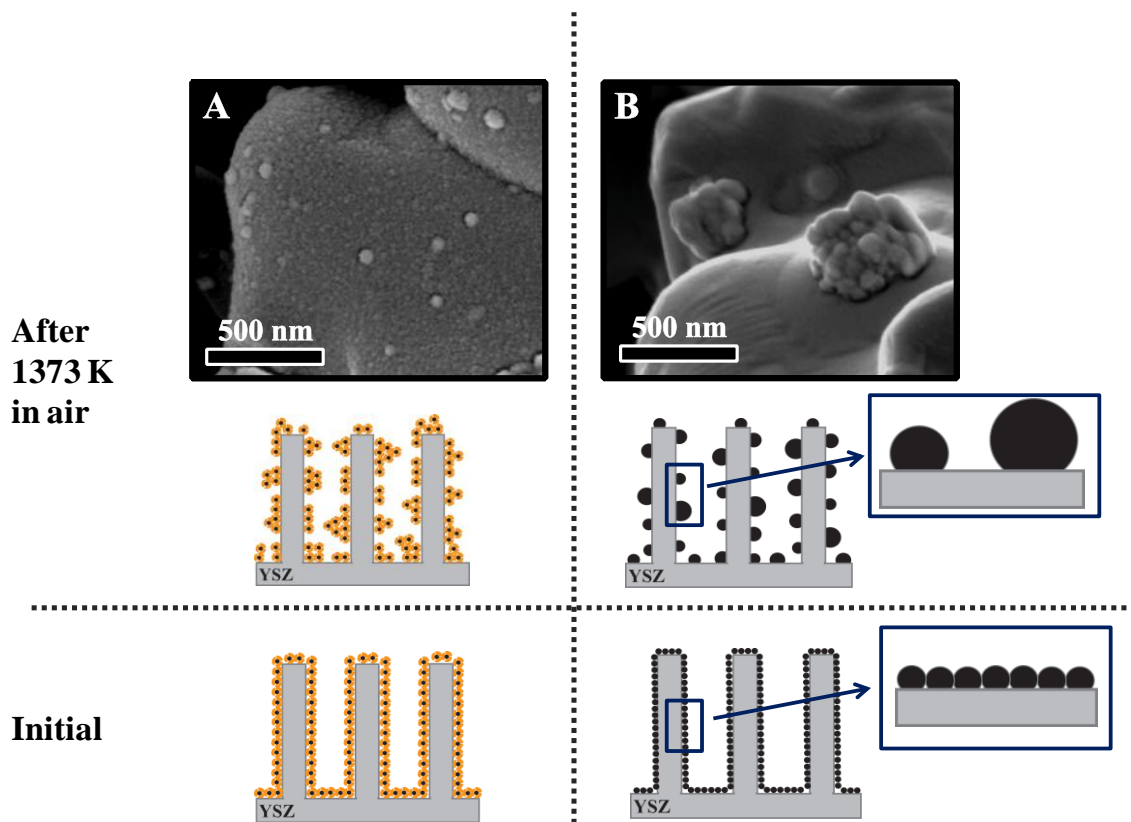


**Figure 8.2:** SEM images, with the schematic representation of the agglomeration of Pd@CeO<sub>2</sub> (Panel A) and 2 nm un-coated Pd (Panel B) nanoparticles deposited on silanated YSZ porous electrode after samples calcined at 1373 K in air.

Note that this treatment caused very little change in the structure of the well-dispersed Pd@CeO<sub>2</sub> catalyst layer that had been grafted onto the TEOOS-treated substrate (image A). In contrast, the SEM image for the sample synthesized with the uncoated 2 nm Pd nanoparticles shows extensive sintering of the Pd particles resulting in the formation of a small number of particles with diameters between 250 and 500 nm. This decrease in dispersion of the Pd and the resulting loss in surface area would be expected to greatly reduce the catalytic activity and performance on an anode. It is noteworthy that these results are consistent with those obtained in our previous AFM study of Pd@CeO<sub>2</sub> and

Pd nanoparticles deposited onto a TEOOS-treated planar, single crystal YSZ(100) support<sup>2</sup>.

While these results demonstrate that a high dispersion of Pd@CeO<sub>2</sub> particles can be produced on TEOOS-treated YSZ surfaces, an electronically conducting phase such as LSCM is required for a working electrode. As noted above, structural characterization of the Pd@CeO<sub>2</sub> particles on a LSCM/YSZ composite electrode is problematic due to the complex structure. We have demonstrated, however, that like YSZ, organosiloxane layers can be deposited on LSCM using TEOOS. Evidence for this is presented in Figure 8.3 which displays photographs of test tubes containing water and a small amount of pristine and TEOOS-treated YSZ or LSCM powders.

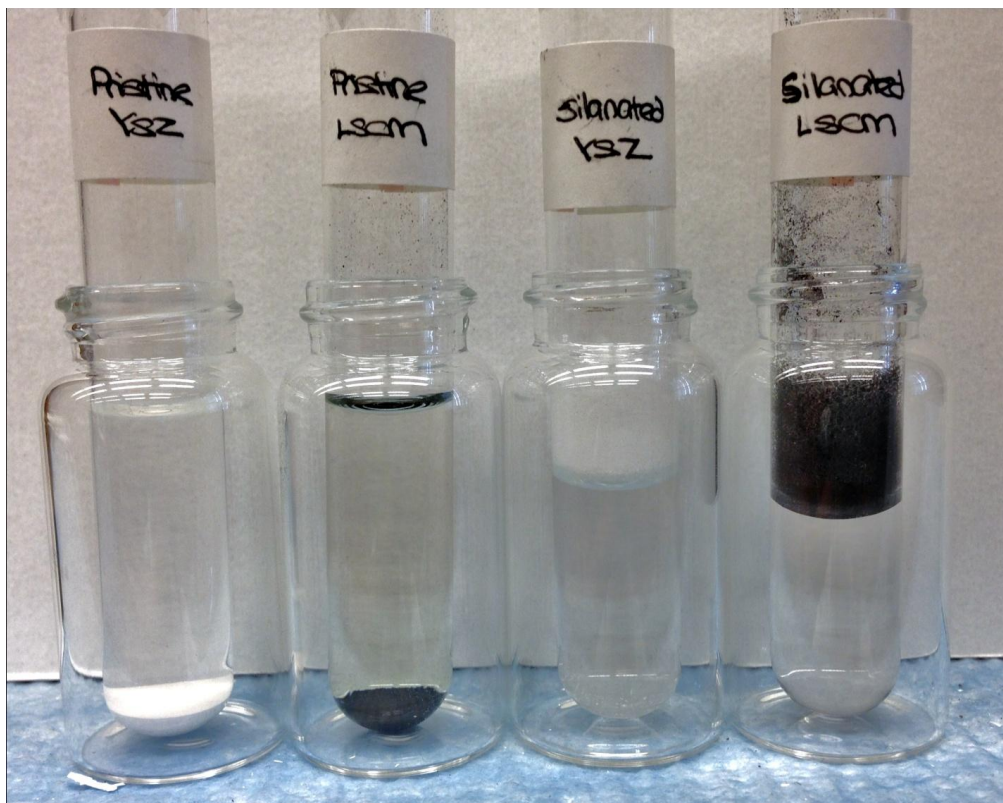


**Figure 8.3:** Image of hydrophobicity test with YSZ and LSCM, before and after treatment with TEOOS. 0.1 g of each powder was then placed in a test tube filled with 5 ml of H<sub>2</sub>O.



The surfaces of the pristine powders are terminated with hydroxyl groups making them hydrophilic and both the YSZ and LSCM are easily wetted and sink to the bottom of the tube. On the other hand, after treatment with TEOOS, both the YSZ and LSCM powders float on the surface of the water which is consistent with them being coated with a hydrophobic organosiloxane layer. Based on this result we anticipate that the Pd@CeO<sub>2</sub> particles can be grafted onto the LSCM using the same procedure as that demonstrated above for YSZ.

### *Electrochemical characterization*

#### *Effect of SiO<sub>2</sub> on the electrochemical performance*

It has previously been reported that SiO<sub>x</sub> impurities can segregate to the grain boundaries in YSZ and that this can hinder O<sup>2-</sup> transport<sup>3-5</sup>. Thus, one potential downside of using TEOOS to functionalize the surface of the electrode and facilitate a high dispersion of the Pd@CeO<sub>2</sub> particles is that the resulting SiO<sub>x</sub> layer may have a deleterious effect on cell performance. To determine the effect, if any, on electrochemical performance due to the SiO<sub>x</sub> monolayer produced by reaction of TEOOS on the electrode, two fuel cells with an infiltrated 45 wt. % LSCM-YSZ composite anode that had been calcined to 1473 K were fabricated. Both cells had identical LSF-YSZ cathodes and a 65 μm thick YSZ electrolyte, but only the anode in one of the cells was treated with TEOOS. Both cells were then calcined in air at 723 K followed by addition of 1 wt. % Pd to the anode in order to enhance the catalytic activity. In this case to insure similar catalyst dispersion in both cells the Pd was added by infiltration of an aqueous solution of (NH<sub>3</sub>)<sub>4</sub>Pd(NO<sub>3</sub>)<sub>2</sub>. Figure 8.4 shows the V-i polarization curves and impedance spectra for

the two fuel cells, operating in humidified (3% H<sub>2</sub>O) H<sub>2</sub> at 973 K, with the electrochemical performances summarized in Table 8.1. For comparison purposes, the performance of both cells before the addition of 1 wt. % Pd is also included in Table 8.1.

**Table 8.1:** Electrochemical performance of cells with various anode compositions. The anodes were fabricated by impregnation. All the fuel cells are 45 wt. %  $\text{La}_{0.8}\text{Sr}_{0.2}\text{Cr}_{0.5}\text{Mn}_{0.05}\text{O}_3$ -YSZ composite anodes. The anode ASR can be obtained by subtracting from the total resistance the ohmic ( $0.3 \Omega \text{ cm}^2$ ) and cathode ( $0.2 \Omega \text{ cm}^2$ ) contributions.

| Cell # | Anode composition                           | TEOOS-treated? | Calcination Temp. (K) | Conditions catalyst annealed under | Anode ASR ( $\Omega \cdot \text{cm}^2$ ) | Max. Power ( $\text{W} \cdot \text{cm}^{-2}$ ) |
|--------|---|----------------|-----------------------|------------------------------------|--|--|
| 1      | No catalyst                                 | Y              | 723                   | $\text{O}_2$                       | 3.46                                     | 0.10   |
| 2      | No catalyst                                 | N              | 723                   | $\text{O}_2$                       | 2.95                                     | 0.12   |
| 3      | $(\text{NH}_3)_4\text{Pd}(\text{NO}_3)_2^*$ | Y              | 723                   | $\text{O}_2$                       | 0.24                                     | 0.39   |
| 4      | $(\text{NH}_3)_4\text{Pd}(\text{NO}_3)_2^*$ | N              | 723                   | $\text{O}_2$                       | 0.26                                     | 0.39   |
| 5      | $\text{CeO}_2$                              | Y              | 723                   | $\text{O}_2$                       | 2.52                                     | 0.13   |
| 6      | Pd  | Y              | 723                   | $\text{O}_2$                       | 0.50                                     | 0.30   |
| 7      | Pd  | Y              | 1123                  | $\text{O}_2$                       | 1.30                                     | 0.19   |
| 8      | Pd  | Y              | 1073                  | $\text{H}_2$                       | 0.83                                     | 0.23   |
| 9      | Pd + $\text{CeO}_2$                         | Y              | 723                   | $\text{O}_2$                       | 0.50                                     | 0.33   |
| 10     | Pd@ $\text{CeO}_2$                          | Y              | 723                   | $\text{O}_2$                       | 0.52                                     | 0.30   |
| 11     | Pd@ $\text{CeO}_2$                          | Y              | 1123                  | $\text{O}_2$                       | 0.55                                     | 0.30   |
| 12     | Pd@ $\text{CeO}_2$                          | Y              | 1073                  | $\text{H}_2$                       | 0.52                                     | 0.30   |

\*Different Pd precursor -  $(\text{NH}_3)_4\text{Pd}(\text{NO}_3)_2$  - used and significantly more catalyst used (1 wt. %)

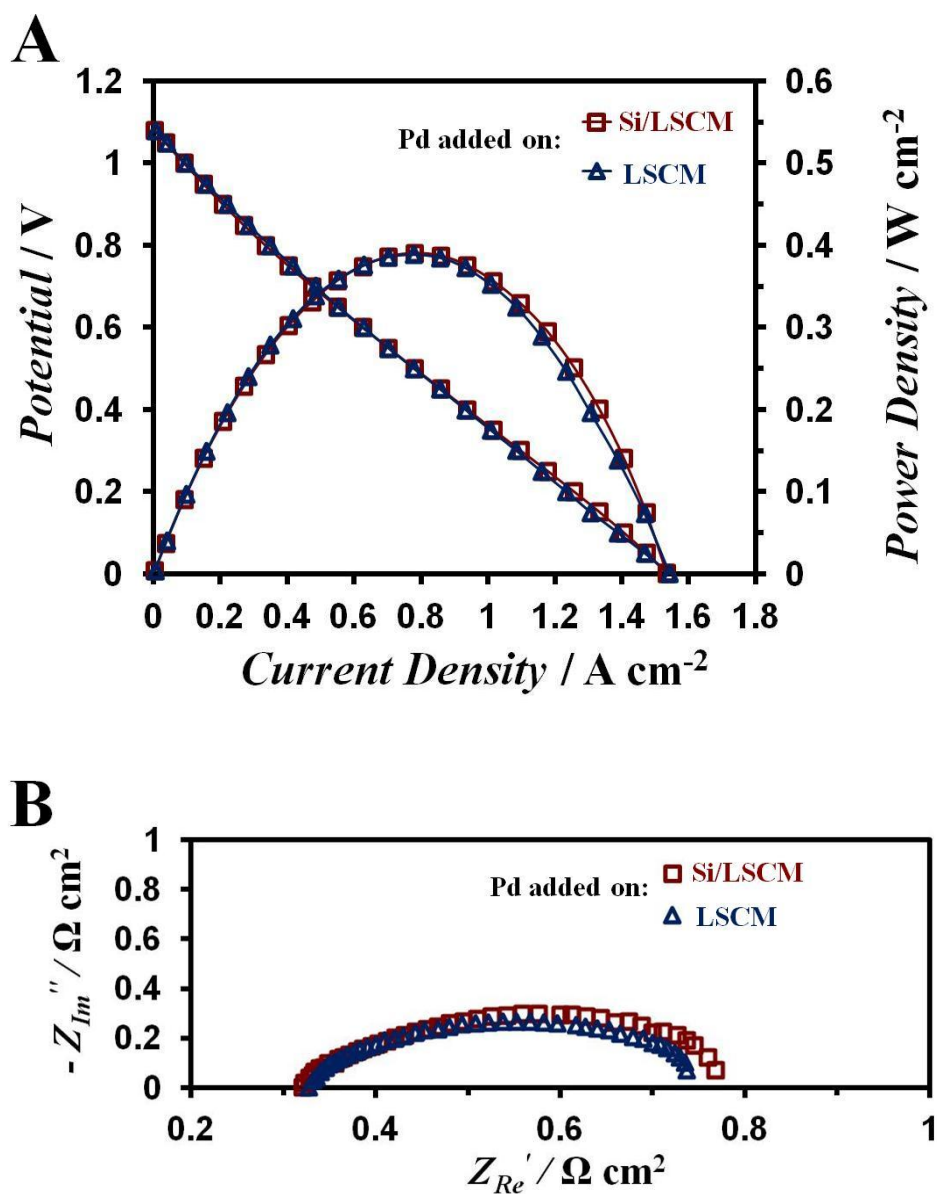


**Figure 8.4:** (A) V-i polarization curves and (B) electrochemical impedance spectra of cells with infiltrated 45 wt. % LSCM-YSZ (blue  $\diamond$ ) with and (red  $\square$ ) without treatment with TEOOS. Both the cells were then calcined in air at 723 K upon addition of 1 wt. % Pd to the TEOOS-treated LSCM anode by infiltration with aqueous solution of  $(\text{NH}_3)_4\text{Pd}(\text{NO}_3)_2$  to enhance the catalytic activity. In order to produce the Pd phase, both the cells were then calcined in air at 723 K before measurement at 973 K with humidified  $\text{H}_2$  fuel (3%  $\text{H}_2\text{O}$ ).

The V-i polarization curves (Figure 8.4A) show that the cells each had an open-circuit potential near the theoretical Nernst value of 1.1 V. The Nyquist plots of the impedance spectra collected at open circuit (Figure 8.4B) also show that the ohmic loss for each cell, calculated from the high-frequency intercept with the real axis, was  $\sim 0.3 \Omega \text{ cm}^2$ , which is close to the expected value for the 65  $\mu\text{m}$  thick YSZ electrolyte. This demonstrates that LSCM provide adequate conductivity for the 50  $\mu\text{m}$  thick anodes used here. Since LSF-YSZ cathodes identical to those used here have previously been shown to have an are specific resistance (ASR) of  $0.2 \Omega \text{ cm}^2$ <sup>7,8</sup>, the anode ASR can be obtained by subtracting from the total resistance the ohmic ( $0.3 \Omega \text{ cm}^2$ ) and cathode contributions. Note that the relatively poor electrochemical performance obtained from both the cells prior to addition of 1 wt. % Pd catalyst (Table 8.1) is due to the low catalytic activity of LSCM. The addition of the Pd catalyst had a dramatic effect on cell performance with the maximum power density of both cells increasing to  $0.39 \text{ W cm}^{-2}$  with an anode ASR of only  $0.25 \Omega \text{ cm}^2$ . The fact that nearly identical performance was obtained for both cells demonstrates that the  $\text{SiO}_x$  layer that was deposited on the surface of one of the anodes via reaction with TEOOS did not hinder oxygen ion transport from the LSCM to the YSZ electrolyte.

#### *Activity of anodes with Pd@CeO<sub>2</sub> catalyst*

The electrochemical performance of a fuel cell with an LSCM/YSZ composite anode that was coated with a film of the Pd@CeO<sub>2</sub> nanostructures using the TEOOS grafting technique described above while operating on humidified H<sub>2</sub> at 973 K is shown in Figure 8.5.

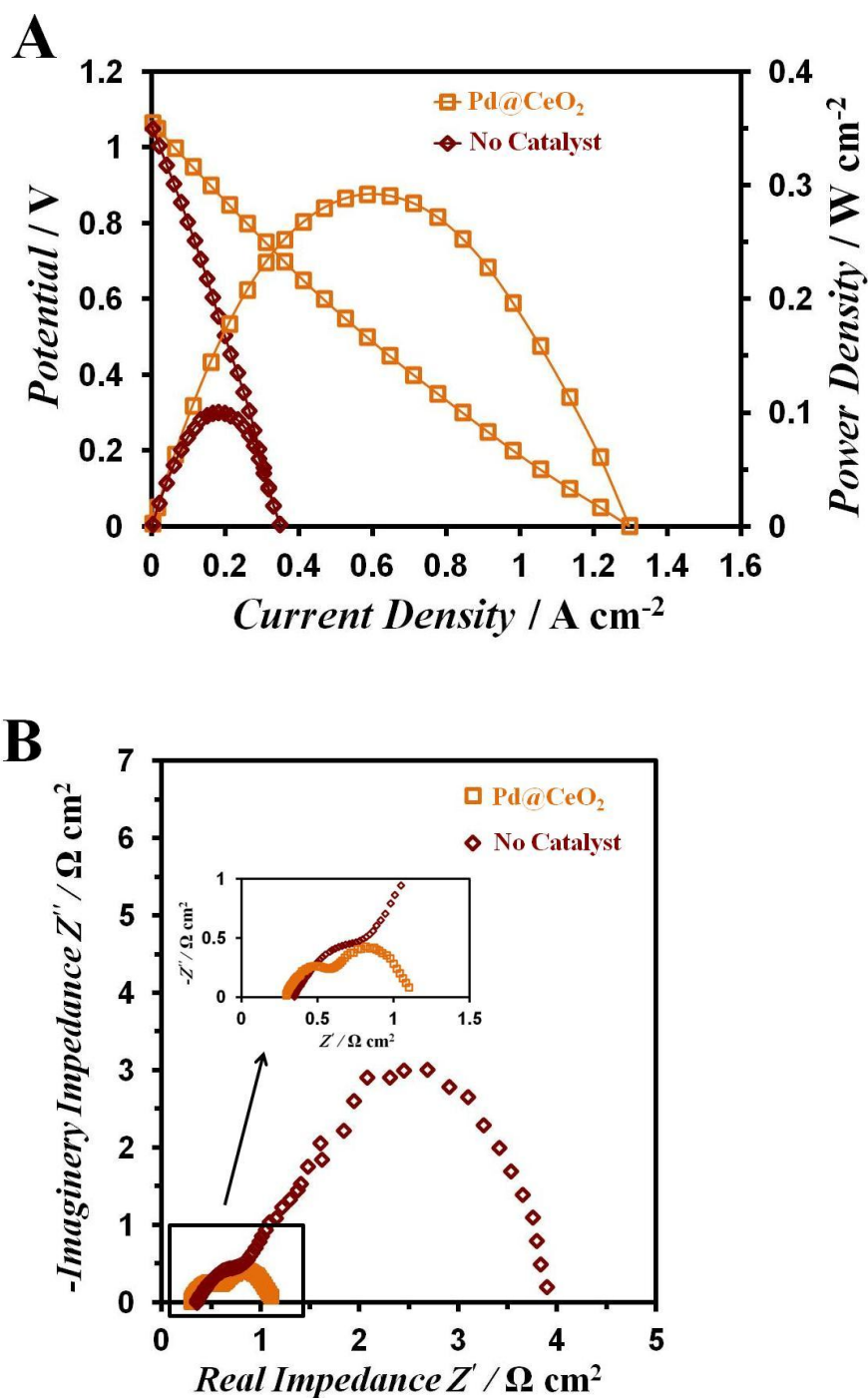


**Figure 8.5:** (A) V-i polarization curves and (B) electrochemical impedance spectra of cells with infiltrated 45 wt. % LSCM-YSZ after treatment with TEOOS containing (orange  $\square$ ) Pd@CeO<sub>2</sub> and (red  $\diamond$ ) no catalyst. The cells were initially calcined at 723 K in air before measurement at 973 K with humidified H<sub>2</sub> fuel (3% H<sub>2</sub>O).

Data for an identical cell for which Pd@CeO<sub>2</sub> nanostructures were not added to the anode is also included in the figure. Note that the grafting technique resulted in a 0.01 wt. % loading of Pd@CeO<sub>2</sub> particles based on the total weight and surface area of the anode (this corresponds to a 0.001 wt. % loading of Pd). Prior to testing the anode side of the cells were calcined in air at 723 K (which removes the capping alkyl groups required for the grafting procedure) and were then reduced in humidified H<sub>2</sub> as the temperature was ramped up to 973 K.

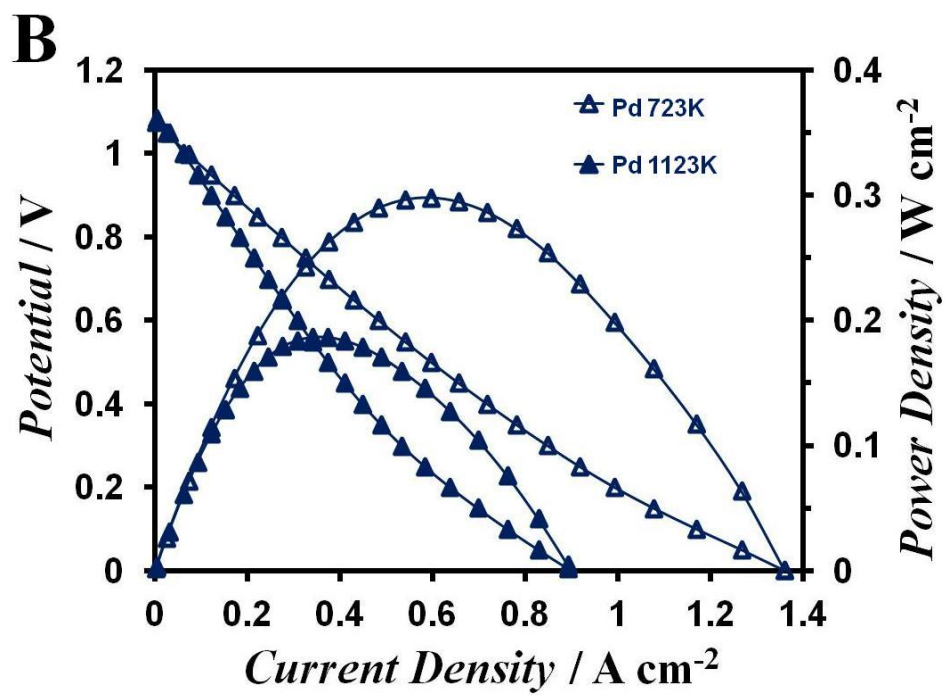
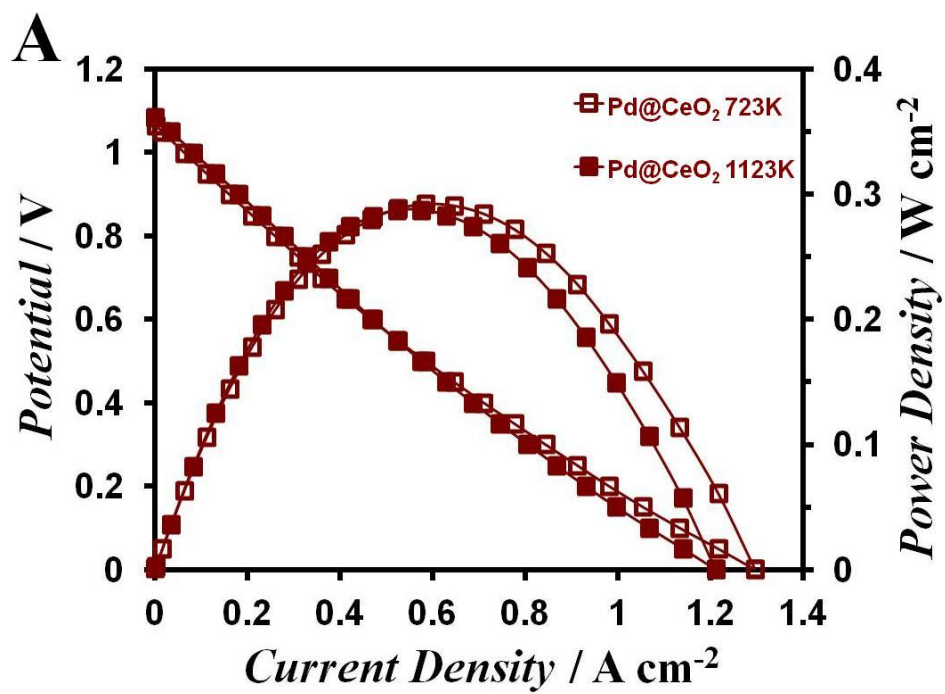
As mentioned above, poor electrochemical performance was obtained when no catalyst was added, demonstrating that LSCM has minimal catalytic activity for H<sub>2</sub> oxidation. Good performance was obtained, however, for the cell in which Pd@CeO<sub>2</sub> had been added to the anode. This cell had a maximum power density of 0.30 W cm<sup>-2</sup> and anode ASR of 0.52 Ω cm<sup>2</sup>. It is noteworthy that the performance of this cell is similar to that of the cell in which the Pd was added by conventional means (Figure 8.4, Table 8.1), even though the total Pd loading was a 1000 times less. This demonstrates that only dopant levels of highly catalytically active metals, such as Pd, are required to enhance the catalytic activity of anodes which use metal oxide electronically conducting phases (e.g. LSCM) to acceptable levels.

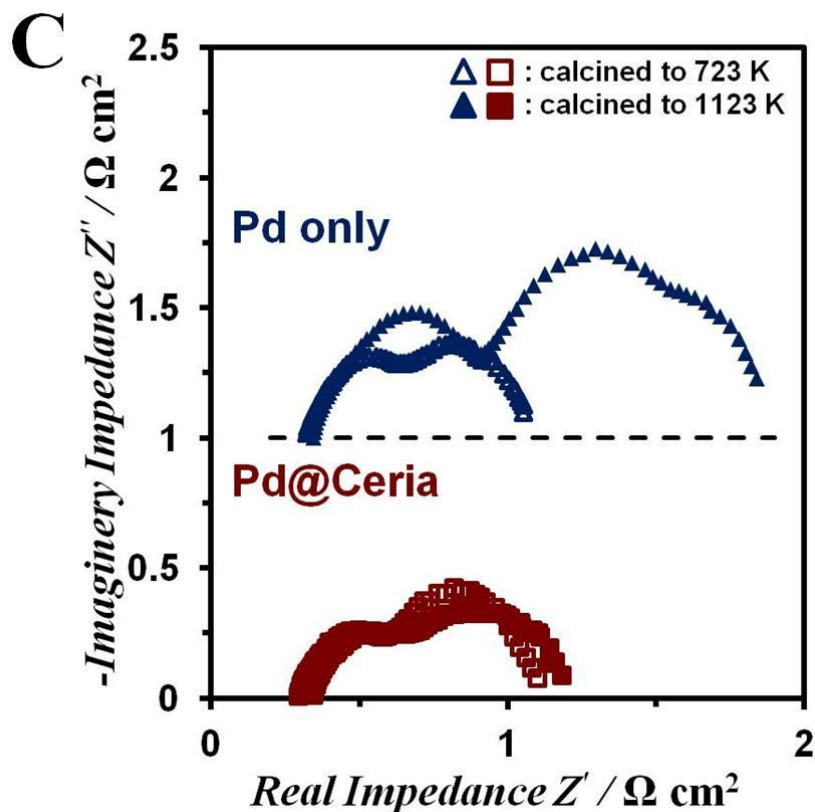
#### *Thermal stability of electrodes with Pd@CeO<sub>2</sub> catalyst*

While high stability of LSCM/YSZ composite anodes with a grafted Pd@CeO<sub>2</sub> catalyst layer can be anticipated based on the SEM results presented above, it was also evaluated in working fuel cells. In these tests the anodes were calcined at temperatures above 1073 K which is at least 100 K higher than the typical cell operating temperature

(973 K) under both oxidizing and reducing conditions in order to simulate performance degradation that would occur over a lengthy fuel cell test. For comparison purposes, cells with un-coated Pd nanoparticles added onto the TEOOS-treated LSCM-YSZ composite anode were also evaluated.



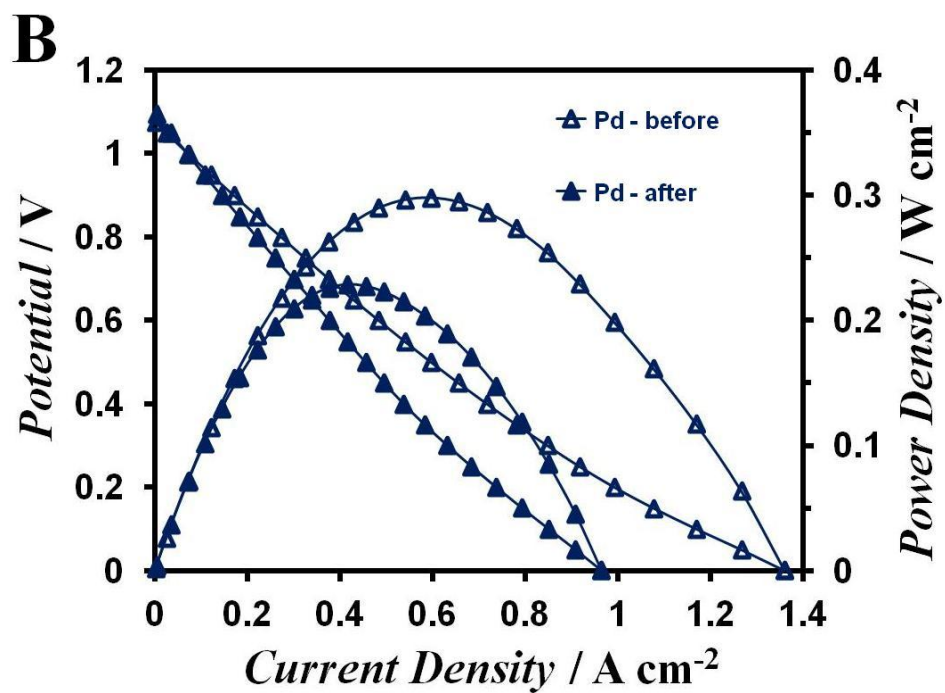
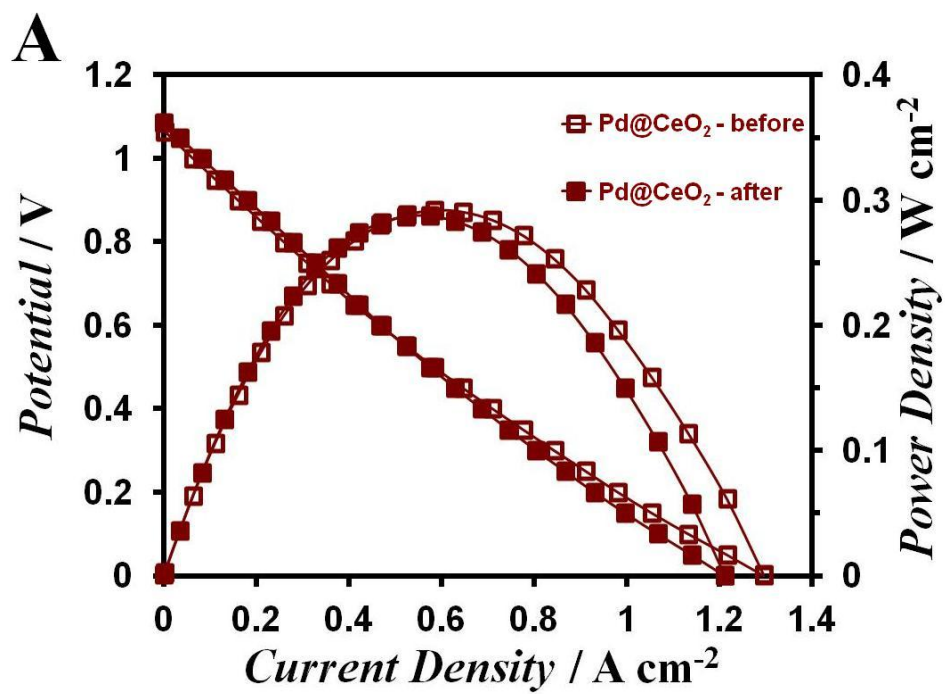




**Figure 8.6:** (A, B) V-i polarization curves and (C) electrochemical impedance spectra of cells annealed under oxidizing conditions at higher temperatures, with infiltrated 45 wt. % LSCM-YSZ after treatment with TEOOS, containing infiltrated (Figure 8.6A) Pd@CeO<sub>2</sub> nanoparticles annealed in air at (□) 723 K and (■) 1123 K, (Figure 8.6B) 2 nm un-coated Pd nanoparticles annealed in air at (Δ) 723 K and (▲) 1123 K. The cells were operated at 973 K with humidified H<sub>2</sub> fuel (3% H<sub>2</sub>O).

As shown by the polarization curves and impedance data in Figure 8.6A,C increasing the temperature at which the anode with the highly dispersed Pd@CeO<sub>2</sub> catalyst was calcined in air from 723 to 1123 K caused only small changes in performance while operating with humidified H<sub>2</sub> fuel at 973 K with the maximum power density and anode ASR remaining close to 0.3 W cm<sup>-2</sup>, and the anode ASR increased slightly from 0.52 to 0.55 Ω cm<sup>2</sup> (the performance for each cell including anode ASR

values are summarized in Table 8.1). This is in sharp contrast to the cell with the uncoated Pd catalyst (Figure 8.6B,C) where the maximum power density decreased from 0.3 to 0.19 W cm<sup>-2</sup> and the anode ASR increased from 0.5 to 1.3 Ω cm<sup>2</sup> upon increasing the air calcination temperature from 723 to 1123 K.



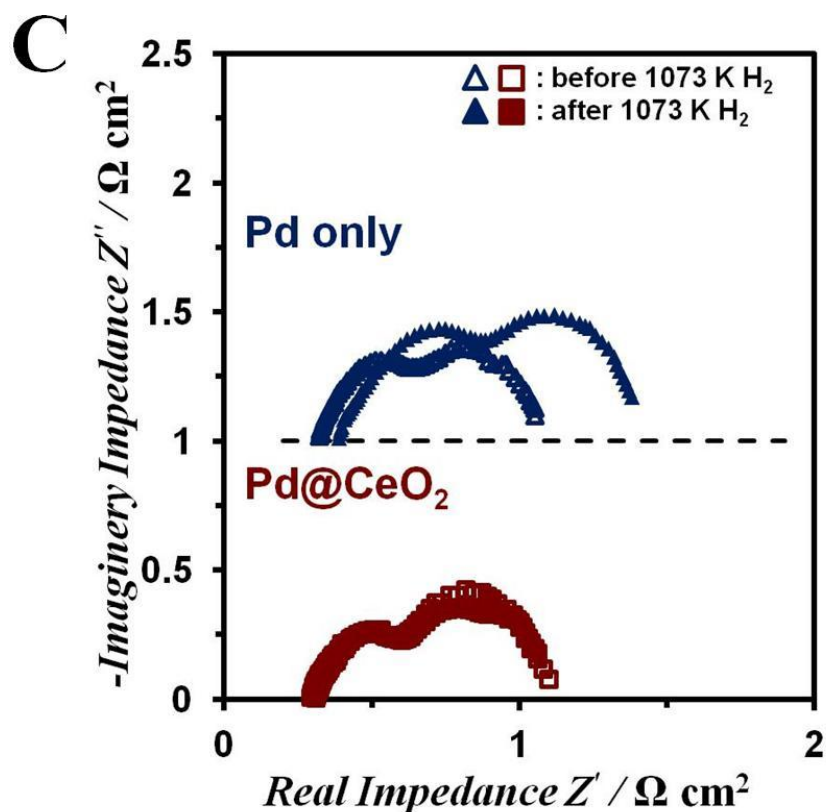


**Figure 8.7:** (A, B) V-i polarization curves and (C) electrochemical impedance spectra of cells annealed under reducing conditions at higher temperatures, with infiltrated 45 wt. % LSCM-YSZ after treatment with TEOOS, containing infiltrated (Figure 8.7A) Pd@CeO<sub>2</sub> nanoparticles (□) before 1073 K and (■) after 1073 K treatment in humidified H<sub>2</sub>, (Figure 8.7B) 2 nm un-coated Pd nanoparticles (□) before 1073 K and (■) after 1073 K treatment in humidified H<sub>2</sub>. The cells were initially calcined at 723 K in air before measurement at 973 K with humidified H<sub>2</sub> fuel (3% H<sub>2</sub>O).

As shown by the polarization and impedance data in Figure 8.7, nearly identical results were obtained for a set of cells where the anodes were aged by annealing in H<sub>2</sub> for 2 h at 1073 K. This treatment again had only a small effect on the performance of the anode with the Pd@CeO<sub>2</sub> catalyst, while a large decrease in performance was observed for the cell with the Pd nanoparticle catalyst.

### *Performance with CH<sub>4</sub> fuel*

While the data presented above obtained with H<sub>2</sub> fuel provides considerable insight into the activity and stability of the Pd@CeO<sub>2</sub> nanostructures, one of the primary advantages of Pd@CeO<sub>2</sub>/LSCM/YSZ electrodes over more conventional Ni/YSZ anodes is their ability to utilize hydrocarbon fuels. Thus, performance tests were also carried out using CH<sub>4</sub> as the fuel. Polarization curves for fuel cells with 0.01 wt % Pd@CeO<sub>2</sub> and with 0.01 wt % 2 nm un-coated Pd nanoparticles added to the anode are shown in Figure 8.8. The anodes were initially calcined at 723 K for 4 h in air and were then reduced in humidified H<sub>2</sub> as the temperature was ramped up to 973 K before the cells were operated in dry CH<sub>4</sub> at 973 K. For comparison purposes, a cell with an LSCM/YSZ anode with no added catalyst was also tested.

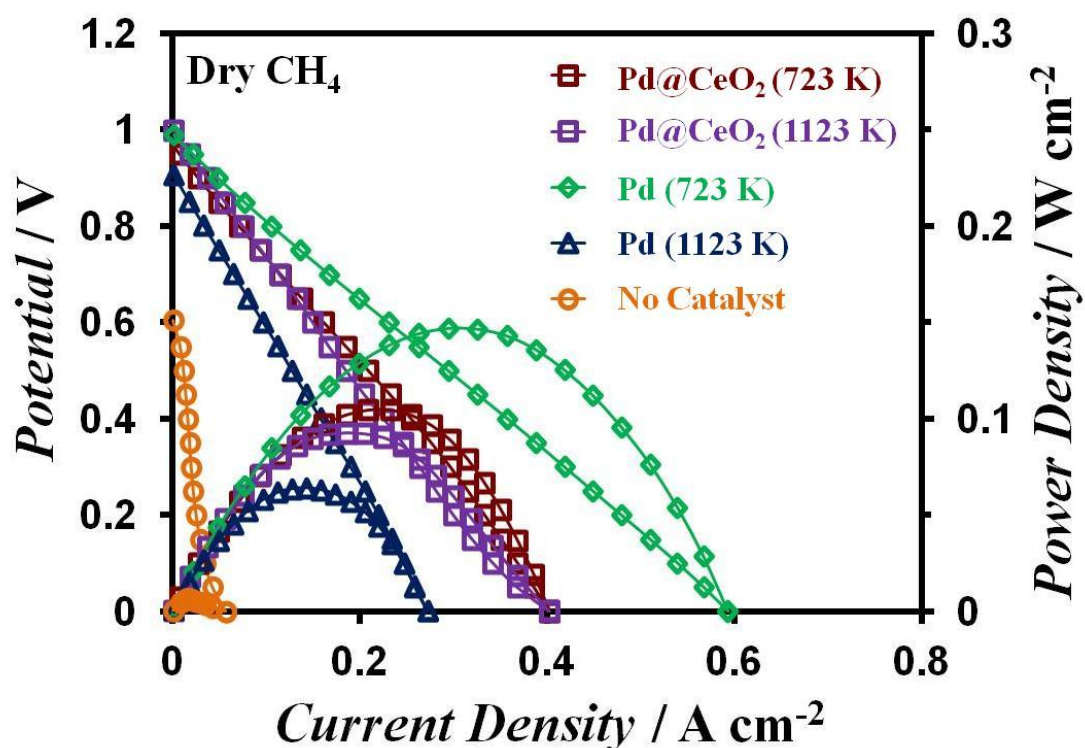


**Figure 8.8:** V-i polarization curves of with infiltrated 45 wt. % LSCM-YSZ after treatment with TEOOS, containing infiltrated ( $\square$ ) Pd@CeO<sub>2</sub> and ( $\diamond$ ) 2 nm un-coated Pd nanoparticles calcined at 723 K and 1123 K in air, and ( $\circ$ ) no catalyst. Measurements were taken at 973 K in dry CH<sub>4</sub>.

As expected this cell exhibited very poor performance with a maximum power density of only 0.01 W cm<sup>-2</sup>. Much higher performance was obtained from the cells with the added Pd@CeO<sub>2</sub> and Pd anode catalysts which had maximum power densities of 0.11 W cm<sup>-2</sup> and 0.15 W cm<sup>-2</sup>, respectively. Note that this performance is lower than that obtained for H<sub>2</sub> fuel due to the higher activation barrier for methane oxidation. To investigate the thermal stability of the Pd and Pd@CeO<sub>2</sub> catalysts, the anodes were then calcined in air at 1123 K for 4 h followed by measuring the cell performance at 973 K with CH<sub>4</sub> fuel.

Consistent with the catalyst characterization studies presented above, this rapid thermal aging treatment caused the maximum power density of the cell with the uncoated Pd nanoparticle anode catalyst to decrease by 40 % to  $0.06 \text{ W cm}^{-2}$ . In contrast the maximum power density of the cell with the Pd@CeO<sub>2</sub> catalyst decreased by only 9 % to  $0.10 \text{ W cm}^{-2}$ .

#### **8.4 Conclusion**

In this chapter we have demonstrated the use of TEOOS as a surface modifier to aid in the dispersion of highly catalytic Pd@CeO<sub>2</sub> nanocomposites into porous SOFC anodes. SEM results show that a film of alkyl-capped Pd@CeO<sub>2</sub> particles can be deposited on TEOOS-treated anodes. In contrast to bare Pd particles, it was also demonstrated that high dispersion can be maintained after calcining in air at 973 K to oxidatively remove the organic groups, and under the reducing conditions during fuel cell operation at similar temperatures. Furthermore, the high thermal stability of the dispersed Pd@CeO<sub>2</sub> particles was maintained after calcination in air at 1373 K, suggesting that long-term stability can be expected for SOFC operation using this precursor at 973 K.

An important aspect of the use of TEOOS as surface modifier to obtain a high dispersion of the Pd@CeO<sub>2</sub> particles, is that it allows Pd weight loadings as low as 0.001 % (based on the weight of the porous composite anode) to be used and still obtain high performance when operating on both H<sub>2</sub> and CH<sub>4</sub> fuels. In addition, high-temperature calcination under both oxidizing and reducing conditions in H<sub>2</sub> and CH<sub>4</sub> fuel caused only small changes in performance for the anode with the Pd@CeO<sub>2</sub> catalyst. This is in sharp



contrast to the cell with the uncoated Pd catalyst where large decrease in performance was observed when similar high temperature treatment was used.

## 8.5 References

- 1 Kim, J. S. *et al.* Highly Active and Thermally Stable Core-Shell Catalysts for Solid Oxide Fuel Cells. *J Electrochem Soc* **158**, B596-B600, doi:Doi 10.1149/1.3571039 (2011).
- 2 Adijanto, L. *et al.* Exceptional Thermal Stability of Pd@CeO<sub>2</sub> Core-Shell Catalyst Nanostructures Grafted onto an Oxide Surface. *Nano Lett* **13**, 2252-2257, doi:Doi 10.1021/nl4008216 (2013).
- 3 Hauch, A., Jensen, S. H., Bilde-Sorensen, J. B. & Mogensen, M. Silica segregation in the Ni/YSZ electrode. *J Electrochem Soc* **154**, A619-A626, doi:Doi 10.1149/1.2733861 (2007).
- 4 Lankin, M., Du, Y. H. & Finnerty, C. A Review of the Implications of Silica in Solid Oxide Fuel Cells. *J Fuel Cell Sci Tech* **8**, doi:Artn 054001, Doi 10.1115/1.4003980 (2011).
- 5 Zhang, T. S. *et al.* Different conduction behaviors of grain boundaries in SiO<sub>2</sub>-containing 8YSZ and CGO20 electrolytes. *Solid State Ionics* **177**, 1227-1235, doi:DOI 10.1016/j.ssi.2006.05.006 (2006).
- 6 Park, S., Gorte, R. J. & Vohs, J. M. Tape cast solid oxide fuel cells for the direct oxidation of hydrocarbons. *J Electrochem Soc* **148**, A443-A447 (2001).
- 7 Adijanto, L., Kungas, R., Bidrawn, F., Gorte, R. J. & Vohs, J. M. Stability and performance of infiltrated La<sub>0.8</sub>Sr<sub>0.2</sub>Co<sub>x</sub>Fe<sub>1-x</sub>O<sub>3</sub> electrodes with and without Sm<sub>0.2</sub>Ce<sub>0.8</sub>O<sub>1.9</sub> interlayers. *J Power Sources* **196**, 5797-5802, doi:DOI 10.1016/j.jpowsour.2011.03.022 (2011).

- 8 Adjianto, L., Kungas, R., Park, J., Vohs, J. M. & Gorte, R. J. SOFC anodes based on infiltration of tungsten bronzes. *Int J Hydrogen Energ* **36**, 15722-15730, doi:DOI 10.1016/j.ijhydene.2011.09.059 (2011).
- 9 Cargnello, M. *et al.* Novel embedded Pd@CeO<sub>2</sub> catalysts: a way to active and stable catalysts. *Dalton T* **39**, 2122-2127, doi:Doi 10.1039/B916035c (2010).
- 10 Cargnello, M., Wieder, N. L., Montini, T., Gorte, R. J. & Fornasiero, P. Synthesis of Dispersible Pd@CeO<sub>2</sub> Core-Shell Nanostructures by Self-Assembly. *J Am Chem Soc* **132**, 1402-1409, doi:Doi 10.1021/Ja909131k (2010).
- 11 Bakhmutsky, K. *et al.* A Versatile Route to Core-Shell Catalysts: Synthesis of Dispersible M@Oxide (M=Pd, Pt; Oxide=TiO<sub>2</sub>, ZrO<sub>2</sub>) Nanostructures by Self-Assembly. *Chemsuschem* **5**, 140-148, doi:DOI 10.1002/cssc.201100491 (2012).
- 12 Cargnello, M. *et al.* Exceptional Activity for Methane Combustion over Modular Pd@CeO<sub>2</sub> Subunits on Functionalized Al<sub>2</sub>O<sub>3</sub>. *Science* **337**, 713-717, doi:DOI 10.1126/science.1222887 (2012).
- 13 Wieder, N. L. *et al.* Study of the Water-Gas-Shift Reaction on Pd@CeO<sub>2</sub>/Al<sub>2</sub>O<sub>3</sub> Core-Shell Catalysts. *J Phys Chem C* **115**, 915-919, doi:Doi 10.1021/Jp102965e (2011).
- 14 Corre, G. *et al.* Activation and Ripening of Impregnated Manganese Containing Perovskite SOFC Electrodes under Redox Cycling. *Chem Mater* **21**, 1077-1084, doi:Doi 10.1021/Cm803149v (2009).

## **Chapter 9. Stability and Performance of Infiltrated $\text{La}_{0.8}\text{Sr}_{0.2}\text{Co}_x\text{Fe}_{1-x}\text{O}_3$ Electrodes with and without $\text{Sm}_{0.2}\text{Ce}_{0.8}\text{O}_{1.9}$ Interlayers\***

### **Summary**

The chemical stability of composite electrodes produced by the infiltration of  $\text{La}_{0.8}\text{Sr}_{0.2}\text{Co}_x\text{Fe}_{1-x}\text{O}_3$  (LSCF) into a porous yttria-stabilized zirconia (YSZ) scaffold were investigated as a function of the Co:Fe ratio in the LSCF and the LSCF calcination temperature. XRD and impedance spectroscopy results indicate that for an LSCF calcination temperature of 1123 K, reactions between the LSCF and YSZ do not occur to a significant extent. Reactions producing  $\text{La}_2\text{Zr}_2\text{O}_7$  and  $\text{SrZrO}_3$  at the interface were observed, however, for a calcination temperature of 1373 K and x values greater than 0.2. In addition to determining the conditions for which reactions between LSCF and YSZ occur, the effectiveness of infiltrated SDC interlayers in preventing reactions at the LSCF-YSZ interface and their influence on the overall performance of LSCF/YSZ composite electrodes was studied.

---

\* This chapter was published as a research paper in the Journal of Power Sources, 196 (2011) 5797. Copyright: 2011, Elsevier.

## 9.1 Introduction

The most commonly used cathode in solid oxide fuel cells (SOFC) consists of a porous composite of electronically conducting Sr-doped lanthanum manganite (LSM) and the electrolyte, yttria-stabilized zirconia (YSZ). While the performance of these cathodes is acceptable at temperatures above 1073 K, their electrochemical performance is marginal at lower temperatures due to the relatively low electronic conductivity of the LSM. The push to lower the operating temperature of SOFC has, therefore, also motivated the development of cathodes with higher performance at lower temperatures. Using mixed conducting (i.e. electronic and ionic) perovskites such as Sr-doped lanthanum ferrite ( $\text{La}_{0.8}\text{Sr}_{0.2}\text{FeO}_3$ , LSF)<sup>1-6</sup> and Sr-doped lanthanum cobaltite ( $\text{La}_{0.8}\text{Sr}_{0.2}\text{CoO}_3$ , LSC)<sup>7-11</sup> is one approach that is being used to enhance cathode performance at intermediate temperatures (873-973 K). The ionic conductivity in these materials allows  $\text{O}^{2-}$  ions to be transported through the perovskite to the YSZ thereby providing more active surface area. LSC has relatively high electronic conductivity at ( $1220 \text{ S cm}^{-1}$  at 1073 K<sup>12</sup>) and good oxygen exchange characteristics<sup>13-16</sup> making it particularly attractive for cathode applications. Unfortunately LSC reacts with YSZ at temperatures above 1273 K<sup>17</sup> forming non-conducting phases at the LSC-YSZ interface; thus, low-temperature electrode synthesis procedures are required in order to fabricate LSC/YSZ composite cathodes. When such approaches are used (e.g. sol gel<sup>18</sup> or wet infiltration<sup>19-24</sup>) LSC-YSZ cathodes exhibit excellent initial performance at 973 K, but rapid degradation due to reaction at the interface still occurs<sup>8</sup>.

LSF appears to be more chemically compatible with YSZ and the reactions between these materials producing new phases only becomes evident via XRD at temperatures above 1673 K<sup>8,19,25,26</sup>. It has been suggested that a small amount of Zr<sup>+4</sup> may become incorporated into the B site of LSF at the LSF-YSZ interface and this may affect properties<sup>4,26</sup>, but changes in the LSF lattice parameter which would signify this type of substitution have only been observed at temperatures higher than those used in the preparation of the LSF-YSZ electrodes<sup>19</sup>. Additionally, it has reported that a La<sub>0.8</sub>Sr<sub>0.2</sub>Fe<sub>0.9</sub>Zr<sub>0.1</sub>O<sub>3</sub> cathode exhibits performance similar to LSF<sup>19</sup>. While reactions between LSF and YSZ do not appear to be problematic, the performance of LSF-YSZ cathodes is limited by their lower electronic conductivity relative to LSC<sup>27</sup>. As a compromise between LSC and LSF, solid solutions of these materials (La<sub>1-y</sub>Sr<sub>y</sub>Co<sub>x</sub>Fe<sub>1-x</sub>O<sub>3</sub>, LSCF) are often used, and LSCF-YSZ composite cathodes have been reported to exhibit excellent performance<sup>28-30</sup>.

Thin interlayers of ionically conducting ceria doped with samaria (SDC) or gadolinia (GDC) are often used to separate LSF or LSC from YSZ in order to enhance cathode performance<sup>3,4,31</sup>. For LSC, the ceria interlayer prevents reaction with the YSZ both during fabrication and cell operation. The effect of ceria interlayers on the performance of LSF and LSCF cathodes is less clear. While preventing reactions with the YSZ is often used as justification for the need for a ceria interlayer when using LSF, as noted above, reaction of LSF with the YSZ does not appear to occur for typical SOFC fabrication conditions. Nonetheless, it has been reported that SDC interlayers still significantly enhance the performance of LSF cathodes<sup>4,31</sup>. Simner, et al. have suggested

that the improved performance is a consequence of the higher ionic conductivity and surface reaction exchange kinetics of SDC relative to YSZ<sup>4</sup>. While ceria interlayers are also generally used for LSCF cathodes, the mechanism by which the interlayer affects performance is again not well understood. Preventing Co from reacting with the YSZ is one potential role, but the conditions at which such reactions may occur for LSCF and the effect of the Co to Fe ratio have yet to be determined.

Infiltration in which the constituent ions in the perovskite phase (e.g. LSF, LSCF) of the cathode are added to a YSZ porous electrode scaffold in the form of aqueous solutions and then calcined in air to form the desired phase has become a popular method for cathode synthesis<sup>19-24</sup>. This approach has the advantage of significantly reducing the sintering temperature required when adding the perovskite phase, which in some cases, such as LSC, allows reactions with the YSZ to be avoided. This synthesis method also produces a unique structure in which the active component coats the YSZ rather than forming a random composite of the two materials. Issues relating to mismatches in the coefficients of thermal expansion (CTE) of the two materials are also often avoided using the infiltration method. We have recently shown that doped-ceria interlayers can be incorporated into cathodes using infiltration<sup>17</sup>. In this work it was shown that wet infiltration of the constituent ions in SDC followed by calcination at 1123 K produces a porous coating of SDC nanoparticles over the YSZ. This porous layer, however, can be transformed into a dense coating by calcination at 1473 K. Infiltrated, dense SDC coatings were found to prevent reaction between LSC (also added by infiltration) and YSZ for calcination temperatures up to 1373 K and LSC/SDC/YSZ electrodes produced

in this manner were found to exhibit excellent performance with an ASR of 20-30 m $\Omega$  cm<sup>2</sup> at 973 K.

The use of infiltration techniques for cathode synthesis when comparing the performance of electrodes with different compositions has the benefit that electrodes with very similar structures can be produced for a range of compositions, thereby eliminating large structural variations as one possible cause for performance variations. In the present study we have used infiltration to produce La<sub>1-y</sub>Sr<sub>y</sub>Co<sub>x</sub>Fe<sub>1-x</sub>O<sub>3</sub> (0 ≤ x ≤ 1)-YSZ composite electrodes both with and without SDC interlayers and have investigated the range of compositions of LSCF for which the formation of new phases via reaction with YSZ does not occur for typical SOFC fabrication and operating temperatures. We have also studied how SDC interlayers affect the performance of LSF and LSCF cathodes with the goal of determining whether preventing reactions at the LSF- and LSCF-YSZ interfaces plays a significant role in enhancing cathode performance.

## 9.2 Experimental

The fuel cells used in this study were fabricated using porous-dense-porous YSZ scaffolds that were produced via sintering laminated green YSZ (Tosoh Corp., 8 mol% Y<sub>2</sub>O<sub>3</sub>-doped ZrO<sub>2</sub>, 0.2 $\mu$ m) tapes as described in Chapter 2<sup>32</sup>. The tapes that were used to produce the porous layers contained graphite as a sacrificial pore former in addition to YSZ. For each cell, the dense electrolyte layer was 100 $\pm$ 5  $\mu$ m in thickness and 1 cm in diameter. The two porous layers, which were used for the electrodes, were each 50 $\pm$ 2  $\mu$ m in thickness and 0.67 cm in diameter. They were also ~65% porous with a BET surface



area  $0.3 \text{ m}^2\text{g}^{-1}$ . LSF, LSC, and LSCF cathodes were prepared using the infiltration method developed in our lab<sup>6,8,19,20</sup>. Aqueous solutions of  $\text{La}(\text{NO}_3)_3 \cdot 6\text{H}_2\text{O}$  (Alfa Aesar, 99.9%),  $\text{Sr}(\text{NO}_3)_2$  (Alfa Aesar, 99%),  $\text{Co}(\text{NO}_3)_2 \cdot 6\text{H}_2\text{O}$  (Aldrich, 99%) and  $\text{Fe}(\text{NO}_3)_3 \cdot 9\text{H}_2\text{O}$  (Fisher Scientific) were used as the precursor solutions. Citric acid (Fisher Scientific) was added, in a 1:1 ratio for each cation, as a complexing agent to allow formation of the perovskite phase at a lower temperature. Multiple infiltration steps were required to reach the desired 40 wt. % loading of perovskite and the samples were calcined to 723 K after each infiltration. After reaching the desired loading, the samples were calcined to either 1123 K or 1373 K for 4 h. Cells were fabricated for the following perovskite compositions:  $\text{La}_{0.8}\text{Sr}_{0.2}\text{FeO}_3$  (LSF),  $\text{La}_{0.8}\text{Sr}_{0.2}\text{CoO}_3$  (LSC) and  $\text{La}_{0.8}\text{Sr}_{0.2}\text{Co}_x\text{Fe}_{1-x}\text{O}_3$  (LSCF) with  $0 \leq x \leq 1.0$  (LSC20F for  $x = 0.2$ , LSC40F for  $x = 0.4$ , etc).

Cells were also fabricated in which  $\text{Sm}_{0.2}\text{Ce}_{0.8}\text{O}_{1.9}$  (SDC) was used as an interlayer between the perovskite and the YSZ. The SDC interlayer was prepared using multiple infiltration steps with an aqueous mixture of  $\text{Ce}(\text{NO}_3)_3 \cdot 6\text{H}_2\text{O}$  (Alfa Aesar, 99.5%) and  $\text{Sm}(\text{NO}_3)_3 \cdot 6\text{H}_2\text{O}$  (Alfa Aesar, 99.9%) followed by heating in air to 723 K. After sufficient SDC had been added to produce a dense coating  $\sim 0.1 \mu\text{m}$  in thickness over the YSZ, the cell was calcined in air at 1473 K for 4 h. As we have reported previously, this annealing treatment produces a dense, continuous SDC coating over the YSZ<sup>17</sup>. After fabricating the SDC interlayer, LSF, LSC, or LSCF were added using the infiltration procedure described above.

After preparing the cathodes, 50 wt. %  $\text{CeO}_2$  and 0.5 wt. % Pd was added to the porous YSZ layer on the other side of the cell using a similar infiltration procedure to

produce the anode. Silver paste was used as the current collector for both the anode and cathode and the cells were mounted onto an alumina tube with a ceramic adhesive (Aremco, Ceramabond 552). All cell testing was performed with the anode exposed to humidified  $H_2$  (3%  $H_2O$ ) and the cathode to ambient air. X-ray diffraction (XRD) using Cu  $K\alpha$  radiation was used to determine the phases present in the LSCF-YSZ cathode. Electrochemical impedance spectroscopy (Gamry Instruments) and V-I polarization curves were used to characterize the performance of each cathode formulation. The impedance spectra were measured galvanostatically at various currents in the frequency range of 300 kHz to 0.01Hz, with a 1 mA AC perturbation.

### **9.3 Results and Discussion**

#### *XRD results*

XRD was used to investigate the reaction of LSCF with YSZ as a function of the ratio of the B-site cations and temperature. XRD patterns of 40 wt. % LSCF-YSZ composites which had been calcined at 1123 K for 4 h are shown in Figure 9.1 for x values between 0 and 1.

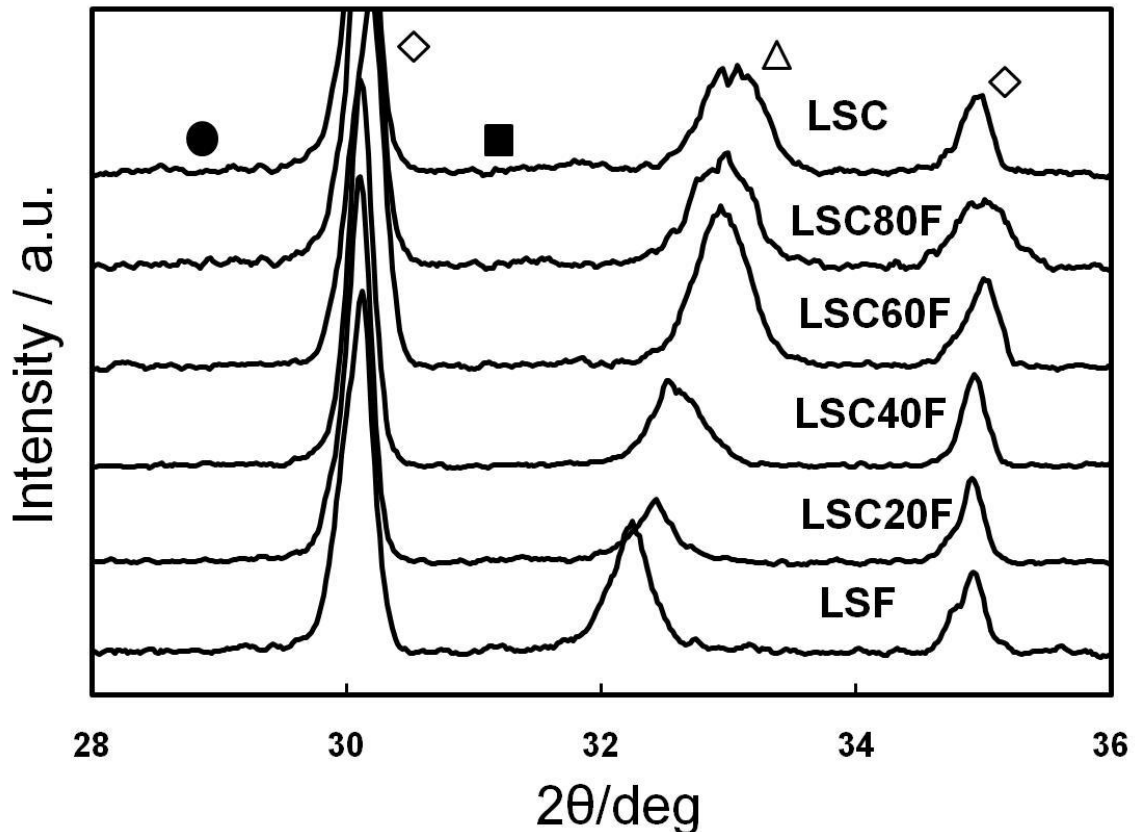


**Figure 9.1:** XRD patterns of  $\text{La}_{0.8}\text{Sr}_{0.2}\text{Co}_x\text{Fe}_{1-x}\text{O}_3$ -YSZ composites that had been calcined to 1123 K with the indicated compositions. The peak positions correspond to: ●- $\text{La}_2\text{Zr}_2\text{O}_7$ , ■- $\text{SrZrO}_3$ , ◊-YSZ, and ▲- $\text{La}_{0.8}\text{Sr}_{0.2}\text{Co}_x\text{Fe}_{1-x}\text{O}_3$ .

The peaks at  $30^\circ$  and  $35^\circ$  correspond to the fluorite lattice of the YSZ substrate. The peak at  $32.1^\circ$  in the spectrum of LSF is indicative of the orthorhombic structure of this material<sup>33,34</sup>. The position of this peak shifts to higher values upon the incorporation of Co into the lattice and appears at  $32.5^\circ$  for a Co:Fe ratio of 4:6 (i.e., LSC40F). Some broadening of the peak is also evident at this Co:Fe ratio. Since pure LSC has a rhombohedral structure<sup>17,35</sup> for which this peak splits into two peaks, the observed broadening with Co addition is likely due to this phase transformation. For higher Co:Fe ratios, the peaks indicative of the rhombohedral distortion of the perovskite structure

remain fixed at  $33.0^\circ$ . A slight shift to  $33.2^\circ$  is observed for the pure LSC. Even for the LSC it was not possible to resolve the two separate components of this peak. This is likely due to the presence of relatively small crystallites in the 1123 K annealed samples resulting in significant line broadening. An important aspect of the XRD data in Figure 9.1 is that there is no evidence for the formation of secondary phases, such as  $\text{La}_2\text{Zr}_2\text{O}_7$  or  $\text{SrZrO}_3$ , which would result from the reaction of the LSCF with the YSZ.

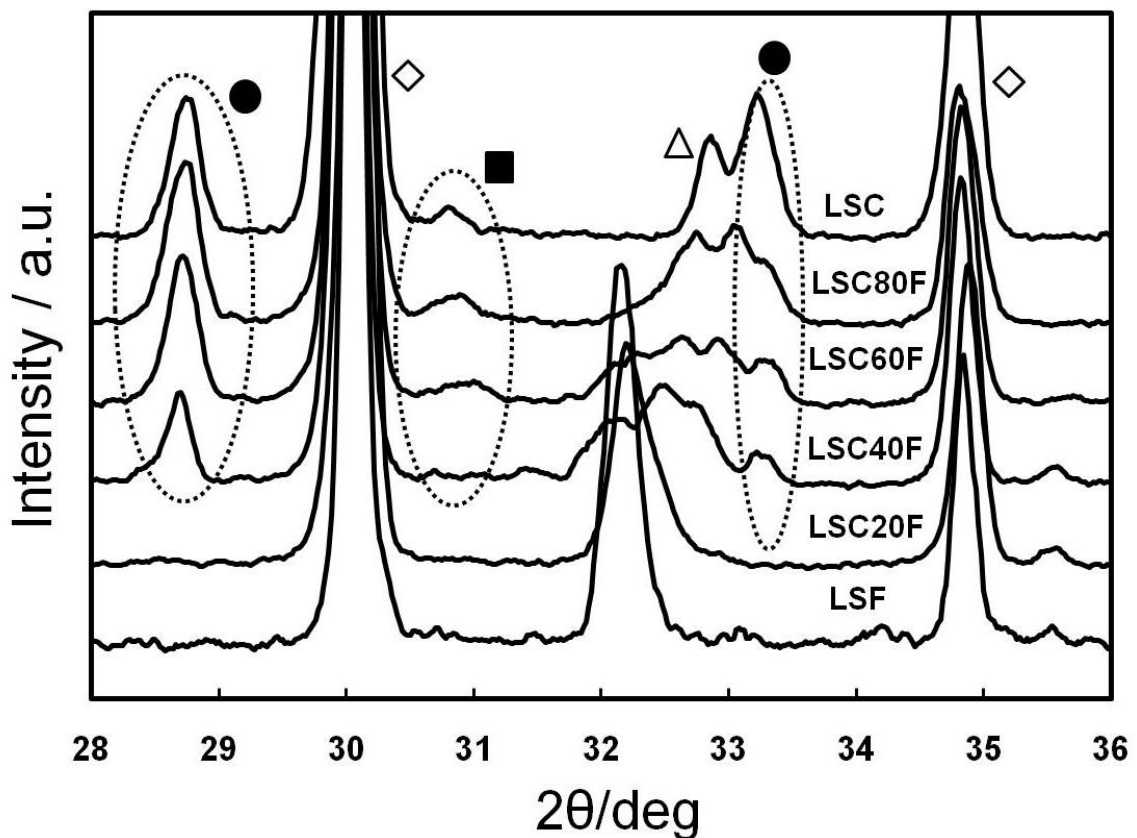


**Figure 9.2:** XRD patterns of  $\text{La}_{0.8}\text{Sr}_{0.2}\text{Co}_x\text{Fe}_{1-x}\text{O}_3$ -YSZ composites that had been calcined to 1373 K with the indicated compositions. The peak positions correspond to: ●- $\text{La}_2\text{Zr}_2\text{O}_7$ , ■- $\text{SrZrO}_3$ , ◇-YSZ, and △- $\text{La}_{0.8}\text{Sr}_{0.2}\text{Co}_x\text{Fe}_{1-x}\text{O}_3$ .

An analogous set of XRD data for a 40 wt. % LSCF-YSZ composites, which had been calcined at 1373 K for 4 h, are shown in Figure 9.2. The patterns for the LSF-YSZ and LSC20F-YSZ samples are essentially identical to those of the corresponding samples calcined at only 1123 K, except the peaks are narrower indicating a larger crystallite size. Thus for these compositions, the XRD data indicates that LSCF does not react with YSZ for temperatures up to 1373 K. This result is consistent with previous studies that have also shown that LSF does not react with YSZ for calcination temperatures up to 1473 K<sup>4,36</sup>. For larger values of  $x$ , however, the XRD results clearly show reaction at the LSCF-YSZ interface occurs. For  $x \geq 0.4$  new peaks emerge at  $28.5^\circ$  and  $33.5^\circ$  which correspond to lanthanum zirconate,  $\text{La}_2\text{Zr}_2\text{O}_7$ . Additionally for  $x \geq 0.6$ , a small peak at  $30.9^\circ$  is evident which corresponds to strontium zirconate,  $\text{SrZrO}_3$ . The remaining peaks in these patterns, i.e. the doublet between  $32.5^\circ$  and  $34^\circ$ , correspond to LSCF. The positions of these peaks increase with increasing Co:Fe ratio, consistent with what was observed for the samples calcined at 1123 K. The fact that the doublet is now resolved also indicates a larger average crystallite size in the LSCM film in the samples calcined at 1373 K relative to those calcined at only 1123 K.

Effect of cobalt concentration

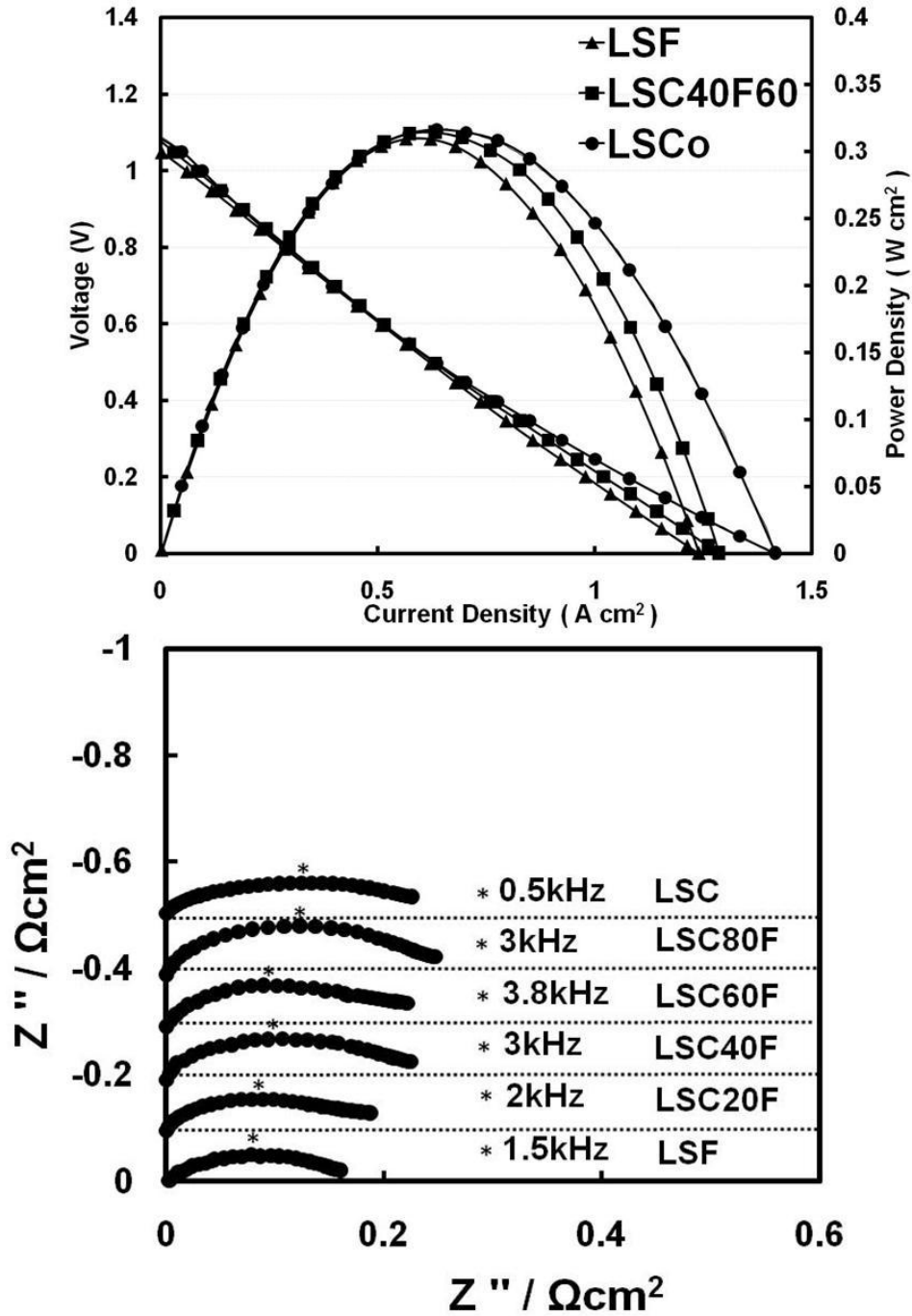


**Figure 9.3:** a) Performance curves and b) Electrochemical impedance spectra obtained at open circuit for fuel cells with infiltrated LSCF cathodes that had been calcined at 1123 K. The composition of the LSCF used in each cell is indicated in the figure.

Figure 9.3 displays Nyquist plots of the open-circuit electrochemical impedance data at 973 K for all of the LSCF -YSZ composites that were sintered at 1123 K. The ohmic impedances of the cells varied by less than  $0.1 \Omega \text{ cm}^2$  and have been subtracted from the spectra to facilitate comparison. LSC has a higher electronic and ionic conductivity than LSF and increasing the Co to Fe ratio in the perovskite would therefore be expected to extend the width of the active TPB region and give higher performance<sup>1,12,19,20,28,30</sup>. As shown in the figure, this is not what was observed and instead the ASR of the electrodes increased from  $0.18 \Omega \text{ cm}^2$  for LSF to  $0.22$  and  $0.21 \Omega \text{ cm}^2$  for LSC80F and LSC, respectively. The XRD results in Figure 9.1 do not provide evidence for reaction between LSC or LSCF and YSZ for a calcination temperature of only 1173 K, but the impedance results suggest that some reaction at the interface may still occur for these conditions. The possibility that slight structural variations are the origin of the small differences can also not be completely ruled out.

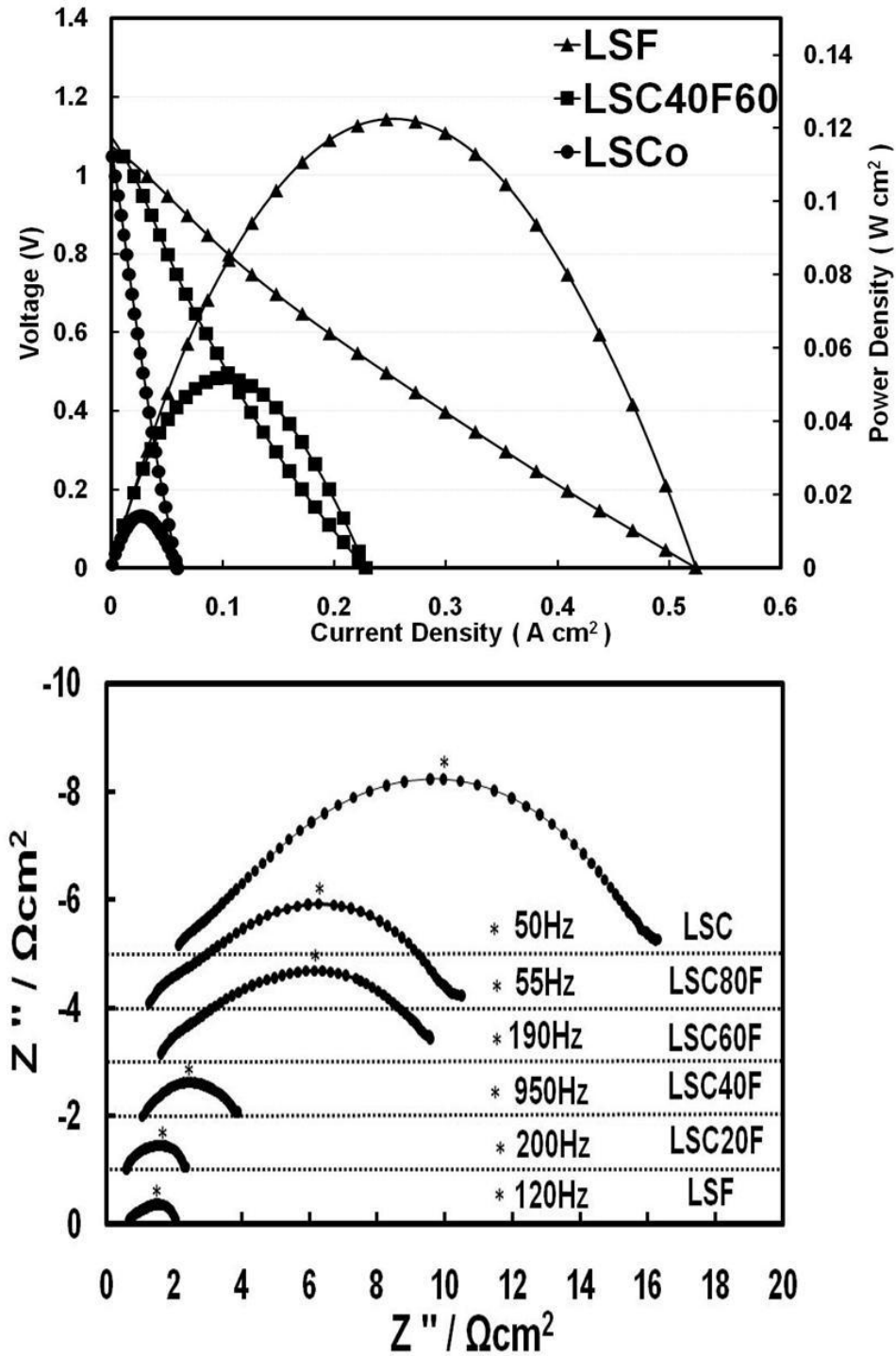


**Figure 9.4:** a) Performance curves and b) Electrochemical impedance spectra obtained at open circuit for fuel cells with infiltrated LSCF cathodes that had been calcined at 1373 K. The composition of the LSCF used in each cell is indicated in the figure.



The open-circuit impedance spectra at 973 K for LSCF-YSZ composites that were calcined at 1373 K are shown in Figure 9.4. Declines in performance were observed and the ASR of the electrodes all increased for this higher calcination temperature. The increases were much more precipitous, however, for the higher cobalt content electrodes. For example, the ASR of the LSF- and LSC20F-YSZ composite electrodes increased by  $\sim 1.2 \text{ } \Omega \text{ cm}^2$  upon increasing the calcination temperature from 1173 to 1373 K. In contrast for LSC60F, LSC80F and LSC, the ASR increased by 7.6, 8.5, and  $13.7 \text{ } \Omega \text{ cm}^2$ , respectively. We have previously shown that significant coarsening of the LSCF particles occurs upon calcination at  $1373 \text{ K}^{27}$ . This causes a decrease in TPB sites and is likely the cause of the increase in the ASR for the LSF- and LSC20F-YSZ composites. The large increases for high Co:Fe ratios, however, are almost certainly due to reaction of the LSCF and the YSZ forming insulating  $\text{La}_2\text{Zr}_2\text{O}_7$  or  $\text{SrZrO}_3$  phases at the interface as demonstrated by the XRD results in Figure 9.2.

The data in Figure 9.4 also show that the ohmic resistance of the cells increased with increasing Co content in the perovskite. This occurred in spite of the fact that increasing the Co content increases the electronic conductivity of the LSCF and provides additional evidence for the formation of insulating phases at the LSCF-YSZ interface. The data also show, however, that the propensity for the LSCF to react with the YSZ to form  $\text{La}_2\text{Zr}_2\text{O}_7$  or  $\text{SrZrO}_3$  is a strong function of the Co:Fe ratio in the perovskite. Note that formation of these insulating phases is much less problematic for Co concentrations less than 40 %. Indeed the ASR of LSC20F is nearly identical to that of LSF, even after calcining at 1373 K. This suggests that the LSC20F composition may provide a good

compromise between the increase in electronic conductivity and the decrease in chemical stability that added Co imparts to LSF.

#### *Effectiveness of SDC interlayers*

As noted above, thin ceria layers between the YSZ and the perovskite phase are often used to enhance or stabilize cathode performance. For some cathode materials such as LSC, ceria interlayers clearly act as a protective barrier that prevents reactions at the LSC-YSZ interface<sup>13,17,37,38</sup>. Even for cathode materials, such as LSF, which do not appear to react with YSZ under typical synthesis and operating conditions, there are reports in the literature that ceria interlayers still enhance performance<sup>4,31</sup>. In this case, the mechanism by which the ceria could enhance performance is less clear, although increasing the active surface area and improving the O<sub>2</sub> surface exchange kinetics<sup>4,22,31</sup> have both been proposed. To further investigate these possibilities we investigated the effect of an SDC interlayer prepared using infiltration methods on the performance and stability of LSF-, LSC20F-, and LSC-YSZ composite cathodes.

SDC layers, approximately 0.1 μm in thickness, were added to the porous YSZ scaffolds using wet infiltration as described in the experimental section and were calcined at 1473 K for 2 h prior to adding the perovskite phase and then calcined at 1373 K for 4 h. We have previously shown that the 1473 K calcination treatment for the SDC layer produces a continuous, dense SDC coating over the YSZ<sup>17,39</sup>.

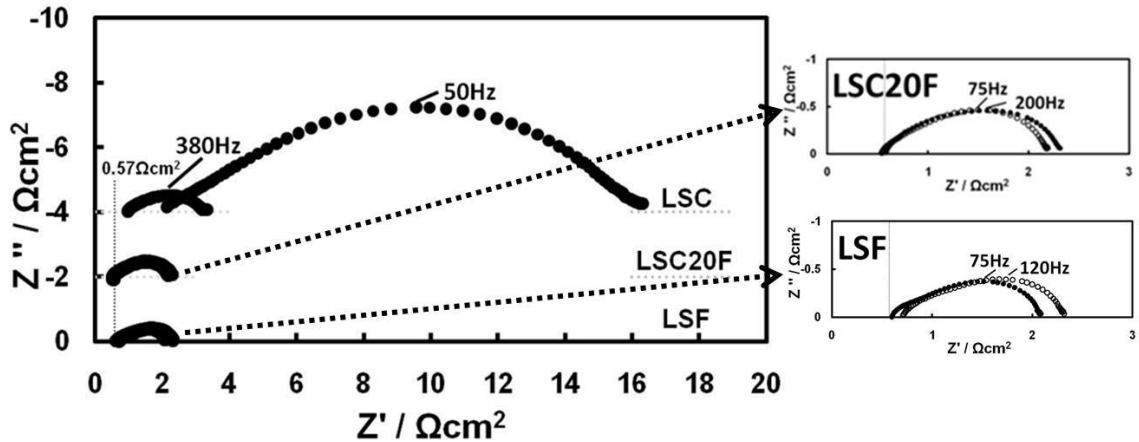


**Figure 9.5:** Electrochemical impedance spectra obtained at open circuit for fuel cells with infiltrated LSC, LSC20F, and LSF cathodes with (open symbols) and without (filled symbols) infiltrated SDC interlayers. The cathodes were calcined at 1373 K prior to collecting the data.

Figure 9.5 shows electrochemical impedance spectra for the LSF-, LSC20F-, and LSC-based electrodes, both with and without the SDC interlayer, at 973 K. Note that for the LSF and LSC20F cathodes the addition of the SDC interlayer had a negligible effect on the impedance characteristics and thermal stability. The ohmic and non-ohmic ASR for both LSF and LSC20F calcined at 1373 K were  $0.57 \pm 0.1 \Omega \text{ cm}^2$  and  $1.5 \pm 0.1 \Omega \text{ cm}^2$ , respectively, with or without the SDC layer. These results are consistent with the XRD data in Figure 9.2 which shows that these materials do not react with YSZ at temperatures up to 1373 K.

As shown by a comparison of the data in Figure 9.3 and 9.5, the performance of the infiltrated LSF and LSC20F electrodes, with or without SDC interlayers, still degraded upon increasing the calcination temperature of the perovskite phase from 1123 to 1373 K. As we have reported previously for LSF-YSZ electrodes<sup>19</sup>, we believe that this degradation results from additional coarsening of the LSF and LSC20F particles at

the higher calcination temperature resulting in a loss of active surface area and the formation of a more dense coating of the perovskite phase over the YSZ. This decreases the concentration of exposed TPB sites and increases the average distance that the oxygen ions must travel through the LSCF. A decrease in the performance of screen-printed LSCF electrodes upon increasing the calcination temperature from 1353 to 1393 K has also been partly attributed to a loss in surface area by Mai, et al.<sup>36</sup>.

Our observation that SDC interlayers do not affect the performance and stability of infiltrated LSF and LSC20F electrodes is different than what has been reported in previous studies of screen printed electrodes in which positive effects for ceria interlayers have been observed<sup>4,26,31</sup>. For example, Simner, et al.<sup>4</sup> report significant performance enhancements when a several micron thick porous SDC layer is placed between the LSF and the dense YSZ electrolyte. Mai, et al. report similar results for LSC20F using gadolinia-doped ceria (GDC)<sup>36</sup> interlayers. In both of these studies it is suggested that the improvement in performance is at least partially due to the high ionic conductivity of the doped ceria, which presumably increases the density of active TPB sites. Mai, et al. also suggest that for LSC20F that contains a high ratio of Sr to La, preventing the formation of SrZrO<sub>3</sub> via reaction with the YSZ still plays a role.

The suggestion that ceria interlayers enhance performance via increasing ionic conductivity may indeed be the case when conventional methods are used for cathode fabrication, such as screen printing a slurry containing particles of the perovskite onto an already dense YSZ electrolyte layer, followed by calcination in air. In this approach the calcination temperature, must be low enough to prevent reaction between the perovskite

and the YSZ and is typically between 1423K and 1523K, which may be too low to form a well sintered, interconnected perovskite phase in the electrode. For electrodes formed in this manner there may be relatively few channels for oxygen ion transport in the mixed conducting perovskite. This will limit the thickness of the active TPB region and degrade overall performance. For electrodes with this structure, a porous SDC interlayer may help to enhance  $O^{2-}$  ion transport and produce electrodes with thicker electrochemically active regions. The situation is different, however, for the infiltrated cathodes used in this study where the electrode architecture consists of a thin film of the perovskite covering a highly porous, well sintered, YSZ or SDC-coated YSZ backbone, both of which provide channels for ion conduction and therefore large TPB regions.

In contrast to LSF and LSC20F, the addition of an SDC interlayer had a dramatic effect on the performance and stability of the LSC-YSZ composite electrode. Without the SDC layer the ohmic and non-ohmic ASR were  $2.1 \Omega \text{ cm}^2$  and  $14 \Omega \text{ cm}^2$ , respectively. Note that the non-ohmic ASR is  $1.5 \Omega \text{ cm}^2$ , greater than the expected value for the 100  $\mu\text{m}$  thick YSZ electrolyte. As shown by the XRD data in Figure 9.2, the high ohmic and non-ohmic ASR are clearly due to reaction at the LSC-YSZ interface resulting in the formation of insulating layers of  $\text{La}_2\text{Zr}_2\text{O}_7$  and  $\text{SrZrO}_3$ . Placing an SDC layer between the LSC and YSZ was effective in preventing these deleterious reactions from taking place although modest increases in the ohmic and non-ohmic ASR to  $0.97 \Omega \text{ cm}^2$  and  $2.1 \Omega \text{ cm}^2$ , respectively, were still observed.

## 9.4 Conclusion

The propensity of infiltrated layers of  $\text{La}_{0.8}\text{Sr}_{0.2}\text{Co}_x\text{Fe}_{1-x}\text{O}_3$  to react with YSZ was studied as a function of the LSCF calcination temperature and the Co:Fe ratio. For a calcination temperature of 1123 K, both XRD and impedance spectroscopy did not provide any evidence for significant reaction at the LSCF-YSZ interface for all LSCF compositions. For a calcination temperature of 1373 K, however, reaction at the interface to form insulating  $\text{La}_2\text{Zr}_2\text{O}_7$  and  $\text{SrZrO}_3$  phases was observed for x values greater than 0.2. This result suggests that LSC20F may provide a good compromise between the higher electronic conductivity and lower chemical compatibility with YSZ that occurs with increasing Co concentration in the LSCF.

Infiltrated SDC interlayers were also shown to be effective in preventing deleterious, solid-state, reactions at the LSCF-YSZ interface. In contrast to previous studies of LSCF electrodes with doped-ceria interlayers that were produced by screen printing, infiltrated SDC interlayers covering a porous YSZ electrode scaffold were not found to provide any enhancement of the overall performance of LSF or LSC20F.

## 9.5 References

- 1 Kishimoto, H. *et al.* Cation transport behavior in SOFC cathode materials of  $\text{La}_{0.8}\text{Sr}_{0.2}\text{CoO}_3$  and  $\text{La}_{0.8}\text{Sr}_{0.2}\text{FeO}_3$  with perovskite structure. *Solid State Ionics* **178**, 1317-1325, doi:DOI 10.1016/j.ssi.2007.07.001 (2007).
- 2 Ralph, J. M., Rossignol, C. & Kumar, R. Cathode materials for reduced-temperature SOFCs. *J Electrochem Soc* **150**, A1518-A1522, doi:Doi 10.1149/1.1617300 (2003).
- 3 Simner, S. P. *et al.* Optimized lanthanum ferrite-based cathodes for anode-supported SOFCs. *Electrochem Solid St* **5**, A173-A175, doi:Doi 10.1149/1.1483156 (2002).
- 4 Simner, S. P. *et al.* Development of lanthanum ferrite SOFC cathodes. *J Power Sources* **113**, 1-10, doi:Pii S0378-7753(02)00455-X (2003).
- 5 Simner, S. P., Anderson, M. D. & Stevenson, J. W.  $\text{La}(\text{Sr})\text{FeO}_3$  SOFC cathodes with marginal copper doping. *J Am Ceram Soc* **87**, 1471-1476 (2004).
- 6 Huang, Y. Y., Vohs, J. M. & Gorte, R. J. Fabrication of Sr-doped  $\text{LaFeO}_{(3)}$ YSZ composite cathodes. *J Electrochem Soc* **151**, A646-A651, doi:Doi 10.1149/1.1652053 (2004).
- 7 Horita, T. *et al.* Oxygen reduction mechanism at porous  $\text{La}_{1-x}\text{Sr}_x\text{CoO}_{3-d}$  cathodes/ $\text{La}_{0.8}\text{Sr}_{0.2}\text{Ga}_{0.8}\text{Mg}_{0.2}\text{O}_{2.8}$  electrolyte interface for solid oxide fuel cells. *Electrochim Acta* **46**, 1837-1845 (2001).

- 8 Huang, Y. Y., Ahn, K., Vohs, J. M. & Gorte, R. J. Characterization of Sr-doped LaCoO<sub>3</sub>-YSZ composites prepared by impregnation methods. *J Electrochem Soc* **151**, A1592-A1597, doi:Doi 10.1149/1.1789371 (2004).
- 9 Skinner, S. J. Recent advances in Perovskite-type materials for solid oxide fuel cell cathodes. *Int J Inorg Mater* **3**, 113-121 (2001).
- 10 Uchida, H., Arisaka, S. & Watanabe, M. High performance electrodes for medium-temperature solid oxide fuel cells: Activation of La(Sr)CoO<sub>3</sub> cathode with highly dispersed Pt metal electrocatalysts. *Solid State Ionics* **135**, 347-351 (2000).
- 11 Kungas, R., Kivi, I., Lust, K., Nurk, G. & Lust, E. Statistical method to optimize the medium temperature solid oxide fuel cell electrode materials. *J Electroanal Chem* **629**, 94-101, doi:DOI 10.1016/j.jelechem.2009.01.033 (2009).
- 12 Sun, C. W., Hui, R. & Roller, J. Cathode materials for solid oxide fuel cells: a review. *J Solid State Electr* **14**, 1125-1144, doi:DOI 10.1007/s10008-009-0932-0 (2010).
- 13 Shiono, M. *et al.* Effect of CeO<sub>2</sub> interlayer on ZrO<sub>2</sub> electrolyte/La(Sr)CoO<sub>3</sub> cathode for low-temperature SOFCs. *Solid State Ionics* **170**, 1-7, doi:DOI 10.1016/j.ssi.2004.02.018 (2004).
- 14 Mizusaki, J., Tabuchi, J., Matsuura, T., Yamauchi, S. & Fueki, K. Electrical-Conductivity and Seebeck Coefficient of Nonstoichiometric La<sub>1-x</sub>Sr<sub>x</sub>CoO<sub>3-Delta</sub>. *J Electrochem Soc* **136**, 2082-2088, doi:Doi 10.1149/1.2097187 (1989).



- 15 Teraoka, Y., Zhang, H. M., Okamoto, K. & Yamazoe, N. Mixed Ionic-Electronic Conductivity of  $\text{La}_{1-x}\text{Sr}_x\text{Co}_{1-y}\text{Fe}_y\text{O}_{3-\Delta}$  Perovskite-Type Oxides. *Mater Res Bull* **23**, 51-58, doi:Doi 10.1016/0025-5408(88)90224-3 (1988).
- 16 Sekido, S., Tachibana, H., Yamamura, Y. & Kambara, T. Electric Ionic-Conductivity in Perovskite-Type Oxides,  $\text{Sr}_x\text{La}_{1-x}\text{Co}_{1-y}\text{Fe}_y\text{O}_{3-\Delta}$ . *Solid State Ionics* **37**, 253-259, doi:Doi 10.1016/0167-2738(90)90184-S (1990).
- 17 Kungas, R., Bidrawn, F., Vohs, J. M. & Gorte, R. J. Doped-Ceria Diffusion Barriers Prepared by Infiltration for Solid Oxide Fuel Cells. *Electrochem Solid St* **13**, B87-B90, doi:Doi 10.1149/1.3432253 (2010).
- 18 Peters, C., Weber, A. & Ivers-Tiffée, E. Nanoscaled  $(\text{La}_{0.5}\text{Sr}_{0.5})\text{CoO}_{(3-\Delta)}$  thin film cathodes for SOFC application at 500 degrees C < T < 700 degrees C. *J Electrochem Soc* **155**, B730-B737, doi:Doi 10.1149/1.2909552 (2008).
- 19 Wang, W. S., Gross, M. D., Vohs, J. M. & Gorte, R. J. The stability of LSF-YSZ electrodes prepared by infiltration. *J Electrochem Soc* **154**, B439-B445, doi:Doi 10.1149/1.2709510 (2007).
- 20 Vohs, J. M. & Gorte, R. J. High-Performance SOFC Cathodes Prepared by Infiltration. *Adv Mater* **21**, 943-956, doi:DOI 10.1002/adma.200802428 (2009).
- 21 Jiang, S. P. A review of wet impregnation - An alternative method for the fabrication of high performance and nano-structured electrodes of solid oxide fuel cells. *Mat Sci Eng a-Struct* **418**, 199-210, doi:DOI 10.1016/j.msea.2005.11.052 (2006).

- 22 Sholklapper, T. Z., Lu, C., Jacobson, C. P., Visco, S. J. & De Jonghe, L. C. LSM-infiltrated solid oxide fuel cell cathodes. *Electrochem Solid St* **9**, A376-A378, doi:Doi 10.1149/1.2206011 (2006).
- 23 Shah, M. & Barnett, S. A. Solid oxide fuel cell cathodes by infiltration of  $\text{La}_{0.6}\text{Sr}_{0.4}\text{Co}_{0.2}\text{Fe}_{0.8}\text{O}_{3-(\delta)}$  into Gd-Doped Ceria. *Solid State Ionics* **179**, 2059-2064, doi:DOI 10.1016/j.ssi.2008.07.002 (2008).
- 24 Hansen, K. K., Wandel, M., Liu, Y. L. & Mogensen, M. Effect of impregnation of  $\text{La}_{0.85}\text{Sr}_{0.15}\text{MnO}_3$ /yttria stabilized zirconia solid oxide fuel cell cathodes with  $\text{La}_{0.85}\text{Sr}_{0.15}\text{MnO}_3$  or  $\text{Al}_2\text{O}_3$  nano-particles. *Electrochim Acta* **55**, 4606-4609, doi:DOI 10.1016/j.electacta.2010.03.017 (2010).
- 25 Holc, J., Kuscer, D., Hrovat, M., Bernik, S. & Kolar, D. Electrical and microstructural characterisation of  $(\text{La}_{0.8}\text{Sr}_{0.2})(\text{Fe}_{1-x}\text{Al}_x)\text{O}_3$  and  $(\text{La}_{0.8}\text{Sr}_{0.2})(\text{Mn}_{1-x}\text{Al}_x)\text{O}_3$  as possible SOFC cathode materials. *Solid State Ionics* **95**, 259-268, doi:Doi 10.1016/S0167-2738(96)00595-4 (1997).
- 26 Simner, S. P., Shelton, J. P., Anderson, M. D. & Stevenson, J. W. Interaction between  $\text{La}(\text{Sr})\text{FeO}_{(3)}$  SOFC cathode and YSZ electrolyte. *Solid State Ionics* **161**, 11-18, doi:Doi 10.1016/S0167-2738(03)00158-9 (2003).
- 27 Bidrawn, F., Kim, G., Aramrueang, N., Vohs, J. M. & Gorte, R. J. Dopants to enhance SOFC cathodes based on Sr-doped  $\text{LaFeO}_3$  and  $\text{LaMnO}_3$ . *J Power Sources* **195**, 720-728, doi:DOI 10.1016/j.jpowsour.2009.08.034 (2010).
- 28 Esquirol, A., Brandon, N. P., Kilner, J. A. & Mogensen, M. Electrochemical characterization of  $\text{La}_{0.6}\text{Sr}_{0.4}\text{Co}_{0.2}\text{Fe}_{0.8}\text{O}_3$  cathodes for intermediate-temperature

- SOFCs. *J Electrochem Soc* **151**, A1847-A1855, doi:Doi 10.1149/1.1799391 (2004).
- 29 Jiang, S. P. A comparison of O-2 reduction reactions on porous (La,Sr)MnO<sub>3</sub> and (La,Sr)(Co,Fe)O<sub>3</sub> electrodes. *Solid State Ionics* **146**, 1-22 (2002).
- 30 Kim, J. H., Park, Y. M. & Kim, H. Nano-structured cathodes based on La<sub>0.6</sub>Sr<sub>0.4</sub>Co<sub>0.2</sub>Fe<sub>0.8</sub>O<sub>3-delta</sub> for solid oxide fuel cells. *J Power Sources* **196**, 3544-3547, doi:DOI 10.1016/j.jpowsour.2010.12.029 (2011).
- 31 Martinez-Amesti, A. *et al.* Reactivity between La(Sr)FeO<sub>3</sub> cathode, doped CeO<sub>2</sub> interlayer and yttria-stabilized zirconia electrolyte for solid oxide fuel cell applications. *J Power Sources* **185**, 401-410, doi:DOI 10.1016/j.jpowsour.2008.06.049 (2008).
- 32 Park, S., Gorte, R. J. & Vohs, J. M. Tape cast solid oxide fuel cells for the direct oxidation of hydrocarbons. *J Electrochem Soc* **148**, A443-A447 (2001).
- 33 Orlovskaya, N., Anderson, H., Brodnikovskyy, M., Lugovy, M. & Reece, M. J. Inelastic deformation behavior of La<sub>0.6</sub>Sr<sub>0.4</sub>FeO<sub>3</sub> perovskite. *J Appl Phys* **100**, doi:Artn 026102, Doi 10.1063/1.2218026 (2006).
- 34 Dann, S. E., Currie, D. B., Weller, M. T., Thomas, M. F. & Alrawwas, A. D. The Effect of Oxygen Stoichiometry on Phase-Relations and Structure in the System La<sub>1-x</sub>Sr<sub>x</sub>FeO<sub>3-Delta</sub> (0-Less-Than-or-Equal-to-X-Less-Than-or-Equal-to-1, 0-Less-Than-or-Equal-to-Delta-Less-Than-or-Equal-to-0.5). *J Solid State Chem* **109**, 134-144, doi:DOI 10.1006/jssc.1994.1083 (1994).

- 35 Jiang, Y. *et al.* Study of the local distortions of the perovskite system  $\text{La}_{1-x}\text{Sr}_x\text{CoO}_3$  ( $0 \leq x \leq 0.35$ ) using the extended x-ray absorption fine structure technique. *Phys Rev B* **80**, doi:Artn 144423  
Doi 10.1103/Physrevb.80.144423 (2009).
- 36 Mai, A., Haanappel, V. A. C., Uhlenbruck, S., Tietz, F. & Stover, D. Ferrite-based perovskites as cathode materials for anode-supported solid oxide fuel cells Part I. Variation of composition. *Solid State Ionics* **176**, 1341-1350, doi:DOI 10.1016/j.ssi.2005.03.009 (2005).
- 37 Sase, M. *et al.* Interfacial reaction and electrochemical properties of dense (La,Sr)  $\text{CoO}_{3-\delta}$  cathode on YSZ(100). *J Phys Chem Solids* **66**, 343-348, doi:DOI 10.1016/j.jpcs.2004.06.057 (2005).
- 38 Rossignol, C., Ralph, J. M., Bae, J. M. & Vaughey, J. T.  $\text{Ln}_{(1-x)}\text{Sr}_x\text{CoO}_{(3)}$  (Ln=Gd, Pr) as a cathode for intermediate-temperature solid oxide fuel cells. *Solid State Ionics* **175**, 59-61, doi:DOI 10.1016/j.ssi.2004.09.021 (2004).
- 39 Kim, G., Vohs, J. M. & Gorte, R. J. Enhanced reducibility of ceria-YSZ composites in solid oxide electrodes. *J Mater Chem* **18**, 2386-2390, doi:Doi 10.1039/B718931a (2008).

## Chapter 10. Conclusions

While Ni/YSZ cermets have been used successfully in SOFCs, they also have several limitations, thus motivating the use of highly conductive ceramics to replace the Ni components in SOFC anodes. Ceramic electrodes are promising for use in SOFC anodes because they are expected to be less susceptible to sintering and coking, be redox stable, and be more tolerant of impurities like sulfur. For the catalytic studies, the infiltration procedure has been used to form composites which have greatly simplified the search for the best ceramics for anode applications. Although some progress has been made in achieving this goal using mixed oxides based on titanates, manganates, and chromates with the perovskite structure, these materials have bulk electronic conductivities  $< 5 \text{ S cm}^{-1}$  under typical SOFC anode operating conditions. When used in a porous perovskite-YSZ composite anode, the overall conductivity will be 1-2 orders of magnitude lower. Thus, for these materials to be used in SOFC anodes the electrode must be very thin ( $< 50 \text{ }\mu\text{m}$ ) in order to limit ohmic losses or the perovskite must be restricted to a thin functional layer near the electrolyte.

Another class of oxides, which has not been fully explored for use in SOFC anodes but whose members have very high electronic conductivities under reducing conditions, is the tungsten bronzes. In Chapter 3, several highly conductive tungsten bronzes SOFC anodes were investigated for use in SOFC anodes. While the  $\text{Na}_{0.8}\text{WO}_{3-\delta}$ -YSZ composite exhibited high conductivities as high as  $130 \text{ S/cm}$  at  $973 \text{ K}$ , the tungsten bronzes are not stable as they tend to be reduced to metallic tungsten under reducing conditions at temperatures higher than  $1073 \text{ K}$ . Nevertheless, they could still find application at

temperatures below 1073 K. Because the tungsten bronzes have only modest catalytic activity, good anode performance requires the addition of a catalytic component.

Rare earth (RE) vanadates (REVO<sub>4</sub>), such as CeVO<sub>4</sub>, are another class of oxides that can have high electronic conductivities under some conditions and are chemically stable in a variety of fuels including H<sub>2</sub>, H<sub>2</sub>S, and CH<sub>4</sub>, and, therefore, show some promise for use in SOFC anodes. The effect of partial substitution of alkaline earth (AE) ions, Sr<sup>2+</sup> and Ca<sup>2+</sup>, for the rare earth (RE) ions, La<sup>3+</sup>, Ce<sup>3+</sup>, Pr<sup>3+</sup>, and Sm<sup>3+</sup>, on the physical properties of REVO<sub>4</sub> compounds were investigated and described in Chapter 4. The use of the Pechini method to synthesize the vanadates allowed for high levels of AE substitution to be obtained compared to those prepared using conventional solid-state synthesis routes. Coulometric titration was used to measure redox isotherms for these materials and showed that the addition of the AE ions increased both reducibility and electronic conductivity under SOFC anode conditions, through the formation of compounds with mixed vanadium valence. In spite of their high electronic conductivity, the alkaline earth doped, rare earth vanadates-YSZ composite anodes exhibited only modest performances when used in SOFCs operating with H<sub>2</sub> fuel at 973 K due to their low catalytic activity. High performance was obtained, however, after the addition of a small amount of catalytically active Pd to the anode.

While promising results have been obtained with ceramic-based anodes, it is clear that high performance can only be achieved after the addition of nanoparticles of a highly catalytic metal (e.g. Ni, Pt, or Pd) to the surface of the oxide. The catalytic metals are generally added using standard wet infiltration techniques. Due to the high operating

temperatures, deactivation of the metal catalyst by sintering and/or coking is a severe problem as loss of metal surface area due to sintering limits catalyst lifetime and efficiency. Two approaches aimed at mitigating metal catalyst deactivation which were achieved by: 1) designing a catalyst that is resistant to coking and sintering and 2) developing a new method for catalyst deposition, were presented.

The first approach involved synthesizing a self-regenerating, “smart” catalyst, in which Co, Cu, or Ni were inserted into the B-site of a perovskite oxide under oxidizing conditions and then brought back to the surface under reducing conditions. The physical and electrochemical properties of cerium vanadates in which a portion of the cerium cations have been substituted with transition metals ( $\text{Ce}_{1-x}\text{TM}_x\text{VO}_{4-0.5x}$ , TM = Ni, Co, Cu) were investigated and was described in Chapter 5. These materials have shown to exhibit unusually high redox stability as the lost surface area of sintered metal particles can be restored through an oxidation/reduction cycle. While high performance was achieved with both the Co and Ni doped cerium vanadates, they are not hydrocarbon tolerant due to the fact that both Co and Ni catalyze the formation of carbon filaments when exposed to hydrocarbons under reducing conditions.

In order to produce catalytic materials that have relatively high hydrocarbon tolerance using the exsolution method, the cerium cations are substituted with mixed transition metal systems ( $\text{Ce}_{0.8}\text{Sr}_{0.1}\text{Cu}_{0.05}\text{TM}_{0.05}\text{VO}_{4-0.5x}$ , TM = Ni or Co) and their suitability for use in SOFC anodes was examined in Chapter 6. The  $\text{Ce}_{0.8}\text{Sr}_{0.1}\text{Cu}_{0.05}\text{Co}_{0.05}\text{VO}_3$  appears to have high activity and relatively high hydrocarbon tolerance, suggesting that intimate contact between the exsolved Cu and Co and that the

majority of the Co nanoparticles must be at least partially coated with the Cu. The electrochemical performance when used in anodes operating on hydrogen has been characterized, and the results demonstrate the exsolution of both metals from the host lattice; but observed dynamic changes in the structure of the resulting metal nanoparticles as a function of SOFC operating conditions complicate their use in SOFC anodes.

The second strategy involves depositing novel highly active and thermally stable Pd@CeO<sub>2</sub> core-shell nanostructure catalysts onto a substrate surface which had been chemically modified to anchor the nanoparticles. Characterization of the deposition of Pd@CeO<sub>2</sub> particles on model planar YSZ single crystal supports was examined in Chapter 7. The results demonstrate that monolayer films of Pd@CeO<sub>2</sub> core-shell, nanocomposites can be produced on a planar YSZ(100) support using alkyl coupling agents, and that these films exhibit exceptionally high thermal stability and resistance to sintering compared to bare Pd particles on the same support. Additionally it was shown that the ceria shells in these nanostructures have unique properties being more reducible than bulk ceria which may play a role in the high activity of these materials for some reactions, such as methane combustion.

The similar approach used to graft monolayer films of highly catalytically active, Pd@CeO<sub>2</sub> core-shell nanocomposites onto a high surface area metal oxide powders or planar supports was also performed in a porous SOFC electrode, with the study described in Chapter 8. The SEM results indicated that the monolayer films of alkyl-capped Pd@CeO<sub>2</sub>, in contrast to bare Pd particles, remained highly dispersed even after calcination in air at 1373 K, suggesting that long-term stability can be expected for SOFC



operation at 973 K. Solid oxide fuel cells (SOFC) with monolayer films of the Pd@CeO<sub>2</sub> (0.01 wt. %) deposited on the TEOOS-treated LSCM-YSZ composite anode exhibited high electrochemical activity when operating on both H<sub>2</sub> and CH<sub>4</sub> fuels. In contrast to the cell with Pd nanoparticle catalyst where large decrease in performance was observed, high temperature calcination under both oxidizing and reducing conditions had only a small effect on the performance of the anode with the Pd@CeO<sub>2</sub> catalyst. The high electrochemical performance exhibited by these cells also suggest that the SiO<sub>x</sub> layer that was deposited on the surface of the anodes via reaction with TEOOS was shown to have any effect in hindering the oxygen ion transport from the LSCM to the YSZ electrolyte.

In the last chapter of the thesis, the propensity of infiltrated layers of LSCF to react with YSZ was studied as a function of the LSCF calcination temperature and the Co:Fe ratio. For a calcination temperature of 1123 K, both XRD and impedance spectroscopy did not provide any evidence for significant reaction at the LSCF-YSZ interface for all LSCF compositions. For a calcination temperature of 1373 K, however, reaction at the interface to form insulating La<sub>2</sub>Zr<sub>2</sub>O<sub>7</sub> and SrZrO<sub>3</sub> phases was observed for x values greater than 0.2. Infiltrated SDC interlayers were also shown to be effective in preventing deleterious, solid-state, reactions at the LSCF-YSZ interface. In contrast to previous studies of LSCF electrodes with doped-ceria interlayers that were produced by screen printing, infiltrated SDC interlayers covering a porous YSZ electrode scaffold were not found to provide any enhancement of the overall performance of LSF or LSC20F.